AN INVESTIGATION OF RADIO-WAVE SCATTERING IN THE INTERPLANETARY MEDIUM.

By

B. D. WARD B.Sc. (Hons)

A Dissertation presented for the Degree of

Doctor of Philosophy

at the

UNIVERSITY OF ADELAIDE

Department of Physics

July 1975.

I give consent to this copy of my thesis, when deposited in the University Library, being available for loan and photocopying.

Date .....8/9/75..... Signed .....

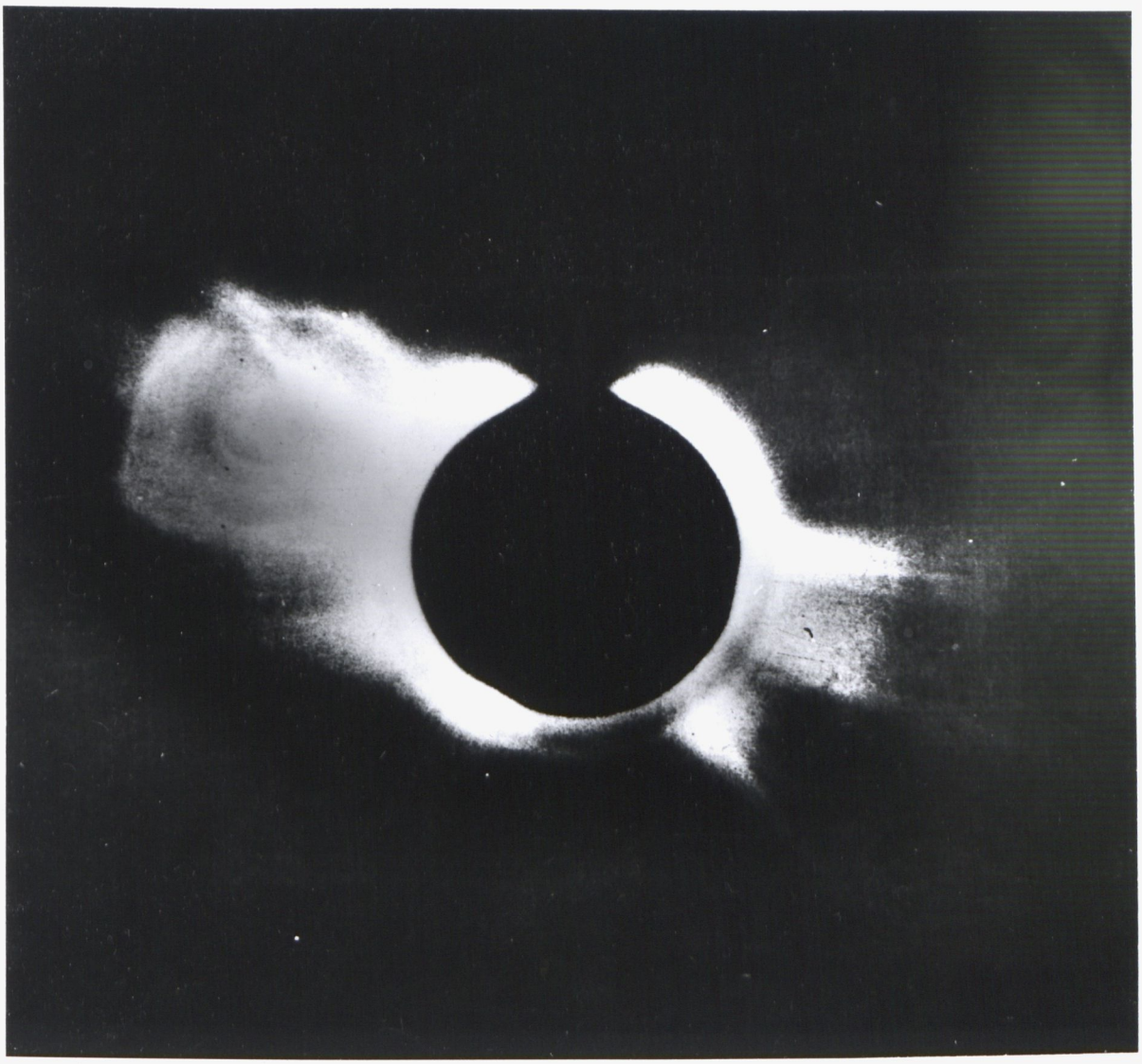

FRONTISPIECE

The solar corona at 0953 UT on June 10, 1973 as seen from Skylab.
(courtesy Dr. G. Newkirk, HAO)

C O N T E N T S

Contents continued.....

Contents continued.....

SUMMARY

This thesis contains a study of the outer corona and interplanetary medium based on observations of the effect of the scattering or radio waves by irregularities of electron density in the medium.

Chapter 1 provides a review of our current knowledge of conditions in the corona and interplanetary medium, with an emphasis on those aspects related to the present study. The basic theory relevant to radio-wave scattering studies is outlined in Chapter 2 together with a brief review of the results of previous studies of coronal broadening and interplanetary scintillation.

A system of three receivers located at the apex of a triangle of side ~100km North of Adelaide has been constructed to measure the solar wind velocity using interplanetary scintillations. The base station for this system was brought into operation during 1972 and the full system completed late in 1974. A description of the design and construction of this system is presented in Chapter 3. Scintillation observations were also recorded with the C.S.I.R.O. Radioheliograph at Culgoora, NSW. Details of the data recording and analysis procedures for both systems are discussed in Chapter 4. This chapter also presents the preliminary results available from the full spaced-receiver system.

By observing a "grid" of scintillating radio sources spaced around the sky it is possible to investigate the propagation of large-scale, flare-produced disturbances into the ambient interplanetary medium. In Chapter 5 the daily variations of a number of sources have been combined with spacecraft observations of the interplanetary plasma to derive a picture of the large scale expansion pattern of five such disturbances. Each of the

events can be related to a specific solar flare which exhibits evidence for both shock-wave and energetic plasma ejection into the corona. Each of the disturbances extended over a wide area of the interplanetary medium by the time the shock wave had reached 1AU, but exhibited marked deviation from the spherical symmetry suggested by some spacecraft observations. Evidence for distortion of the shock front, resulting from propagation into an inhomogeneous ambient medium containing large-scale, corotating structures, is also presented.

Much of the interpretation of interplanetary scintillation data has in the past been based on the scintillation index and power spectrum of the intensity fluctuations. Recently there has been some examination of the probability density functions (p.d.f.) of the intensity fluctuations. In Chapter 6 the p.d.f's for scintillation observations at 80, 111.5 and 160MHz are compared with the two theoretical forms predicted by radio-wave scattering theory. It is found that at these frequencies the p.d.f. is generally intermediate in form between the Rice-squared and lognormal forms but with a tendency to be more nearly Rice-squared than lognormal.

The power spectrum of the intensity fluctuations can, in the case of weak scattering, be directly related to the nature of the electron density irregularities in the interplanetary medium. Chapter 7 presents an investigation of the power spectra of interplanetary scintillations recorded at 80, 111.5 and 160MHz. The effects of a three-dimensional scattering medium and uncertainties in the structure of the radio sources make it difficult to distinguish between Gaussian and power-law forms for the irregularities in electron density with the observational data available.

Fresnel structures, which have been reported only rarely in the literature, have been found in some records. It is shown that these only occur where a strong perturbation in the density of the interplanetary plasma exists close to the Earth. Under normal conditions the effect of scattering along an extended line of sight is to "fill-in" these structures.

Chapter 8 presents a discussion of coronal broadening observations of the Crab Nebula made with the C.S.I.R.O. Radioheliograph during June 1972 to 1974. These results continue previous two-dimensional 80MHz observations into the decreasing phase of the solar cycle and extend the technique to 160MHz. The results are in agreement with previous interferometer observations and reveal a marked decrease in axial ratio of the density irregularities with the decreasing activity.

A summary of the results presented in the thesis and suggestions for future work in these areas are discussed in the final chapter.

P R E F A C E

This dissertation contains no material which has been submitted to any other University and to the best of the author's knowledge no material previously published by other persons, except where due reference is made. This thesis contains no material which has been accepted for the award of any degree or diploma in any University.

B.D. WARD.

UNIVERSITY OF ADELAIDE
15.8.75.

ACKNOWLEDGEMENTS

The work described in this thesis was carried out in the Department of Physics at the University of Adelaide, initially under the supervision of Dr P.A. Dennison and subsequent to his resignation by Dr B.H. Briggs, and Professor J.R. Prescott. The author is grateful to them, and to Dr W.G. Elford, for encouragement throughout the course of the work and for many helpful discussions.

The Adelaide Spaced-receiver array described in this thesis was under construction when the author joined the group. The receivers were designed by Dr P.A. Dennison and Mr R. Lomax. The Buckland Park and Burra aerial arrays were constructed by Mr Lomax and Drs M. Wiseman and R.G. Blesing. The author's contribution to this project involved the construction of the Kadina array, phasing of the three arrays and the design and construction of the telemetry and digital recording equipment. The author is indebted to Mr R.E. Lomax for his technical support in the construction and maintenance of the receiving equipment and to Mr W.H. Foo, who replaced Mr Lomax, for help with the operation of the system.

Some of the data analysed in this thesis was obtained with the CSIRO Radioheliograph at Culgoora, N.S.W . The author wishes to thank the CSIRO Division of Radiophysics for providing access to these facilities during visits in June 1971 to 1974, January 1974 and September 1974. In particular the author would like to thank Mr W.J. Payten and the staff of the heliograph for their helpful co-operation in maintaining the equipment during observations. Helpful discussions with Drs G.J. Nelson and S. Smerd are also acknowledged.

Several investigators provided spacecraft data prior to publication for the investigation of flare-produced disturbances. They are Dr S.J. Bame (Vela), Dr J.M. Wilcox (Pioneer 6,7), Dr J.H. Wolfe (Pioneer 9,10), Dr H. Rosenbauer (Heos-2) and Dr P.C. Hedgecock (Heos-2). Dr J.I. Vette of the World Data Centre also provided spacecraft data.

Finance for the projects was supplied by the Australian Research Grants Committee and the University of Adelaide. During the course of this work the author was supported by a Commonwealth Postgraduate Research Award.

CHAPTER 1

THE SOLAR CORONA AND INTERPLANETARY MEDIUM

1.1 INTRODUCTION

This thesis is concerned with the use of radio-wave scattering observations as a technique for probing the outer corona and the interplanetary medium. A review of the structure of these regions is presented in this chapter. The material reviewed has been obtained by a variety of techniques, including optical and radio observations of the sun, indirect probing of the interplanetary medium using radio-wave and cosmic ray propagation experiments, and direct sampling of the interplanetary plasma between 0.8 AU and 5.0 AU by spacecraft experiments.

The radio-wave scattering techniques provide a valuable method of investigating the properties of the interplanetary medium over a wide range of heliocentric co-ordinates. In particular they can be applied to those regions inaccessible to other methods. An outline of the theory associated with these techniques is presented in Chapter Two, along with a review of their application to the interplanetary medium.

1.2 THE SOLAR CORONA

The corona is the outermost layer of the sun's atmosphere and is characterized by its high temperature and low density relative to the underlying layers. Much of our knowledge of conditions in the corona comes from its white-light emission. Even though the temperature is high the low densities result in the white-light intensity being a factor of at

least 10^6 times lower than the photospheric emission. Most of the coronal emission in the visible region of the spectrum results from the scattering of photospheric light either by free electrons (K - corona) or from dust particles (F - corona). The K corona is the dominant component from 1.0 to 2.3 R_o beyond which the F corona becomes predominant.

The distribution of material within the corona is by no means uniform (see frontispiece) but is marked by features such as dense streamers and regions of lower than average density known as 'coronal holes'. These structures are determined primarily by the underlying photospheric magnetic fields and their extension into the corona. Streamers are regions of higher than normal density which form above the neutral line between extended photospheric regions of opposite polarity (Altschuler and Perry, 1970) while coronal holes are regions of weak, diverging magnetic fields which have a significantly lower density than the surrounding magnetically-closed regions (Altschuler et al., 1972).

The general shape and extent of such streamers are dependent on the phase of the solar activity cycle. At solar maximum the corona shows well-developed streamers at all position angles and as a whole, while not exactly spherical, is more nearly uniform than at solar minimum. During the period of low solar activity the streamers are concentrated around the equator and may show remarkable extension, although with little internal structure, and the polar regions possess a brush-like structure of fine plumes.

The most widely used technique for determining the average electron density distribution is the photometric observation of the K -

corona. Van de Hulst (1950) found that at solar maximum the variation of density with height above the solar surface could be described for all position angles by a single distribution. At solar minimum separate distributions were required to describe the densities above equatorial and polar regions. Newkirk (1959) derived a model for the quiet corona in which the electron density is approximately twice that of Van de Hulst's model. On average the density in an active streamer is twice that of the quiet corona (Newkirk, 1961). Considerable variations exist between observations even in the undisturbed corona (Leblanc et al., 1973) but most observations fall within the shaded region in Figure 1.1. The characteristics of type III radio bursts are consistent with electron densities twice those of the Newkirk active streamer model (8 - 10x VdH). This is probably indicative that these bursts are generated in the most dense portions of streamers.

Extension of photometric observations to large distances from the sun becomes uncertain due to the difficulty in accurately separating the contributions of the F and K coronas. This technique is generally considered reliable only below 10 R_o. Type III radio bursts have recently been detected at frequencies as low as 50kHz with spacecraft-borne receivers. Fainberg and Stone (1971) found a density distribution which is consistent with type III observations close to the sun and which indicate densities some 16 times those predicted by Newkirk's model corona. Alvarez and Haddock (1973) developed a model based on type III observations which maps well into electron densities measured in the lower corona and proton densities measured near the Earth's orbit.

Electron densities in the range 5 to 80 R_o can be obtained from the occultation of discrete radio sources. The degree of scattering which results when the radio wave passes through the outer corona can be related

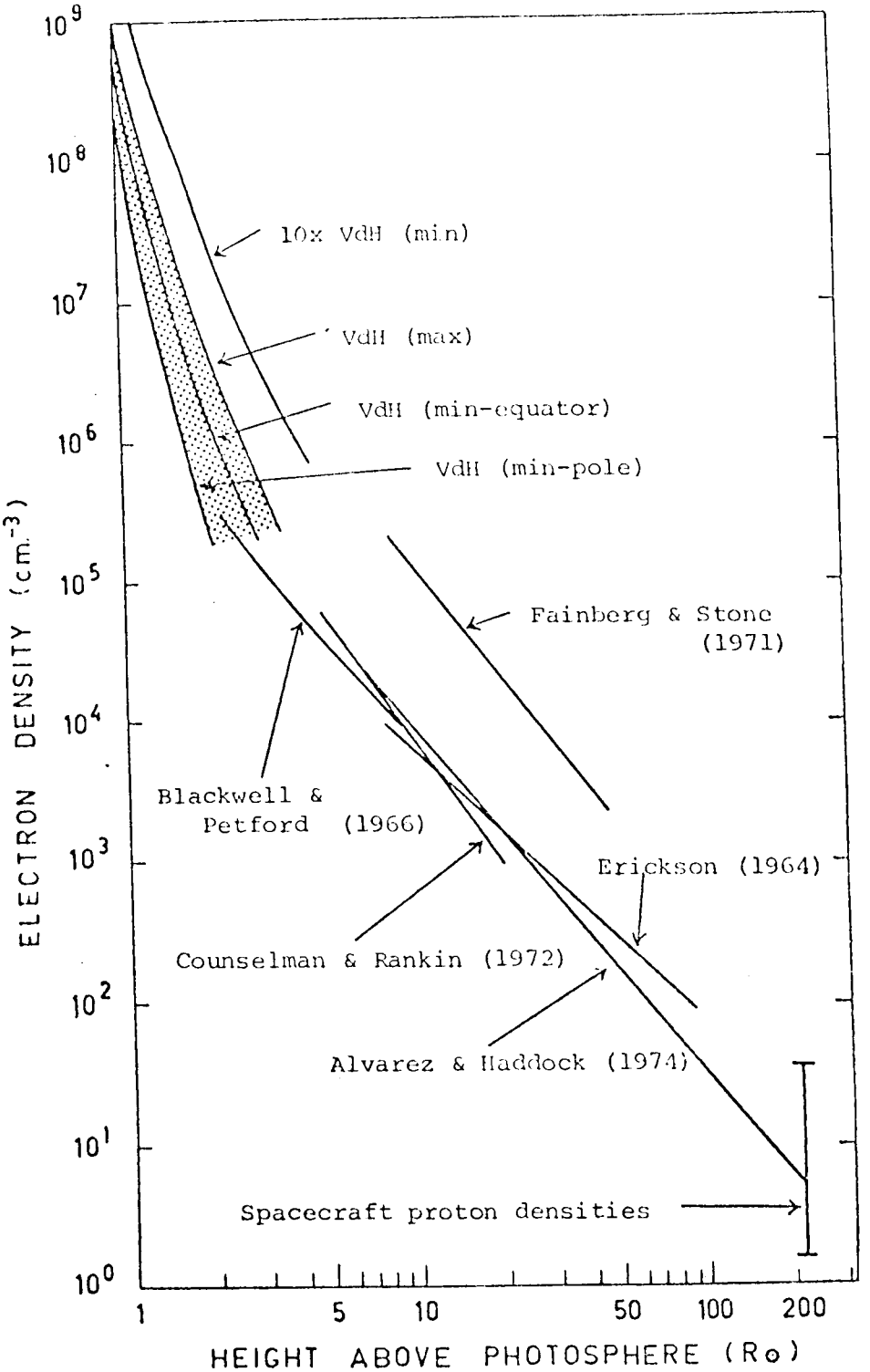

FIGURE 1.1 Electron densities in the corona and interplanetary medium.

to the electron density fluctuations in the corona (Erickson, 1964). This technique is discussed in more detail in Chapter Two. Measurement of the dispersion of pulses from the Crab Nebula pulsar as it is occulted by the corona yields the integrated density along the line of sight without the assumptions required by the scattering technique (Counselman and Rankin, 1972).

Altschuler and Perry (1972) have developed a technique for obtaining the three-dimensional electron density distribution of the corona from photometric observations. This technique depends on the fact that solar rotation has the effect of scanning the coronal structure past the observer, and assumes that the coronal structure remains static for the 14 days over which the observations are made. Recent synoptic observations from the Skylab coronagraph (Newkirk, private communication) reveal that the corona is in fact undergoing continual modification on a time scale at least as short as one hour.

1.3 THE SOLAR WIND AND INTERPLANETARY MEDIUM

The high temperature of the corona results in the continuous, supersonic expansion of the coronal plasma into the interplanetary medium (Parker, 1958), forming what has become known as the 'solar wind'. Relative motion of the plasma transverse to the photospheric magnetic field lines can only occur slowly since the hot plasma has a high electrical conductivity. Consequently the photospheric magnetic field will also be transported into the interplanetary region by the outflowing material. While the plasma moves radially outwards the magnetic field lines are swept back into a characteristic Archimedean spiral by the rotation of the sun.

The solar wind plasma is not uniform but exhibits significant variations over a wide range of time scales. Conditions within the plasma must reflect the properties of either the coronal plasma or the expansion mechanism. In this section we review the 'average' properties of the solar wind and related models of the coronal expansion. The two succeeding sections will review large scale perturbations of the ambient solar wind.

Most of our knowledge of the properties of the solar wind plasma has been determined from in-situ observations by spacecraft experiments. The flow speed and proton density can be obtained from measurements of the energy-per-charge distribution of the positive ion flux using electrostatic analyzers (e.g. Snyder and Neugebauer, 1964). The components of the interplanetary magnetic field can be measured with magnetometers (e.g. Ness et al, 1964). To date, most space probes have been restricted to heliocentric distances in the range 0.8 to 1.2 AU and limited to within $\pm 7^{\circ}$ of the ecliptic plane. Interplanetary scintillation observations have provided estimates of the solar wind velocity over a wider range of heliocentric latitude and distance. (e.g. Dennison and Hewish, 1967).

The solar wind speed near the Earth's orbit fluctuates on a time scale of hours within the range 250 to 1000 km sec^{-1}, the average speed being ~400 km sec^{-1}. Figure 1.2a shows the distribution of hourly-average wind speeds during 1967 (Hundhausen et al, 1970). This distribution has not shown any significant changes with the changing phase of the solar cycle (Gosling et al, 1971; Diodata et al, 1974). In particular it is interesting to note that there is no tendency for the solar wind speed to increase with the increase in solar activity.

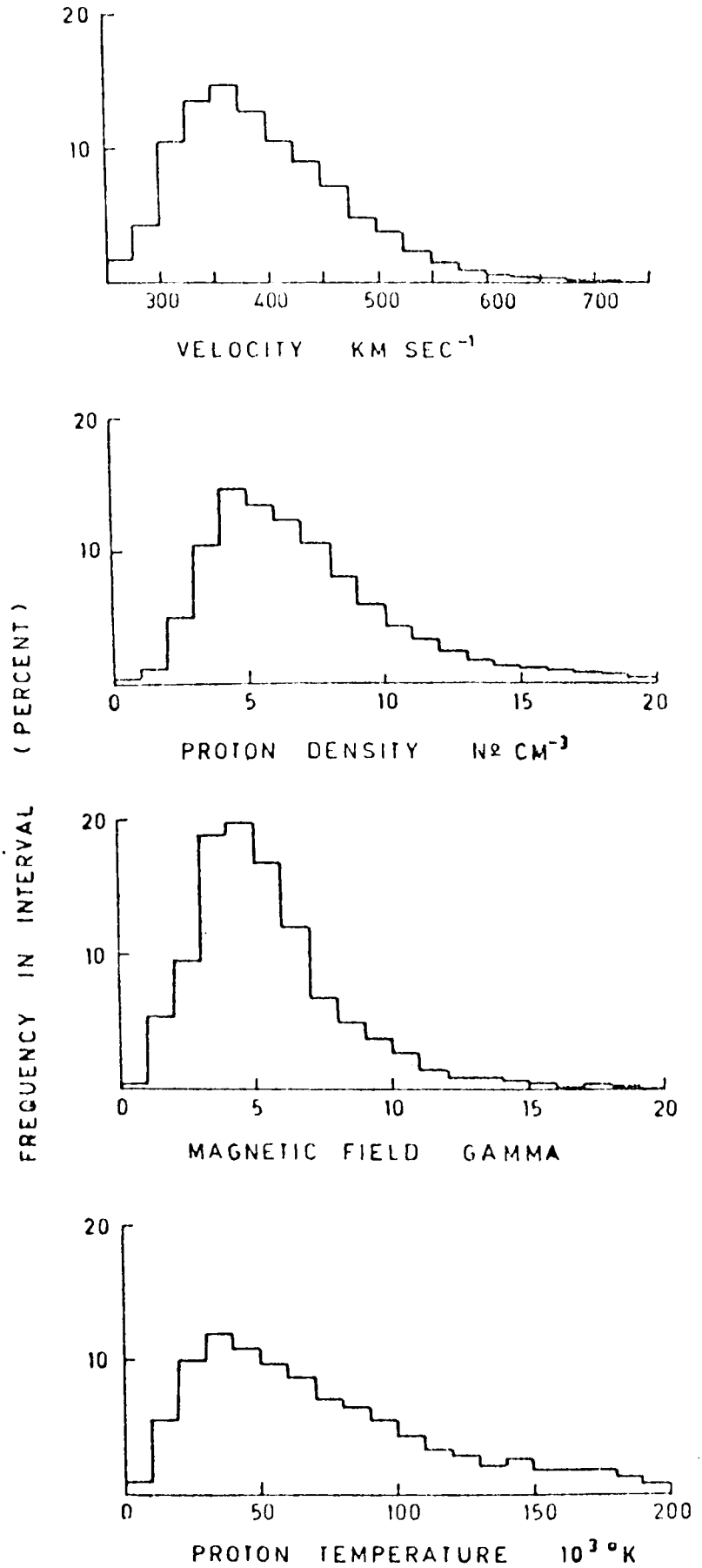

FIGURE 1.2 Average distributions of the solar wind plasma parameters.

The mean direction of flow of the plasma is ~1.5° from the East with an rms deviation ~3° (Strong et al, 1966). Deviations greater than 10° from the radial are rare but deviations up to 6° occur frequently (Wolfe et al, 1966). This mean flow direction results from a slight corotation of the plasma with the sun, giving rise to an azimuthal velocity ~ 10 km sec^{-1} at the Earth's orbit.

The proton density also shows large variations on a time scale of hours. Density measurements range from 0.1 to 100 cm^{-3} near 1 AU, with an average density of 5 cm^{-3}. The distribution of proton densities during 1967 (Hundhausen et al, 1970) is shown in Figure 1.2b. Unlike the wind speed, the yearly distribution of densities shows a marked dependence on the phase of the solar cycle. In particular the yearly mean density decreased by 40% from 1967 (near solar minimum) to 1969-70 (solar maximum). This appears to reflect latitudinal changes in the solar wind, presumably resulting from latitudinal changes in the solar activity (Diodata et al, 1974). Electron density measurements are more difficult to obtain but they are usually equal to the proton density within the errors of measurement (Bame et al, 1968).

The temperature of the interplanetary plasma is defined in terms of the velocity dispersion in the frame of reference moving at the bulk speed of the plasma. The mean proton temperature at 1 AU is ~ 5×10^4 °K while the mean electron temperature is ~ 1.5×10^5 °K. When averaged on a time scale of several solar rotations the proton temperature increases monotonically with the bulk speed. On a shorter time scale the temperature-velocity relation can be resolved into two components, one of which is the same as the macro-scale relation (Burlaga and Ogilvie, 1973). This implies that the macro-scale relation is determined primarily by the

proton heating mechanism within 50 R_0 rather than by other nonsteady interplanetary processes.

The proton velocity distribution is asymmetrical, with the axis of the anisotropic distribution aligned with the direction of the magnetic field. This anisotropy can be expressed in terms of two temperature components, one parallel and the other transverse to the field lines. The average temperature anisotropy $T_{//} / T_{\perp} \simeq 2.0$ implies a transport of heat energy along the magnetic lines of force (Hundhausen et al, 1967a). The electron temperature anisotropy is smaller (~1.2) but the energy flux due to electron thermal conduction is greater than that due to proton thermal conduction.

In addition to protons and electrons the solar wind plasma also contains He^{++} ions. The average He/H abundance is approximately 4.5% (Robbins et al, 1970) which is somewhat smaller than the average 20% existing in the corona. This separation occurs because the unequal ratio of gravitational and pressure gradient forces on electrons and ions produces, and is counteracted by, an electric field. The basic interplay between charge separation field and gravity accounts for the settling of heavy ions in the corona (Parker, 1963; Hundhausen, 1970).

Unlike other properties of the solar wind plasma the state of ionization is unaffected by the tremendous expansion of the coronal material. Since the low densities in the interplanetary medium result in very small ionization-recombination rates the ionization state of the solar wind is established deep within the corona. Observations made at a time of unusually low proton temperature ($T_p \lesssim 10^4$ °K) have shown the presence of

$^{3}He^{++}$, $^{4}He^{+}$, $^{16}O^{+5}$, $^{16}O^{+6}$, $^{16}O^{+7}$ and other unidentified ions (Bame et al, 1968). The relative abundance of the O^{+6} and O^{+7} ions can be used to infer a coronal temperature of 2×10^{5} ^{0}K, but care must be taken with such inferences as the observations were made at a time when the plasma was rather cool so they may not be entirely typical.

The interplanetary magnetic field is intimately connected with the solar wind, originating in the outwards extension of the photospheric fields during the plasma expansion. For a mean wind speed of 400 km sec^{-1} in the radial direction solar rotation leads to the development of a characteristic Archimedean spiral with an angle of 45^{0}. When averaged over several hours the measured field shows a clear tendency to follow a spiral angle of 45^{0} although there is a considerable amount of local irregularity (Ness et al, 1966). The average field intensity near 1 AU is approximately 5 gamma (see Figure 1.2c).

Averaging of the magnetic polarity observed near 1 AU reveals the existence of a large scale pattern in which the magnetic field tends to point predominantly toward or away from the sun (along the basic spiral configuration) for several days. Figure 1.3 shows the 3-hour averages of the direction of the field measured over one solar rotation by IMP-1 during 1963. Observations from two spacecraft with an appreciable separation in heliographic longitude have established that most of the structure in the interplanetary field corotates with the sun (Ness, 1966) with the same synodic rotation rate as the underlying photospheric fields (Wilcox and Ness, 1965).

This magnetic sector structure shows a dependence on the phase of the solar cycle. At the last solar minimum (1963-64) there were four well-defined sectors which remained stable for almost 18 months with a

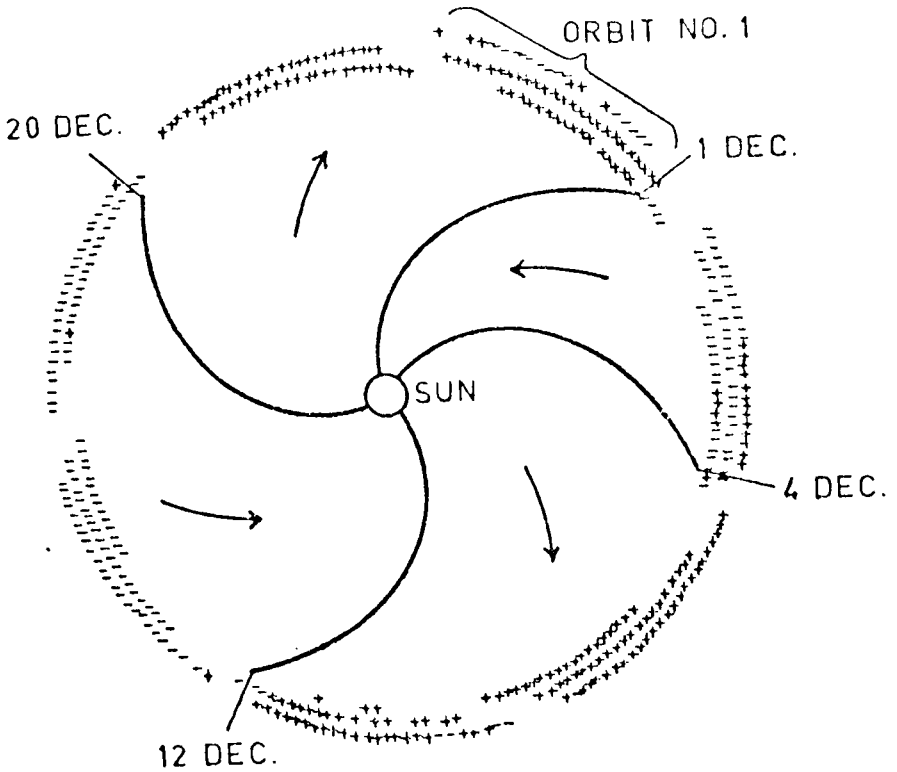

FIGURE 1.3 Polarity of the interplanetary magnetic field observed over one solar rotation during 1963. The sign of each three-hour average of the radial field component is shown at the solar longitude of the observation.
(after Wilcox and Ness, 1965)

corotation period of 27 days. The change from the old to the new cycle during 1965 was marked by an increase in the recurrence period from 27 to 28 days (Ness and Wilcox, 1967). During the rising portion of the cycle (1965-67) there were considerable changes in the structure on succeeding solar rotations, with simple recurrences occuring only rarely. During the period of maximum activity (1969-70) the pattern again became stable but with only two major sectors present, one boundary having a recurrence period of 27 days and the other 28 days (Wilcox, 1970; Fairfield and Ness, 1974). The decrease in activity during 1971-72 was again marked by a more complex, variable pattern although individual boundaries usually persisted for several rotations. This magnetic sector structure is intimately linked with the occurrence of corotating streams of high-speed plasma. The nature and origin of these streams is discussed in Section 1.4.

The fact that the solar wind exhibits a wide variety of conditions poses a problem when comparing theoretical models of the coronal expansion with observational data. It would seem reasonable to compare the models with solar wind parameters measured during quiet, undisturbed conditions but it is not entirely obvious what constitutes undisturbed conditions. Frequently when one of the plasma parameters remains constant for a period the other parameters may fluctuate considerably. Hundhausen (1972) has suggested that periods of low-speed solar wind ($V \simeq 300$-325 km sec^{-1}) may constitute the undisturbed medium although such periods rarely persist for more than two days at a time. Table 1.1 lists the average properties of periods of low-speed solar wind.

Table 1.1 Average properties of the low-speed solar wind

Velocity - radial*	300-325	km sec^{-1}
- azimuthal	8	km sec^{-1}
Density - proton/electron	8.7	cm^{-3}
Temperature - proton	4×10^4	^0K
- electron	1.5×10^5	^0K
Thermal anisotropy - proton	2.0	
- electron	1.1	
Magnetic field - intensity	5	gamma
- longitudinal direction	140^0	

* by definition.

Parker's initial model for the expansion of the corona into interplanetary space has formed the basis for most models of the solar wind. His model (Parker 1958, 1963) was a 'one-fluid' model in which it was assumed that the proton and electron temperatures were equal and varied with radial distance from the sun with an assumed functional form. This model predicted densities and velocities which were considerably higher than observed. Noble and Scarf (1963) modified the Parker model to include the effect of energy transport by heat conduction. Their model gave better agreement between theoretical and observed velocities and densities but predicted much higher temperatures than are observed. Both of these models are based on the assumption that the kinetic energy flux is everywhere smaller than the heat conduction flux, a poor approximation near and beyond 1 AU. Whang and Chang (1965) added a further constraint by assuming that at large distances there is negligible heat conduction, all energy transport being convective. This model improved the predictions but still over-estimated the temperature and underestimated the velocity. It is considered

as the basic 'one-fluid' model.

The proton and electron temperatures will only be equal if the two species interact strongly enough to maintain an equipartition of the thermal energy. While the Coulomb collisions between protons and electrons deep within the corona are sufficiently frequent to ensure equipartition the collision rate in interplanetary space is much lower due to the low densities. The average observed temperatures $T_e \simeq 1.5 \times 10^5$ ^{0}K and $T_p \simeq 4 \times 10^4$ ^{0}K indicate that near 1 AU the collision rate is not sufficient to constrain the protons and electrons to have equal temperatures. 'Two-fluid' models of the solar wind therefore incorporate separate energy equations for the two components.

Sturrock and Hartle (1966) and Hartle and Sturrock (1968) developed a two-fluid model in which energy transport was solely due to the thermal conduction of the two species and in which energy exchange between the species resulted from Coulomb collisions. Their model predicts densities twice those measured near 1 AU and velocities somewhat lower than those measured even under quiet conditions. Its major fault is that it seriously underestimates the proton temperature and overestimates the electron temperature. Neither the one-fluid nor the two-fluid model is capable of explaining the observed parameters adequately. Two different approaches have been adopted to modify the basic heat conduction models to overcome their limitations.

Parker (1964) and Hartle and Sturrock (1968) suggested the existence of an additional non-thermal heating mechanism in the outer corona.

Hartle and Barnes (1970) incorporated an extended heating source into a two-fluid model and varied its strength and spatial distribution to determine the general requirements for such a source. They found that by depositing energy over an extended range (2 - 30 R_o) they could improve the agreement between theory and observations. Barnes et al. (1971) modified this model to explicitly account for the dissipation of hydromagnetic waves propagating outwards from 2 R_o. The flow speed and proton temperature were in reasonable agreement with observations but the density remained too high. Barnes (1968, 1969) has shown that the effect of collisionless damping of hydromagnetic waves in the solar wind is to enhance the component of kinetic temperature parallel to the average field direction without affecting the transverse component. This could explain the observed temperature anisotropy in the solar wind.

The second approach has been to improve the predictions of steady, spherically symmetric models of the coronal expansion by including one or more factors ignored in the basic models rather than invoking an additional non-thermal energy source. The inclusion of the interplanetary magnetic field increases the flow speed due to the conversion of magnetic energy into kinetic and thermal energies but the change is relatively small. The presence of the field also modifies the transport processes in the plasma. In particular the heat conduction transverse to the magnetic field is significantly reduced. A one-fluid model incorporating magnetically-inhibited heat conduction (Gentry and Hundhausen, 1969) yielded better agreement with observations than either of the two basic models.

Inclusion of the effects of viscosity, while ignoring the magnetic field, removes so much energy that the flow speed is drastically reduced (Whang et al, 1965). The presence of the magnetic field modifies the

viscosity in a similar manner to that described for the thermal conductivity. This effect is sufficient on its own to bring the proton temperatures into agreement with observations (Wolff et al, 1971).

The relatively low Coulomb collision frequencies in interplanetary space drive the plasma away from the equilibrium state that it would attain if the collision frequency were higher, giving rise to instabilities in the medium (Scarf, 1970). These ion instabilities modify the thermal conductivity (Forslund, 1970) and may give rise to additional non-collisional exchange mechanisms between the protons and electrons (Toichi, 1971). Wolfe et al (1971) incorporated all of these corrections in a two-fluid model. They concluded that it is possible to modify the two-fluid model to bring it into agreement with observations without the need to invoke the existence of additional extended energy sources.

There are thus two distinct approaches to this problem. The two most detailed models available are the extended source model of Hartle and Barnes (1968) and the modified conductivity model of Wolff et al, (1971). Observational data for comparison with these models is only available within the corona (2-20 R_o) and near 1 AU. Table 1.2 compares model predictions with observations at 1 AU. The effect of adding additional parameters to the basic two-fluid model is to increase the number of degrees of freedom. This makes it possible to optimize the agreement between the model predictions and observations at these two distances from the sun. As can be seen from Figure 1.4 the two modified models are in reasonable agreement at those distances where they are constrained to match the observations but differ markedly at other distances from the sun. In particular the extended source model only adds energy in the range 10-30 R_o by wave damping whereas the modified conductivity model adds energy over the entire range from 10 - 214 R_o as a consequence of the effects of viscosity.

Both of these models are physically realistic and there is no real

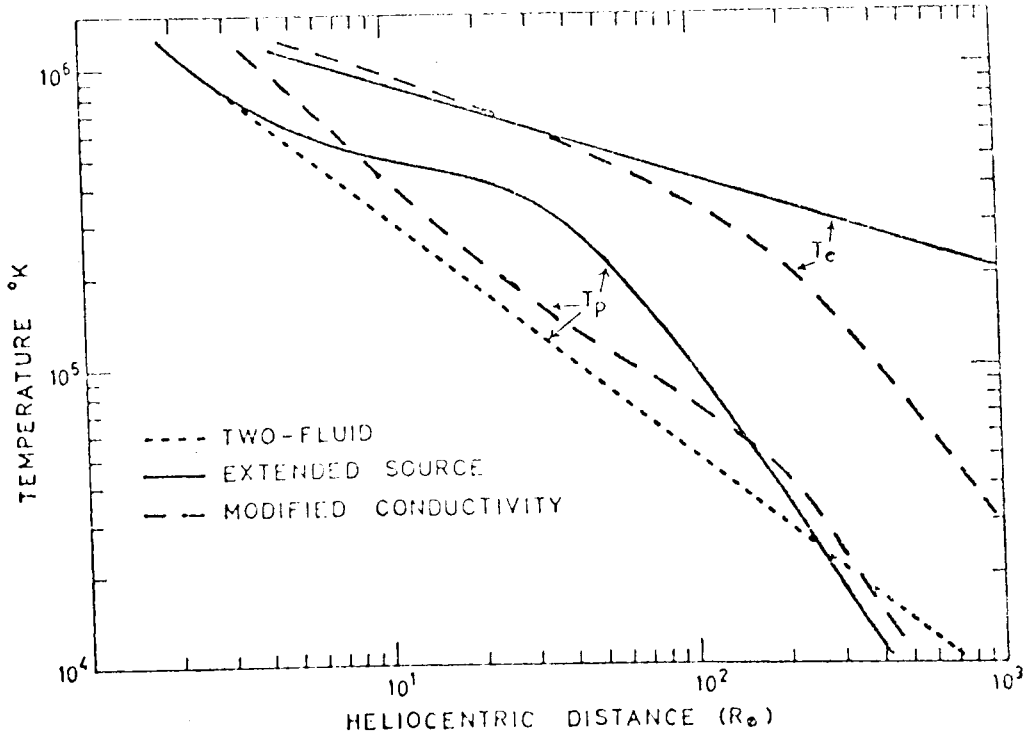

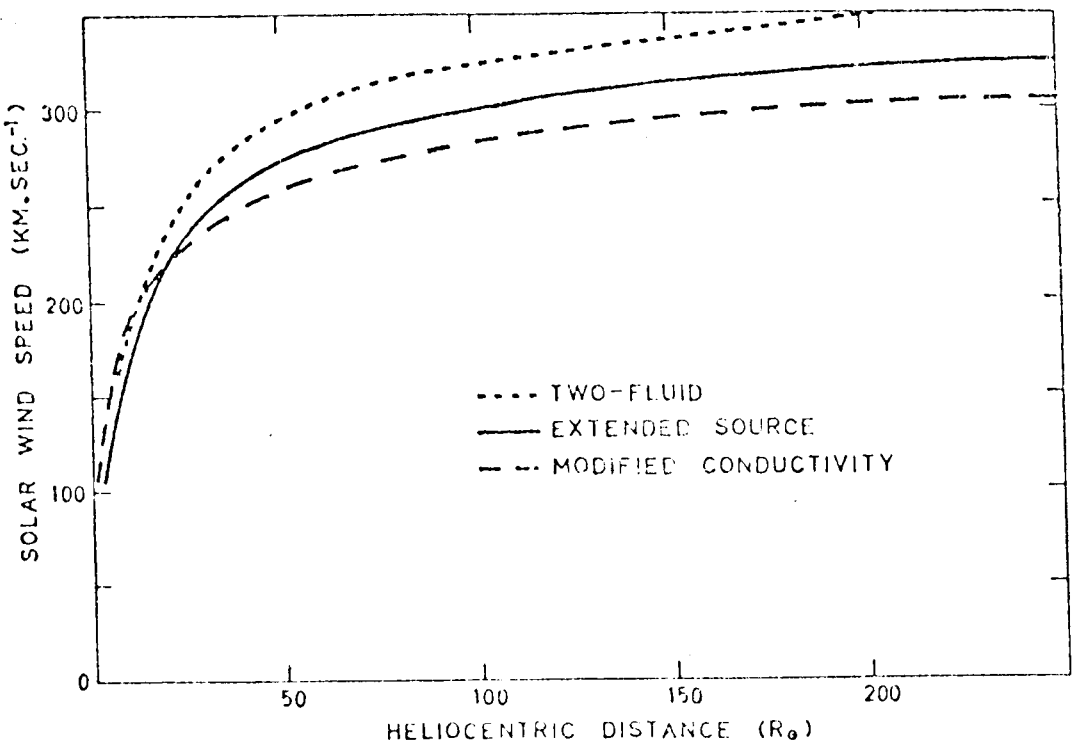

FIGURE 1.4 Temperature and velocity variations as a function of heliocentric distance for theoretical solar wind models.

basis on which to choose between them. More detailed information about the conditions in the solar wind at intermediate distances from the sun is required to resolve these differences. Modification of the basic theories to include non-spherical symmetry also requires observations out of the ecliptic plane. One promising source of such information is the measurement of solar wind speeds by the radio scintillation method.

Table 1.2 Comparison of solar wind models with observations at 1 AU

	Density cm^{-3}	Velocity km sec^{-1}	Proton Temp ^0K	Electron Temp ^0K
Observed	9	320	4.0×10^4	1.5×10^5
One-fluid	8	260	1.6×10^5	1.6×10^5
Two-fluid	15	250	4.4×10^3	3.4×10^5
Extended source	13	320	3.7×10^4	3.4×10^5
Modified conductivity	9	303	4.0×10^4	2.0×10^5

1.4 COROTATING STRUCTURES IN THE SOLAR WIND

The first solar wind data obtained from detectors on the Mariner 2 spacecraft during 1962 (Neugebauer and Snyder, 1966) revealed the existence of plasma streams of higher than average speed which usually persisted for several solar rotations. Subsequent observations (e.g. Siscoe et al, 1969; Ness et al, 1971) have shown that such corotating high-speed streams occur frequently and have provided detailed information about their properties.

The structure of a plasma stream of higher than ambient velocity is strongly influenced by the effect of solar rotation. At any distance r from the sun in the solar equatorial plane, the angle ϕ between a spiral magnetic field line and the radial direction is given by

$$\cos^2 \phi = \frac{1}{1 + \frac{\omega r}{V}^2} \qquad \ldots(1.1)$$

where ω is the angular velocity of the solar rotation and V the flow speed. Consequently the field lines for the ambient flow must intersect the less tightly wound field lines of the high-speed stream. Interpenetration of the two plasma streams is however prevented by the high electrical conductivity of the magnetized plasma. The ambient plasma will be compressed and forced to flow parallel to the interface between the two streams. This boundary will not be crossed by either plasma or field lines and is therefore a tangential discontinuity. A region of rarefaction will similarly form at the trailing edge of the high-speed stream. An idealized cross-section of the interaction of a stream with the ambient solar wind in the equatorial plane is shown in Figure 1.5a.

The relative motion of the plasma stream in the equatorial plane is entirely a consequence of solar rotation. No such effect is present in the direction normal to the solar equatorial plane and therefore the stream could have quite different dimensions and structures in solar latitude and longitude. The shape of the stream in the meridional plane will probably reflect any pressure differences between high-speed and ambient plasma, and the latitudinal extent of such streams will be related to the latitudinal distribution of the coronal source regions. Observations of

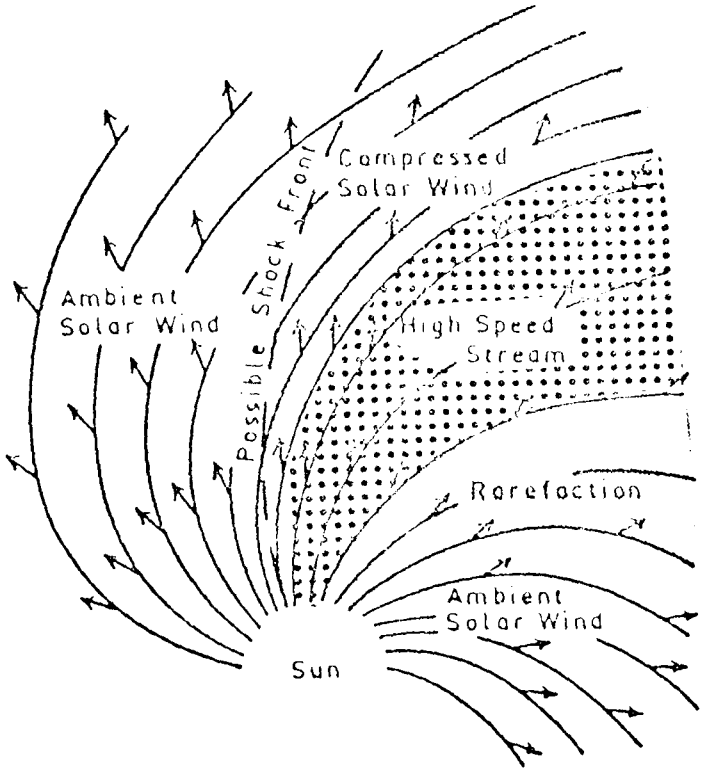

FIGURE 1.5a Equatorial cross-section of a high speed plasma stream embedded in the ambient medium. (after Hundhausen, 1972b)

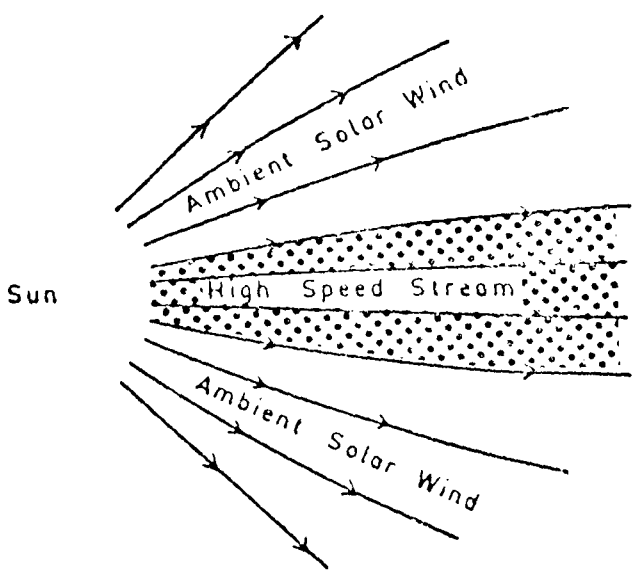

FIGURE 1.5b Meridional cross-section of a high speed plasma stream. (after Hundhausen, 1972b)

corotating streams based on the interplanetary scintillation of radio sources suggests that the streams occupy a sector ~ 25^0 in the ecliptic plane and extend to latitudes of up to 40^0 (Houminer and Hewish, 1972). Figure 1.5b shows one possible structure for the case in which the pressure within the stream decreases more rapidly with heliocentric distance than in the ambient medium and in which it is assumed that there are no instabilities in the flow.

The leading edge of a stream is usually sharply defined, with the velocity increasing from ~ 350 to ~ 600 km sec^{-1} within a day. The velocity then decreases more gradually over several days. A density enhancement lasting usually for about one day precedes the velocity increase. This enhancement is followed by a rarefaction which persists for several days, returning to the prestream level at about the same time as the velocity. The proton temperature profile through the stream is similar to the velocity profile but the electron temperature shows little variation. Figure 1.6a shows a typical stream observed by Explorer 33 during April 1968. This stream persisted for more than six solar rotations although showing considerable variations on successive rotations.

The sharp transition in the longitudinal direction ϕ of the magnetic field on April 5 marks the passage of a sector boundary past the spacecraft. Superposition of plasma parameters with respect to the magnetic sector structure (Wilcox and Ness, 1965; Ness et al, 1971) shows that such high speed streams are frequently associated with sector boundaries. Figure 1.6b shows the average variation of the plasma parameters within the sectors observed by IMP-1 during 1963. Those streams which are not associated with sector boundaries usually occur in regions possessing a predominant magnetic polarity.

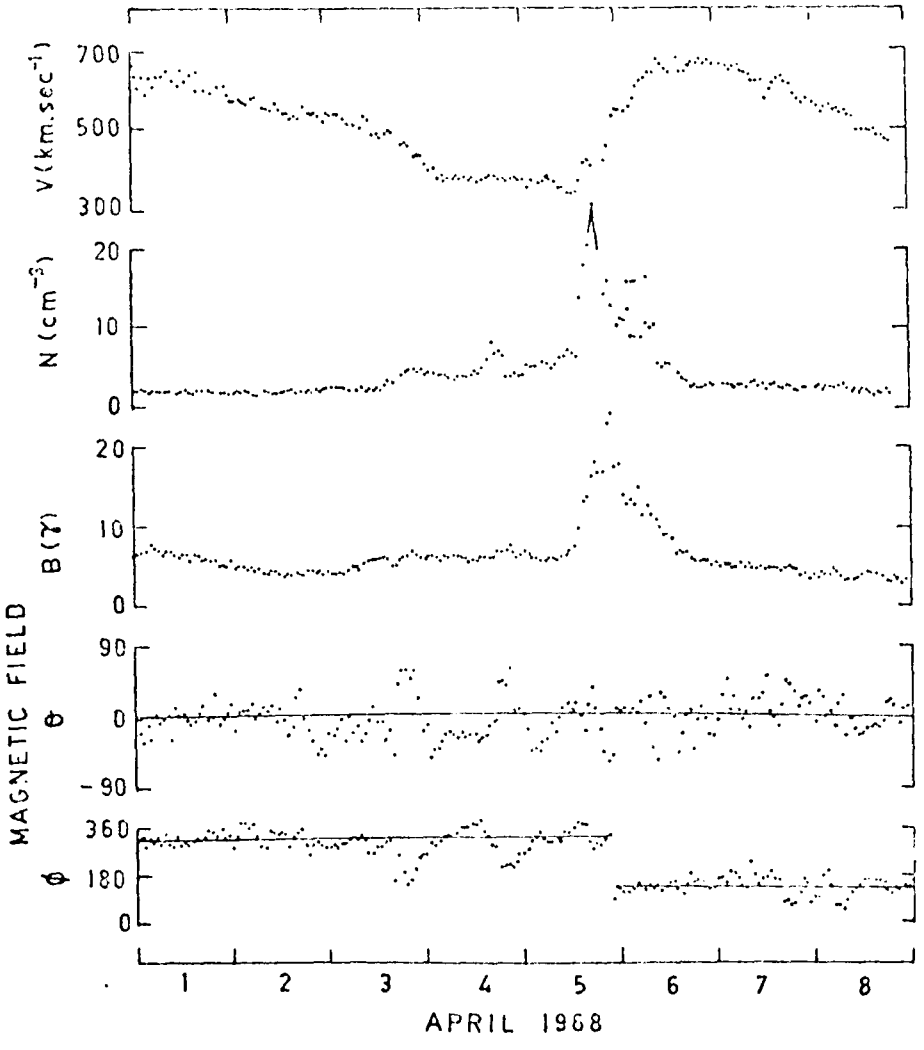

FIGURE 1.6a Variation of solar wind parameters at Explorer 33 during April 1968.

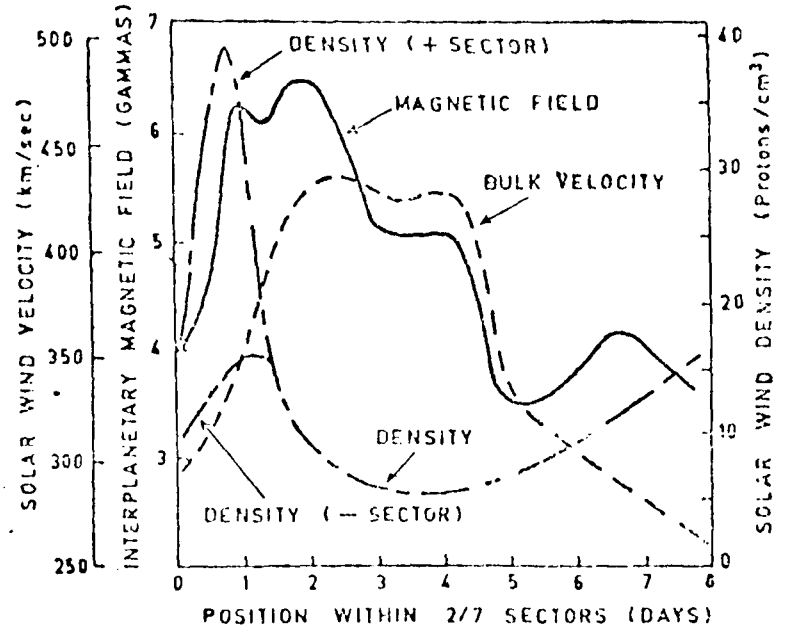

FIGURE 1.6b Variation of plasma parameters within a typical magnetic sector, as determined by a superposed epoch analysis of a large number of sectors.
(after Hundhausen, 1970)

The theoretical models of the coronal expansion discussed in the previous section were based on the assumption of spherical symmetry. The introduction of a spatially non-uniform flow within the ambient medium introduces several new independent variables into the conservation equations, greatly increasing the mathematical complexity of their solutions. Consequently theoretical models of corotating streams frequently neglect some of the complicating features found to be significant in the coronal expansion models.

Carovillano and Siscoe (1969) considered the effect of a small perturbation on a steady, spherical-symmetric ambient solar wind. The boundary conditions for their solution involved specification of spatially periodic flow parameters at an inner boundary at 0.05 AU. The effect of a small sinusoidal variation in velocity was the evolution of a density compression and rarefaction at the leading and trailing edges respectively.

This model was extended to include arbitrary perturbations at the inner boundary by Siscoe and Finley (1972). Their solution gave a complete description of the linearized hydrodynamic problem for corotating, time-stationary inhomogeneities. They found that the stream structure at 1 AU is most strongly influenced by temperature perturbations at the inner boundary. The phases of the density, temperature and velocity variations at 1 AU are in agreement with observations. The linearization inherent in this model restricts its applicability to small perturbations in the plasma parameters. This is not strictly representative of the high-speed streams.

Goldstein (1971) numerically integrated the nonlinear equations of motion in the eclipcic plane. The effect of including the nonlinear terms is to steepen the initially symmetrical velocity with increasing distance from

the sun, producing a steep increase followed by a more gradual decline. The density enhancement becomes more extreme and of shorter duration while the rarefaction becomes less pronounced but of longer duration. This model produces reasonable stream profiles at 1 AU. A more rigorous numerical integration of the nonlinear equations including the magnetic field (Nakagawa & Welck 1973) produces streams that bear a strong resemblance to observed streams.

An alternative nonlinear approach attempts to approximate the high-speed stream by computing the transient adiabatic motion of a spherically-symmetric disturbance in the ambient medium (Hundhausen, 1973). This method is valid for small deviations from radial flow and is capable of providing profiles which are in close agreement with actual observed profiles.

Historically it has usually been argued that the high-speed streams, and their related terrestrial geomagnetic effects, are related to specific solar features such as streamers which indicate the presence of localized emission of plasma from active regions. Associations between observed streams and specific solar features (Snyder and Neugebauer, 1966; Couturier and Leblanc, 1970) have not been convincing. The lack of any relationship between changes in solar activity and the solar wind velocity argues strongly against this suggestion.

Billings and Roberts (1964) suggested that the radial temperature gradients existing above active regions leads to the emission of *low-speed* solar wind above an active region. Wilcox (1968) modified this suggestion to include the effects of the photospheric sector structure as suggested by

the association of high-speed streams with large photospheric regions of predominant polarities. Recent synoptic observations of the corona have shown that high-speed streams can be reliably mapped back to coronal holes (Roelof, 1973a, 1973b), in accord with this suggestion.

1.5 TRANSIENT DISTURBANCES IN THE CORONA AND SOLAR WIND

Solar flares are generated within a small region of the chromosphere occupied by oppositely-directed magnetic field lines (Petschek, 1964), the principle source of energy being the magnetic energy stored within the complex fields above active regions. A typical flare will release in the order of 10^{31} ergs of energy into the chromosphere and lower corona. Much of this energy is dissipated by the ejection of plasma and shock waves from the flare region.

Flare sprays visible in Hα photographs indicate the ejection of material into the corona with speeds in the range 100 - 600 km sec^{-1}. Moreton waves are features in which a bright front of emission sweeps across the chromosphere with velocities between 400 and 600 km sec^{-1} (Moreton, 1964; Dodson and Hedeman, 1968). As it propagates the wave may interact with the ambient magnetic fields causing small regions of the chromosphere to brighten up and may sometimes even trigger 'sympathetic' flares in far distant active regions (Beckers, 1958). These waves appear to be highly directional with the fronts subtending angles of less than 90^0 (Smith and Harvey, 1971).

Type II radio bursts are generated by the passage of a collisionless magnetohydrodynamic (MHD) shock wave through the corona. As the disturbance passes through a given level of the corona it excites radiation at the plasma frequency and its second harmonic. Type II sources are usually of large dimensions with large and rapid variations in brightness over the

source region (Wild, 1969). The shock wave appears to travel out radially, essentially parallel to open magnetic field lines (Dulk et al, 1971), with velocities between 600 and 3000 km sec^{-1}. The recent detection of type II bursts at frequencies as low as 30 kHz (Malitson et al, 1973a, 1973b) promises to yield a valuable means of detecting shocks at heliocentric distances between 0.05 and 1 AU.

Numerical simulation of MHD shock waves using realistic models of the coronal density and magnetic fields (Uchida, 1968, 1973a) has shown that both Moreton waves and type II sources are a natural consequence of the propagation of a weak MHD wave into a region of low Alfven velocity v_A. Type II bursts occur when the wave is refracted into a region of low v_A in which the shock strength is strongly enhanced (Uchida, 1973b). Moreton waves only occur in those cases where a region of low v_A is located on the chromosphere-corona interface close to the flaring point (Uchida et al, 1973). The properties of type II bursts and Moreton waves are consistent with the propagation of MHD waves over a wide angle in the corona.

Moving metre-wavelength type IV radio bursts are generated by synchrotron radiation from groups of high energy electrons moving outwards with velocities between 100 and 1000 km sec^{-1}. The almost invariable association of type IV-m sources with active or disappearing filaments suggests that prominence material and magnetic fields may be ejected from the lower corona. In some cases the field structure may remain tied to the photospheric fields resulting in an expanding arch type IV source (Wild, 1969). In other cases magnetic reconnection may occur producing a self-contained plasmoid which appears as an isolated source moving away from the sun (Riddle, 1970).

The expansion patterns of type II and IV sources are usually different (Wild and Smerd,1972), the type II sources having higher velocities than the associated type IV sources (Sakurai and Chao, 1974a). Combination of white-light, H_α, and radio observations provides evidence that these disturbances are similar to the'magnetic bottles' originally proposed by Gold (1958). A shock wave from the flare propagates through the lower corona with a velocity ~1000 km sec^{-1} driven by flare ejecta travelling at 500 km sec^{-1}. The type IV, H_α flare spray and intense white-light clouds are associated with the ejected plasma, while the type II source is associated with the shock wave which moves ahead of the ejected plasma. The disturbance driving the flare ejecta may also cause the expulsion of large amounts of material from the mid-coronal regions with masses comparable to those measured in interplanetary shocks (Stewart et al, 1973a, 1973b).

As the disturbance travels outwards the ambient plasma and magnetic field lines must be compressed and swept aside by the expanding flare ejecta. Figure 1.7 is a sketch which combines the observed features of flare-produced interplanetary shock waves. There are basically three different regions of plasma; (1) the undisturbed solar wind plasma, (2) old plasma which was present prior to the flare and which has been compressed by the advancing disturbance, and (3) new plasma ejected from the flare. If the speed of the ejected material exceeds the ambient solar wind speed by more than the local Alfven velocity a shock front will form at the boundary between regions (1) and (2). In all cases $V_2 > V_1$, $|B_2| > |B_1|$, $T_2 > T_1$ and $\rho_2 > \rho_1$.

The compressed spiral form of the magnetic field in region (2) is constrained to follow the leading edge of the ejected plasma around to its origin near the flare site. The boundary between regions (2) and (3) will be a tangential discontinuity which will help to preserve any thermodynamical or chemical differences between the ambient and flare plasma. For example,

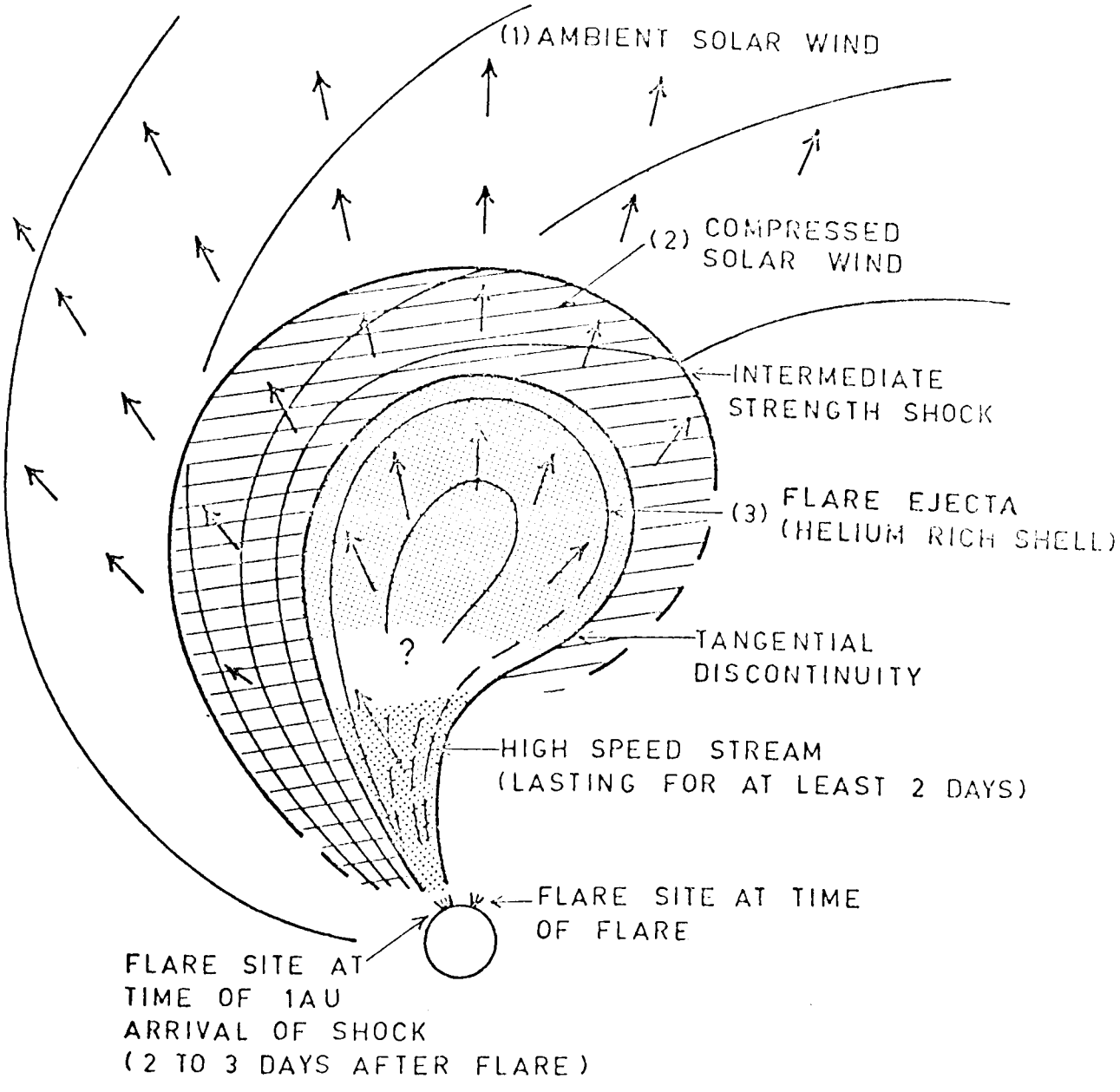

FIGURE 1.7 Idealized cross-section of a transient, flare-produced interplanetary disturbance. (after Hundhausen, 1972a)

the flare-ejected plasma is marked by a thin disk of higher than average He content (Hirshberg et al,1972).

The structure of the magnetic field and plasma within region (3) is strongly dependent on the details of the flare process. There is some doubt about the magnetic field configuration at the tail of the disturbance where the field lines must connect back to the flare site unless reconnection occurs (Petschek, 1966). There is evidence that in at least some cases reconnection does occur (Gosling et al, 1973) giving rise to a bottle of magnetic flux and plasma which is completely isolated from the surrounding plasma.

Figure 1.7 shows the disturbance undergoing an anisotropic expansion eastwards from the flare site. This was originally proposed by Hirshberg (1968) on the basis of the effectiveness of flares in producing geomagnetic storms as a function of their solar longitude. It is also suggested by the distributions of the peak flux densities of type IV bursts (Sakurai, 1973b), of disturbance transit times to 1 AU (Sakurai, 1973b) and of the He-enriched plasma shells (Hirshberg et al, 1972).

Determination of the shape of the shock front from spacecraft observations of shock normals has proved ambiguous. Taylor (1969) has suggested a spherical shock front with radius of curvature of 0.75 AU centred on the sun. On the other hand Bavassano et al (1974) have suggested that the shock front is not spherical but corresponds to theoretical models (see later) for plasma ejection into a cone of half-angle between 30^0 and 60^0.

The orientations in the ecliptic plane of all published shock normals are plotted in figures 1.8a and 1.8b as a function of the solar longitude of the parent flare, together with the shapes suggested by

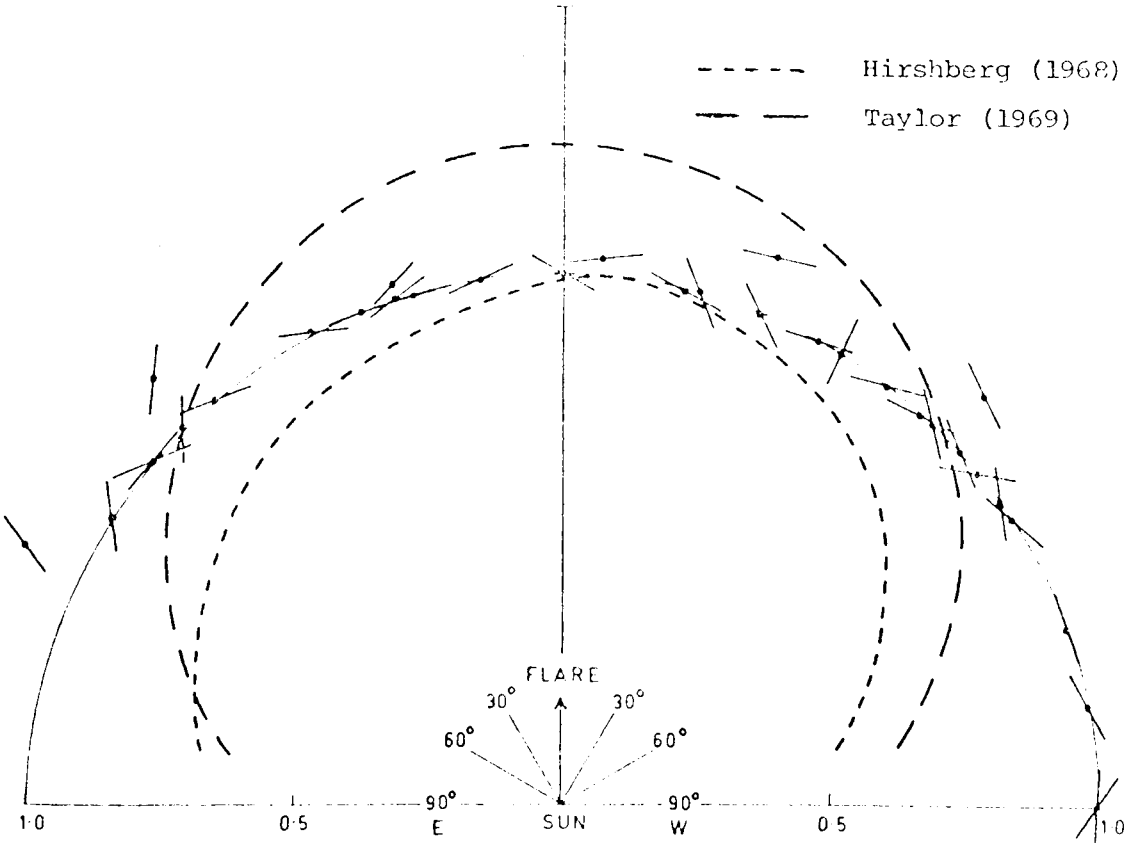

FIGURE 1.8a Orientation of local shock surfaces in the ecliptic plane. Each normal has been plotted at the solar longitude of the parent flare.

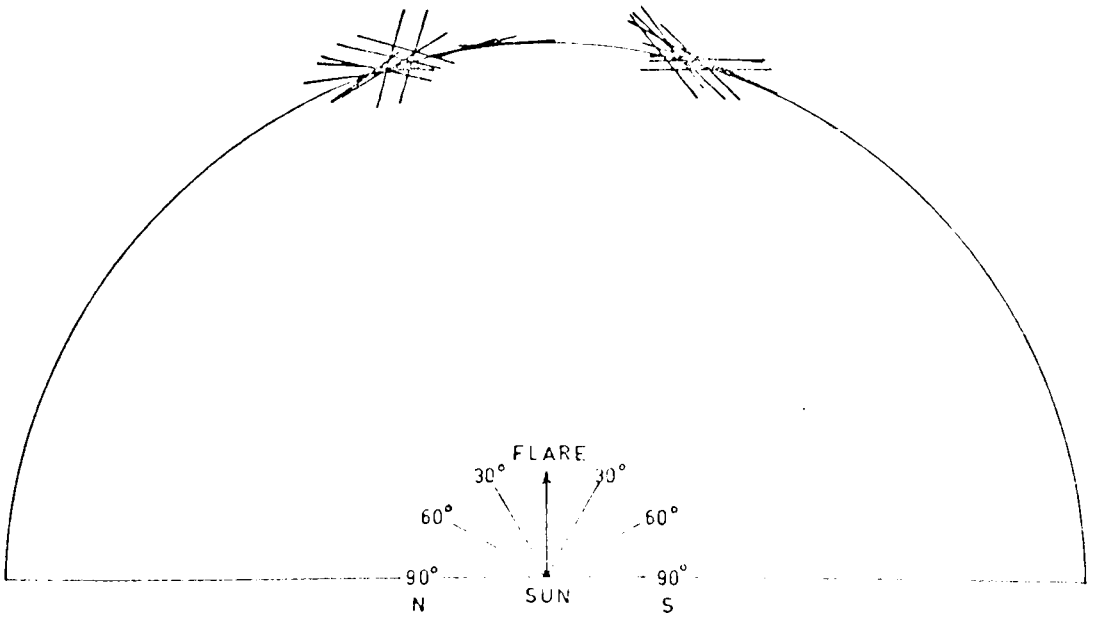

FIGURE 1.8b Orientation of local shock surfaces in the meridional plane. Each normal has been plotted at the solar latitude of the parent flare.

Hirshberg (1968) and Taylor (1969). In the ecliptic plane the individual shocks deviate markedly from any average shape. In the meridional plane they show a tendency to cluster in latitude sectors approximately 20^0 above and below the ecliptic (Bavassano et al, 1973). Although in general the deviation of shock normals is within 30^0 from the radial direction there have been cases reported (Hirshberg et al, 1970; Greenstadt et al, 1970) in which a shock normal is tilted at a large angle out of the ecliptic plane, well away from the radial direction. Such large deviations from the radial may reflect either local perturbations on the shock front or gross distortions introduced by propagation into an inhomogeneous solar wind.

Most interplanetary shocks appear to suffer a strong decelaration as they move away from the sun. Type II source velocities in the corona ($\sim$ 1200 km sec^{-1}) are generally higher than the average sun-earth transit velocities (800 km sec^{-1}) which in turn are higher than the local instantaneous shock velocity at 1 AU ($\sim$ 500 km sec^{-1}) detected by space-craft (eg Pinter, 1974).

The properties of the shock, as observed at 1 AU, are dependent on the duration of the initial disturbance. There are two limiting classes of behaviour; 'blast waves' in which the initial disturbance is impulsive, and, 'piston-driven shocks' in which plasma injection from the flare continues for a period comparable to the sun-earth transit time for the leading edge of the disturbance. The properties of the blast wave are solely determined by the interaction of the shock with the ambient plasma whereas those of the piston-driven disturbance are strongly affected by the nature of the driving plasma.

The quantitative theoretical treatment of the propagation of disturbances into the ambient solar wind involves the time-dependent integration of the conservation equations for mass, energy and momentum. Even in the one-fluid formulation these calculations are extremely complicated and require further simplification. Most attention has been paid to models in which it is assumed that both the ambient medium and the disturbance are spherically symmetric.

The principle analytical approach has been that of similarity theory in which the essential physics is arranged such that the properties of the disturbed medium can be described in terms of limiting mathematical idealizations. The first similarity solutions (Parker, 1963b, Simon and Axford, 1965) were relevant only to strong shocks and neglected the presence of the ambient solar wind. These models have been extended to include the presence of the azimuthal magnetic field (Lee and Chen, 1972) and the ambient wind speed (Dryer, 1972). The principle limitation of similarity solutions is their lack of flexibility in specification of the initial conditions and the existence of non-physical features at the contact discontinuity between the compressed ambient plasma and the flare-ejected material.

A more flexible approach is the use of numerical solutions of the time-dependent hydrodynamic equations. Hundhausen and Gentry (1969a, 1969b) investigated the propagation of a shock in a non-magnetic, spherically-symmetric solar wind. The shock was introduced by increasing the plasma parameters at 0.1 AU for a period τ before returning them to their original values. Development of the shock was followed by time-dependent numerical integration of the equations of motion. Figure 1.9 shows the flow speed and proton density as a function of heliocentric distrance at three stages in the development of the shock. Development of the disturbance is dependent on

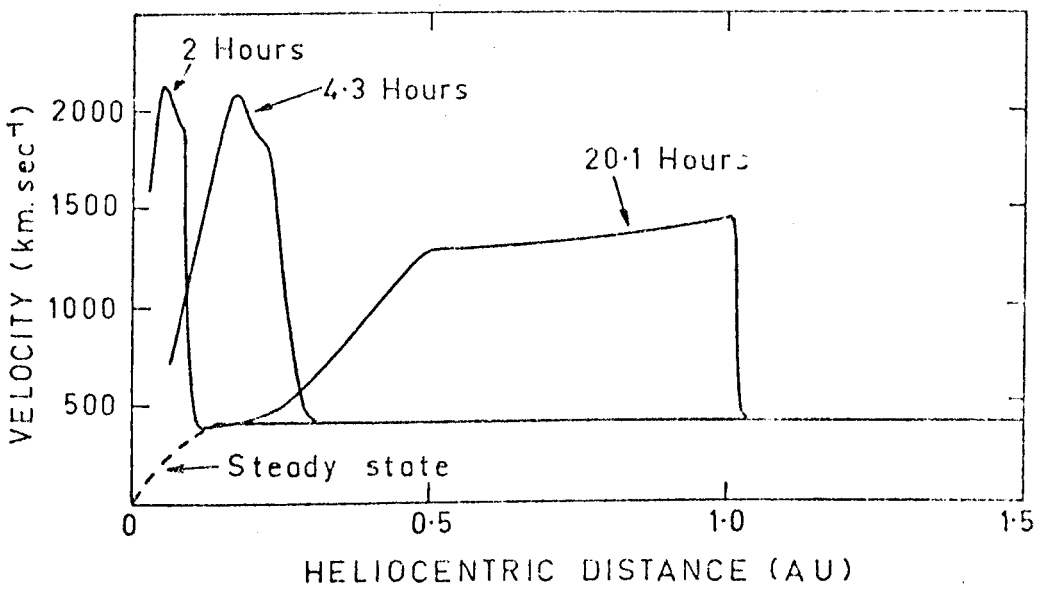

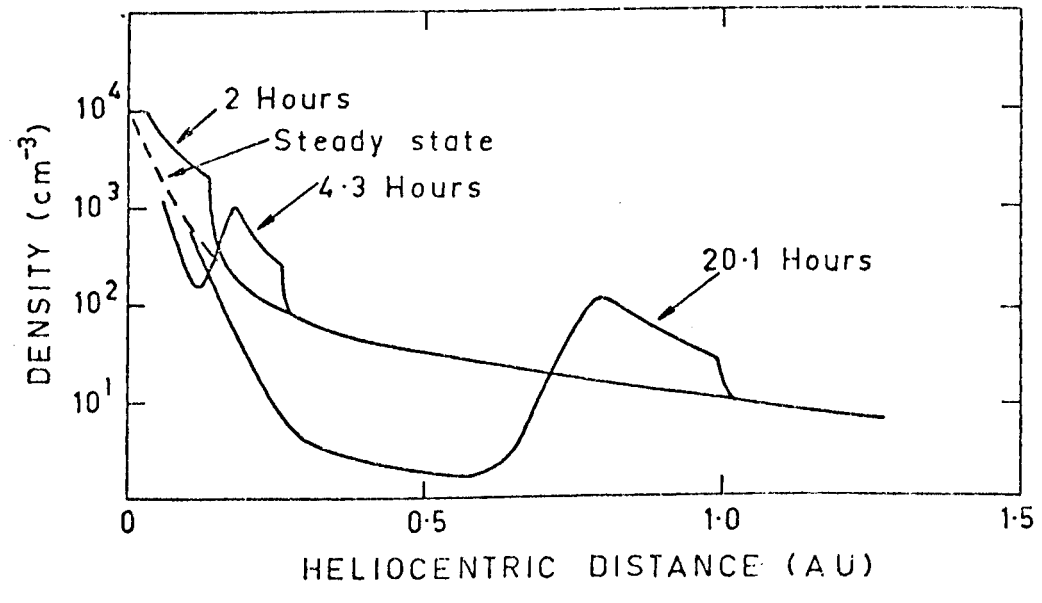

FIGURE 1.9 Variation of solar wind speed and proton density at several times after shock injection into the ambient medium. (after Hundhausen and Gentry, 1969)

the initial disturbance time τ relative to the transit time to 1 AU, T. The shock front is marked by the sudden increase in velocity and density. If $\tau > 0.45T$ a reverse shock, marked by density decrease and velocity increase, will develop further back behind the contact surface. If $\tau < 0.45T$ a rarefaction develops when the plasma parameters return to the ambient level. This rarefaction catches up with the reverse shock as the disturbance moves away from the sun and if $\tau < 0.1T$ there will be no evidence of the reverse shock by the time it reaches 1 AU.

Inclusion of the magnetic field modifies the variation of density and velocity with heliocentric distance (Steinolfson et al, 1973). Comparison with Heos-1 observations of a double-shock pair shows that the magnetic model provides a better simulation of the radial velocity and density profiles than the non-magnetic models.

The numerical models are dependent on the initial conditions with which the shock is started. Most models have been initiated by superimposing a shock of specified velocity on the steady-state solar wind at 0.1 AU. Steinolfson et al (1973) found that pulses in the radial velocity or thermal pressure produced multiple, non-linear variations in the density and magnetic field, unlike the shock-initiated models, although the radial velocity variations were similar as shown in figure 1.10b.

De Young and Hundhausen (1971, 1973), have relaxed the assumption of spherical symmetry and considered the development of disturbances which are symmetric about an axis extending radially away from the sun. Figure 1.11a shows the shape of the disturbance as a function of time for an impulsive blast-wave initially injected into a 15^0 half-angle cone. The shock front undergoes transverse expansion and develops into a broad, roughly spherical shape at 1 AU with a radius of curvature $\sim$ 0.5 AU. The effect of varying the size of the

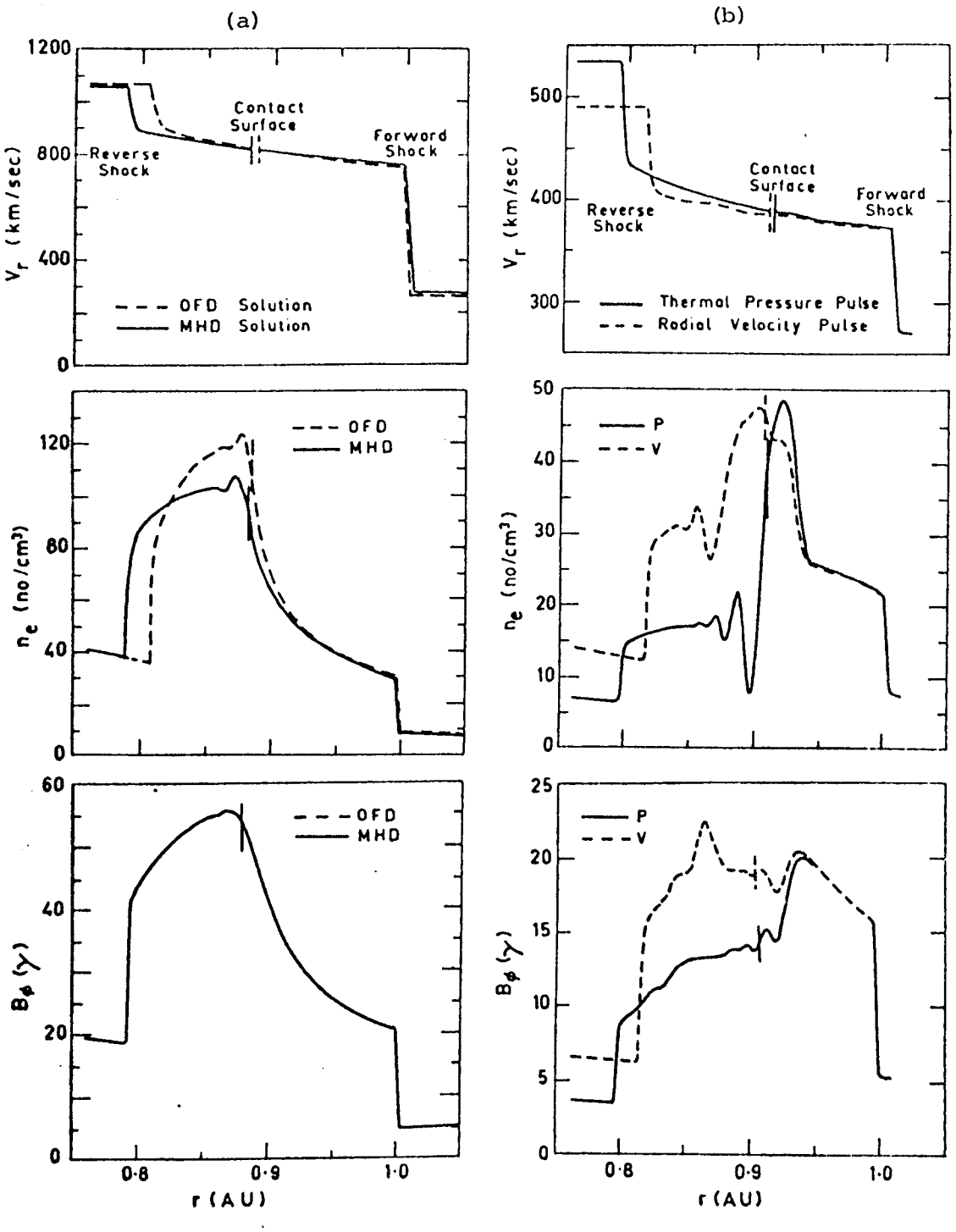

FIGURE 1.10 Radial velocity, proton density and azimuthal magnetic field profiles in a numerical simulation of double shock ensembles.

(a) Comparison of ordinary fluid dynamic and magnetohydrodynamic models.

(b) Dependence on initial starting conditions for shock injection.

(after Steinolfson et al,1973)

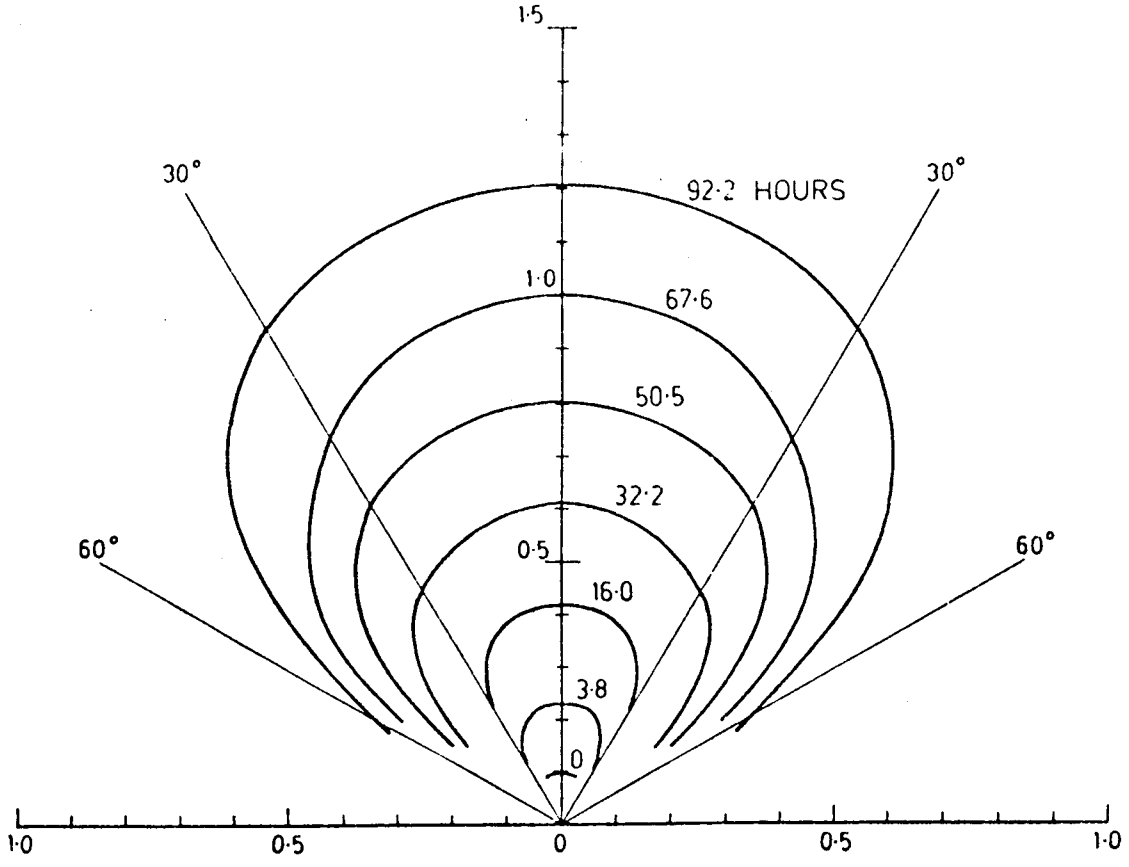

FIGURE 1.11a Shock configuration as a function of time produced by a shell of energetic plasma initially injected into a 15° half-angle cone. (after DeYoung and Hundhausen, 1971)

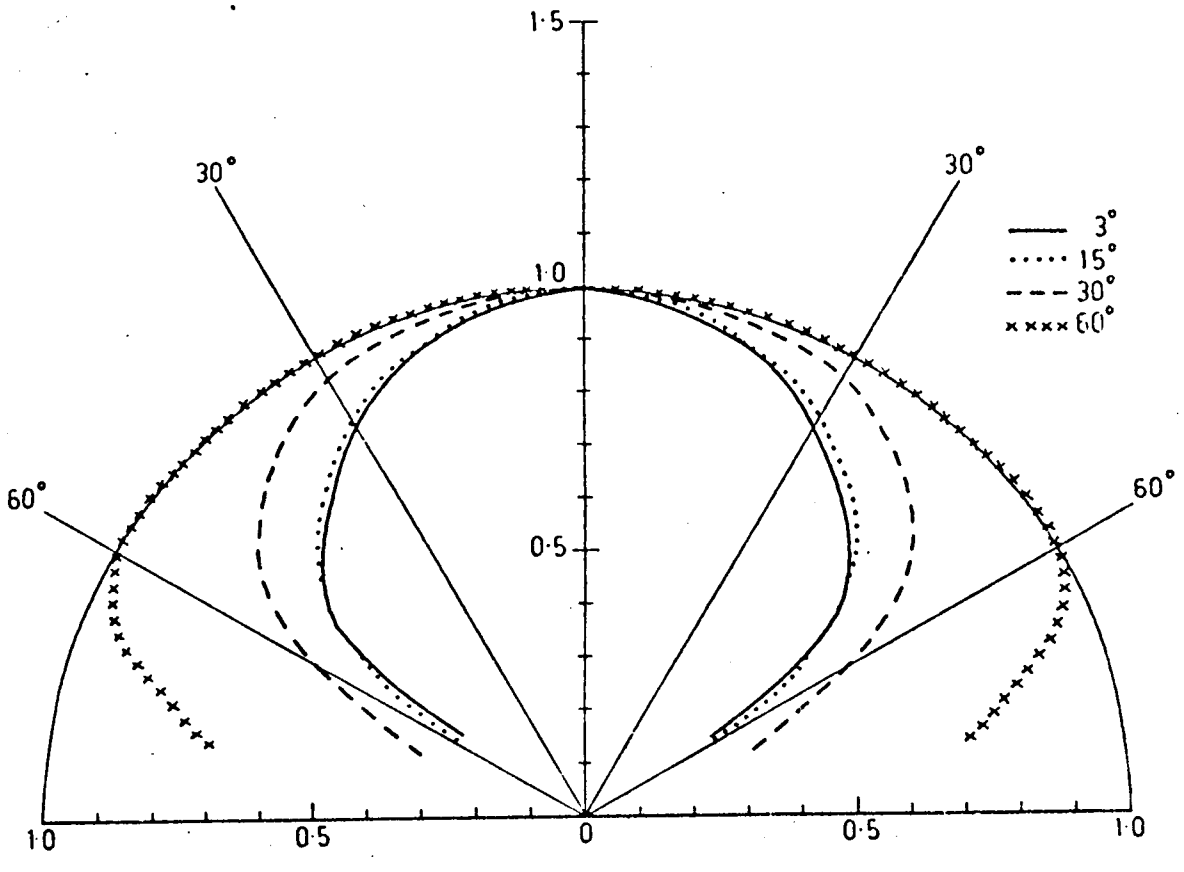

FIGURE 1.11b Shock configuration near 1 AU produced by injection of energetic plasma into cones of varying half-angle. (after DeYoung and Hundhausen, 1971)

cone into which the material is ejected is shown in figure 1.11b. Piston-driven disturbances show slightly less transverse expansion than the blast waves illustrated.

Deceleration of the disturbance is a strong function of the total energy, unlike the disturbance geometry. Those shock waves containing less energy and momentum are decelerated the most strongly. The deceleration is most pronounced at small heliocentric distances as a result of the higher disturbance velocity and higher ambient plasma density in these regions. For a disturbance of given total energy the deceleration is greatest for an axi-symmetric piston-driven shock and least for a spherically-symmetric blast wave. Comparison of the energy-transit time relationships and post-shock plasma flows with available spacecraft data suggest that the injection of energetic material into many flare-produced disturbances may persist for 10 or more hours (De Young and Hundhausen, 1973).

Heinemann and Siscoe (1974) adopted a linear, non-magnetic model to study the propagation of a strong, spherically-symmetric shock into an inhomogeneous solar wind which is time-stationary in a reference frame corotating with the sun. They found agreement between theoretical E-W distributions of shock normals and 54 observed shocks. Their results suggest that regions of higher than normal density impede the motion of the shock.

A more sophisticated non-linear magnetic model has been developed by Hirshberg et al, (1974). They investigated the development of a spherically-symmetric disturbance into an ambient medium containing a typical high-speed corotating stream. The velocity and density structure of the undisturbed stream, as observed as a function of time by a spacecraft located 1 AU from the sun, is shown in figure 1.12a. Perspective representations of the magnitude of

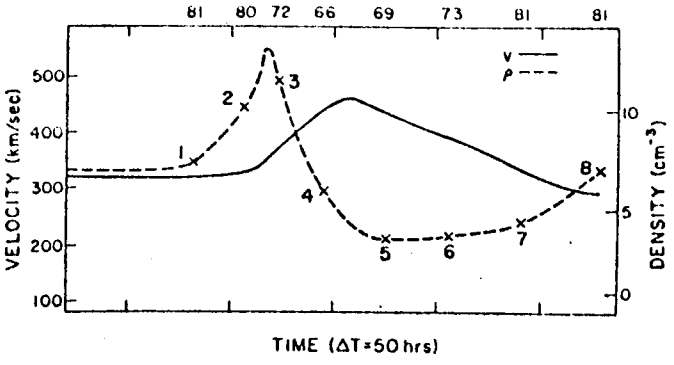

(a) Variation of velocity and density in the corotating stream seen as a function of time by an observer at a fixed point 1 AU from the sun

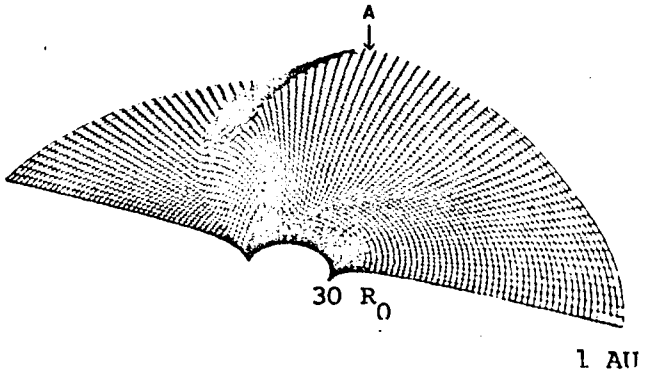

(b) Perspective view of the solar wind velocity profile in the ambient medium at the time of shock injection at 30 R_o.

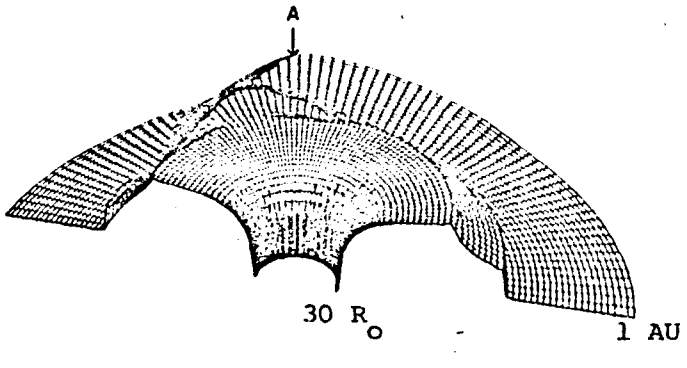

(c) Perspective view of the velocity profile 50 hours after the initial shock injection.

FIGURE 1.12 Model of shock wave propagation into an ambient medium containing a corotating high-speed plasma stream. (after Hirshberg et al,1974)

the solar wind velocity from 30 R_o out to 1 AU (figure 1.12b) and 50 hours after initiation of the disturbance (figure 1.12c) show that after 50 hours the disturbance has propagated further in the high-speed stream than elsewhere. The transit time of the shock to 1 AU at various points within the stream is given by the numbers along the top of figure 1.12a.

The disturbances seen by a spacecraft located at 1 AU will depend largely on the relative phasing of the stream and shock arrivals at the spacecraft. In such cases deduction of the disturbance geometry from a single spacecraft may be highly ambiguous and multi-disciplinary observations are clearly required. The observation of the interplanetary scintillation of a 'grid' of radio sources spaced around the sun provides one promising technique for the study of flare-produced disturbances over a wide range of heliocentric co-ordinates. Such observations are described in Chapter 5.

CHAPTER 2

RADIO-WAVE SCATTERING IN THE INTERPLANETARY MEDIUM

2.1 INTRODUCTION

Since the first observations of radio-wave scattering in the interplanetary medium (Machin and Smith, 1952) developments in the study of the scattering of radiation from extra-terrestrial radio sources have established many of the properties of the outer corona and solar wind. Such techniques have provided data about regions at distances between $5R_o$ and 1AU, and over a wide range of heliocentric latitudes.

This chapter provides an outline of the theory relevant to the scattering of radio-waves in the interplanetary medium. The problem of wave propagation in random media has been treated theoretically by a number of authors (Fejer, 1952; Hewish, 1952; Ratcliffe, 1956; Pisareva, 1959; Tatarski, 1961; Bowhill, 1961; Mercier, 1962; Budden, 1965; Bramley 1967; Salpeter, 1967; Budden and Uscinski, 1970, 1971; Buckley, 1971a, 1971b, 1975) and only a brief summary will be presented here. A review of the applications of this theory to interplanetary scintillation and coronal broadening follows the summary.

2.2 RADIO-WAVE SCATTERING THEORY

To discuss the nature of radio-wave scattering we refer to Figure 2.1a. Broadband radiation from a radio source encounters the solar wind plasma which is expanding radially outwards with speed V. We adopt the rectangular co-ordinate system in Figure 2.1b in which the wave

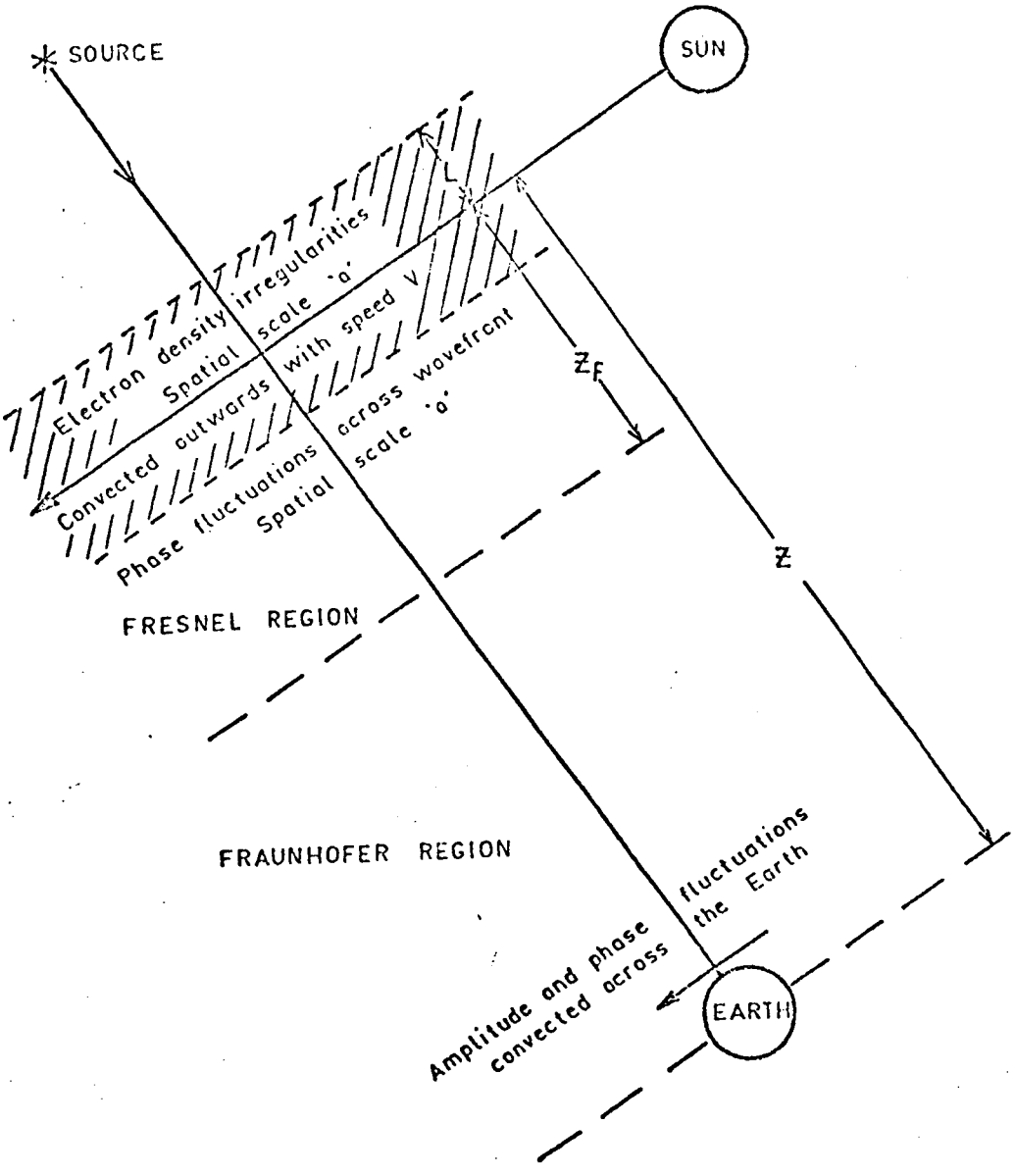

FIGURE 2.1a Origin of interplanetary scintillation

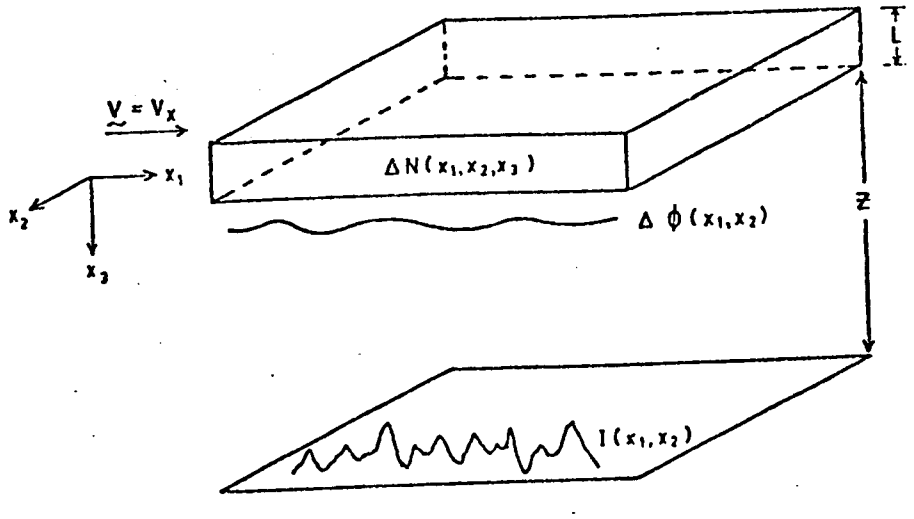

FIGURE 2.1b Geometry of the scattering problem

propagates in the x_3 (or z) direction and the solar wind velocity is in the x_1 direction. Initially we also restrict the discussion to consideration of monochromatic radiation, of wavelength λ, from a point source.

The refractive index μ of the medium is given by

$$\mu \approx 1 - \frac{r_e \lambda^2 N}{2\pi} \qquad \text{---- (2.1)}$$

where r_e is the classical radius of the electron, and N is the mean electron density. The electron density in the medium is not uniform but contains random fluctuations of magnitude ΔN about the mean density. If we define

$$\Delta N (\underset{\sim}{x}) = N (\underset{\sim}{x}) - \langle N (\underset{\sim}{x}) \rangle \qquad \text{---- (2.2)}$$

the density fluctuations can be characterized by their 3D spatial auto-correlation function $\rho_{Ns}(\underset{\sim}{r})$;

$$(\Delta N_o)^2 \ \rho_{Ns}(\underset{\sim}{r}) = \langle \Delta N(\underset{\sim}{x}) \ \Delta N (\underset{\sim}{x} + \underset{\sim}{r}) \rangle \qquad \text{---- (2.3)}$$

where $\Delta N_o = \langle (\Delta N(\underset{\sim}{x})^2 \rangle^{\frac{1}{2}}$ is the rms fluctuation in the density. Alternatively, the density fluctuations may be described in terms of their three-dimensional spatial power spectrum $P_{Ns}(\underset{\sim}{k})$, which is the Fourier transform of $\rho_{Ns}(\underset{\sim}{r})$:

$$P_{Ns}(\underset{\sim}{k}) = \frac{(\Delta N_o)^2}{(2\pi)^3} \int_{-\infty}^{\infty} \rho_{Ns}(\underset{\sim}{r}) \ e^{-i\underset{\sim}{k}.\underset{\sim}{r}} \ d^3\underset{\sim}{r} \qquad \text{---- (2.4)}$$

Since the mean electron density is a rapidly decreasing function of distance from the sun the scattering can be considered to be confined to a region of thickness L along the line of sight centred at the point of closest approach to the sun. This region will hereafter be

referred to as the "scattering screen". The phase change suffered by the wave in propagating through the screen is

$$\phi(\underset{\sim}{x}) = \frac{2\pi}{\lambda} \int \Delta\mu .\, dz$$

$$= -r_e \lambda \int \Delta N(\underset{\sim}{x}) .\, dz \qquad \text{---- (2.5)}$$

Thus propagation through the scattering region imposes a random phase fluctuation $\phi(x_1 , x_2)$ on the wavefront, but provided that the screen is sufficiently thin the amplitude of the wave will be unaffected. The phase fluctuations in the wavefront leaving the screen can be described in terms of their two-dimensional spatial auto-correlation function $\rho_{\phi s}(\underset{\sim}{r})$ and power spectrum $P_{\phi s}(\underset{\sim}{k})$:

$$\phi_0^2 \, \rho_{\phi s}(\underset{\sim}{r}) = < \phi \, (\underset{\sim}{x}) .\, \phi \, (\underset{\sim}{x} + \underset{\sim}{r}) > \qquad \text{---- (2.6)}$$

$$P_{\phi s}(\underset{\sim}{k}) = \frac{\phi_0^2}{(2\pi)^2} \int_{-\infty}^{\infty} \rho_{\phi s}(\underset{\sim}{r}) \, e^{-i \, \underset{\sim}{k} . \underset{\sim}{r}} \, d^2 \underset{\sim}{r} \qquad \text{---- (2.7)}$$

where ϕ_0 is the rms phase deviation.

Provided that the radio wavelength is much smaller than the size of the density irregularities, to ensure small angle scattering, we can substitute (2.6) into (2.5) and obtain

$$\phi_0^2 \;\; \rho_{\phi s}(r_1 , r_2) = (r_e \lambda)^2 \int_0^L \int_0^L \Delta N \, (R_1 , R_2 , R_3) \; \Delta N \, (R_1 + r_1 , R_2 + r_2 , r_3) \, dR_3 \, dr_3$$

---- (2.8)

If the screen thickness L is much greater than the irregularity scale the random density fluctuations at different levels in the screen are independent and (Chandrasekhar, 1952)

$$\phi_0^2 \quad \rho_{\phi s}(r_1, r_2) = L(r_e \lambda \Delta N_o)^2 \int_{-\infty}^{\infty} \rho_{Ns}(r_1, r_2, r_3)\, dr_3 \qquad \text{---- (2.9)}$$

Taking the Fourier transform of (2.9) gives (Tatarski 1961, Equation 6.34)

$$P_{\phi s}(k_1, k_2) = 2\pi \; L \; (r_e \lambda)^2 \; P_{Ns}(k_1, k_2, k_3 = 0) \qquad \text{---- (2.10)}$$

The rms phase deviation ϕ_0 can be obtained from Equation (2.8). If we assume that the electron density fluctuations possess a Gaussian auto-correlation function of the form

$$\rho_{Ns}(r_1, r_2, r_3) = \exp\left[- \left(\frac{r_1^2}{a_1^2} + \frac{r_2^2}{a_2^2} + \frac{r_3^2}{a_3^2} \right) \right] \qquad \text{---- (2.11)}$$

where a_i is the characteristic scale size of the density fluctuations in the x_i direction, the rms phase deviation is given by (Bramley, 1954).

$$\phi_0 = \pi^{\frac{1}{4}} (La_3)^{\frac{1}{2}} \; r_e \lambda \; \Delta N_0 \qquad \text{---- (2.12)}$$

The physical basis of (2.12) can be seen by considering the screen as a series of blobs of size a_3 along the line of sight. Propagation through one blob introduces a phase shift

$$\Delta\phi = \frac{2\pi \; a_3 \; \Delta\mu}{\lambda} \quad \alpha \quad a_3 \; \lambda \Delta N_0$$

The wave passes through $N = L/a_3$ such blobs, but since each blob may be either positive or negative with respect to the mean density the effects add randomly and the total phase deviation is proportional to the square root of the number of irregularities, and thus $\phi_0 \; \alpha \; \Delta N_0^{\frac{1}{2}} \; . \; \Delta\phi$.

Propagation of the wave away from the screen is a diffraction problem. For simplicity we initially restrict our discussion to a screen in which the phase fluctuation $\phi(x)$ is one-dimensional. The field across the wave-front at the exit plane of the screen is

$$E(x) = E_0 \exp(i\phi(x)) = E_0 \left[1 + \sum_{n=1}^{\infty} \frac{(i\phi)^n}{n!} \right] \quad \text{---- (2.13)}$$

where E_0 is the amplitude of the incident wave. Provided that $\phi_0 \ll 1$ radian we can use the first-order approximation

$$E(x) \approx E_0 (1 + i\phi(x)) \quad \text{---- (2.14)}$$

A random phase function $\phi(x)$ can be Fourier analyzed into a series of sinusoidal components and since the approximation (2.14) is linear there is a one-to-one correspondence between individual Fourier components in $\phi(x)$ and $E(x)$. We can therefore consider each Fourier component separately.

If $\phi(x)$ consisted of only one Fourier component of the form

$$\phi(x) = \phi_\ell \cos \frac{2\pi x}{\ell} \quad \text{---- (2.15)}$$

the emergent wavefront would consist of an unscattered component plus scattered components at angles $\Theta \approx \pm \lambda/\ell$ in quadrature with the unscattered component. As the wave propagates away from the screen the scattered waves change their phase relationship with the unscattered wave giving rise to amplitude fluctuations. As the distance from the screen increases there will be certain planes in which the fluctuations exist entirely as amplitude, or entirely as phase, variations with intermediate planes having fluctuations of both amplitude and phase.

For a random screen with characteristic scale 'a' the emergent wavefront consists of an unscattered component plus an angular spectrum of waves occupying a cone of angle $\Theta_s \approx \lambda/a$. At the exit plane the wavefront contains phase fluctuations which are made up of a large number of Fourier components of the form of (2.15). As the wave propagates away from the screen each of these components changes periodically between amplitude

and phase fluctuations but the changes occur at different distances for different components. The wide angle components change their phase relationship most and so close to the screen the scale of the amplitude pattern will be smaller than the scale of the phase pattern at the screen. As the distance from the screen increases the individual Fourier components are continually changing between phase and amplitude fluctuations, but at any given distance there will always be some components present in the form of amplitude fluctuations. At a given distance Z the Fourier components of scale greater than the radius of the first Fresnel zone $(Z\lambda)^{\frac{1}{2}}$ do not contribute to the amplitude fluctuations, although they may produce refractive variations in position. Consequently, the amplitude fluctuations build up until at a distance $Z_F = ka^2$ the amplitude and phase fluctuations contain approximately equal energy. Beyond this distance the amplitude fluctuations saturate and become independent of Z. The region of space for which $Z < Z_F$ is defined as the 'near-field' or 'Fresnel diffraction' region, and that region where $Z > Z_F$ is defined as the 'far-field' or 'Fraunhoffer diffraction' region.

Figure 2.2a shows the way in which the amplitude fluctuations develop with distance from a one-dimensional and an isotropic two-dimensional phase screen with a Gaussian auto-correlation function (Bowhill, 1961). Within the near-field the size of the diffraction pattern will not be equal to the phase pattern at the exit-plane, as is shown in figure 2.2b for an isotropic 2D screen and in figure 2.2c for an anisotropic screen with axial ratio 2:1.

The intensity fluctuations in a plane at a distance Z from the scattering screen can be characterised by their two-dimensional spatial auto-correlation function $\rho_{Is}(\underset{\sim}{r})$ or their power spectrum $P_{Is}(\underset{\sim}{k})$, defined in a similar manner to $\rho_{\phi s}(\underset{\sim}{r})$ and $P_{\phi s}(\underset{\sim}{k})$. Provided that the thin screen, weak

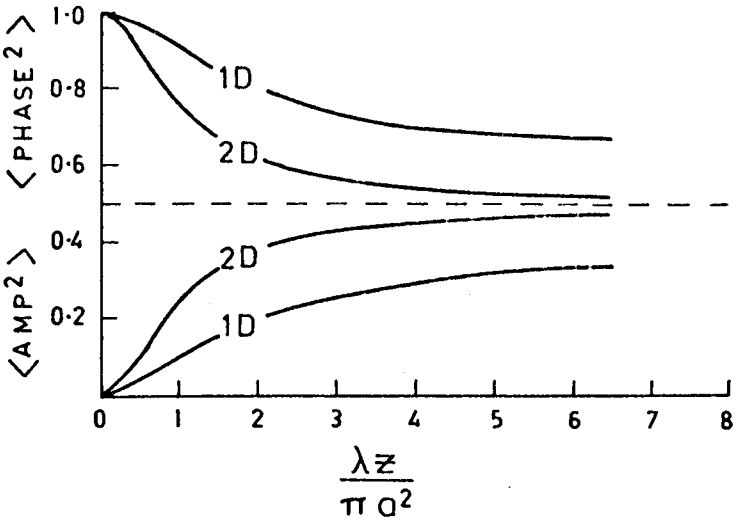

(a) Variation of the mean square diffracted signal with distance from a one-dimensional and isotropic two-dimensional phase screen.

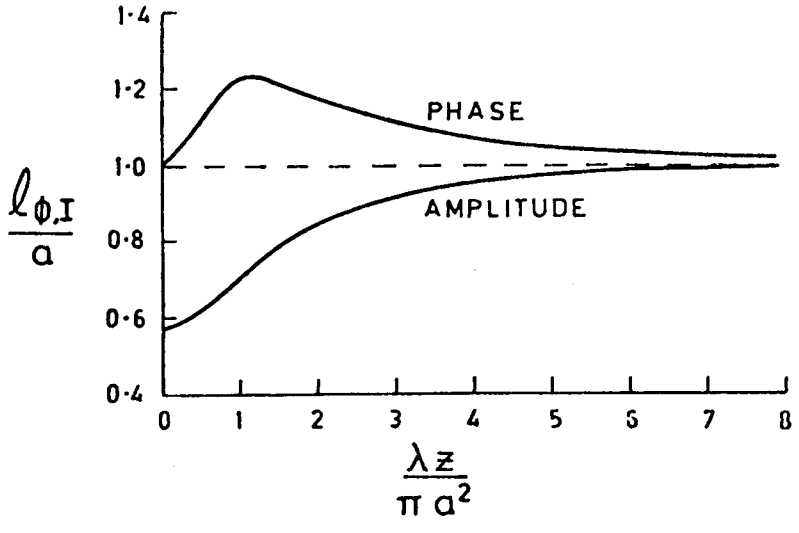

(b) Variation of the structure sizes l_ϕ and l_I with distance from an isotropic ($a_1 = a_2 = a$) two-dimensional phase screen.

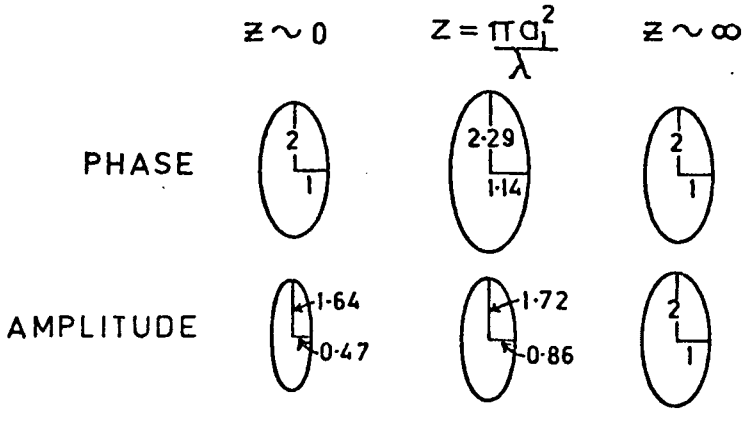

(c) Spatial correlograms of the wave diffracted from an anisotropic two-dimensional phase screen.

FIGURE 2.2 Development of the diffraction pattern from a thin random phase screen. (after Bowhill, 1962)

scattering theory is valid ($L < ka^2$, $\phi_0 < 1$) the intensity fluctuations at a distance Z are related to the phase fluctuations at the exit plane by (Bowhill, 1962; Salpeter, 1967)

$$P_{Is}(\underset{\sim}{k}) = 4\, P_{\phi s}(\underset{\sim}{k}) \sin^2 (k^2/k_f^2) \qquad \text{---- (2.16)}$$

where $k^2 = k_1^2 + k_2^2$ and $k_f^2 = 4\pi/\lambda Z$. The $\sin^2$ term has become known as the 'Fresnel filtering function' since it is closely related to the effect of propagation in the near-field or Fresnel diffraction zone. As noted above phase fluctuations with scale greater than $(\lambda Z)^{\frac{1}{2}}$ do not contribute to the intensity fluctuations at a distance Z. Thus the effect of propagation within the near-field is to act as a high-pass filter, rejecting spatial fluctuations with wave numbers less than $(4\pi/\lambda Z)^{\frac{1}{2}}$. This can be seen in the perspective view of equation (2.16) shown in figure 2.3 where filtering of the low spatial wavenumber components produces the depression at $k_1 = k_2 = 0$. The periodic zeros at large wavenumbers are those wavenumbers at which, for this distance, the fluctuations exist purely in the form of phase variations.

The two-dimensional diffraction pattern is swept across an observer at a fixed point in space as a consequence of the motion of the solar wind plasma. The observer therefore measures a fluctuating intensity as a function of time which is a cross-section through the two-dimensional pattern. If we assume that the solar wind plasma possesses a constant velocity V in the x_1 direction spatial Fourier components of wave number k_1 will appear as temporal Fourier components of frequency

$$f = \frac{k_1 V}{2\pi} \qquad \text{---- (2.17)}$$

Any given point in the pattern will cover a distance $r_1 = V\tau$ in a time τ , and the temporal auto-correlation function is related to the two-dimensional spatial auto-correlation function by (Salpeter, 1967)

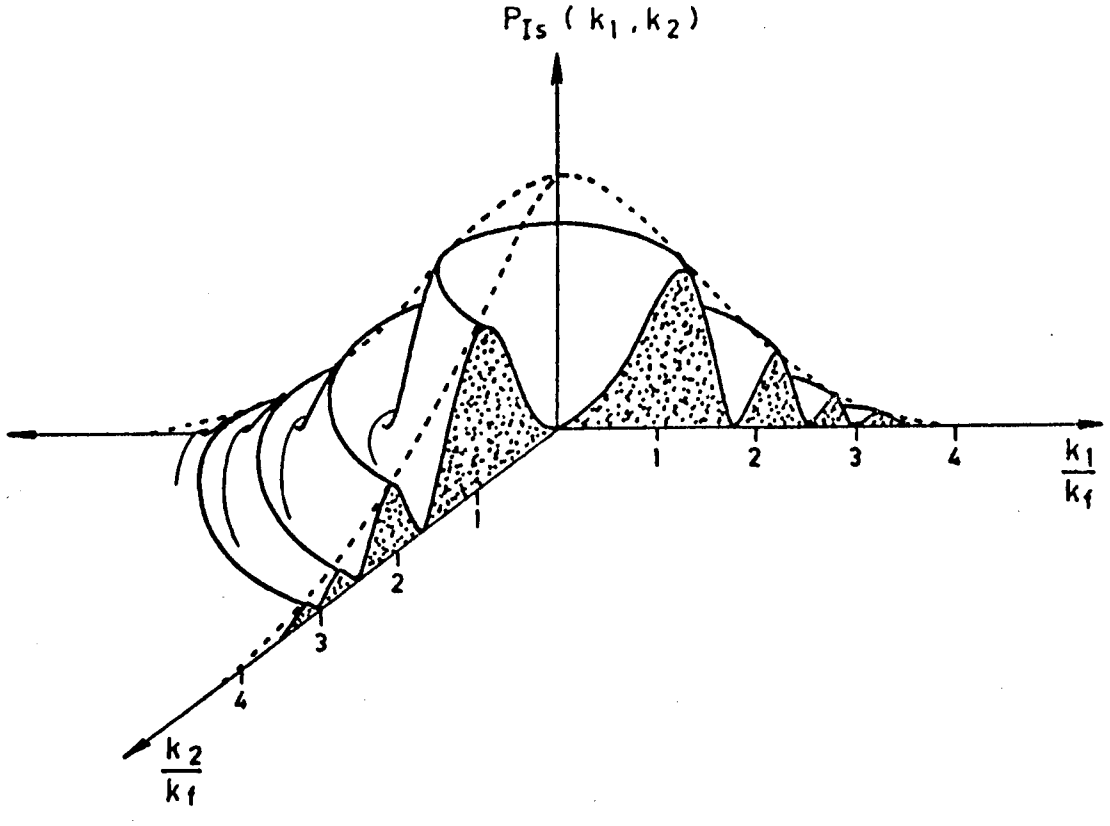

FIGURE 2.3 Perspective view of the two-dimensional spatial intensity spectrum $P_{Is}(k_1,k_2)$ at a distance from a thin randon phase screen.

$$\rho_{It}(\tau) = \rho_{Is}(r_1 = V\tau,\ r_2 = 0) \qquad \text{---- (2.18)}$$

The temporal power spectrum $P_{It}(f)$ of the intensity fluctuations is

$$P_{It}(f) = \frac{1}{2\pi}\int_{-\infty}^{\infty} e^{2\pi i f\tau}\ \rho_{It}(\tau)\ d\tau$$

$$= \frac{1}{2\pi V}\int_{-\infty}^{\infty} e^{ik_1 r_1}\ \rho_{Is}(r_1, r_2 = 0)\ dr_1 \qquad \text{---- (2.19)}$$

where $r_1 = V\tau$ and $k_1 = 2\pi f/V$. Substitution into relations (2.10) and (2.16) gives

$$P_{It}(f) = \frac{1}{V}\int_{-\infty}^{\infty} P_{\phi s}\left(k_1 = \frac{2\pi f}{V},\ k_2\right) dk_2$$

$$= \frac{8\pi L (r_e\lambda)^2}{V}\int_{-\infty}^{\infty} P_{Ns}(k_1, k_2, 0)\ \sin^2(k^2/k_f^2)\ dk_2 \qquad \text{---- (2.20)}$$

Thus the measured temporal power spectrum is a projection of the two-dimensional spectrum onto one dimension. The effect of this projection is to 'fill in' the Fresnel depression at $k = 0$ and the periodic zero's at higher wave numbers, the degree to which these features are filled in being dependent on the exact form of $P_{Ns}(\underset{\sim}{k})$.

Lovelace et al (1970) have noted that if the electron density fluctuations are approximately isotropic the spatial auto-correlation function ρ_{Is} can be defined in terms of a single variable r defined by (Lovelace 1971)

$$r_1 = r\cos\theta$$

$$r_2 = r\sin\theta \qquad \text{---- (2.21)}$$

where θ is an appropriate orientation angle. Similarly the spatial spectrum can be defined in terms of a single wave number k where

$$k_1 = k \cos \psi$$

$$k_2 = k \sin \psi \qquad \text{---- (2.22)}$$

where ψ is an appropriate orientation angle. In this instance the scintillation index m and auto-correlation function $\rho_{Is}(r)$ are related to $P_{Is}(k)$ by (Matheson and Little, 1971)

$$m^2 \rho_{Is}(r) = 2\pi \int_{-\infty}^{\infty} P_{Is}(k)\, J_0\,(2\pi k r)\, k\, dk \qquad \text{---- (2.23)}$$

Alternatively,

$$P_{Is}(k_1,k_2) = \frac{1}{2\pi} \int \rho_{Is}(r)\, J_0\,(kr)\, r\, dr$$

$$= \frac{V^2}{2\pi} \int_{-\infty}^{\infty} \tau\ \rho_{It}(\tau)\ J_0\,(2\pi f \tau)\ d\tau \qquad \text{---- (2.24)}$$

if the pattern is drifting with velocity V. This led Lovelace et al (1970) to define a Bessel transform

$$B_{It}(f) = \frac{1}{2\pi} \int_{-\infty}^{\infty} \tau\ J_0\,(2\pi f \tau)\ \rho_{It}(\tau)\, d\tau \qquad \text{---- (2.25)}$$

which on substitution into the above relations gives

$$B_{It}(f) = \frac{8\pi\ L\ (r_e \lambda)^2}{V^2}\ P_{Ns}(k_1, k_2, 0)\ \sin^2\ (k_f^2) \qquad \text{---- (2.26)}$$

A convenient measure of the degree of scintillation of a source is the scintillation index m which is defined as the rms intensity fluctuation relative to the steady (unscattered) component

$$m = \frac{\langle (I - I_0)^2 \rangle^{\frac{1}{2}}}{I_0} \qquad \text{---- (2.27)}$$

where I is the fluctuating intensity and I_0 is the mean value. The scintillation index is equal to the area under the projected spectrum

$$m^2 = \int_{-\infty}^{\infty} P_{It}(f)\, df \qquad \text{---- (2.28)}$$

and in the far-field is related to the rms phase deviation ϕ_0 by (Mercier, 1962)

$$m = 1 - \exp(-\phi_0^2) \qquad \text{---- (2.29)}$$

In the limit of weak scattering (2.29) becomes $m \approx \sqrt{2}\,\phi_0$, but in the near-field the intensity fluctuations are not fully developed and $m < \sqrt{2}\,\phi_0$.

The discussion to this point has been valid only in the weak scattering limit. When $\phi_0 > 1$ higher order terms in relation (2.13) must be included and the problem becomes non-linear. Mercier (1962) has considered the problem of diffraction in the far-zone due to large random phase fluctuations with a Gaussian auto-correlation function and has deduced analytic expressions for the even-order moments of the amplitude fluctuations. The variance of the intensity in the near-zone can be calculated numerically (Mercier, 1962; Bramley and Young, 1967). For $\phi_0 > 1$ the scintillation index approaches a maximum value greater than unity near the point where the focussing of rays by individual irregularities occurs. Buckley (1971a) has considered this problem analytically for very large phase deviations in a one-dimensional screen. The scintillation index increases with distance from the screen $\alpha\ Z^2$, reaching a maximum value

$$m = 1 + \tfrac{1}{2}\ln \phi_0 \qquad \text{---- (2.30)}$$

due to focussing by individual irregularities at a distance approximately equal to that predicted by geometrical optics. At large distances the index approaches unity. The diffraction pattern scale l is independent of ϕ_0 close to the screen and depends on the smaller scales within the screen. It reaches a minimum value

$$l \approx \frac{a\sqrt{\ln \phi_0}}{\phi_0} \qquad \text{---- (2.31)}$$

just in front of the focussing region, and at large distances approaches the value $\ell = a/\phi_0$. These results were based on the assumption of a Gaussian phase screen with characteristic scale 'a'. The effect of having a large range of irregularity sizes (e.g. a Kolmogorov turbulence spectrum) is to produce focussing over a larger range of distances. These results also apply qualitatively to the more realistic two-dimensional screen (Buckley, 1971b). Theoretical diffraction patterns for arbitrary values of ϕ_0 have been generated numerically by Buckley (1975). These are in agreement with the analytic results for $\phi_0 = 1$ and $\phi_0 = 20$ radians. In particular, they show that focussing occurs over a range of distances, corresponding to varying gradients in the (Gaussian) random phase fluctuation, as shown in Figure 2.4.

The degree of correlation between scintillation observations recorded simultaneously at two frequencies has been investigated for the case of a thin, weak-scattering screen by Budden (1965) and for an extended medium by Bakhareva (1959). For weak scattering the cross-correlation is always high in the near-field whereas in the far-field it is high provided that

$$\frac{\Delta f}{f} \lesssim \frac{2\pi a^2}{Z\lambda} \qquad \text{--- (2.32)}$$

where $f \pm \frac{\Delta f}{2}$ are the two observing frequencies. For a thick screen the cross-correlation approaches a value less than unity. In the case of strong scattering (Salpeter, 1967) the cross-correlation is high in the near-field provided

$$\frac{\Delta f}{f} < \phi_0^{-\frac{1}{2}} \qquad \text{--- (2.33)}$$

and is high in the far-field provided that

$$\frac{\Delta f}{f} < \frac{2\pi a^2}{\phi_0^2 \lambda Z} \qquad \text{--- (2.34)}$$

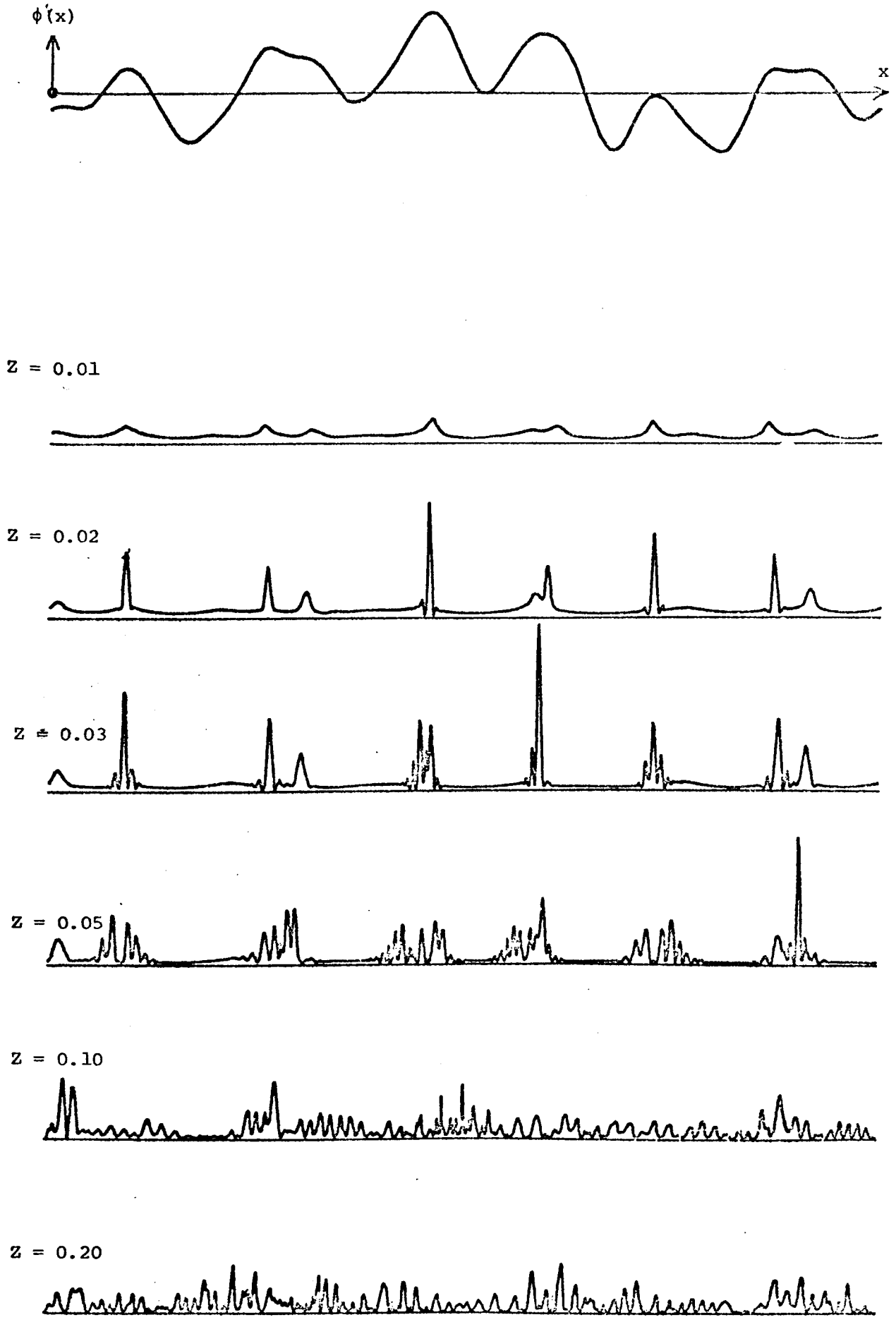

FIGURE 2.4 Intensity patterns as a function of distance from a random phase screen for $\phi_o = 10$.

(after Buckley,1975)

Since a radio star is a broadband noise source the experimental bandwidth will be determined by the receiver response. The above results are important for a consideration of the decorrelation of the signals across the receiver bandwidth (Little, 1968; Uscinski, 1970, 1971). The fluctuations will be seriously decorrelated across the receiver bandwidth, and hence significantly reduced, if relation (2.32) is not satisfied, where Δf is the receiver bandwidth and f the centre frequency of the receiver bandpass.

Salpeter (1967) has defined four regimes for scintillation observations as depicted in Figure 2.5. The character of the scintillations is determined by two parameters; (i) the ratio between the distance Z from the screen and the Fresnel distance $Z_F = ka^2$ for 'blobs' of size a, and (ii) the rms phase deviation ϕ_0. Regions I and II are weak-scattering regions in the near- and far-fields respectively. Region III is the far-field strong-scattering region. Region IV is the near-field strong-scattering region in which the predominant feature is the occurence of high intensity 'spikes' caused by the tendency for individual irregularities to act as focussing lenses.

The discussion so far has been concerned with radiation emitted from a point source. If the source has a finite angular diameter ψ it can be considered as a group of point sources and the resulting diffraction pattern is the sum of the diffraction patterns from each of these points. Each pattern is slightly displaced from the other patterns and their addition results in the blurring of the intensity fluctuations and therefore a reduction in the scintillation index. This effect modifies equation (2.16) to give (Salpeter, 1967)

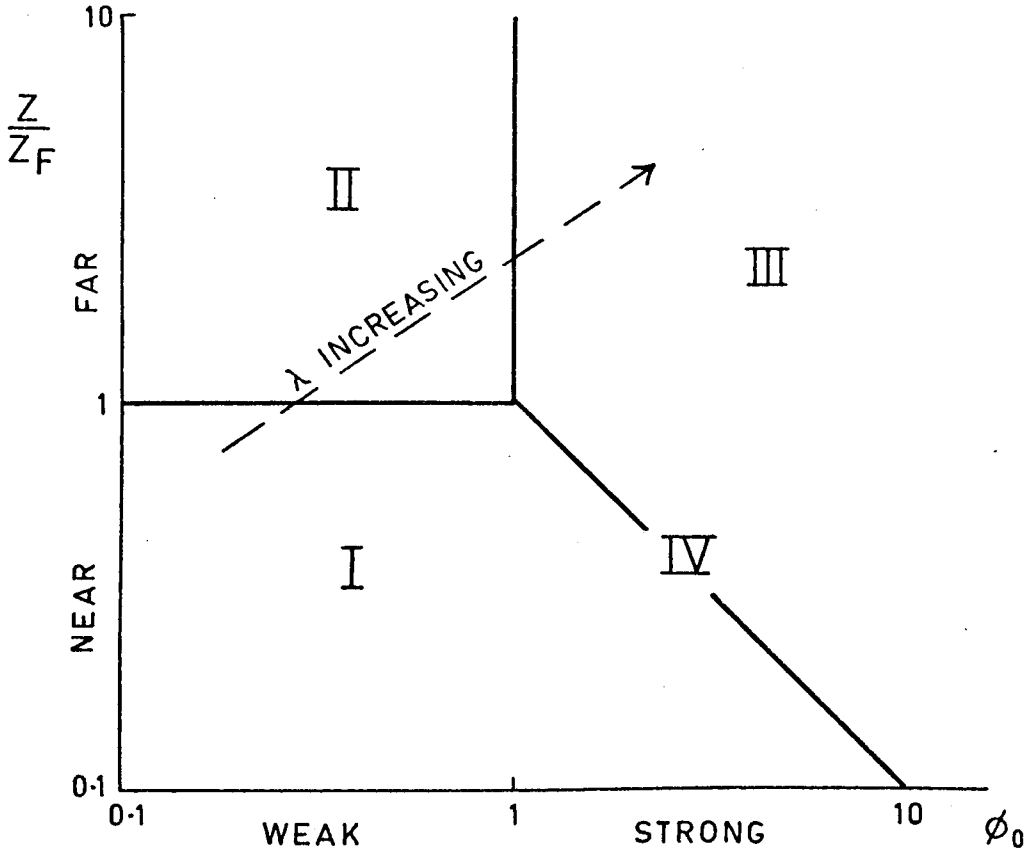

FIGURE 2.5 Interplanetary scintillation diffraction regimes (after Salpeter,1967)

$$P_{Is}(\underset{\sim}{k}) = P_{\phi s}(\underset{\sim}{k}) \sin^2 (k^2/k_f^2) F_{source}(k,Z) \quad \text{---- (2.35)}$$

where $k = k_1^2 + k_2^2$, and $F_{source} = |V(k,Z)|^2$, with V the source visibility function. For example, a source with a symmetrical Gaussian brightness distribution $B(\theta) = \exp(-\theta^2/2\theta_0^2)$ has a visibility function $V(r) = \exp(-r^2\theta_0^2/2)$. The effect of the factor F_{source} is to act on the power spectrum as a low-pass filter with a cut-off wavenumber $k_s = \frac{1}{Z\theta_0}$

2.3 CORONAL BROADENING

In a paper published in 1951 Machin and Smith pointed out that the radiation emitted by a radio source, would be refracted in passing through the corona and at a certain distance would be effectively occulted. The radio source in the Crab Nebula, which lies close to the ecliptic plane and passes within $5R_o$ of the sun during June each year, was observed with interferometers at 38 and 81.5MHz. The fringe visibility was observed to gradually decrease within about $10R_o$ (Machin and Smith, 1952) but the observations did not agree with a model (Link, 1951) based purely on refraction within the corona. Machin and Smith suggested that the radio waves were scattered by irregularities in the electron density in the corona, causing an apparent broadening of the source.

These observations were continued by Hewish (1955) at the same frequencies but on more than one interferometer baseline. Hewish showed that his observations could be explained by a scattering theory developed by Fejer (1952). The decrease in fringe amplitude could have arisen in one of two ways. If the total phase deviation after traversing the scattering region is less than one radian, the radiation consists of an unscattered component plus an angular spectrum of scattered waves. In this case the source would appear as a point source surrounded by a halo. The fringe

amplitude would decrease if the angular spectrum was considerably greater than the angle between the interference maxima of any of the interferometers so that only the unscattered component was measured. Alternatively, if most of the radiation was scattered ($\phi_0 >> 1$ rad) but the spread of the angular spectrum was comparable with the angle between the interference maxima the fringe amplitude would be dependent on the interferometer spacing. Hewish showed that the apparent variations of intensity and angular size agreed with this second case and concluded that the mechanism was one of multiple scattering. Subsequent observations (Hewish, 1958; Erickson, 1964) have shown that the angle of scattering is proportional to the square of the wavelength between 26 and 160MHz, in accord with the multiple scattering theory.

Two-element interferometry has been the most extensively used technique for coronal broadening observations. Special care must be taken to avoid the effects of solar radiation, particularly from intense, small angular diameter active sources. While most observations have used the strong radio source in the Crab Nebula, the use of large collecting areas enables observations to be made using other weaker sources with lines of sight which intersect different regions of the corona. One disadvantage in using phase-switched interferometers is the difficulty in distinguishing between an apparent increase in the angular diameter of the source and a decrease in the source intensity. Fan or pencil beams derived from long arrays or compound interferometers are more suitable for measuring the source intensity during the occultation. The use of several interferometers with baselines in different directions provides model-dependent estimates of the size and shape of the broadened image. The recent development of the Culgoora radio-heliograph has made it possible to measure the complete two-dimensional brightness distribution of the broadened image.

Anisotropy in the shape of the image became apparent with Hewish's (1958) data obtained from interferometers with baselines at three different position angles. The elongation and orientation of the image was estimated assuming a simple elliptical Gaussian model for the brightness distribution. The image showed a tendency to be elongated perpendicular to the radial direction, as might be expected for scattering from irregularities in the electron which were aligned along the radial magnetic field lines. Similar results were found by Slee (1959) using pencil and fan beams in addition to an interferometer. Erickson (1964) found that between 20 and 60 R_o the scattering irregularities are more random in orientation although showing a slight preference for the radial direction. Measurements of the complete two-dimensional brightness distribution (Harries et al, 1969; Blesing and Dennison, 1972) have confirmed the radial alignment within 20 R_o.

The degree of scattering is closely related to the phase of the solar activity cycle, with the radial scattering angle at distances between 5 and 20 R_o from the sun being well correlated with the smoothed sunspot number over two complete solar cycles (Hewish, 1958; Okoye and Hewish 1967; Matheson and Little, 1971; Ward, 1975). Slee (1966) showed that this relationship existed at distances up to 80 R_o from the sun during the decreasing phase of the previous cycle (1960-62). The scattered distribution typically has an axial ratio ~2.1 at solar maximum (Blesing and Dennison 1972) but this decreases to $\lesssim$ 1.3:1 towards solar minimum (Slee, 1966; Ward, 1975). During the solar maximum the axial ratio beyond 10 R_o the axial ratio appeared to increase to ~ 4.1.. It will be shown in chapter eight that this effect has not been evident since 1971.

This leads us to one of the main topics of discussion in the literature on coronal broadening, the variation of scattering with radial

distance from the sun. Early attempts to fit the observed scattering angles to power-law variations with distance (Slee, 1961; Hewish and Wyndham, 1963; Erickson, 1964) were confused by the inclusion of data at different phases of the solar cycle. When comparing such observations it is necessary to take into account the solar cycle variations of scattering, the changing orientation of the anisotropic scattered distribution, and the shape of the corona during solar maximum and minimum. Slee (1966) found agreement between the radial variations determined by several authors when these effects were taken into account. The radial gradient of the scattering appears to be largely independent of the solar cycle, the decrease in anisotropy resulting from a change in the tangential scattering (Slee, 1961; Ward, 1975).

One remaining effect which has been investigaged in detail by Okoye and Hewish (1967) is the tendency for the power law index to vary with distance from the sun. These authors observed various sources including the Crab Nebula and 3C123 over a wide range of heliocentric distance (10 - 100 R_o). The observed radial scattering angles combined with values from previous years revealed a gradual decrease in the power law index with increasing distance from the sun. The effect of different phases of the solar cycle was merely to shift the complete scattering curve up or down leaving its general shape the same. Okoye and Hewish (1967) suggested that the reduction in the power-law index might be due to plasma instabilities producing extra irregularities away from the sun.

Under conditions of multiple scattering, the scattering angle θ is (Slee, 1966)

$$\theta \alpha \int \Delta N^2 (Z) \; k (z) \; a^{-1} (z) \; dz \qquad \text{--- (2.36)}$$

where the integral is evaluated along the line of sight, $\Delta N(z)$ is the rms fluctuation of electron density, $k(z) \leq 1$ is a space filling factor, and

a(z) is the rms size of the irregularities. Thus to find $\Delta N(Z)$ or a(Z) it is necessary to solve the integral equation based on some model of the corona. Hewish (1955) showed that the multiple scattering theory places a lower limit

$$a_{min} \approx \frac{\lambda}{\pi \phi_o} \qquad \text{--- (2.37)}$$

on the scale, which is of the order of 1 km at 5 R_θ. Hewish and Wyndham (1963) derived an upper limit a_{max} based on the fact that scattering angles as small as 6" had been observed at 60 R_o, implying that the density irregularities had a scale $\leqslant 5 \times 10^3$ km. Several estimates of the electron density fluctuation have been made (Erickson, 1964; Slee, 1966) based on a range of values of the scale within these limits. The results suggest that there is a relatively small (< 10%) modulation of a smoothly varying mean electron density.

The availability of complete two-dimensional images of the broadened source has enabled a detailed comparison to be made of the scattered intensity distribution with theoretical predictions. Dennison and Blesing (1972) showed that the observed brightness distribution was consistent with scattering irregularities which possessed a single dominant scale structure rather than a power-law variation in scale sizes. Similar results were obtained by Matheson and Little (1971) on the basis of multiple-baseline interferometer observations.

2.4 INTERPLANETARY SCINTILLATION

During a 178MHz survey of radio sources (Hewish, Scott and Wills, 1964) it was noticed that some sources exhibited random fluctuations in intensity similar to ionospheric scintillations but of a much shorter period. The

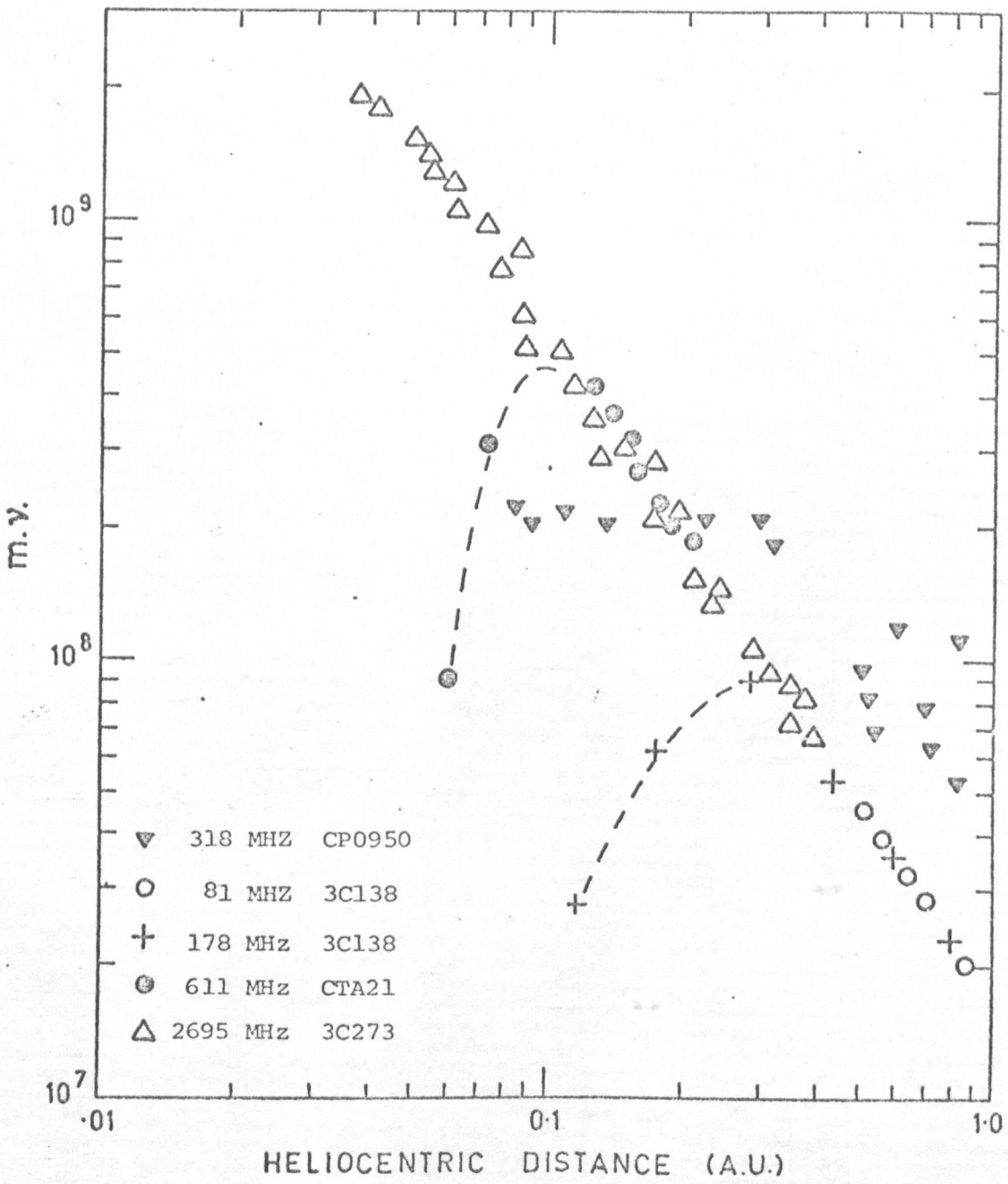

FIGURE 2.6 Variation of scintillation index as a function of solar elongation or heliocentric distance.

81.5 MHz Hewish and Symonds (1969)
178 MHz Little and Hewish (1967)
314 MHz Zeissig and Lovelace (1972)
611 MHz Harris and Hardebeck (1969)
2695 MHz Bourgois (1969)

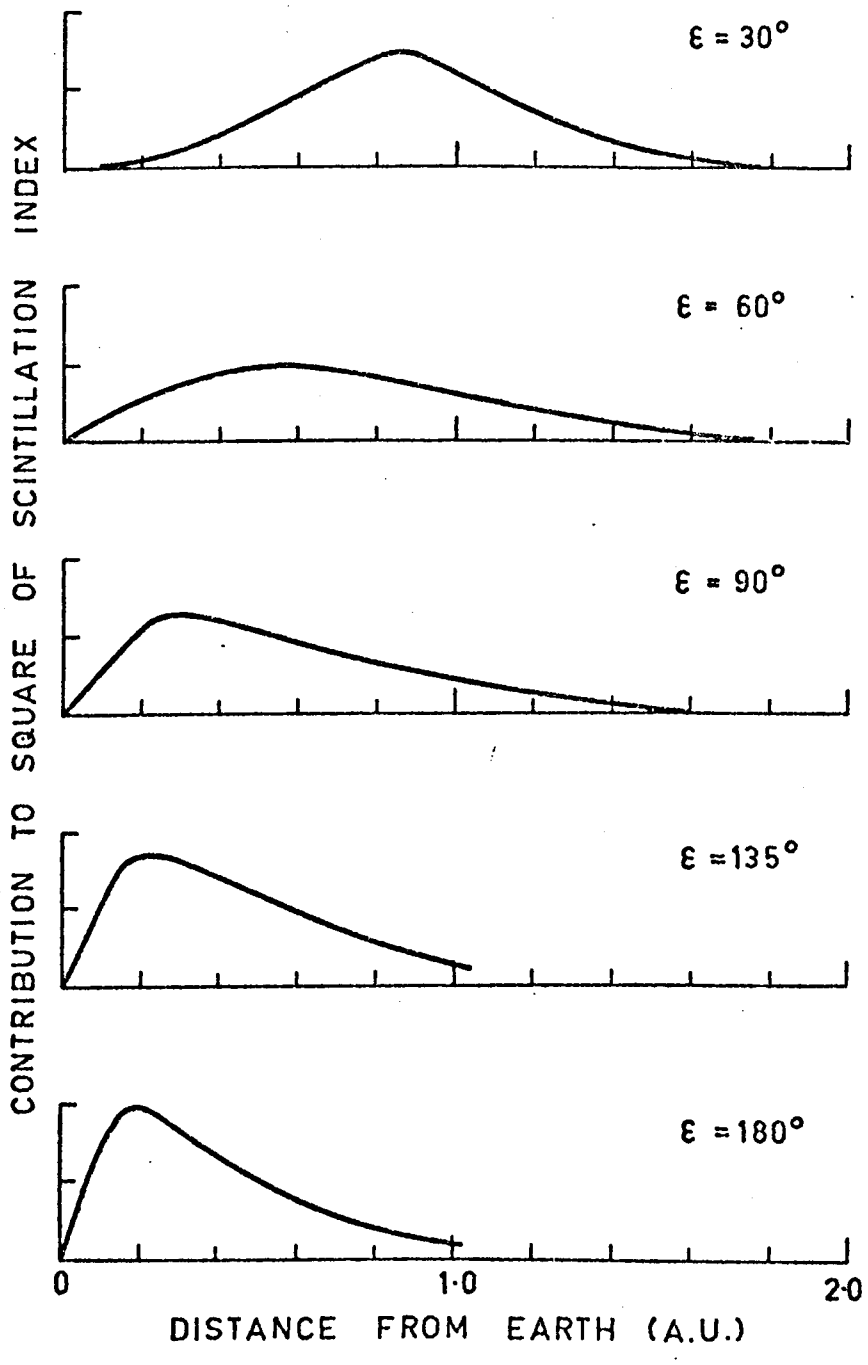

FIGURE 2.7 Contribution of elements of the line of sight to the total scattering along a path as a function of solar elongation ε. (after Redhead,1972)

fluctuations were peculiar to sources of very small angular diameter ($\lesssim$ 1" arc) and it was concluded that they resulted from scattering by irregularities in electron density in the interplanetary medium. More extensive observations revealed a strong heliocentric dependence of the scintillation as well as suggesting a dependence on source dimensions.

The usefulness of interplanetary scintillation as a method for estimating the parameters of the interplanetary medium was at first in doubt because coronal broadening observations closer to the sun had indicated that the rms phase deviation was greater than one radian. Little, Hewish and Dennison (1966) measured the scintillation of the radio source 3C48 at 81.5 and 178MHz simultaneously along a line of sight passing 0.5AU from the sun. They found that the ratio of scintillation indices and the cross-correlation between the fluctuations were consistent with a weak scattering origin.

At a given frequency the scintillation index increases as the source elongation ϵ decreases, as shown in Figure 2.6. For an extended source the index will decrease close to the sun due to diameter blurring effects. The scintillation is the consequence of scattering at many points along the line of sight. Redhead (1972) has used the index-elongation variation to derive the dependence of scattering on the radial distance from the sun, and hence to derive the contribution to the scintillation of different elements along the line of sight, shown as a function of the source elongation ϵ in figure 2.7.

By applying a full correlation analysis (Briggs et al, 1950; Phillips and Spencer, 1955) to scintillation observations recorded at three spaced receiving sites, it is possible to estimate the velocity, size and shape of

the diffraction pattern and hence deduce information about conditions in the medium itself. The movement of the source relative to the sun can be used to probe conditions over a wide range of heliocentric co-ordinates. The first spaced-receiver observations were conducted at Cambridge, U.K. (Dennison and Hewish, 1967; Hewish and Symonds, 1969). Subsequently spaced-receiver experiments have been carried out in the USSR (Vitkevitch and Vlasov, 1970), Japan (Watanabe et al, 1974) and the USA (Armstrong and Coles, 1972).

These observations have confirmed that the solar wind outflow is radial to within the experimental accuracy of $\pm 10^{0}$. One feature of interest is the variation of the solar wind velocity as a function of heliocentric latitude since regions out of the ecliptic plane are not accessible to present generation spacecraft but are of importance to theoretical models of the coronal expansion. During 1966 the velocity increased from $\sim$300 km sec^{-1} near the ecliptic plane to $\sim$450 km sec^{-1} near the North solar pole but this variation was not evident during 1967 (Dennison and Hewish, 1967; Hewish and Symonds, 1969). This increase in velocity with increasing latitude was again evident in 1972 but not in 1973 (Coles and Maagoe, 1972; Watanabe et al, 1974). The solar wind velocity is inversely correlated with the brightness of the solar EUV corona in the source region, the high velocities out of the ecliptic plane during 1972 corresponding to regions of low EUV brightness at high heliographic latitudes (Watanabe et al, 1974). This has provided confirmation that the regions of high velocity solar wind usually originate in coronal holes. Normal bi-polar active regions are usually associated with low solar wind velocities ($\lesssim$ 400 km sec^{-1}) but more complex multipolar active regions are associated with high velocities ($\lesssim$ 500 km sec^{-1}) (Watanabe, 1975).

The solar wind velocity at distances between 6 and 40 R_{o} from the

sun has been measured using two spaced receivers at 2295MHz (Ekers and Little, 1971). This region is of particular interest since it is the region in which the coronal plasma is being accelerated. The mean velocity was found to increase with distance as predicted by models of the coronal expansion but below $30R_o$ there was also a significant random velocity component. Golley and Dennison (1970) applied the technique of dispersion analysis to spaced-receiver observations at larger distances from the sun. They found that, while most of the observed dispersion could be accounted for by the effect of the projection of a constant radial velocity across the line of sight, there was evidence for a larger range of velocities than could be explained solely by the projection effect.

As was noted in Section 2.2, if we assume that the electron density irregularities possess a Gaussian auto-correlation function it is possible to estimate the scale size from interplanetary scintillation and coronal broadening observations. In the case of IPS the diffraction pattern scale ℓ is equal to the irregularity scale 'a' of $\phi_o < 1$ rad but is $\ell \sim a/\phi_o$ if $\phi_o > 1$ rad. In the case of coronal broadening the scale size can be estimated from the scattering angle θs using the relation

$$\theta s \approx \frac{\lambda \phi_o}{\pi a} \qquad \text{---- (2.38)}$$

where ϕ_o is estimated using Figure 2.6 and relation (2.29). Estimates of the scale sizes measured by these two techniques over a wide range of frequencies and heliocentric latitudes are shown in Figure 2.8. Perkins (1973) has suggested that the low Coulomb collision frequency in the interplanetary medium leads to the existence of magneto-acoustic instabilities in which the wave energy is concentrated at those wavelengths for which the growth rate of the instabilities is a maximum. The non-linear theory for these instabilities can quantitatively account for both the variation of scale length with radial

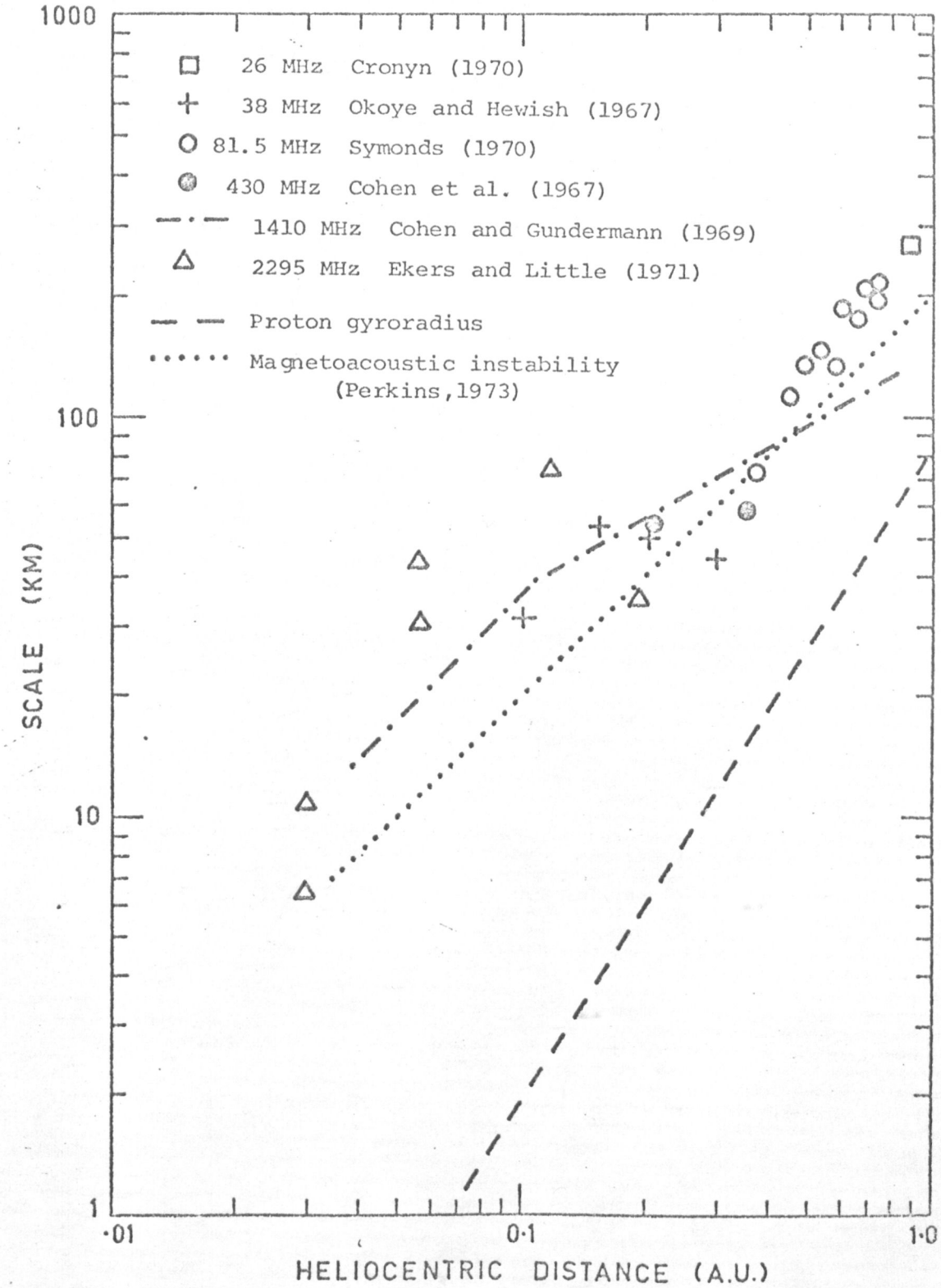

FIGURE 2.8 Variation of electron density irregularity scale with heliocentric distance as deduced from interplanetary scintillation and coronal broadening observations.

distance from the sun and the rms density fluctuation relative to the mean density.

During 1966 to 1969 the anisotropy of the diffraction pattern indicated that the irregularities of electron density were elongated, with an axial ratio ~ 2:1, and oriented along the direction of motion of the plasma flow (Dennison, 1969; Vitkevitch and Vlasov, 1972). The axial ratio measured during 1972 was seldom as high as 1.5:1 (Coles and Maagoe, 1972). This is consistent with the changes in the axial ratio of the irregularities within $20R_o$ of the sun during the decreasing phase of the solar cycle.

The traditional interpretation of coronal broadening and spaced-receiver interplanetary scintillation observations has been based on the assumption that the irregularities of electron density possess a dominant scale size. Hewish (1972) has summarized this model which leads to the conclusion that there is a characteristic microscale for turbulence in the solar wind which increases with radial distance from the sun. An alternative viewpoint has been to explain interplanetary scintillation in terms of a modified power-law spectrum similar to that observed in the magnetic field irregularities (Jokipii and Hollweg, 1970; Cronyn, 1970, 1972). Much of the argument has centred on the variation of scintillation index with radio wavelength and involves combination of data recorded by different observers at different distances from the sun and during different phases of the solar activity cycle. (Hewish, 1971; Little, 1971; Hollweg and Jokipii, 1971; Cronyn, 1972). Alternatively, the spectrum of the density irregularities can be estimated from the scintillation data rising relation (2.20). Lovelace et al (1970) have reported scintillation spectra which possess a power-law variation with frequency, suggesting a power-law variation in the density

spectrum. Several authors (Buckley, 1971; Matheson and Little, 1971; Rickett, 1973) have suggested that the density irregularities possess a power-law spectrum on which is superimposed an enhanced distribution of irregularities with a scale of the order of the ion gyro-radius. Recent measurements of proton density spectra (Unti et al, 1973; Neugebauer, 1974) lend some support to this hypothesis. They suggest a basically power-law variation of the form $P(f) \alpha f^{-3.6}$ with a small but statistically significant power enhancement near the proton gyro-radius scale size superimposed.

Two methods have been developed for estimating the angular structure of radio sources from interplanetary scintillation observations. The Cambridge group developed a technique based on the variation of the scintillation index and pattern scale as a function of solar elongation (Little and Hewish, 1966). Estimates of the angular structure of radio sources were obtained by comparing the variations in index and scale with those of several strong "point" sources. Results of surveys based on this technique have been published by Little and Hewish (1968) and Burnell (1974). A number of sources have shown variations in the index-elongation relation identical to that of a point source but of overall reduced magnitude. This is consistent with a core-halo source in which only the small angular diameter core scintillates. In this case the ratio of the scintillation index for the source to the corresponding index for a point source gives the ratio of flux in the core to the total source flux.

An alternative method for estimating source diameters has been used by the Cornell-Arecibo group (Cohen et al, 1966, 1967) and is based on the fact that the observed diffraction pattern is the convolution of the pattern which would be produced by a point source with the brightness distribution of

the source being observed. As discussed in Section 2.2 the effect of a finite diameter source on the power spectrum of the intensity fluctuations is to act as a low-pass filter with a cut-off frequency

$$f_c \approx \frac{V}{2\theta Z} \qquad \text{---- (2.39)}$$

Measuring this cut-off frequency (or some measure of the spectral width such as the second moment) allows estimation of the source diameter from a single observation. An extensive survey using this technique (Cohen, Gundermann and Harris, 1967) was in fair agreement with the results of Little and Hewish (1968). Another survey (Harris and Hardebeck, 1969) examined a large number of sources north of the ecliptic and obtained statistical information on the structure and degree of scintillation of these sources.

One problem basic to both techniques is that they are based on a calibration against the behaviour of a point source but the effect of the solar wind on the radiation from a point source is not known *a priori*. Common practice has been to use for calibration purposes those sources known, from VLBI or lunar occultation observations, to have small angular diameters. Since the VLBI and occultation observations are generally made at cm wavelengths the use of these sources for calibration of m wavelength scintillation obversations assumes that the source structure does not depend to any major extent on the observing frequency. Recently Armstrong et al (1973) have noted that application of the scintillation technique to the compact scintillating source in the Crab Nebula provides an estimate of the flux density which is a factor of two larger than that measured at the same frequency by VLBI (Vandenburg et al, 1973). This would suggest that the "point" sources used for calibration of the scintillation method may in fact possess extended, non-scintillating components at metre wavelengths. This is also suggested in observations of the interplanetary scintillation of the pulsar CP0950 (Zeissig and Lovelace, 1972) which has an apparent angular diameter $< 1.7 \times 10^{-3}$ arc sec

at 318MHz. Although there is wide scatter in the index values (see Figure 2.6) due to uncertainties in the correction for intrinsic variations in the pulsar intensity the index values are consistently higher than those of the source CTA21 at the same elongation and observing frequency. This suggests that at low frequencies CTA21, which is frequently used as a calibration point source, possesses an extended component in addition to the small ($\approx$0.04) diameter source. Although there are considerable practical problems involved, observations of the interplanetary scintillations of pulsars may provide more accurate point-source calibrations for estimates of source structure at metre wavelengths.

During the early IPS observations it was noted that transient increases in the scintillation index, lasting for one or two days, occurred from time to time. Dennison and Wiseman (1968) showed that it was possible to measure the location of large-scale disturbances in the interplanetary medium from daily variations in the scintillation index of a number of sources spaced around the sky. This technique has been used to measure the properties of corotating structures (Houminer and Hewish, 1972, Wiseman, 1972; Houminer, 1973; Watanabe and Kakinuma, 1972) and of flare-produced disturbances (Wiseman and Dennison, 1972; Armstrong et al, 1973; Watanabe et al 1973; Ward, 1974, 1975). The corotating structures are associated with regions of enhanced plasma density located at the leading edge of high-speed plasma streams and are confined to heliocentric latitudes $\lesssim 40^0$. Flare-produced disturbances extend over a wide area of the medium and are associated with the turbulent plasma in the region of the shock front which moves outwards from the flare site.

CHAPTER 3

SPACED-RECEIVER EXPERIMENT - EQUIPMENT

3.1 INTRODUCTION

The most complete description of the diffraction pattern on the ground would be achieved by a full two-dimensional sampling of the phase and amplitude, as has been done in the case of radio-wave reflections from the ionosphere (Briggs and Holmes, 1973). The large scale size (~ 150 km) of the interplanetary scintillation diffraction pattern makes this impractical. It is possible however to estimate the velocity, shape and size of the electron density irregularities by measuring the correlation and time delay between intensity scintillations recorded at three or more spaced receivers.

The Adelaide IPS project was designed as a three spaced receiver experiment operating at two frequencies simultaneously. This chapter presents a discussion of the factors to be taken into consideration when designing such a system and a description of the complete system.

3.2 DESIGN CONSIDERATIONS

The choice of operating frequency and location of the three receiving sites is largely determined by the characteristics of the scattering processes which produce the intensity fluctuations. Since these processes are wavelength dependent it is advantageous to make simultaneous observations at more than one radio frequency.

As was noted in Chapter 2, there is some uncertainty as to whether the scale of the diffraction pattern measured on the ground represents the true physical size of the electron density irregularities or is merely a measure of the Fresnel radius $(\lambda z)^{\frac{1}{2}}$. If the Gaussian screen is a reasonable

approximation the scale of the diffraction pattern is equal to the scale of the density irregularities provided that the scattering is weak ($\phi_0 < 1$) and the observer is in the far - field. In the case of strong scattering ($\phi_0 > 1$) the relationship between the density and pattern scales is dependent on the value of ϕ_0. Thus in the weak scattering region the measured scales should be equal at the two observing frequencies. By a suitable choice of the two frequencies it is possible to include a range of distances in which the scattering is strong at one frequency and weak at the other, enabling direct estimation of the rms phase deviation ϕ. If, however, the pattern scale is only a measure of the Fresnel radius the scales measured at the two frequencies should exhibit a systematic difference even in the weak scattering region.

Consideration of these factors suggests that to investigate the properties of the solar wind in the range 0.1 to 1.0 AU observations within the frequency range 40 to 250MHz would be desirable. The final choice of frequencies was made in consultation with the Commonwealth Postmaster-General's Department in order to avoid interference from commercial communications networks. The frequencies adopted were 111.5 MHz (Bandwidth 1 MHz) and 235.9 MHz (Bandwidth 2 MHz).

The optimum spacing between the three receiving sites is also dependent upon the nature of the electron density irregularities. As the distance between the receivers increases the correlation between records at two sites decreases and the time delay between similar features in the records increases. A compromise between the time delay and the degree of cross-correlation must be made. Figure 3.1 shows the time delay as a function of receiver separation and solar wind velocity, and the expected correlation as a function of receiver separation and irregularity scale size. The optimum

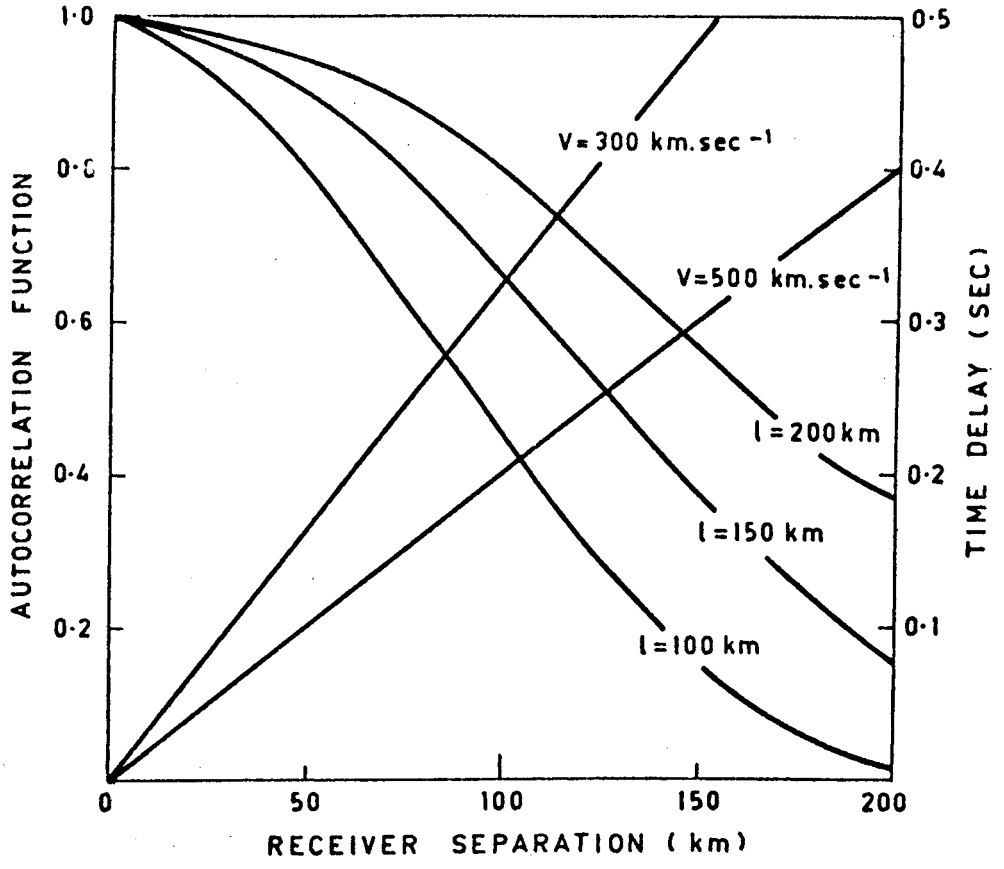

FIGURE 3.1 Time delay and correlation as a function of pattern scale and receiver separation.

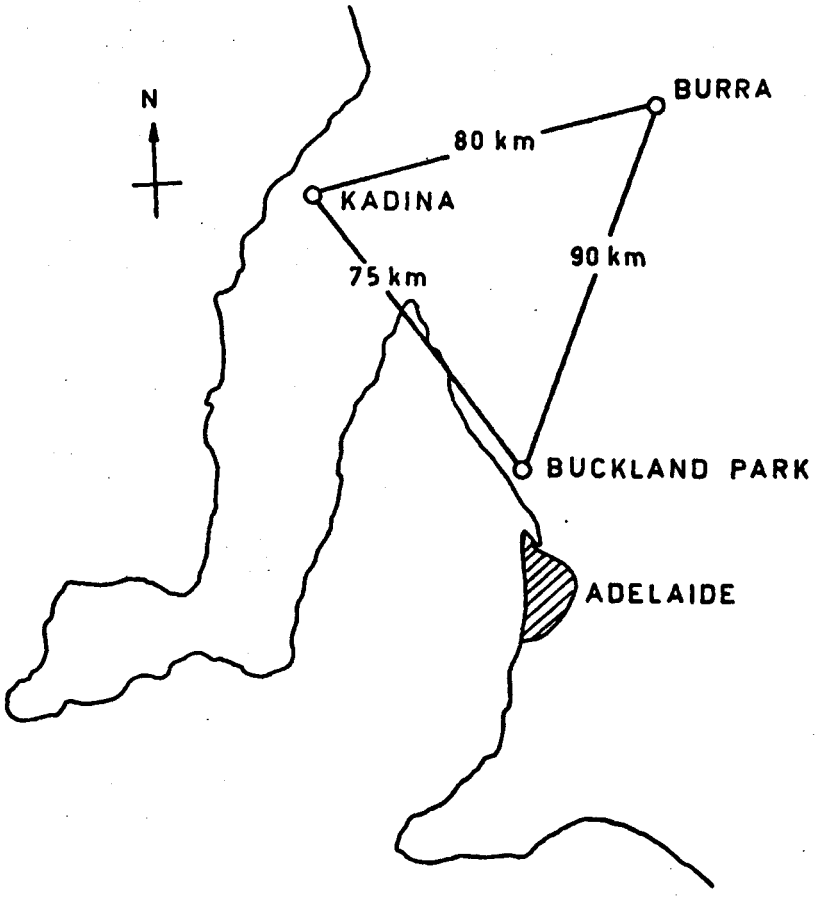

FIGURE 3.2 Location of the receiving sites.

separation is in the order of 100km , giving a time delay ~0.25 sec and a correlation coefficient ~0.5. The base station was constructed at the University's field station at Buckland Park, and the outstations at Burra and Kadina, as shown in figure 3.2.

3.3 SENSITIVITY AND NOISE CONSIDERATIONS

Having decided on the operating frequencies and site locations it is necessary to calculate the antenna collecting area required to observe a radio source of given strength. The sensitivity of a radio-astronomy receiver is usually defined in terms of the minimum detectable noise temperature

$$\Delta T = \frac{2\ T_{sys}}{\sqrt{B\tau}} \qquad \ldots.(3.1)$$

where B is the pre-detection bandwidth, τ the post-detection time constant, T_{sys} the total system noise temperature, and the factor 2 is a constant determined by the receiver type (in this case a phase-switched interferometer).

At metre wavelengths it is possible by careful design of the receiving equipment to ensure that the main contribution to the system noise comes from the galactic background. At 111.5MHz the background sky temperature is ~500 ^{0}K in the direction of the galactic pole, increasing to 4000 ^{0}K at the galactic centre (Krauss, 1966). At 235.9MHz the corresponding temperatures are ~100 ^{0}K and ~1000 ^{0}K. Since the major scintillating sources lie well away from the galactic centre we assume a background sky temperature of 600 ^{0}K at 111.5MHz. If we assume a reasonable receiver noise temperature ~300 ^{0}K we have a typical total system noise temperature T_{sys} of 900 ^{0}K and 500 ^{0}K at 111.5MHz and 235.9MHz respectively.

We now wish to calculate the antenna collecting area required to record at least two or three of the strongest scintillating sources. The antenna temperature T_A produced by a source of flux S is given by

$$T_A = \frac{S.A}{2k} \qquad \ldots.(3.2)$$

where k is Boltzmann's constant and A is the effective collecting area of the antenna. The factor of ½ arises from the fact that only one plane of polarization is recorded. Combining equations (3.1) and (3.2), the collecting area required to produce a signal to noise ratio N, ($N = \frac{T_A}{T}$), for a source of flux S, is given by

$$A = \frac{4\ k\ N\ T_{sys}}{s\ \sqrt{B\ \tau}} \qquad \ldots\ldots(3.3)$$

Table 3.1 lists the fluxes of the strongest scintillating sources, observable in the southern hemisphere, and it can be seen that there are several sources with fluxes greater than 50 f.u. (1 f.u. = 10^{-26} $Wm^{-2}Hz^{-1}$). Substituting values into equation (3.3) we find for a receiving frequency of 111.5MHz with a system temperature T_{sys} = 900 ^{0}K, Bandwidth 1MHz, and time constant τ = 0.1 sec the required collecting area to record a 50 f.u. source with a signal to noise ratio of 5:1 is ~1400m^2. At 235.9MHz a slightly smaller collecting area would be required for the same source.

3.4 ANTENNA SYSTEM

In view of the large collecting area required (nearly half that of the Parkes 64m radio-telescope) and the limited finances available, the only possibility was to construct a transit-type instrument. E-W corner reflectors were chosen in preference to flat reflector screens, to reduce the beam-width in the N-S direction. Within each reflector two dipole arrays were constructed, one for each frequency.

Corner reflectors containing dipole active elements have been studied in detail by Cottony and Wilson (1958) and Wilson and Cottony (1960). The parameters for the final design were obtained from these empirical studies and were chosen for a minimum N-S sidelobe response with maximum gain. The final design, illustrated in figure 3.4, had a 'corner' angle $\theta = 85^0$, width of sides W = 3.8m (~ 3λ at 235.9MHz), and dipole distances from the apex of

TABLE 3.1 FLUX DENSITIES OF SCINTILLATING SOURCES

SOURCE	$S_{111.5MHz}$(f.u.)	$S_{235.9MHz}$(f.u.)
1226+02	100	65
1416+06	90	40
0624-05	85	60
1309-22	50	35
2313+03	40	20
1938-15	35	18
0758+14	30	12

[1 f.u. = 10^{-26} W m^{-2} Hz^{-1}]

0.33λ and 0.4λ at 111.5MHz and 235.9MHz respectively. The length of the corner reflectors was chosen to be 250m giving a physical collecting area of approximately 1400m^2. Four such antennas have been constructed at the Buckland Park base-station and two at each of the outstations. The NS separation between adjacent corner reflectors was equal to 3λ at 111.5MHz. Figure 3.3 shows a photograph of the arrays at Buckland Park, and Figure 3.4 illustrates the principle features of the corner reflectors. The spacing between the wires of the reflector screens was $\frac{\lambda}{20}$ at the highest frequency to obtain reasonably efficient reflection with a front-to-back ratio ≥20dB (Wilson and Cottony, 1960).

Full-wave dipoles were used whose high impedance allowed groups of 10 dipoles to be fed in parallel through open-wire feeders with characteristic impedances of 300Ω. This was achieved by constructing an open-wire feeder along the full length of the aerial and isolating each group of 10 dipoles by λ/4 shorts at each end of the group. The feeder and the connected dipoles can be clearly seen in the photograph. To achieve equal path lengths to the receiver from each part of the corner reflector a 'Christmas tree' feed system was used as illustrated in Figure 3.5. The impedance of each group of 10 dipoles was measured using a VHF bridge and matched to another 300Ω open-line feeder using a λ/4 shorted stub transformer, in order to overcome a large reactive component arising from interaction between the two different frequency arrays. Finally, the feeders were connected by 'baluns' (balanced to unbalanced transformers) to two 50Ω co-axial cables taking the signal from each half of the corner reflector to the phasing unit.

Each corner reflector was operated as an interferometer, one half being phase-switched against the other to remove the galactic contribution to

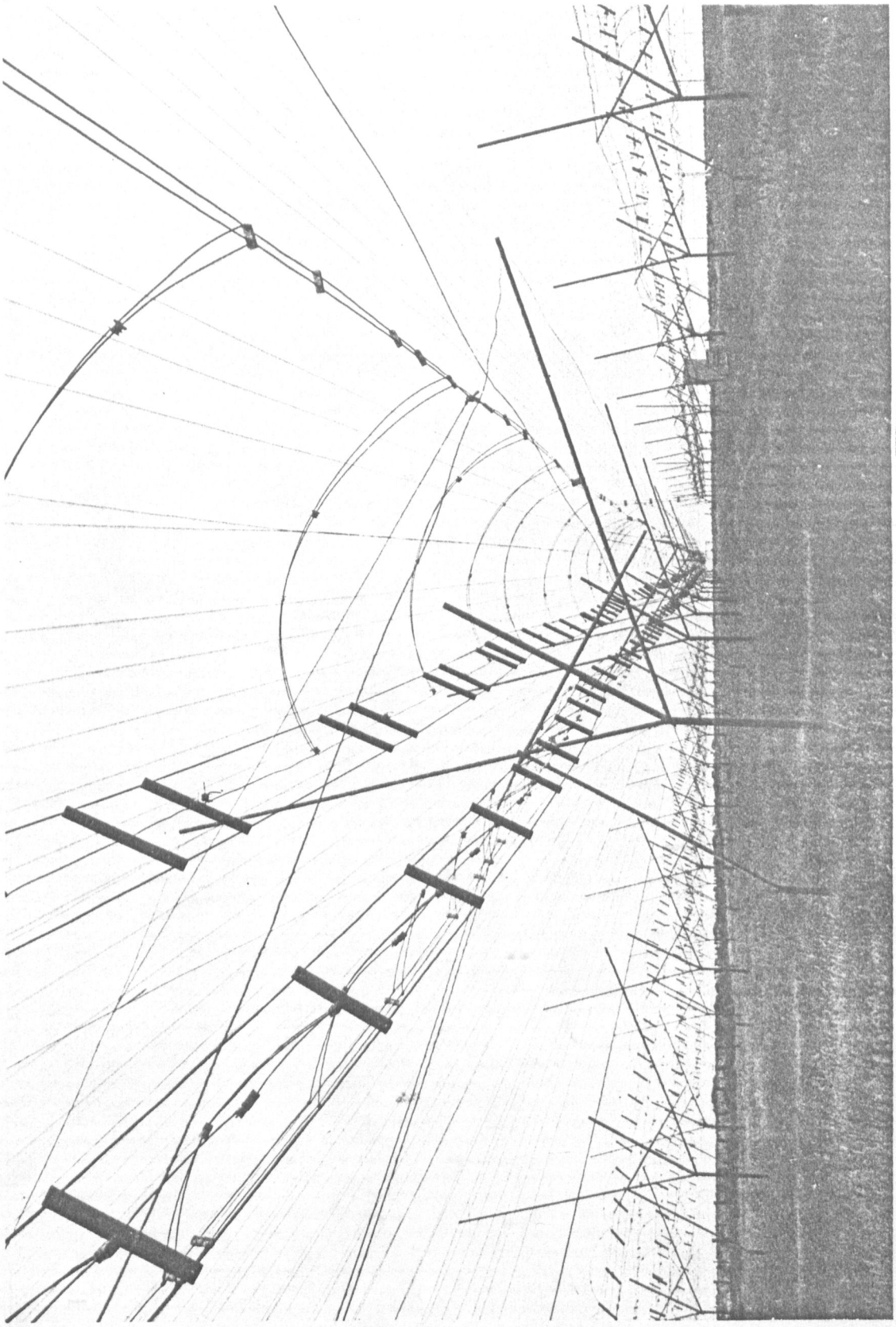

FIGURE 3.3 Aerial arrays at Buckland Park

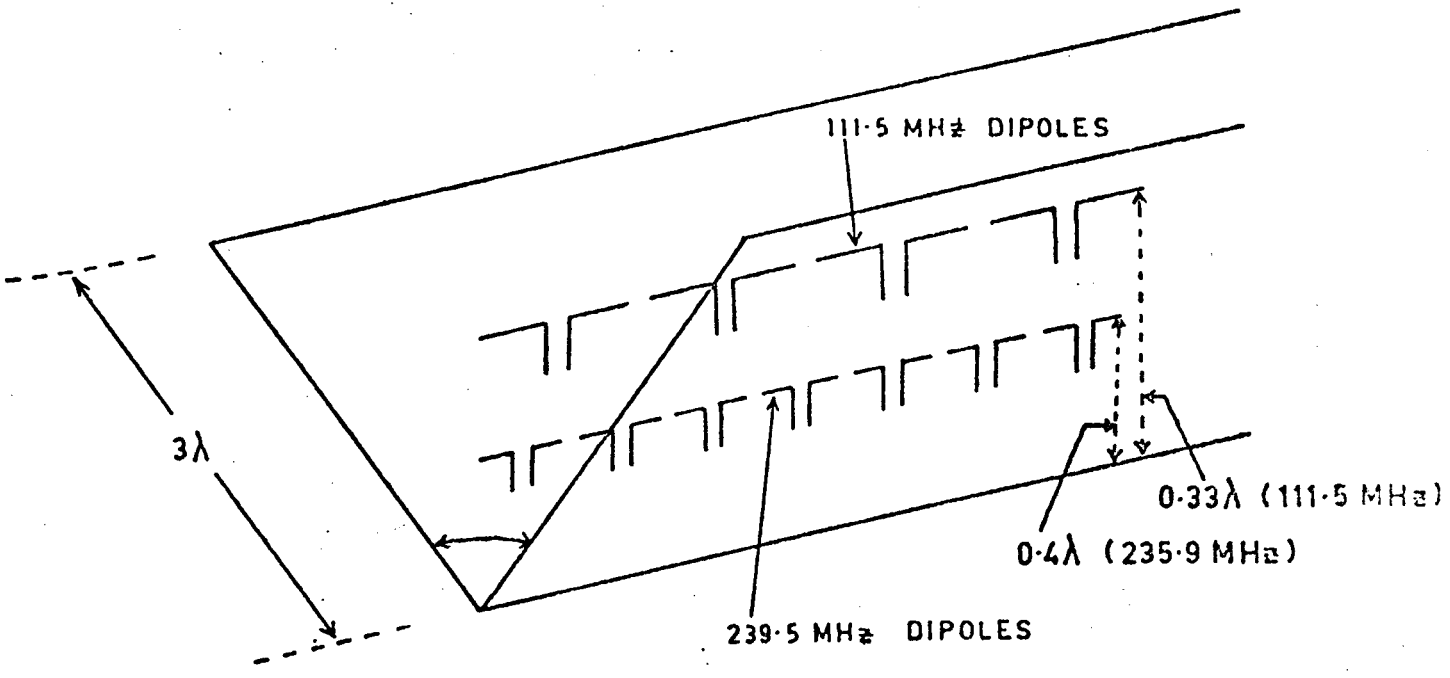

FIGURE 3.4 Details of construction of the corner-reflector aerials

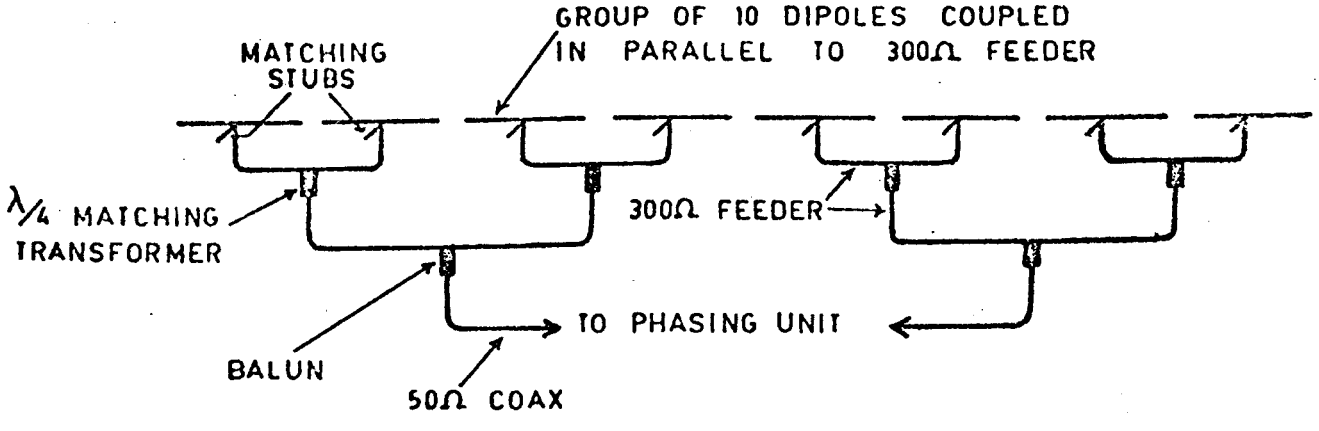

FIGURE 3.5 Phasing of dipoles within each corner-reflector

the signal (Ryle, 1952). The beamwidth (to half-power) in declination of each corner reflector was $\sim 40^0$. Since most of the strong scintillating sources (Table 3.1) occur at declinations in the range $\pm 20^0$ the corner reflectors were constructed such that the centre of the beam pointed towards 0^0 declination. The 40^0 beamwidth of a single corner reflector then allowed observations of sources within the range $\pm 20^0$. When four such reflectors are combined as at Buckland Park the combined response is a series of beams of full width at half power of $\sim 5^0$, spaced at every 20^0 in declination (at 111.5MHz). By combining the aerials in different phase relationships it was possible to move the beams in declination over the 40^0 envelope of a single corner reflector as depicted in Figure 3.6c. A phasing unit based on the use of the 'hybrid ring' (Smith, 1961) was constructed to enable four beam positions in declination to be available for simultaneous recording. A schematic diagram of the phasing unit is shown in Figure 3.6a and the connection of the aerials to this unit in Figure 3.6b. Figure 3.6c shows the four simultaneous responses obtained from the output of the phasing unit. The beams labelled '1' in this figure result from connecting the four aerials in phase, those numbered '2', '3' and '4' are produced by progressive introduction of path differences of $\lambda/4$, $\lambda/2$ and $3\lambda/4$ respectively into the feed-lines of adjacent aerials. All the beams illustrated are contained in the declination response of the individual corner reflectors. A similar unit was constructed at the two outstations using only half of the circuit depicted in Figure 3.6a.

To enable simultaneous observation of a source at all three sites it was necessary to build the arrays at each of the outstations slightly offset from the E-W direction. This offset was dependent on the longitude difference between the outstation and base-station.

3.5 RECEIVERS

As mentioned in the previous section a phase-switched receiving

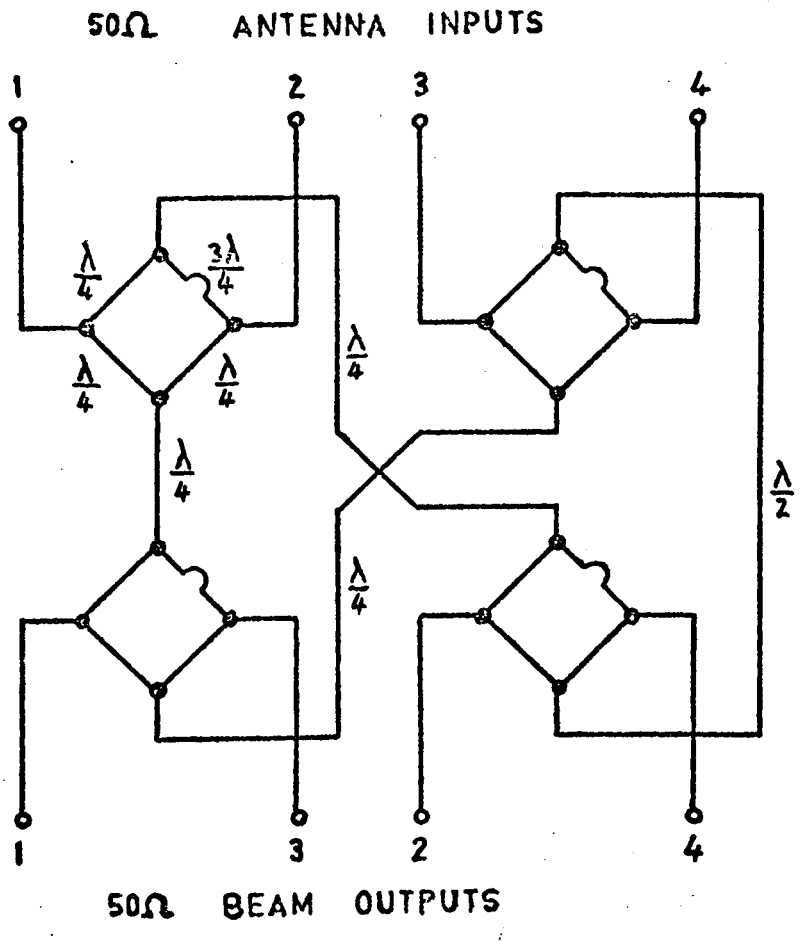

(a) Schematic diagram of the phasing unit

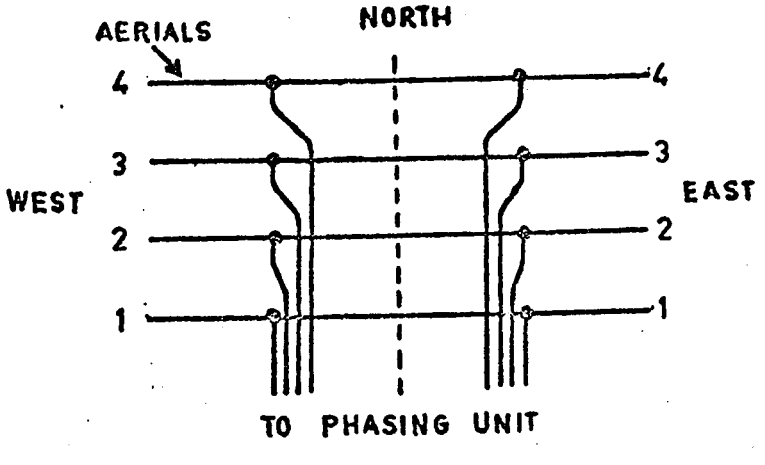

(b) Connection of aerials

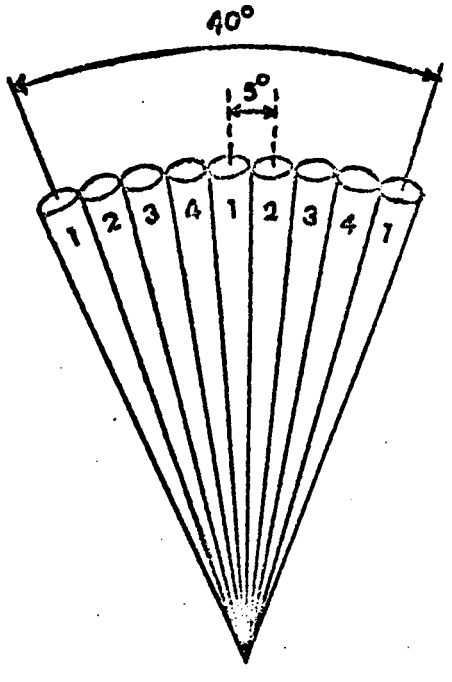

(c) Beam responses produced by the phasing unit

FIGURE 3.6 Phasing of the Buckland Park aerial array

system was chosen in order to reject the galactic contribution to the final receiver output. The principle of the phase-switched receiver is well known and is illustrated in Figure 3.7. The signals from the Eastern and Western halves of the antenna arrays are combined at the input to the receiver by a hybrid to give independent in-phase and out-of-phase signals. These combined signals are then alternately connected to the converter using diode switches operating at 385Hz. A signal received from a radio source of small angular diameter gives rise to a square-wave component at the output of the detector. By reversing the phase of this square wave in the demodulator operating synchronously with the phase switch, a DC output is obtained which is proportional to the flux of the radio source. Galactic noise is uncorrelated at the two antenna halves and does not contribute to the output. The operation of the individual sections of the receiver will be described only briefly here.

To achieve the required low-noise characteristics mentioned earlier in this chapter and also to overcome the cable loss to the receivers, pre-amplifiers were installed at the feed points for each half of each corner reflector. The pre-amplifiers used germanium transistors type GM290 in a simple cascode-pair arrangement and resulted in noise temperatures of ~500 ^{0}K and ~700 ^{0}K at 111.5 and 235.9MHz respectively. This does not meet the design specifications laid down and a low noise FET pre-amplifier is currently being designed to reduce this figure closer to the design value of 300 ^{0}K. The overall gain of the pre-amplifiers was 29dB, so after allowing for approximately 18dB loss in the cables to the receivers the overall gain was in the order of 10dB, sufficient to ensure that they were the determining factor in the overall noise figure of the system.

The phase switch made use of a principle which has been successfully applied at frequencies in the GHz range (Landecker and Wielebinsky, 1970).

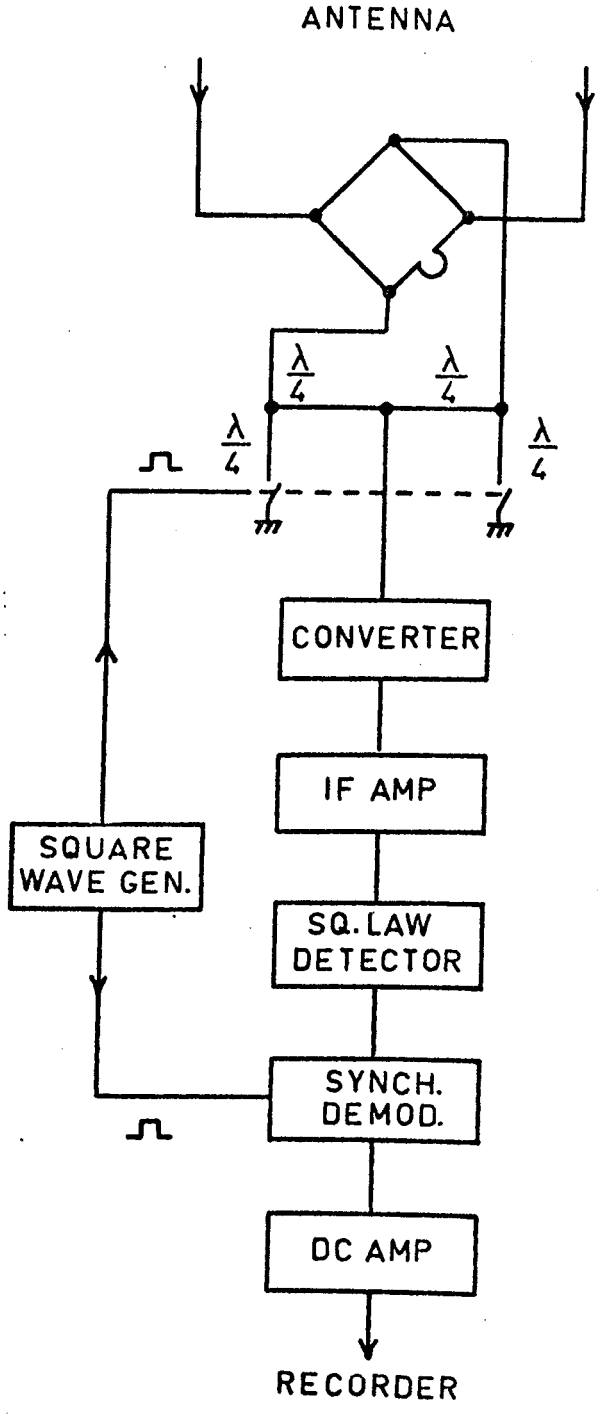

FIGURE 3.7 Block diagram of the phase-switched receiver

Diodes are used to alternately short and open one end of a $\lambda/4$ length of coaxial cable, the other being connected to the signal path as shown in Figure 3.7. The square wave generator used to control the phase switch and synchronous integrator/demodulator was a multivibrator with the 385Hz output frequency carefully set away from harmonics of the 50Hz power supply line.

The converter consisted of a moderately low-noise preamplifier (noise temperature ~1000 ^{0}K at 111.5MHz), crystal local oscillator and mixer all built into a single brass box paying careful attention to shielding and RF bypassing of the DC supply lines. At 111.5MHz the frequency of 81.5MHz from the crystal oscillator was fed directly into the mixer, while at 235.9MHz it was necessary to triple the frequency of a 68.63MHz crystal oscillator to obtain the required 205.9MHz signal. The gain of the converter was 20dB with bandwidths of 5 and 10MHz at the low and high frequencies respectively.

The IF amplifier, with a gain of 65dB, consisted of three stagger-tuned cascode pairs with the damping on each adjusted to provide an overall response centred on 30MHz with a bandwidth of either 1 or 2MHz dependent on the receiver frequency. Automatic gain control was not provided but an overall dynamic range of ~30dB was achieved in the whole receiver and was sufficient for the observations. A switched attenuator, ranging from 3 to 33dB in 3dB steps, was also included in the input to the IF amplifier.

The detector which followed the IF amplifier had a square-law characteristic so that the magnitude of the output square-wave voltage was directly proportional to the output noise power of the pre-detection section of the receiver. The synchronous demodulater followed closely a design of Frater (1965). A feature of the demodulator is the provision for integrating synchronously before demodulation which produces a dynamic range practically independent of the amount of noise present at the input. The final DC

output level was raised to about 2 volts with a single operational amplifier in order to drive a pen recorder. Photographs of the receiver are shown in Figure 3.8 and 3.9.

3.6 REMOTE-STATION DATA LINK

Recording of the signals from the outstations required either transmission back to the base station in real time, or recording on-site and subsequent replay and co-ordination of the records in the laboratory. This latter method presents considerable difficulties both in the manning of the outstation recording equipment and in the synchronization of the recorded signals on replay. It was decided therefore to relay the data back to the base station in real time using FM radio links. The use of telephone lines, either dedicated or dialled, would be preferred but proved too expensive. The final system used commercial FM radio links operating at 169MHz.

The data to be relayed consisted of up to four signal channels, each requiring a bandwidth of 10 to 20Hz. Licensing requirements restricted the frequency response of the data link to the range 300 - 3000Hz. The method chosen to modulate the transmitter was to use a system of FM proportional subcarriers, using the channel spacings and deviations allocated in the IRIG standard. These channels have maximum deviations of ±7.5%; details of the IRIG channels falling within the available bandwidth are given in table 3.2. Channels 4 to 7 are the only channels suitable for this purpose, although it would have been preferable to use alternate channels to reduce cross-talk problems.

The encoding system used at the outstations consisted of a series of voltage-controlled oscillators which were driven by the receiver outputs. A 10Hz low-pass filter was inserted between the receiver and VCO to prevent over-modulation of each channel and to remove 50Hz interference which sometimes was

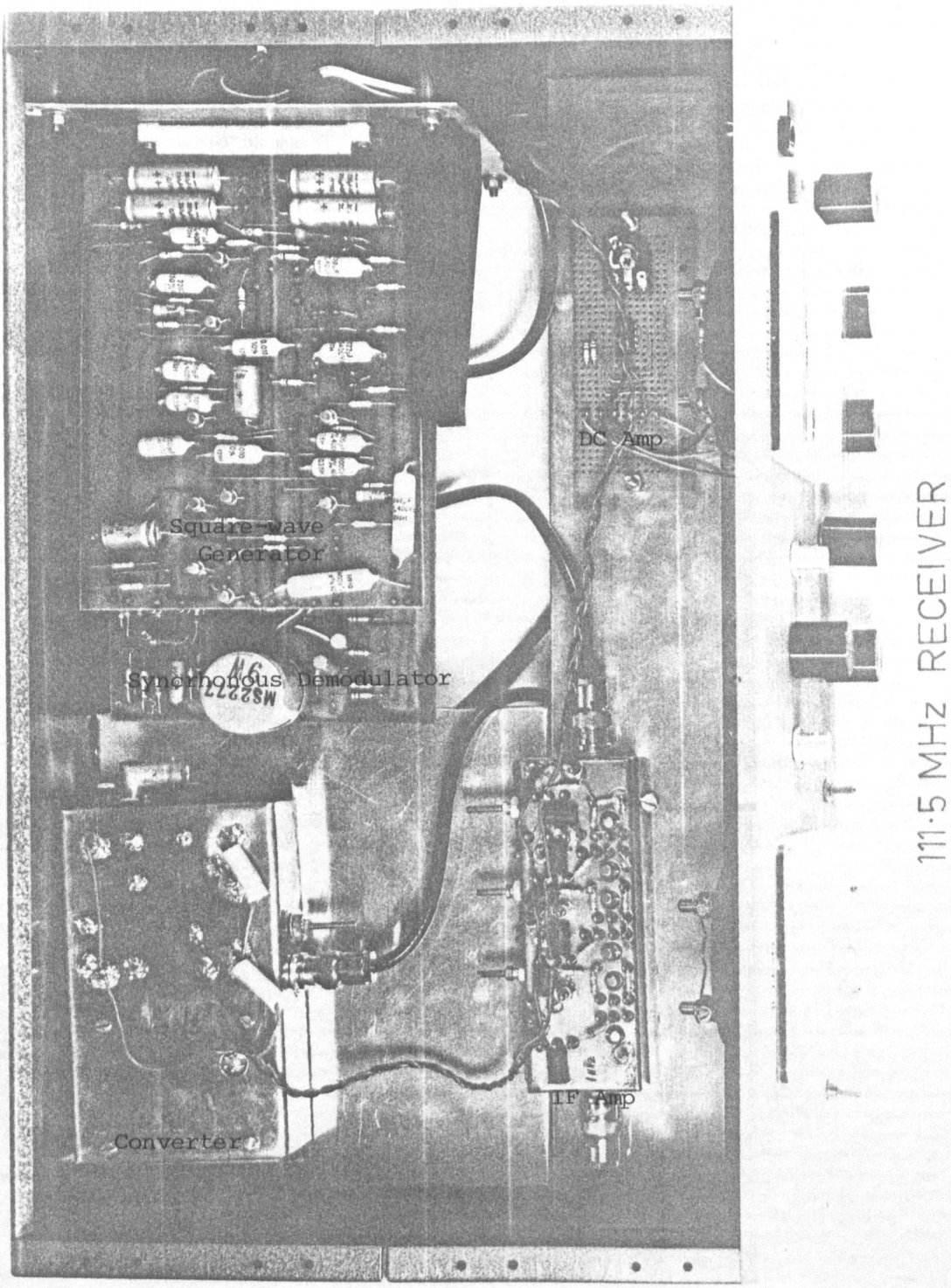

FIGURE 3.8 Construction of the receivers.

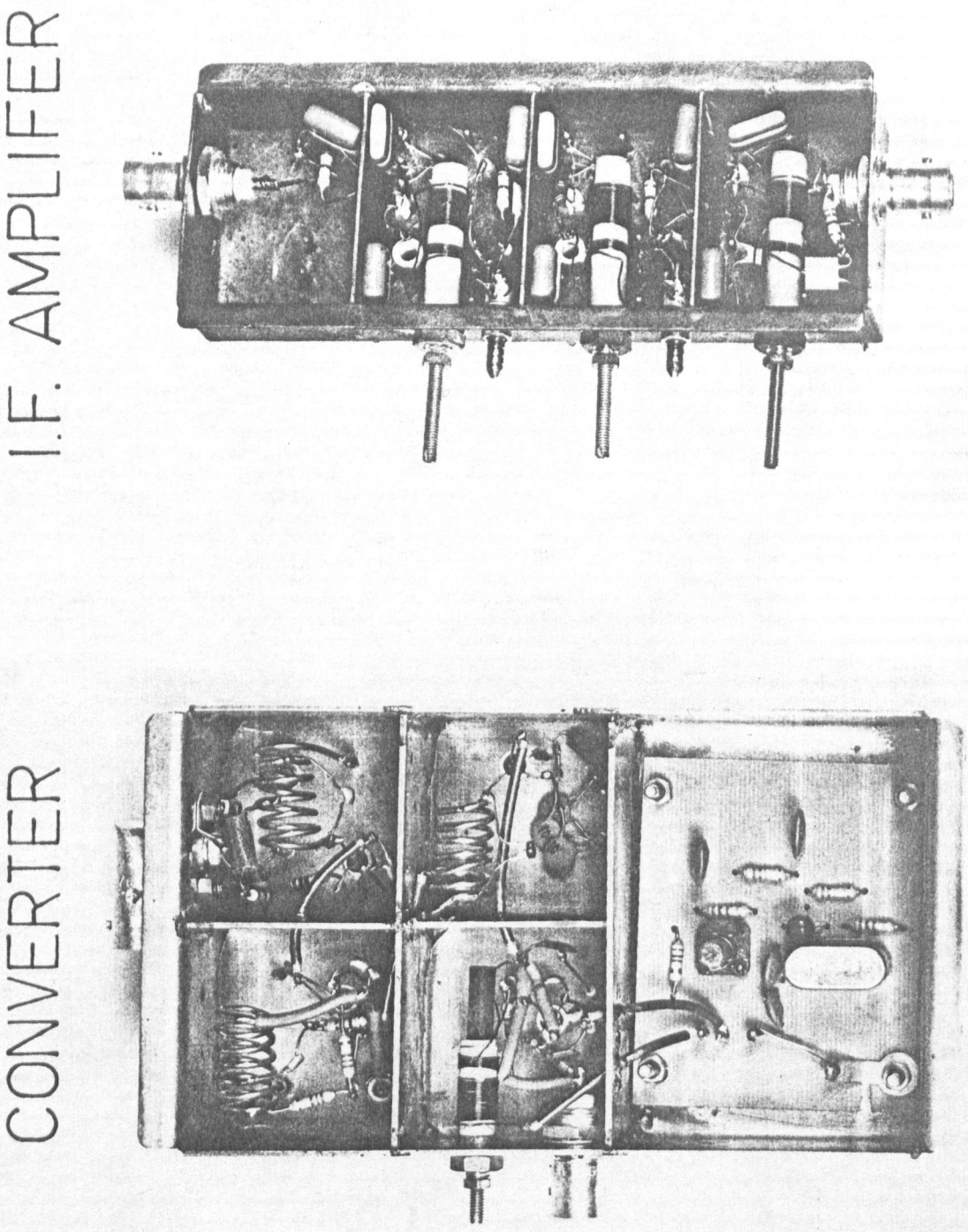

FIGURE 3.9 Construction of the converter and I.F. amplifier

TABLE 3.2 DETAILS OF IRIG FM SUBCARRIER CHANNEL

CHANNEL	CENTRE FREQUENCY (Hz)	DATA CUT-OFF FREQUENCY (Hz)
1	400	6
2	560	8.4
3	730	11
4	960	14
5	1300	20
6	1700	25
7	2300	35

(all channels ± 7% deviation)

a serious problem at Burra where power was supplied along a single-wire earth-return line. The outputs from the VCO's were fed into a mixer which in turn drove the transmitter. In addition a fixed-frequency oscillator was also fed into the mixer.

The decoding system located at the Buckland Park base station consisted of an FM receiver, the output of which was fed into a series of identical FM subcarrier demodulators. In each demodulator the signal was passed through a limiter to remove any amplitude fluctuations and then into a band-pass filter to select the appropriate subcarrier. FM demodulation was achieved by the use of a phase-locked loop system in which a VCO is phase-locked to the input signal. The demodulated output is simply the error signal, arising from a comparison of the phases of the input and VCO signals, used to make the VCO track the input signal frequency. This signal was low-pass filtered to remove traces of the carrier frequency, then amplified to drive the recording equipment.

One serious problem encountered was deep amplitude fading of the radio signal, especially on the Burra - Buckland Park link. When the signal level from the receiver fell below the detection threshold of the phase-locked loop the VCO frequency drifted back towards its free running frequency. In this event the demodulated output was meaningless and had to be identified on the digital record. This was achieved by installing a fixed frequency oscillator at the outstation. The base station equipment had a fifth channel added in which the FM demodulating phase-locked loop was replaced by a phase-locked loop tone decoder. This device operates in a similar way to the demodulator, but gives only a 0v or 5v output, dependent

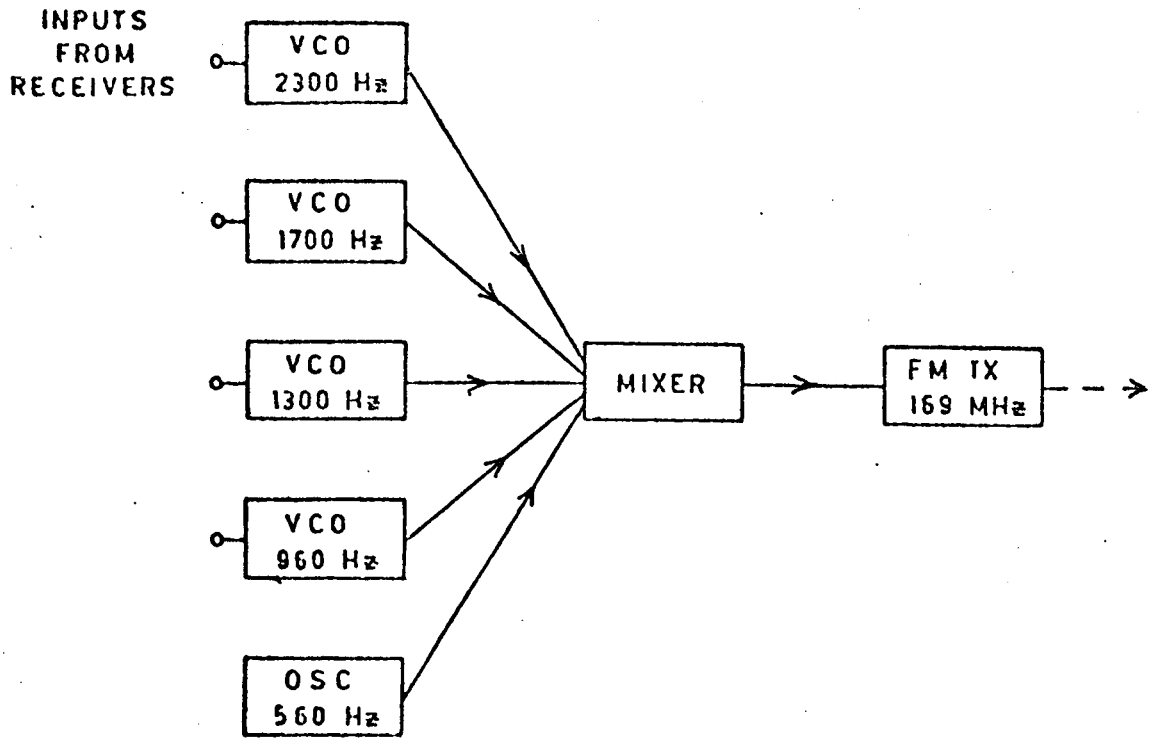

(a) Encoding units at Burra and Kadina

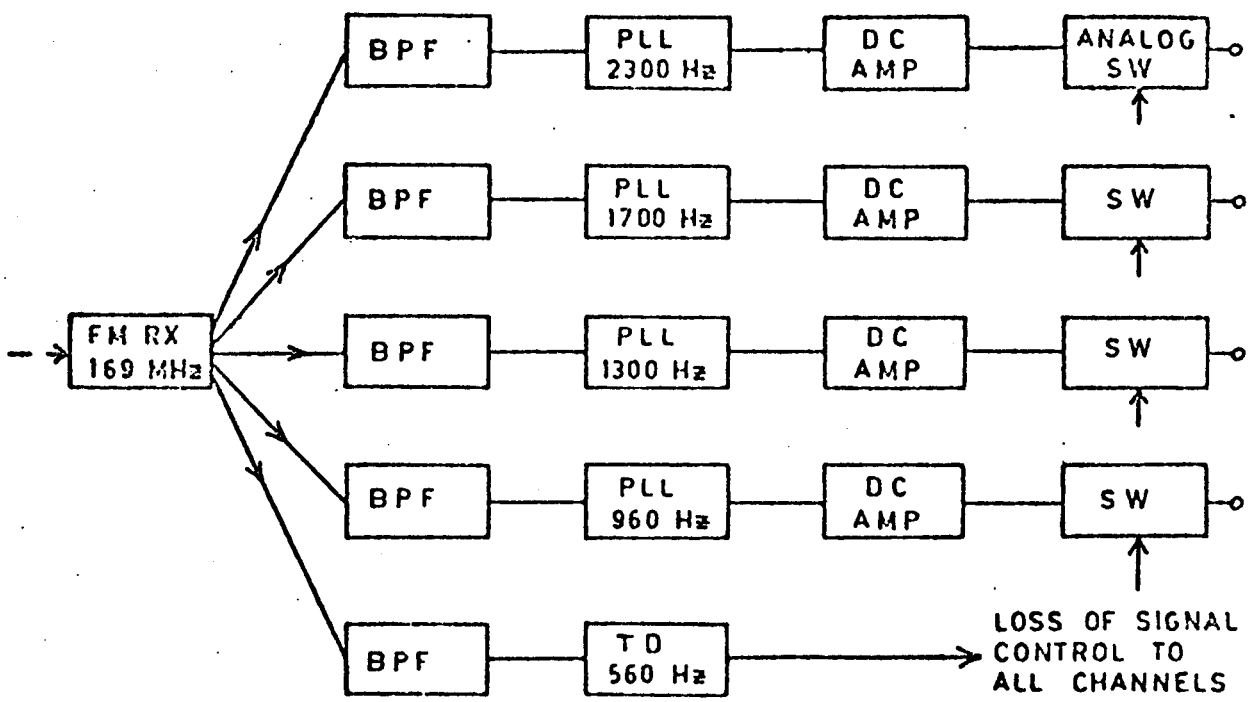

(b) Decoding unit at Buckland Park

FIGURE 3.10 Block diagram of telemetry system

on whether or not a signal within the bandwidth of the decoder is present. The detection threshold of this decoder was set at the same level as the demodulators. The output signal from the tone decoder was used to drive an analogue switch which switched the output to a -10v signal when there was a loss of subcarrier. This -10v signal was readily recognizable as a series of zeroes in the digital record which were removed during computer analysis of the data.

3.7 DATA-RECORDING EQUIPMENT

The basic requirement for the data recording system was to record simultaneously six different signals (three stations at two frequencies) for any given source. The signals were recorded both on an 8 channel analogue chart recorder and on an incremental digital tape recorder. The chart records provided a real-time indication of the signals as well as a reference during computer processing of the digital records.

A block diagram of the recording system is shown in Figure 3.11. The system was operated semi-automatically under the control of a decoding unit which started both recorders at any of five selectable sidereal times, and stopped them ten minutes later. A timing control unit generated the sequence of signals necessary to control the individual units of the digitizing system, and another unit controlled the spead of the chart recorder.

The sampling speed was limited to sixteen samples per second per channel by the writing capability of the digital recorder. Given a sampling rate ΔT, the highest frequency which can be measured is the Nyquist frequency

$$f_N = \frac{1}{2\Delta T} \qquad \ldots.(3.4)$$

Therefore this recording system was limited to sampling frequencies less than 8Hz. Since the majority of the power in interplanetary scintillations occurs

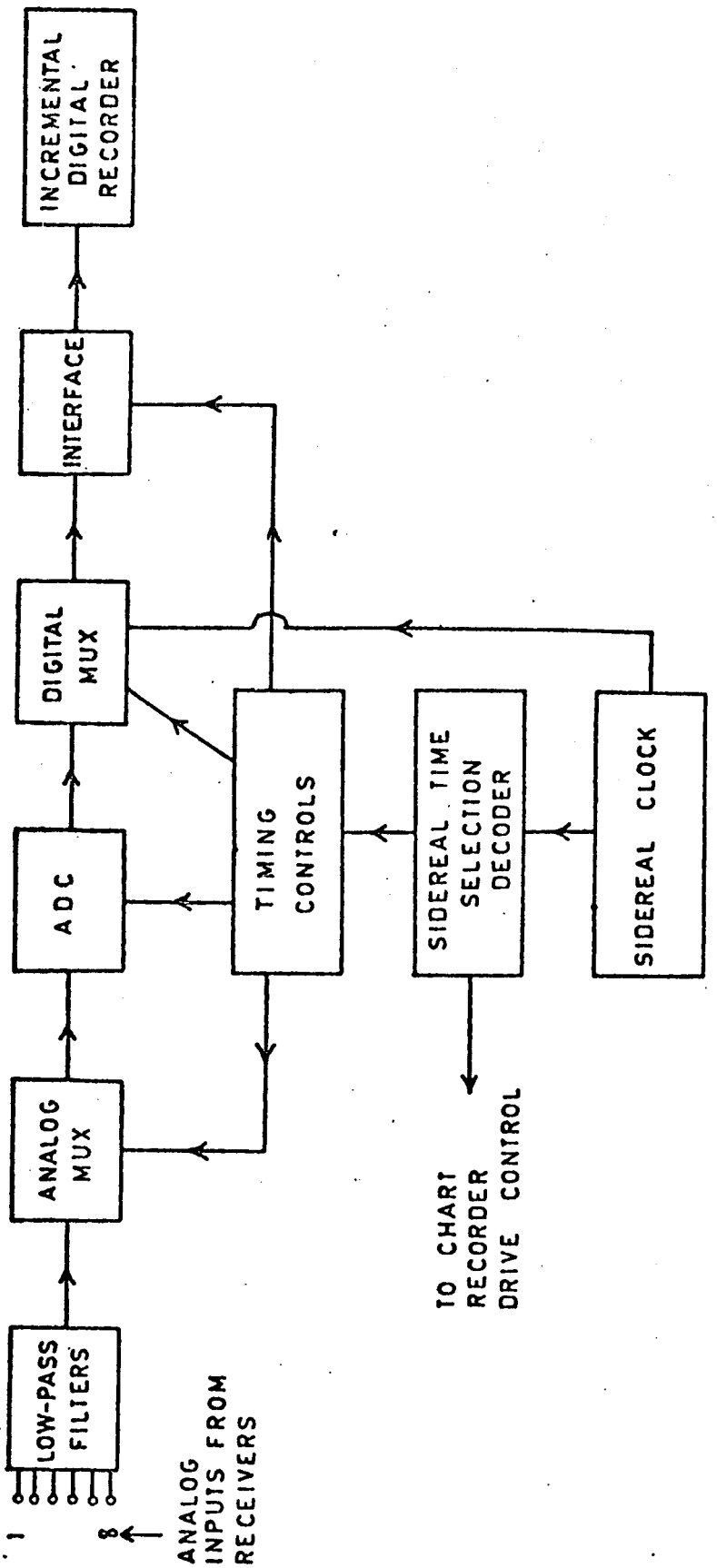

FIGURE 3.11 Block diagram of digital recording system

at frequencies less than about 2Hz this frequency response is sufficient. If the input signal includes a frequency component f higher than the Nyquist frequency then it will appear as an aliased frequency within the frequency response of the system; the aliased frequency f' being

$$f' = (2nf_N \pm f) \qquad \ldots.(3.5)$$

To avoid this aliasing it is necessary to filter the input signals to ensure that no frequency components greater than 8Hz are present.

Each of the eight input channels was sampled sequentially by an analogue multiplexer, the output of which was digitized by an eight-bit analogue-to-digital converter. A digital multiplexer ordered the output of the ADC and the channel number in a form suitable for recording. The data was recorded in blocks of one minute duration and the digital multiplexer was also responsible for writing the block number and sidereal time at the beginning of each block. All data signals and recorder control signals were sent to the recorder through an interface unit which converted the TTL logic levels to levels acceptable to the recorder.

3.8 SUMMARY

The 111.5 MHz aerial array at Buckland Park was completed during April 1972, with adjustments to the phasing of the aerials being carried out over the subsequent six months. The beam response of the 111.5 MHz system is close to that predicted theoretically but the signal to noise ratio is lower than predicted. This is largely due to the fact that the noise temperatures of the aerial preamplifiers is higher than was assumed in the design calculations. New preamplifiers incorporating low noise field-effect transistors are currently being constructed to improve the signal to noise ratio. The 111.5MHz remote stations at Burra and Kadina were completed late in 1974 and preliminary spaced receiver observations recorded with this system are discussed in Chapter 4.

The 235.9 MHz array has been completed at Buckland Park but the aerial response deviates markedly from the theoretical predictions. The sensitivity at present is insufficient to obtain a useful signal to noise ratio for scintillating sources at this frequency. It is believed that the problem arises in cross-coupling between the two sets of dipoles within each corner reflector. A fifth aerial, incorporating only the 235.9MHz dipoles, is under construction at Buckland Park in order to compare the response of this aerial with that of a corner reflector containing both sets of dipoles.

Figure 3.13 shows the recording equipment at the Buckland Park station. The rack on the left-hand side contains (1) the data link receivers, (2) the FM subcarrier demodulators, (3) pen-recorder amplifiers, and (4) receivers. The right-hand rack contains (5) the digital recording equipment, and (6) the 'solar monitor' receivers.

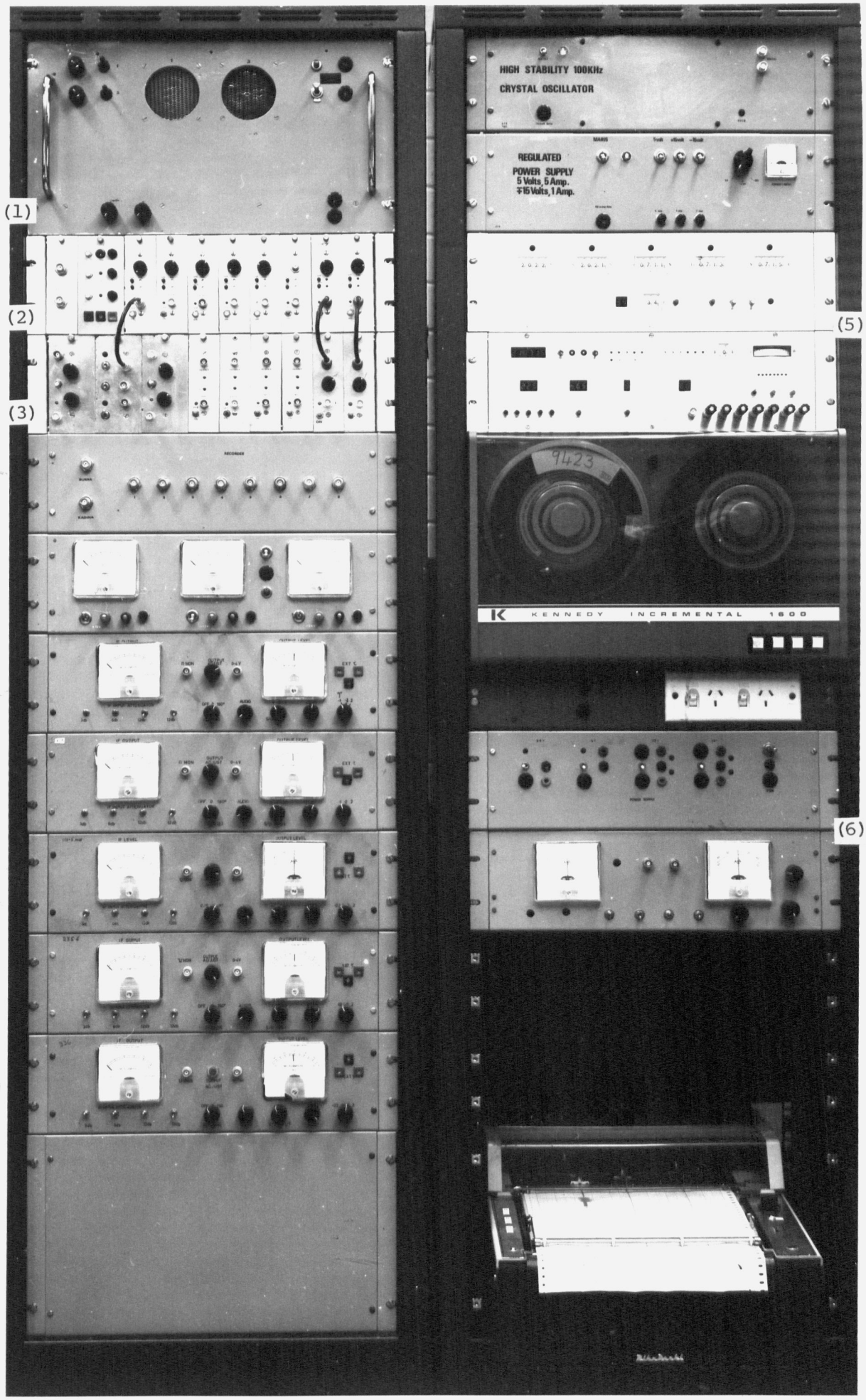

FIGURE 3.13 The receiving equipment at Buckland Park

CHAPTER 4

METHODS OF OBSERVATION AND ANALYSIS

4.1 CULGOORA OBSERVATIONS

Much of the data analyzed in this thesis was recorded using the Culgoora radioheliograph, which prior to May 1972 operated at 80MHz and since that time has operated at either 80 or 160MHz. This instrument has been fully described by Wild et al (1967). It has a physical collecting area of 12,000 m^2 , is fully steerable and produces 48 independent beams spaced in declination. At 80MHz these beams are each of 3.5 width (to half-power) and separated by 2.1 at the zenith, the 160MHz beam parameters being a factor of two smaller. The beams can be steered in hour angle by up to ±2½ hours from the zenith.

This multiple beam facility is extremely useful for scintillation studies since it enables simultaneous recording of both on-source and off-source signals. This has the important advantage of allowing interference effects, both solar and terrestrial, to be recognized and removed during the analysis of the data. In these observations the beams were arranged such that the two central beams straddled the source. Six of the central beams (beams 22 to 27) were recorded on an analog chart recorder with a time constant of 0.1 sec and recording speed of 160 cm min^{-1}. During the June 1971 recording session, only one on-source beam was digitized. The recording system was in fact capable of recording four data channels smultaneously and since June 1972, four channels have been recorded, with beams 24 and 25 providing on-source records and beams 22 and 27 off-source records. Prior to recording, the detector outputs were amplified and passed through a 16Hz low-pass filter to prevent aliasing of signals with frequencies

greater than the Nyquist frequency. The digital records were made with a time constant of 0.02 sec at a sampling rate of 32 samples sec^{-1} and were recorded in blocks of 45 seconds length. The gains of the individual channels were calibrated by injecting the signal from a diode noise source through a multi-channel splitter into the I.F. amplifiers. Calibration of the pre - I.F. stages formed part of the regular heliograph maintenance programme.

The recording procedure is illustrated in Figure 4.1. The beams were fixed at a point several minutes of right ascension earlier than the desired source and the source allowed to drift through the beam. Once the source had drifted out of the beam the beam was moved ahead 2 minutes in right ascension and the source again allowed to drift through the beam. This procedure was repeated several times to provide transit records which were used to estimate the mean source intensity and provide a check on the presence of ionospheric refraction. Refraction in right ascension appeared as a variation in source transit time and in declination as a change in the source intensity on adjacent (declination) beams. After several such transit records were obtained the beams were set to track the source once it was fully in the beam. The source was followed for periods varying between 10 and 40 minutes after which tracking was stopped and the source allowed to drift out of the beam. Once clear of the source the beam was set to track a region of quiet sky for a period of 6 minutes to provide an off-source record on channels 24 and 25. In those cases where refraction was significant and variable the procedure was varied and a sequence of on-source, off-source records was obtained (~ 10 mins ON, ~3 mins OFF) to facilitate estimation of the varying mean source intensity.

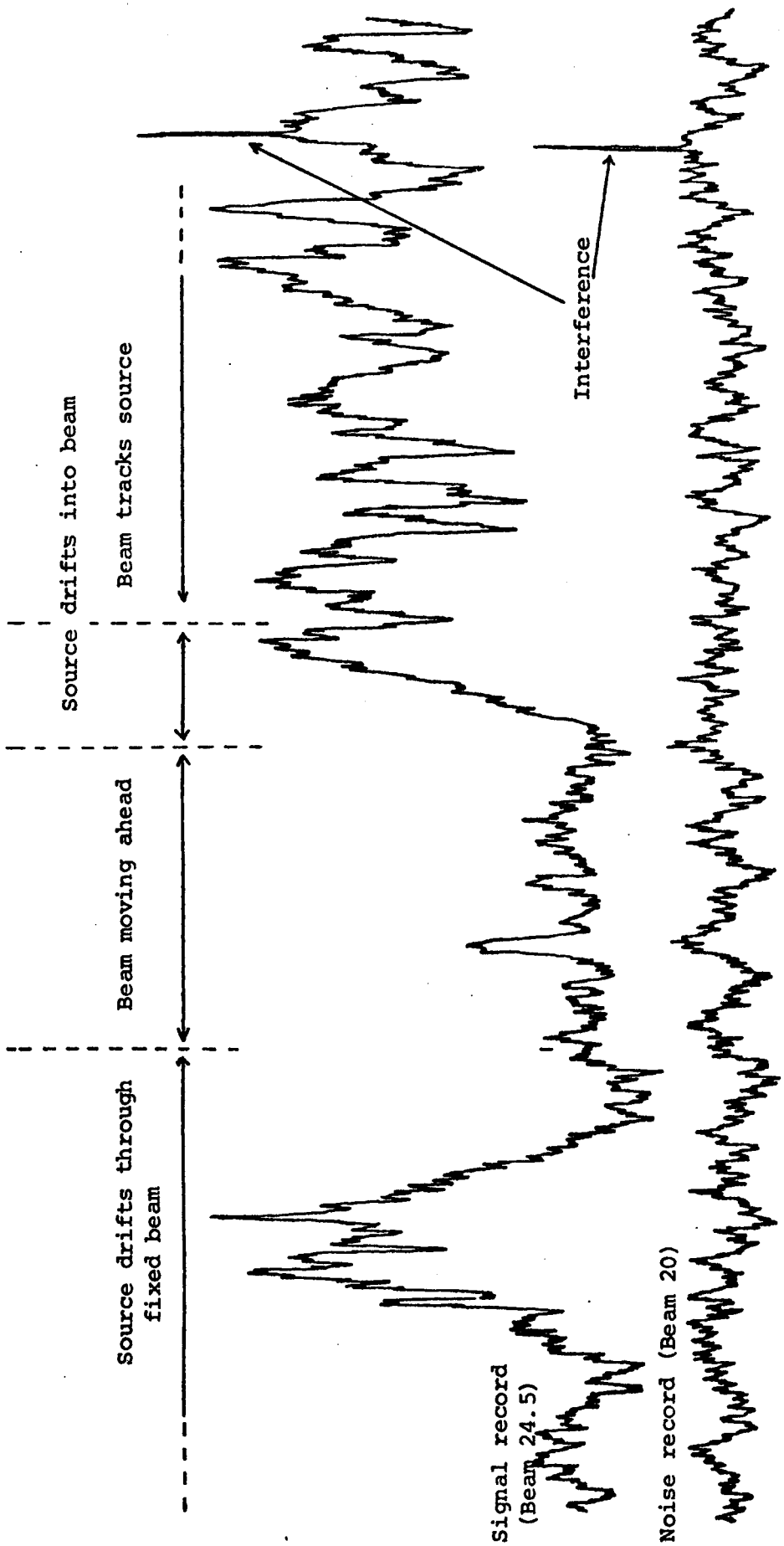

FIGURE 4.1 Details of the recording procedure at Culgoora.

4.2 CULGOORA DATA REDUCTION

The first stage of the analysis procedure involved de-coding of the original magnetic tape recording. Each 45 second block of data contained 2880 values with the 4 channels sampled sequentially. These were de-coded and separated into the 4 separate signals and any undefined data points resulting from digitizer errors were replaced by the average of the two adjacent data points in that channel. This stage of the analysis also involved the removal of interference from the records. During the observing session a log of all recordings was kept and any data blocks suffering from excessive interference were eliminated from the analysis. The analog records were used as a guide during the process of interference removal. In the 1971 data where only one beam was recorded, the position of interference was noted on the analog record and the appropriate section of the digital record was removed. At times the data was contaminated by lightning interference which was detected by comparing the slope between adjacent data points with five times the average slope from the previous 2 seconds of data and the contaminated data points were replaced by an interpolation between existing data on either side of the lightning 'spike'. Since 1972 when simultaneous on-source and off-source signals have been recorded interference has been detected by locating any data points in both off-source records larger than a given threshold above the mean level. The corresponding data points in the on-source records were replaced by an interpolation of the data on either side of the affected points. The computer program printed out any such modifications so as to provide an indication of the quality of each block of data.

On several occasions the data was contaminated by 50Hz hum which

entered the system in the digitizer and was therefore not removed by the 16Hz low-pass filter. The effect of this interference was to introduce a large peak in the power spectrum at the alias frequency of 13.5Hz. Since the noise power spectrum usually exceeded the scintillation spectrum beyond about 2Hz, the 16Hz Nyquist frequency was in fact higher than necessary. Treating the data with an 8-point running mean filter of width 7/32 sec has the effect, in the frequency domain, of multiplying the power spectrum by the function

$$H(f) = \frac{\sin^2 (\pi f\ 7/32)}{(\pi f\ 7/32)^2} \qquad \text{--- (4.1)}$$

This function has zeros at

$$f = 4\ 4/7,\ 9\ 1/7,\ 13\ 5/7, \ldots . \text{Hz}$$

and thus effectively removes the aliased peak at 13.5Hz. The effect of this window on the spectral region below 4Hz was allowed for later in the analysis, but no correction could be applied beyond 4 4/7Hz because of the zeros in H(f). The Nyquist frequency was therefore set at 4Hz by retaining only one in four of the averaged data points. Although not all records were contaminated with 50Hz hum this procedure was applied to all the data since it had negligible effect on the scintillation records.

The subsequent analysis of the data involved computation of the power spectrum, auto-correlation function, probability density function and several related parameters. The practical details of the spectral analysis procedure are discussed in Appendix 2. The Fourier coefficients of the data were obtained by an application of Singleton's (1969) FFT algorithm. Since the data values are real quantities and the FFT algorithm was designed to accept complex values it is possible to split the data into two halves placing them into the real and imaginary arrays respectively. Application of the FFT

then provides a set of Fourier coefficients for each half of the original array. The power spectrum estimates were obtained by computing the square of the modulus of the two sets of coefficients and adding them frequency by frequency. As discussed in Appendix 2 splitting the data in this way reduces the variance of the spectral estimates and a further reduction was achieved by averaging over four adjacent estimates, providing a final power spectrum with a resolution of 0.084Hz. The auto-correlation function was calculated by applying the FFT to the power spectrum. Both the auto-correlation function and the power spectrum for each data block were written on to magnetic tape for subsequent analysis.

The detector output level often tended to drift with periods ~20 sec due either to ionospheric scintillation or the effects of terrestrial interference across the array. For this reason frequencies below 0.1Hz were not included in analysis of the data. The Fourier coefficients for frequencies less than 0.1Hz were set equal to zero and an inverse FFT applied. This provided a (high-pass) filtered record of the intensity fluctuations which was used to determine the probability density function (p.d.f.) The p.d.f. was determined by dividing the range of intensity values in the record into 100 sub-ranges and counting the number of intensity values which fell in each sub-range. The p.d.f's for each data block were also written on to magnetic tape for subsequent analysis.

Interpretation of many of the calculated functions was dependent on an estimation of the mean source intensity. This was estimated from the digital records as the difference between average intensity values of the on- and off-source signals. This method proved reliable when there were four signals recorded simultaneously but was less accurate when only one signal was recorded. In all cases the numerical estimate was compared with values determined manually from the analog records in order to check the accuracy of

the numerical estimates and to correct for sudden D.C. offsets in the level of detector outputs which occasionally occurred on a recording.

Several parameters were determined from the functions calculated for each data block. The central moments (Abramowitz and Stegun, p.928)

$$M_k = \Sigma_j \; (I_j - \bar{I})^k \; p_j(I) \qquad (k = 2,3) \qquad \text{---(4.2)}$$

were calculated from the p.d.f. for all records and the signal to noise ratio

$$S/N = \left[M_2 \; (ON) \; / \; M_2 \; (OFF) \right]^{\frac{1}{2}}, \qquad \text{---(4.4)}$$

the scintillation index

$$m = \frac{M_2^{\frac{1}{2}}}{I_0} \qquad \text{---(4.5)}$$

where I_0 is the mean source intensity, and the skewness coefficient

$$\gamma_1 = \frac{M_3}{M_2^{3/2}} \qquad \text{---(4.6)}$$

were also calculated for each on-source record. The first and second moments (f_1, f_2) of the power spectrum were calculated using the relation

$$f_n^n = \frac{\int_0^{f_c} f^n \, P(f) \; df}{\int_0^{f_c} P(f) \; df} \qquad \text{---(4.7)}$$

where $P(f) = P_{on}(f) - P_{off}(f)$ and f_c is the cut-off frequency at which $P_{off}(f_c) \gtrsim P_{on}(f_c)$. The scintillation index can also be calculated from the relation

$$m^2 = \int_0^{f_c} P(f) \; df. \qquad \text{---(4.8)}$$

In most cases estimates of the scintillation index from relations (4.5) and (4.8) agreed within 5%.

The p.d.f. and power spectrum were averaged over all on-source records for a given observation and corrected for the effects of noise using the average of the off-source records for that observation. The parameters listed above were calculated from the final average functions and compared with the average values derived from the individual blocks of data in order to provide a check on the reliability of the individual stages of the analysis. The final p.d.f. for each observation was plotted by the computer together with the Rice-squared and lognormal functions (see Chapter 6) for the same value of the scintillation index. The final power spectrum was fitted to several models using a least-squares technique and the results plotted. For selected observations the Bessel transform (Lovelace et al, 1970)

$$B_{It}(f) = \frac{1}{2\pi} \int_0^{\tau_m} \tau \; J_o(2\pi f\tau) \; \rho_{I\tau}(\tau) \; d\tau \qquad ---(4.8)$$

or the equivalent sec θ transform (Ward et al, 1972)

$$S(f) = -\frac{d}{df} \int_0^{\pi/2} P_{It} \; (f \sec\theta) \; d\theta \qquad ---(4.10)$$

were also calculated. The results of these analyses are discussed in subsequent chapters.

4.3 BUCKLAND PARK OBSERVATIONS AND ANALYSIS

Observations of interplanetary scintillation at 111.5MHz have been recorded with the base station of the Adelaide spaced-receiver system since April 1972. The 111.5MHz aerial array produces a beam that is 3 minutes wide at the half-power points in R.A. Figure 4.2 shows a transit record for source 0624-05 recorded on 5 May 1972. This example was recorded during the testing phase of the Buckland Park array; the actual experimental records were taken with higher chart speeds.

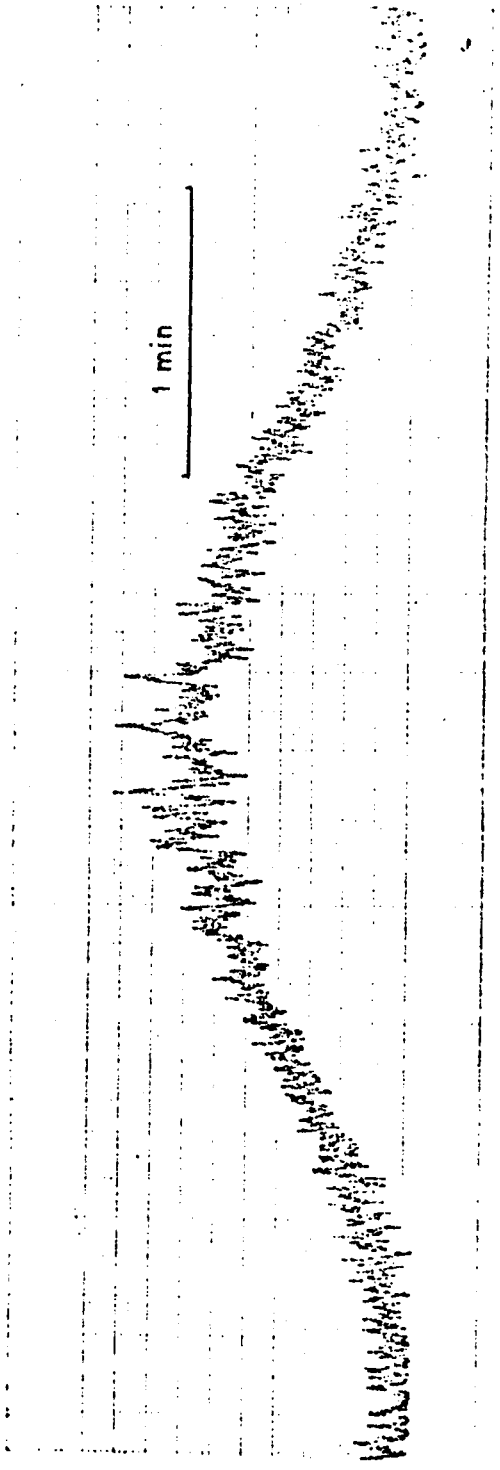

FIGURE 4.2 111.5 MHz transit record for source 0624-05, 5 May 1972

During 1972 and 1973, the only recording system available was an 8 channel analog chart recorder, and all data was reduced manually. An 8-channel digital recorder was brought into operation during 1974 allowing computer reduction of the 1974 data. Recordings were commenced five minutes prior to the source transit and stopped five minutes after transit, providing noise records both before and after the scintillation record and a baseline from which to estimate the mean source intensity. Each of five sources (0532+21, 0624-05, 1226+02, 1309-22, 1416+06) were observed over a five month period centred on the closest approach of the source to the sun.

Manual digitization of the analog records was impractical so analysis was restricted to calculation of the probability density function and related parameters. Orhaug (1965) has noted that for a random signal with a Gaussian p.d.f. the probability of a particular intensity is proportional to the number of times the scintillation signal crosses the intensity level in question. The p.d.f. may therefore be determined by counting the number of times the record crosses each intensity level. This technique was used on several observations for which digital records were available and was found to be accurate for typical scintillation records although they do not possess a Gaussian p.d.f. Noise distributions were not derived for each observation but average noise p.d.f's were determined at regular intervals and used to correct the scintillation p.d.f's for the effects of noise. The scintillation index m and skewness coefficient γ_1 were calculated for each observation using relations (4.5) and (4.6).

Analysis of the 1974 records was carried out using a computer program similar to that described for the Culgoora data reduction. Interference was noted on the analog records and removed from the digital record. This procedure was uncertain when the source position was close to the sun but was aided by the use of a broad beam 'solar monitor' aerial and 111.5MHz total

power receiver. The power spectrum, auto-correlation function and probability density function were calculated for each observation and corrected for the effects of noise using the average of the pre- and post-transit noise records for that observation. The reliability of these functions was less than that for the Culgoora observations due to a lower signal to noise ratio and shorter recording time.

4.4 SPACED-RECEIVER ANALYSIS AND RESULTS

The 111.5MHz spaced-receiver system was completed late in 1974 and some preliminary observations have been recorded with this system. The basic recording procedure was similar to that described in the previous section. A method for the full correlation analysis of spaced receiver observations has been developed by Briggs, Phillips and Shinn (1950), and extended by Phillips and Spencer (1955). This graphical method has been converted into a purely algebraic formulation suitable for direct computer analysis by Fooks (1965). The summary of the analysis procedure given here is based on the graphical methods described in the above papers. A computer program based on Fook's equations was used to process the experimental data.

The diffraction pattern across the ground may be represented by contours of constant amplitude, shown in Figure 4.3a, which have a two-dimensional spatial auto-correlation function $\rho\ (\xi,\eta)$, shown in Figure 4.3b, where it is assumed that the contours of constant correlation are in the form of concentric ellipses. The problem is to find the parameters of such a 'characteristic' ellipse from observations made at three points on the ground separated by distances d_{ij} in directions θ_{ij}, measured clockwise from North.

Temporal auto-correlation functions $\rho_{ii}(\tau)$ and cross-correlation

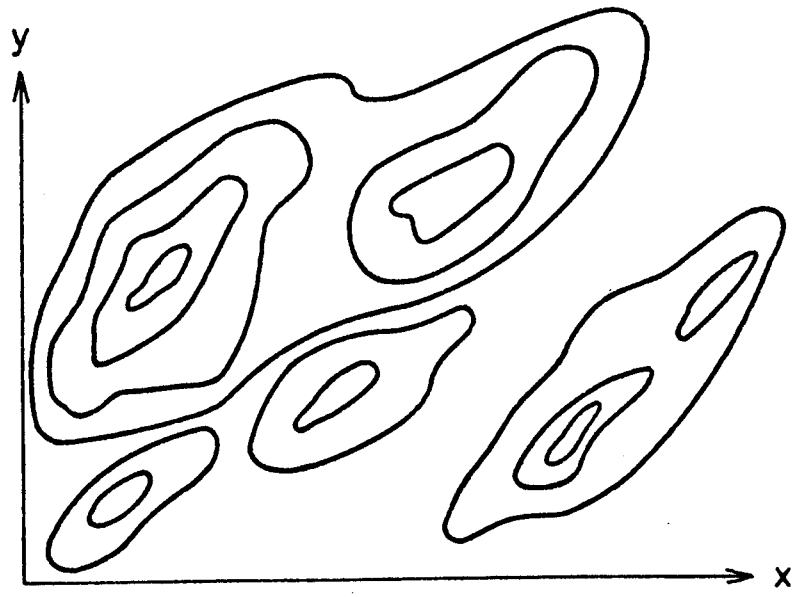

(a) Contours of constant amplitude in the diffraction pattern.

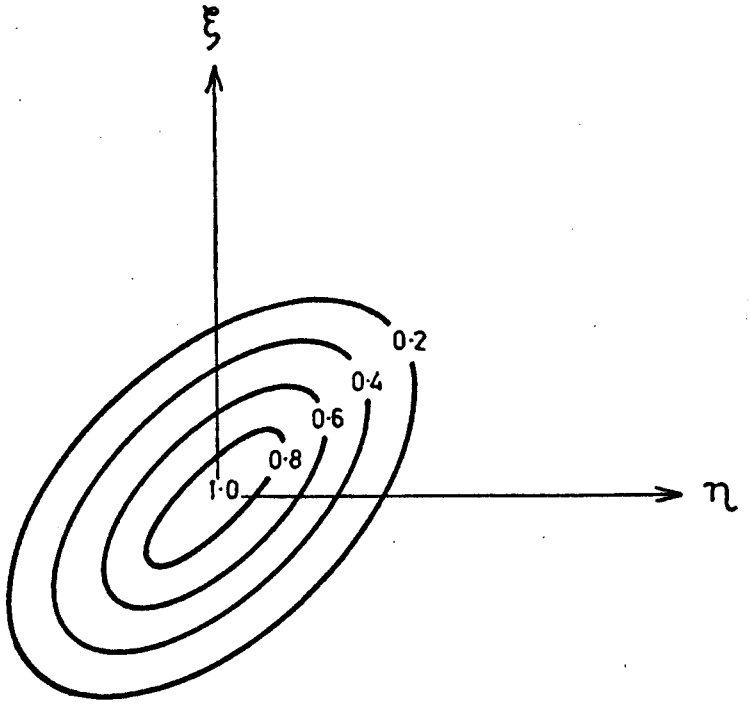

(b) Contours of constant correlation

FIGURE 4.3 Specification of the diffraction pattern for spaced receiver analysis.

functions $\rho_{ij}(\tau)$ are computed from the three records and the autocorrelation functions averaged to provide a mean autocorrelation function $\rho_a(\tau)$. Figure 4.4a shows typical auto- and cross-correlation functions derived from the experimental records and figure 4.4b shows parameters derived from these functions. The values $\rho_{ij}(\tau=0)$ and τ_{ij}, defined such that $\rho_a(\tau_{ij}) = \rho_{ij}(\tau=0)$, are determined from these functions. Three quantities $(V_c')_{ij} = d_{ij}/\tau_{ij}$ are calculated and plotted as vectors in the directions θ_{ij}. A 'characteristic ellipse' is drawn through these points with its centre at the origin, as shown in figure 4.5. The velocity V_c represents the factor by which the τ-scale of the temporal autocorrelation function must be multiplied for it to represent the spatial autocorrelation function along the direction considered.

The dimensions of the 'characteristic ellipse' must be multiplied by $\tau_{0.5}$, defined such that $\rho_a(\tau_{0.5}) = 0.5$, so that any semi-axis represents the scale of the pattern in that particular direction. To obtain the velocity the vectors $V'_{ij} = d_{ij} / \tau'_{ij}$ are plotted, where τ'_{ij} are the time displacements of the maxima of the cross-correlation functions. These three points lie on a straight line and a best fitting line XY is drawn through them. A perpendicular from the origin to this line gives an apparent velocity vector V_a with direction ϕ_o. To obtain the true speed and direction of the pattern movement a tangent is drawn to the V'_c ellipse parallel to the line XY. A line from the origin to the point of contact of this tangent gives the true direction of drift. The lengthof the radius of this ellipse through the point of contact gives a quantity $(V'_c)_V$ which is the value of V'_c in the direction of drift. A further quantity V' is found by extending this line until it meets XY. The true drift speed is then

$$V = \frac{(V'_c)_V^2}{V'}$$

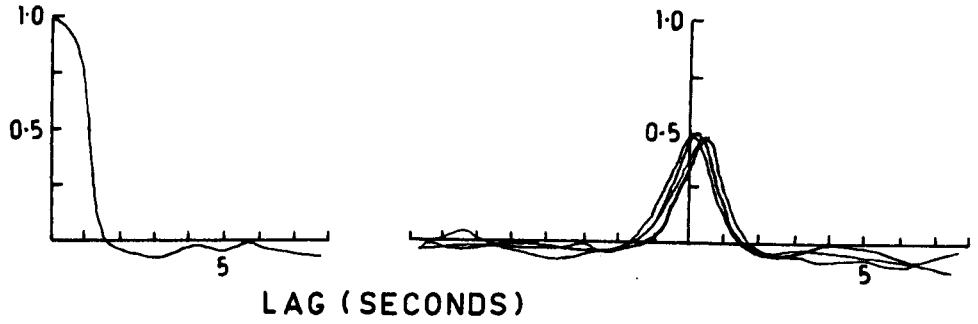

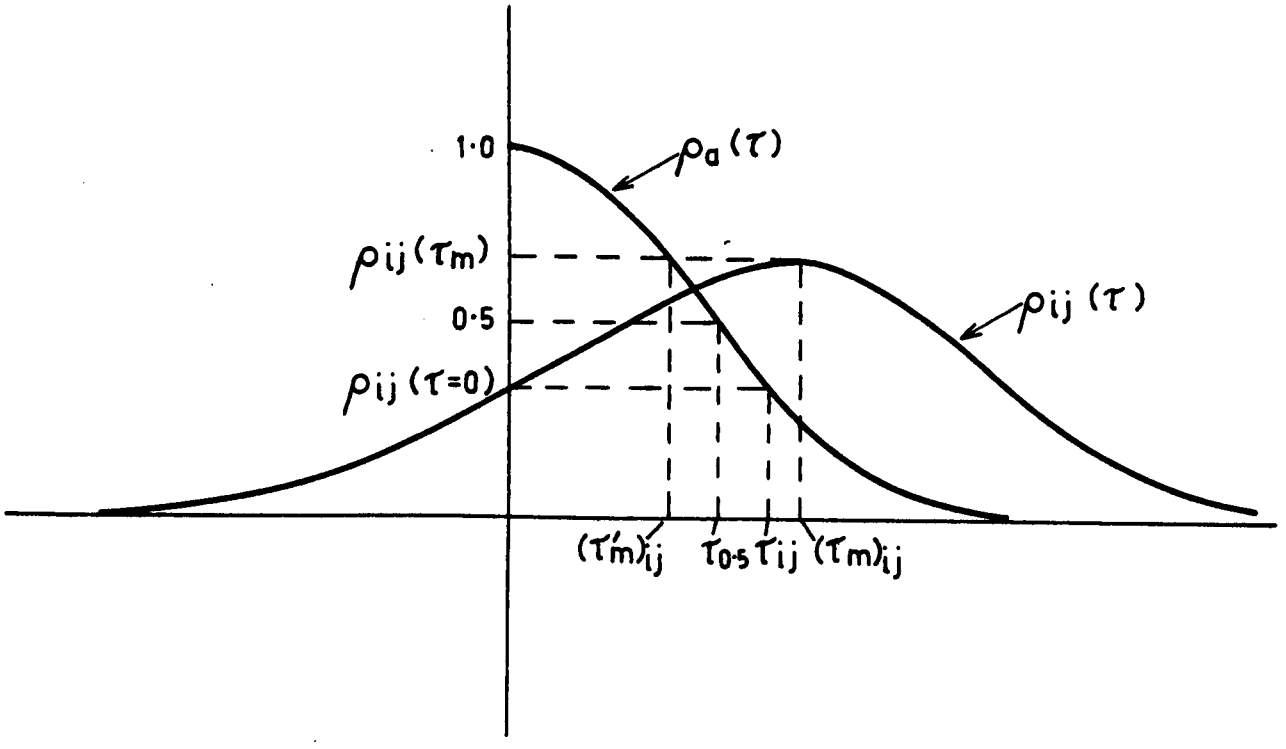

FIGURE 4.4 Experimental autocorrelation and cross-correlation functions and the parameters measured from them.

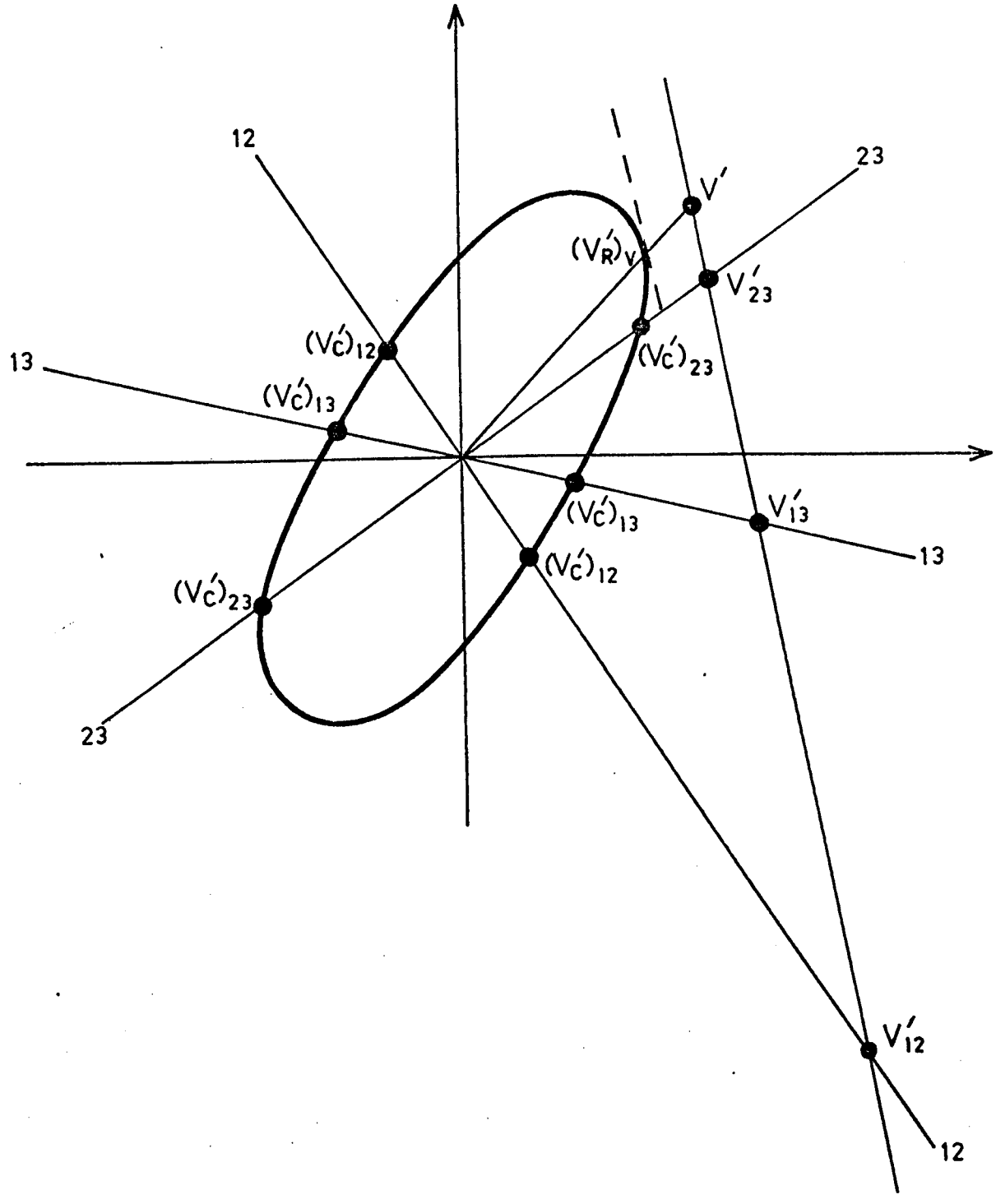

FIGURE 4.5 Construction of the 'characteristic ellipse' and determination of the true drift velocity.

Provided that random changes in the pattern are negligible the value V^1 becomes equal to the true velocity V . The importance of random changes in the pattern may be represented by (Fooks and Jones, 1961)

$$\frac{(V_R)_V}{V} = \left[\left(\frac{V^1}{(V_c^1)_V} \right)^2 - 1 \right]^{\frac{1}{2}}$$

where V_R is the ratio of the pattern size to its mean lifetime and $(V_R)_V$ is the component of V_R along V.

Preliminary spaced receiver observations were recorded with the Adelaide system early in 1975 using the compact source in the Crab Nebula. Altogether 14 observations were recorded with all three receivers. A number of other records were obtained with only one of the outstations due to problems experienced with the telemetry transmitters. The results from these observations were reduced using a computer version of the method outlined above. The average of the results were

$$V = 280 \pm 60 \text{ km sec}^{-1}$$

$$a = 96 \pm 20 \text{ km}$$

$$R = 1.2 \pm 0.3$$

These results are consistent with those reported by other spaced-receiver observations and with spacecraft data, although the solar wind velocity is lower than measured by spacecraft. Jokipei and Lee (1972) have shown that spaced receiver measurements underestimate the true solar wind speed by ~20% due to the geometrical projection effects across the line of sight. A correction of this magnitude would bring the velocity into closer agreement with spacecraft observations although they are still rather low.

These observations have not provided any new information about

the solar wind but have shown that the Adelaide system is now capable of providing estimates of the solar wind velocity. A number of technical difficulties need to be overcome before the system can produce regular results, the main are being a modification to the telemetry transmitters which frequently destroy the output valve which is in short supply in Australia at the present time. Significant advances in these techniques will require a long series of systematic observations. The most significant contribution from the Adelaide system will come with the completion of the 285.9MHz system which will enable the pattern to be measured simultaneously at two frequencies.

CHAPTER 5

IPS AND LARGE SCALE INTERPLANETARY DISTURBANCES

5.1 INTRODUCTION

Measurement of the properties of the interplanetary plasma by in-situ sampling from spacecraft experiments suffers from the limitation that the plasma measurement is made in only one point in space. This means that multiple spacecraft observations are required to determine the large scale properties of disturbances in the medium. Since detailed multiple spacecraft observations are rare much of the work on the large scale properties of interplanetary disturbances has been based on ensemble averaging of single spacecraft observations of a number of disturbances. This approach has the limitation that there may exist quite large variations between individual events.

Dennison and Wiseman (1968) showed that it was possible to trace the motion of large scale structures in the medium by their effect on the scintillation of a group of radio sources spaced around the sky. Their technique involved daily observations of a number of scintillating sources and from the variations in scintillation indices they deduced the existence of a turbulent plasma stream passing the Earth on 28th May 1968. Data subsequently available from spacecraft has shown that this stream was associated with a magnetic sector boundary which existed for more than six solar rotations (e.g. see Figure 1.5) and was responsible for the enhanced scintillation observed by Burnell (1969) during December 1967.

This technique provides a valuable method for investigating the structure of large interplanetary disturbances. In this chapter, we investigate

the properties of transient flare-produced disturbances as they propagate through the interplanetary medium by combining solar, spacecraft and scintillation observations. A comparison is made between the features revealed by this study with the picture of such disturbances derived solely from spacecraft data.

5.2 JUNE 1972

A group of seven scintillating sources were monitored at Culgoora during the period June 10 - 20, 1972. Each source was observed daily at 80MHz for a period of between ten and fifteen minutes followed, after a delay of about five minutes required to change the operating frequency of the radioheliograph, by a similar period of observation at 160MHz. Four of these sources were also observed with the 111.5MHz array at Buckland Park. The data recording and analysis procedures for these observations followed the methods discussed in Chapter 4.

The projection of the line of sight to each of the sources onto the ecliptic plane is shown in Figure 5.1. During the period June 10 - 15 the scintillation of all seven sources was typical of that of quiet, undisturbed conditions in the interplanetary medium. On June 16 a pronounced change in the scintillation was observed to commence at approximately 0505 UT during the course of the 160MHz observation. The striking feature of this event was the dramatic change in the characteristics of the intensity fluctuations on a time scale of about three minutes as shown in the tracing of the record in Figure 5.2. An attempt was made to record an additional 80MHz observation following the sudden change at 160MHz but because the observations had to be made after the routine solar patrol the source was outside the tracking range of the heliograph by the time the instrument was converted back to 80MHz operation. The 111.5MHz transit observations at Adelaide were recorded approximately two hours prior to the

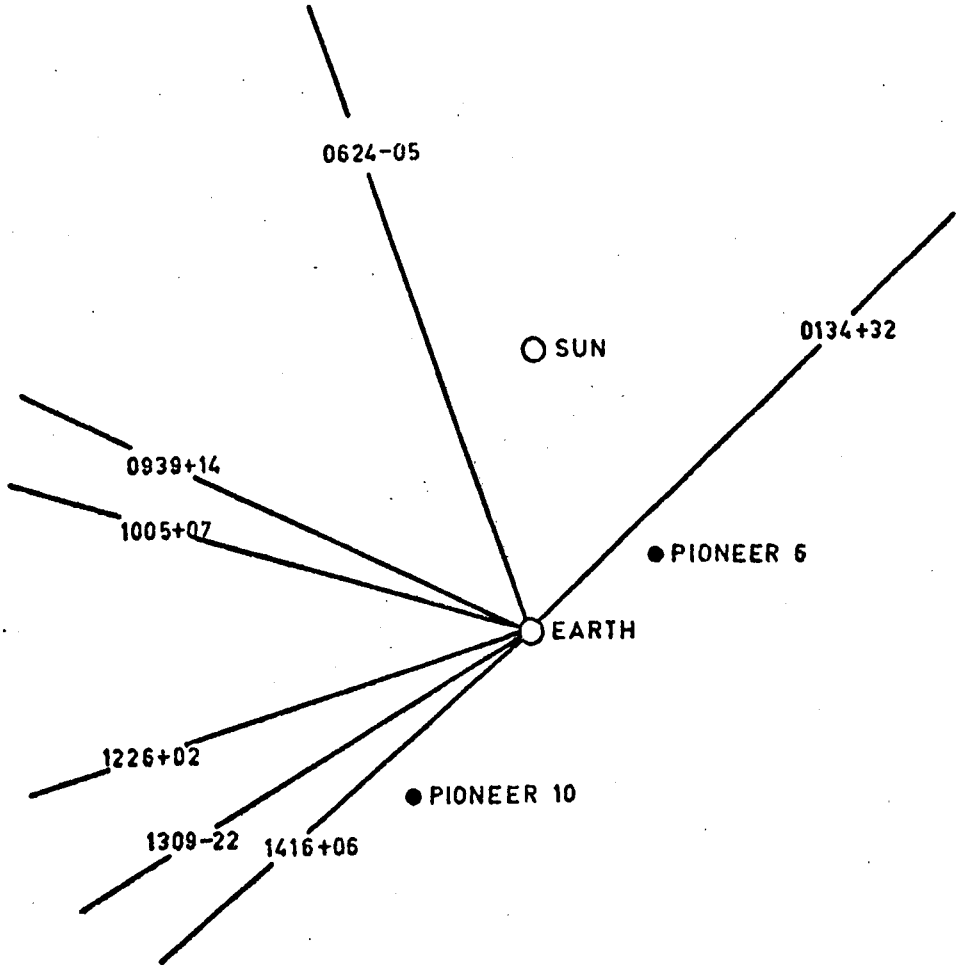

FIGURE 5.1 Ecliptic plane projection of the line of sight to each of the sources during June 1972.

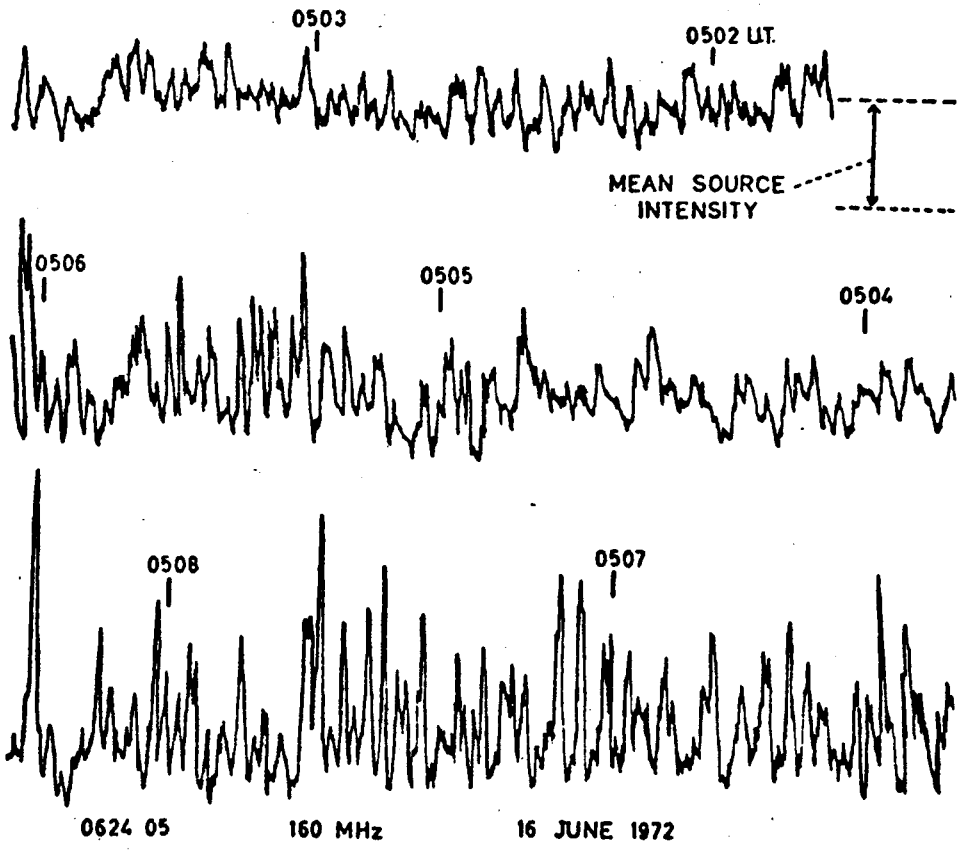

FIGURE 5.2 Recording of scintillation of source 0624-05 at 160 MHz between 0502 and 0508 UT June 16, 1972. The record is continuous from right to left, top to bottom.

Culgoora observations for this particular source.

The average daily scintillation index m and the square-root second moment f_2 of the power spectrum (defined in Chapter 4) are shown in Figures 5.3 and 5.4. The gaps in the 160MHz results were caused by malfunction of the local oscillator for the 160MHz converters. During the period June 10 - 15 the scintillation was weak but typical of the scintillation of sources at these elongations. On June 16 the sources 0624-05, 0939 + 14 and 1005 + 07 were affected by a weak, slow and irregular form of scintillation which was quite different in appearance on the analog records to the scintillation of the previous days. Sources 1226+02 1309 - 22 and 1416 + 06 were affected in a similar manner on June 17. Passage of the main disturbance across a given line of sight was marked by strong and rapid intensity fluctuations, with a large increase in the scintillation index and a change in the power spectrum of the fluctuations from an approximately Gaussian to an exponential form. The disturbance, as revealed by the increase in scintillation index in Figure 5.3, clearly affected each source in turn and the time sequence in which the sources were affected indicates that the disturbance was a transient, rather than corotating event. The effect of the disturbance on any source lasted for only one day.

The numbers below the source names in Figure 5.3 indicate the ecliptic latitudes of the sources. It is apparent that those sources with lines of sight lying south of the ecliptic are affected more strongly than those near the ecliptic plane. Another important feature is that the two sources lying well north of the ecliptic are affected quite differently. Source 0134 + 32 which lies above the ecliptic to the west of the Sun - Earth line was quite clearly affected, whereas 1416 + 06 which lies above the ecliptic to the east of the Sun — Earth line remained unaffected. Source

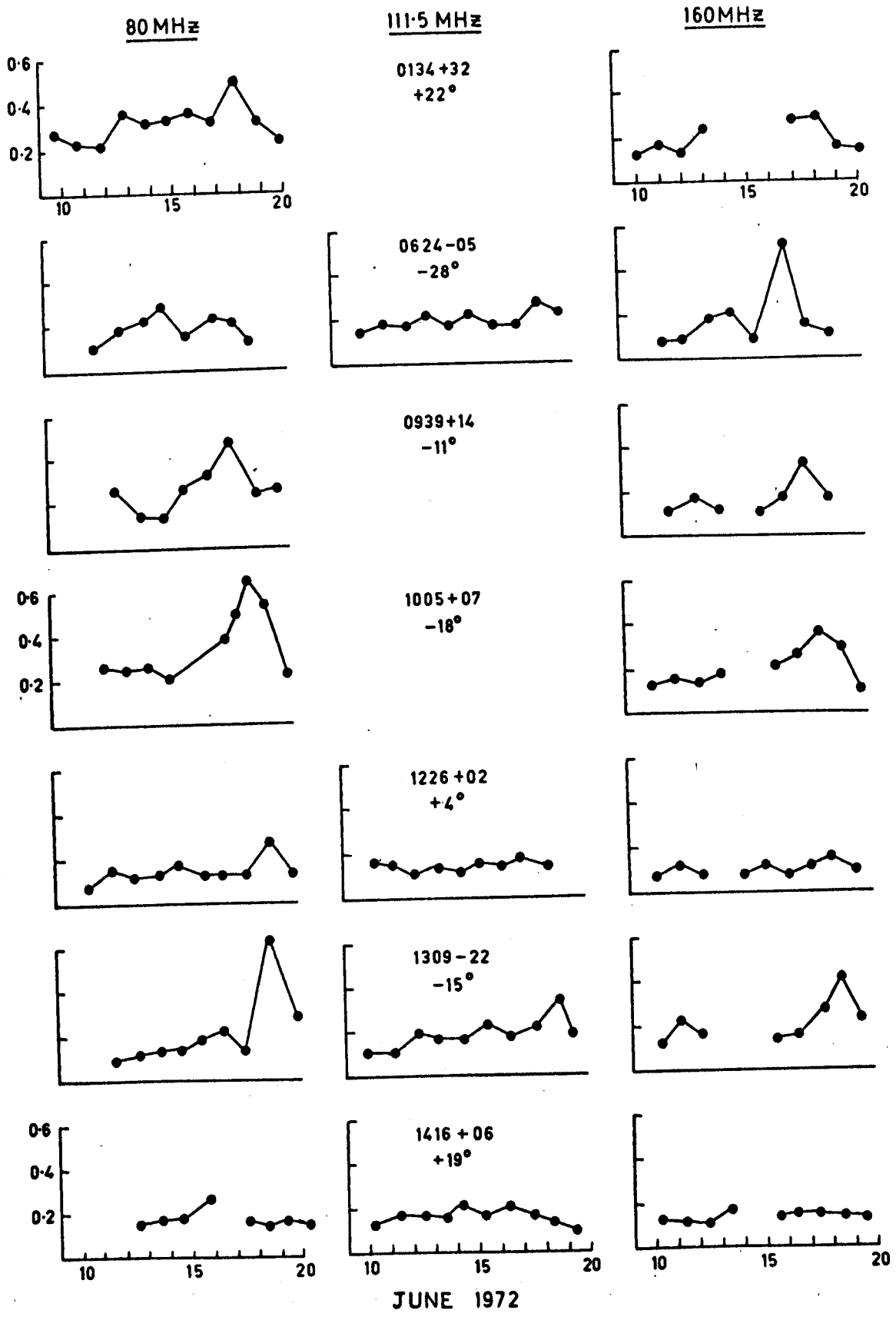

FIGURE 5.3 Scintillation indices during June 1972

1226 + 02, lying slightly above the ecliptic to the east, showed only a minor effect.

We shall now investigate the solar origin of this event and discuss its motion through the interplanetary medium as deduced from the scintillation and spacecraft data. The solar origin of transient disturbances is of great importance to the study of the propagation of such disturbances through the interplanetary medium. The arrival of the disturbance near 1 AU is usually detected as a plasma shock marked by a sudden change in the plasma parameters measured by spacecraft experiments. Interaction of the shock with the Earth's geomagnetic field frequently causes a geomagnetic sudden commencement, followed by a geomagnetic storm. The procedure generally adopted for identifying the specific solar source of a disturbance is to look for a major flare in the period 40 to 60 hours prior to the arrival of the disturbance at 1 AU. These flare-shock associations are often ambiguous as there is frequently more than one major flare within the appropriate time interval. They may also be misleading because some major flares apparently do not produce shock waves detectable at 1 AU whereas other more minor flares may on occasion trigger quite large disturbances. These problems are compounded by the non-uniformity of flare reporting and have led to some controversy over the usefulness of such associations (e.g. Hundhausen, 1972a).

During June 1972 a world-wide co-ordinated campaign (CINOF) for the observation of small solar flares was carried out with the aim of gaining information on the basic flare mechanism, without the complexities inherent in large flares. A summary of the CINOF campaign has been given by de Jager (1974). As a consequence of this program a detailed picture of solar activity during June 1972 is available and it has been possible to identify the flare responsible for the interplanetary disturbance discussed in this section.

McMath region 11926, which rotated over the east limb on June 10 at

13^0 south, was the most active region on the visible disk between June 10 and 15 and was a magnetically complex but quite stable region. It produced a number of subflares during the period June 10 - 14 and became more active on June 14, producing a large number of subflares. These appear to have fed energy into the region until it finally became unstable giving rise to three major flares on June 15. These flares, which occurred at 0925 UT (importance IN, location S05E15), 0950 UT (2B, S12E10) and 1226 UT (IF, S16E01), have been studied in detail by Bruzek (1974).

The 0925 UT flare was preceded by increased activity in region 11926 and led to the disruption of a filament which later reformed. A second, much larger flare occurred in the same position at 0950 UT. This flare showed signs of a sudden acceleration process with multiple type III radio bursts, a large microwave burst and an x-ray burst (Solar Geophysical Data, # 341-I). The most significant optical feature was the occurrence of a "winking" filament and the brief flaring of points of the chromosphere lying outside the original flare region (Bruzek, 1974). These features are shown in Figure 5.5, where the dark filament in the lower right-hand corner of each photograph appears to change in intensity between successive frames. Simultaneous photographs in $H_\alpha \pm 0.5$ Å showed that this change was the result of a Doppler shift of the H_α emission produced by upward and downward oscillations of the filament between 0952 and 1015 UT. This filament continued to move more randomly until at least 1040 UT. The small bright points in the lower portion of the photograph at 1000 UT are some of the points which flared briefly between 0955 and 1004 UT. A type II radio burst was observed at metre wavelengths between 1000 and 1009 UT (Solar Geophysical Data, # 336 - I). A third flare occurred in a different part of the active region and was a slow rising, long endurance flare. Again the onset was accompanied by the generation of a group of type III bursts and enhanced microwave emission, but more significantly it gave rise to a type IV burst which lasted from 1305 to 1411 UT (S.G.D. # 336 - I).

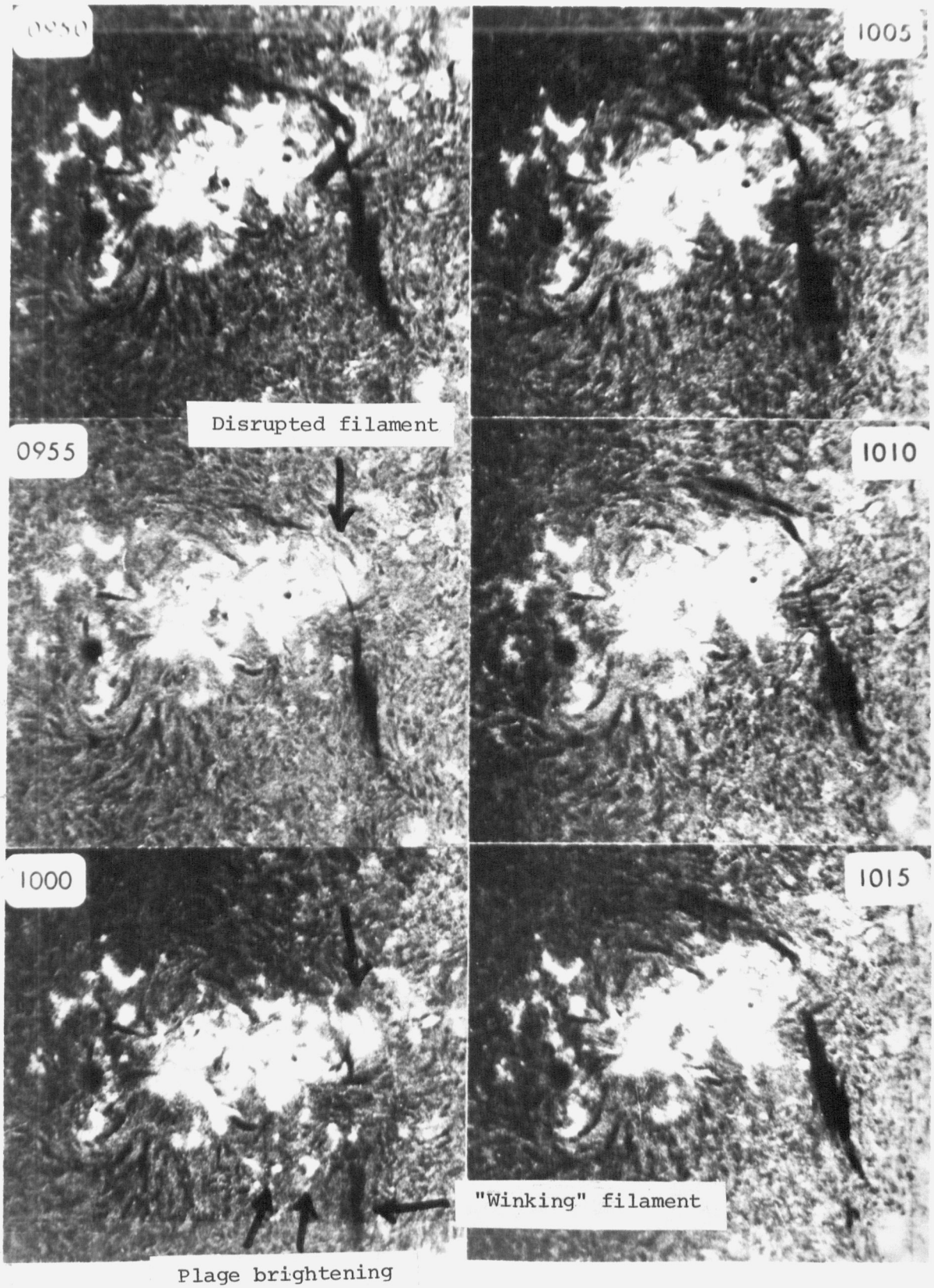

FIGURE 5.5 Flare event of June 15, 1972

Strong type III, microwave and x-ray bursts which occur simultaneously with the flash phase of the optical flare, as in the 0950 UT event, are generally taken to be indicative of a sudden acceleration of material in the flare region. The type II radio burst, winking filament and plage brightening outside of the flare region can be ascribed to the propagation of an MHD shock wave through the corona (Uchida, 1973a). Type IV bursts are associated with the presence of energetic electrons in the corona (e.g. Wild and Smerd, 1972). It would appear therefore that the sudden acceleration of plasma during the flash phase of the 0950 UT flare was responsible for triggering the shock wave observed in the interplanetary medium. Subsequent events in and near the flare-site suggest that energetic material may have been injected into the corona behind the shock wave for some time after its generation and especially during the 1226 UT flare.

The IPS data outlined earlier can be combined with spacecraft observations to investigate the manner in which the shock propagated into interplanetary space. The arrival of the leading edge of the disturbance at 1 AU was marked by a shock detected at the Heos - 2 spacecraft at 1314 UT on June 17 (Hedgecock, 1974; Rosenbauer, private communication) and a geomagnetic sudden commencement on the Earth at 1312 UT, followed by a major geomagnetic storm (S.G.D, # 336-I). The shock passed Pioneer 6 at some time between 1400 UT June 17 and 0820 UT June 18, and Pioneer 10 at ~ 0300 UT on June 19. The Heos - 2 spacecraft was in a geocentric orbit at a distance of 38 R_E, Pioneer 6 was in the ecliptic plane 0.85 AU from the sun and 25^0 west of the Sun - Earth line, and Pioneer 10 was $2^0.1$ south of the ecliptic, 14^0 east of the Sun - Earth line and 1.6 AU from the sun (see Figure 5.1). Table 5.1 lists the average properties of the interplanetary plasma observed at Heos - 2 and Pioneer 10 before and after passage of the shock. Figure 5.6 shows the solar

TABLE 5.1 Solar Wind Properties Observed near the Shock

	Pre-shock	Post-shock
Heos 2 *		
Velocity	495 km sec^{-1}	605 km sec^{-1}
Density	7.3 cm^{-3}	15.5 cm^{-3}
Direction	3^0 E	9^0 E
Mag. Field	10γ	22γ
Pioneer 10 +		
Velocity	420 km sec^{-1}	580 km sec^{-1}
Density	3.6 cm^{-3}	4.6 cm^{-3}
Isotropic Temp.	5×10^4 ^{0}K	2.8×10^5 ^{0}K

* One-hour averages

\+ six-hour averages

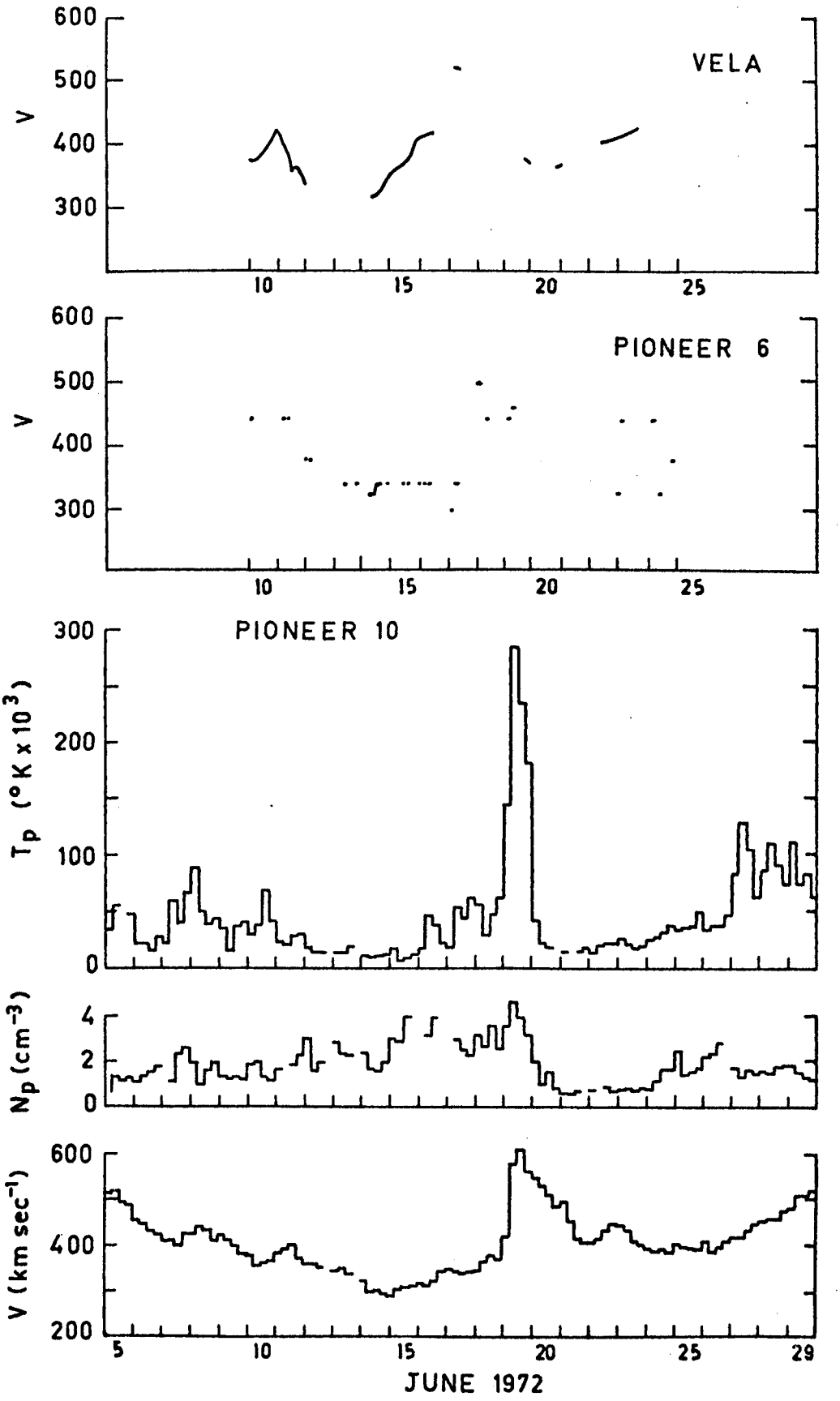

FIGURE 5.6 Solar wind parameters during June 1972

wind velocity at the Vela - 5 (geocentric orbit) and Pioneer 6 spacecraft, and the plasma parameters measured at Pioneer 10.

The variation in plasma parameters at both Heos - 2 and Pioneer 10 are characteristic of the passage of an interplanetary shock past the spacecraft. The arrival of the shock at Heos - 2 was indicated by a rapid increase in the magnetic field, bulk velocity and proton density. Similar effects were observed at Pioneer 10, with increases in the bulk velocity, proton temperature and proton density. The enhanced temperature lasted approximately 20 hours at Pioneer 10, indicating that the swept-up plasma shell had a thickness $\sim 4 \times 10^7$ km near the ecliptic plane. Following passage of the disturbance the velocity slowly decreased and the density remained low for several days, typical of the rarefaction which develops in the interplanetary medium following the passage of a flare-produced disturbance.

The scintillation observations can provide information about the shape and location of the disturbance, especially in regions away from the ecliptic, which is supplementary to that obtained from the spacecraft data. Since the scintillation is the result of an integrated effect along the line of sight, and the observations on each source are made for only a relatively short period each day, it is not possible to locate the exact time and position at which the disturbance crosses a given line of sight, but it is possible to infer the approximate shape and direction of motion of the disturbance from the sequential changes in scintillation index. This problem is considered in more detail in section 5.6 where a numerical integration of the scattering along several lines of sight is calculated for a variety of disturbances in a spherically symmetric ambient medium. Comparison of these models with the observed index variations suggests that near 1 AU the

disturbance occupied a cone of angle of at least 80^0 centred on the flare site, although in cases where the motion is approximately radially outward from a flare near central meridian, as in this case, it is not possible to accurately estimate the angular width of the disturbance. The dependence of the index variations on the position of the line of sight to the sources discussed previously, shows that the bulk of the disturbance propagated southwards out of the ecliptic plane but that the overall disturbance differed quite markedly from a spherically, or even axially, symmetric form.

The results of several studies of shock normals derived from spacecraft data (Ogilvie and Burlaga, 1969; Taylor 1969) have shown that the shock normals commonly exhibit an average deviation $\lesssim 30^0$ from the radial and have only a low inclination to the ecliptic. There is however considerable uncertainty as to the exact shape of the shock fronts. Bavassano et al (1973) suggest that the average shock front corresponds closely to the shapes obtained in the numerical simulations of De Young and Hundhausen (1971) while Chao and Lepping (1974) suggest that the average shape is essentially spherical. Several cases of shock normals tilted strongly out of the ecliptic plane have been reported (Greenstadt et al, 1970; Hirshberg et al, (1970). These shock normals derived from spacecraft data obtained at one or at most two points in space may represent local perturbations of the shock front rather than the direction of the whole shock or there may be large variations between individual shocks. Hirshberg et al (1970) suggested that these tilted shocks may be cases in which the disturbance is not spherically symmetric but resembles a flattened disk tilted out of the ecliptic. This model would be capable of explaining the observed variations in scintillation index if we assume that the disk was tilted in such a manner that it extended well above the ecliptic to the west of the Sun - Earth line but not to the east.

An alternative, and physically more realistic, possibility is that the disturbance was not in fact a simple "smooth" surface but possessed a

rather irregular shape, with two or more "tongues" extending in different directions. Several theoretical studies have suggested physical mechanisms for the development of such irregular structures. Two such mechanisms are shock wave propagation into an ambient medium containing a non-homogeneous distribution of plasma (Hirshberg et al, 1974) or a non-homogeneous magnetic topology (Greenstadt et al, 1974). Figure 5.7 shows the structure of the interplanetary magnetic sector structure on June 16,1972 interpolated from observations of the sector polarity at the Earth (Fairfield and Ness, 1974). Provided that the sector structure is stable over several solar rotations it is possible to estimate the position of the boundaries on any given day to within about $\pm 5^0$. During 1972 the sector pattern was variable and the positions of the boundaries distant from the Earth are rather uncertain, but the important feature is the boundary which passed the Earth at 1219 UT on June 16 (Hedgecock, private communication). As discussed in Chapter 1, such boundaries are usually associated with high-speed corotating plasma streams. Thus the ambient medium at the time of this event was not dissimilar to those investigated in the theoretical models of Hirshberg et al (1974) and Greenstadt et al (1974). These scintillation observations therefore provide the first conclusive evidence for the distortion of the shock front by propagation into an inhomogeneous ambient medium.

The rapid change in the scintillation for source 0624-05 on June 16 presents an interesting problem. Under quiescent conditions for a source at this position the major contribution to the scintillation would come from a length ~0.2 AU of the line of sight centred ~0.8 AU from the Earth (Redhead 1971). It is unlikely that such a large region could be affected in the 180 seconds that it took for the change to occur, so the effective scattering region was probably much thinner than normal. This implies a correspondingly large increase in the rms density fluctuation. The passage of the shock past Heos 2 was accompanied by an abrupt increase in the magnetic field strength, jumping from 10 to 23 γ in less than

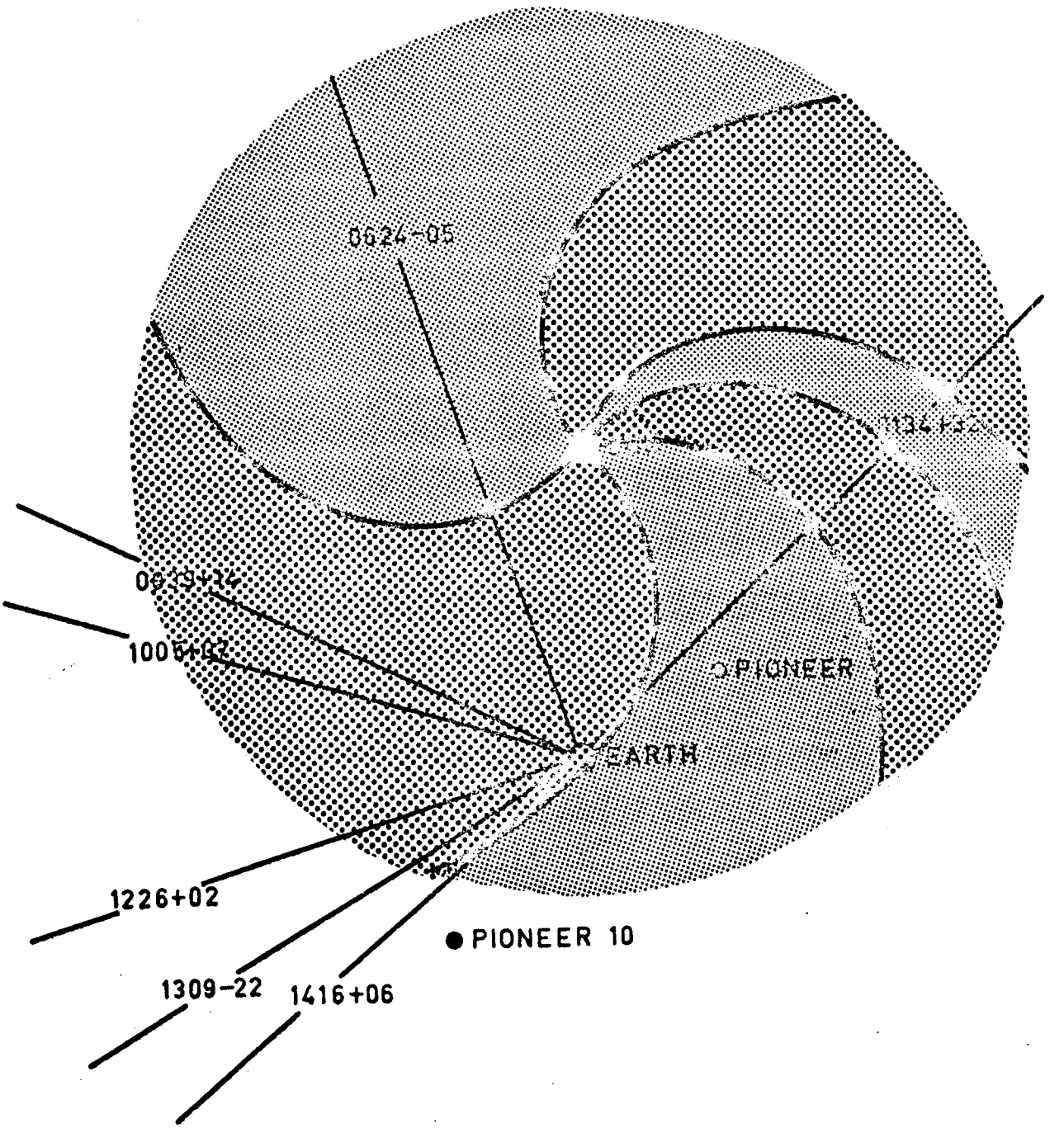

FIGURE 5.7 Sector structure of the interplanetary magnetic field on June 16, 1972.

The location of the sector boundaries at 1 AU have been interpolated from the observations of the sector boundaries as they corotate past the Earth (Fairfield and Ness, 1974). The spiral shapes shown assume a solar wind speed $\sim$ 500 km sec^{-1} in the vicinity of the boundary.

10 seconds. It is probable that this region of steep magnetic field gradient causes the onset of plasma turbulence, resulting in a much enhanced rms density fluctuation in the vicinity of the shock front.

One other feature of interest in the scintillation observations was the behaviour of the sources prior to the major disturbance. All of the sources showed this effect which was readily recognizable on the analog records although more difficult to define quantitatively. It consisted of relatively weak, slow intensity fluctuations with occasional bursts (~10 sec every 40 sec) of slightly stronger, more rapid fluctuations. This behaviour may have been associated with the passage of the magnetic sector boundary although the temporal sequence between the sources is faster than is usual for corotating events. There is reason to believe that there may have been some large scale structure present in the medium at the time associated either with the sector boundary or with active region 11926. Figure 5.8 shows the solar cosmic ray flux measured during June 1972 (Shea and Smart, 1974). The sudden increase in flux on June 8 is believed to have originated in a flare near or behind the west limb of the sun. The sharp peak in the flux on June 17 is an energetic solar particle event associated with the 0905 UT June 15 flare and shows a marked change in anisotropy at 1311 UT with the passage of the shock (Allum, 1974). Shea and Smart (1974) concluded that the general increase in flux which commenced on June 14, although almost certainly connected with McMath region 11926, was not attributable to any specific flare activity within that region. It would seem likely that the irregular features in the IPS observations were associated with this large scale disturbance in the medium prior to the flare-produced shock wave. Unfortunately the limited amount of spacecraft data available for this period does not make it possible to investigate this further.

The interpretation of spacecraft observations of plasma shocks is

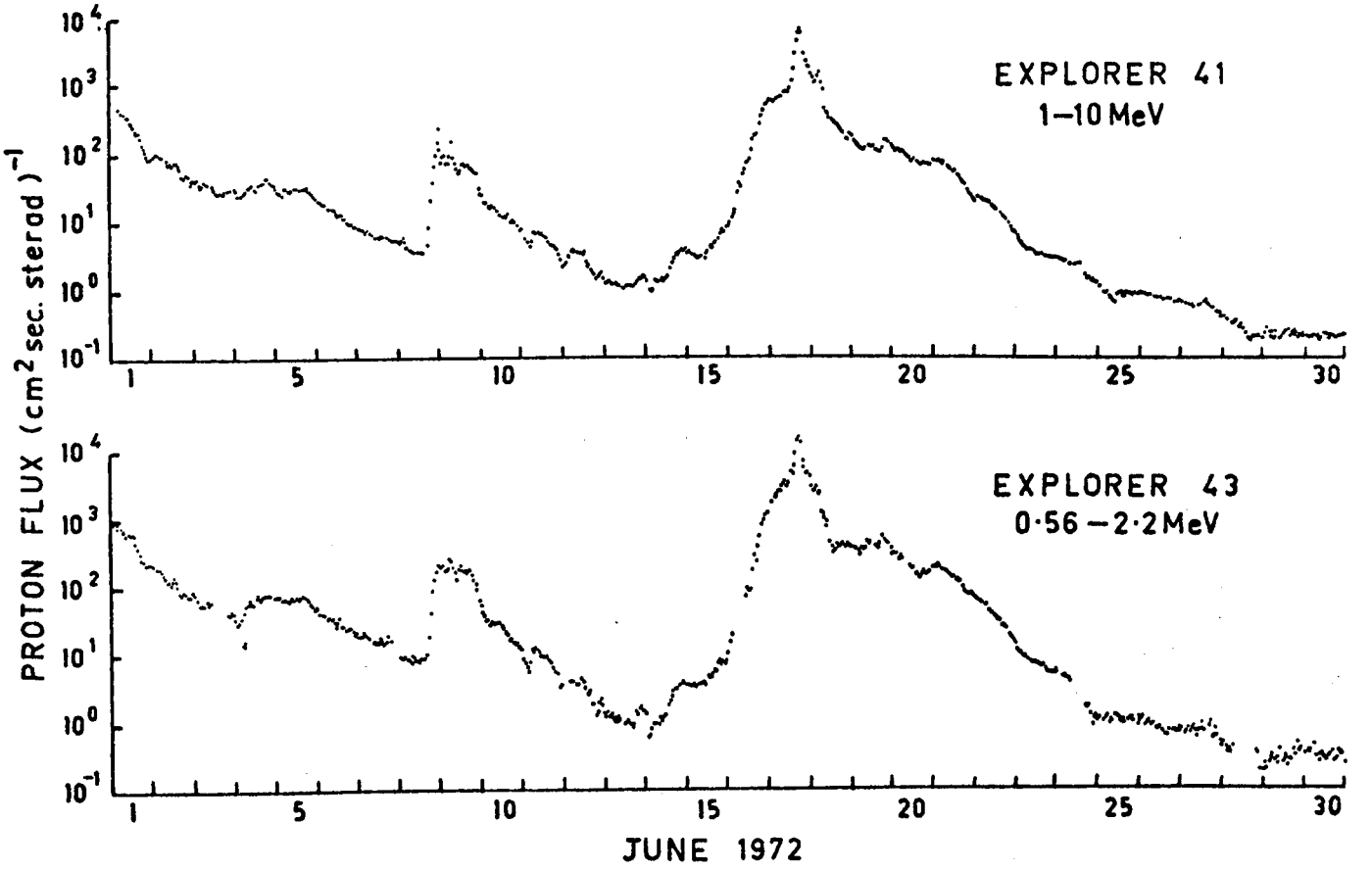

FIGURE 5.8 Cosmic ray fluxes measured at the Explorer 41 and 43 satellites during June 1972.

generally based on the Rankine - Hugoniot relations which express the conservation of mass, momentum, energy and magnetic flux through the shock front. In particular, if the normal to the shock surface is assumed to point radially from the sun, conservation of mass in a stationary frame of reference (neglecting ions other than 'H+) gives (Tidman and Krall, eq 1.33)

$$n_1 \cdot (V_1 - V_{shock}) = n_2 (V_2 - V_{shock}) \qquad \text{--- (5.1)}$$

where V_{shock} is the local instantaneous velocity of the shock front, n_1, V_1 and n_2, V_2 are the density and velocity ahead of and behind the shock respectively. Rearranging (5.1) gives

$$V_{shock} = \frac{n_2 V_2 - n_1 V_1}{n_2 - n_1} \qquad \text{--- (5.2)}$$

The Alfven Mach number $^{(Ma)}$ of the shock is

$$\frac{n_2}{n_1} = \frac{4M_a^2}{(3+M_a^2)} \qquad \text{--- (5.3)}$$

Applying these relations to the Heos 2 data in Table 5.1 gives V_{shock} = 700 km sec^{-1} and $M_a \approx 1.8$. Thus the shock at 1 AU was of intermediate strength. A similar calculation cannot be made for the shock when it arrived at Pioneer 10 because only 6-hour averages of the plasma parameters are available.

The velocity of the shock in the corona can be estimated from the observed frequency drift rate of the type II radio burst, the spectrum of which was kindly supplied by Dr H. Ubarz. It is necessary to assume a model for the coronal electron density in this calculation. Assuming a 2_X Newkirk active streamer model for the density gives a velocity of ~1150 km sec^{-1} based on the frequency drift rate between 40 and 30MHz. A Newkirk active streamer model and a 10 times Van de Hulst model predict velocities of 880

and 1250 km sec^{-1} , respectively,

The average velocity between the Sun, Earth, Pioneer 6 and Pioneer 10 can be derived from the observed time of arrival of the shock front at each of the detectors. An estimate of the shock velocity between the sun and the line of sight to source 0624-05 can be calculated if some assumptions are made about the point on the line of sight which is affected by the disturbance. Figure 5.9 shows the derived velocities where the dots represent the average transit time between pairs of detectors, and the triangle is the instantaneous shock velocity at 1 AU calculated from the Heos 2 data. Pioneer 10, Earth, and Heos 2 are close to the normal direction from the flare site and Figure 5.9 shows that the shock was decelerated on its way out from the sun. The points labelled "Jupiter' are based on the suggestion by Dryer et al (1974) that a non-Io-associated radio burst from Jupiter on July 1 was associated with passage of the shock past Jupiter. While this is by no means certain, it does fit the observed deceleration.

The average velocity of the disturbance between the Sun and Pioneer 6 is uncertain because of limited spacecraft data but is clearly lower than the velocity between the Sun and the Earth. This suggests that expansion of the shock front in directions away from the normal direction from the flare site is slower than in the normal direction. The velocity of the shock between the Sun and the line of sight to source 0624-05 is also uncertain due to lack of knowledge of the exact point at which the disturbance crossed the line of sight but it is significantly higher than the other average values. This probably represents a difference in the propagation speed of different parts of the disturbance since 0624-05 lies well south of the ecliptic whereas the other average values were all determined in or near the ecliptic plane. The possible asymmetry of flare-produced disturbances should be kept in mind when attempting to use velocities determined from widely separated detectors

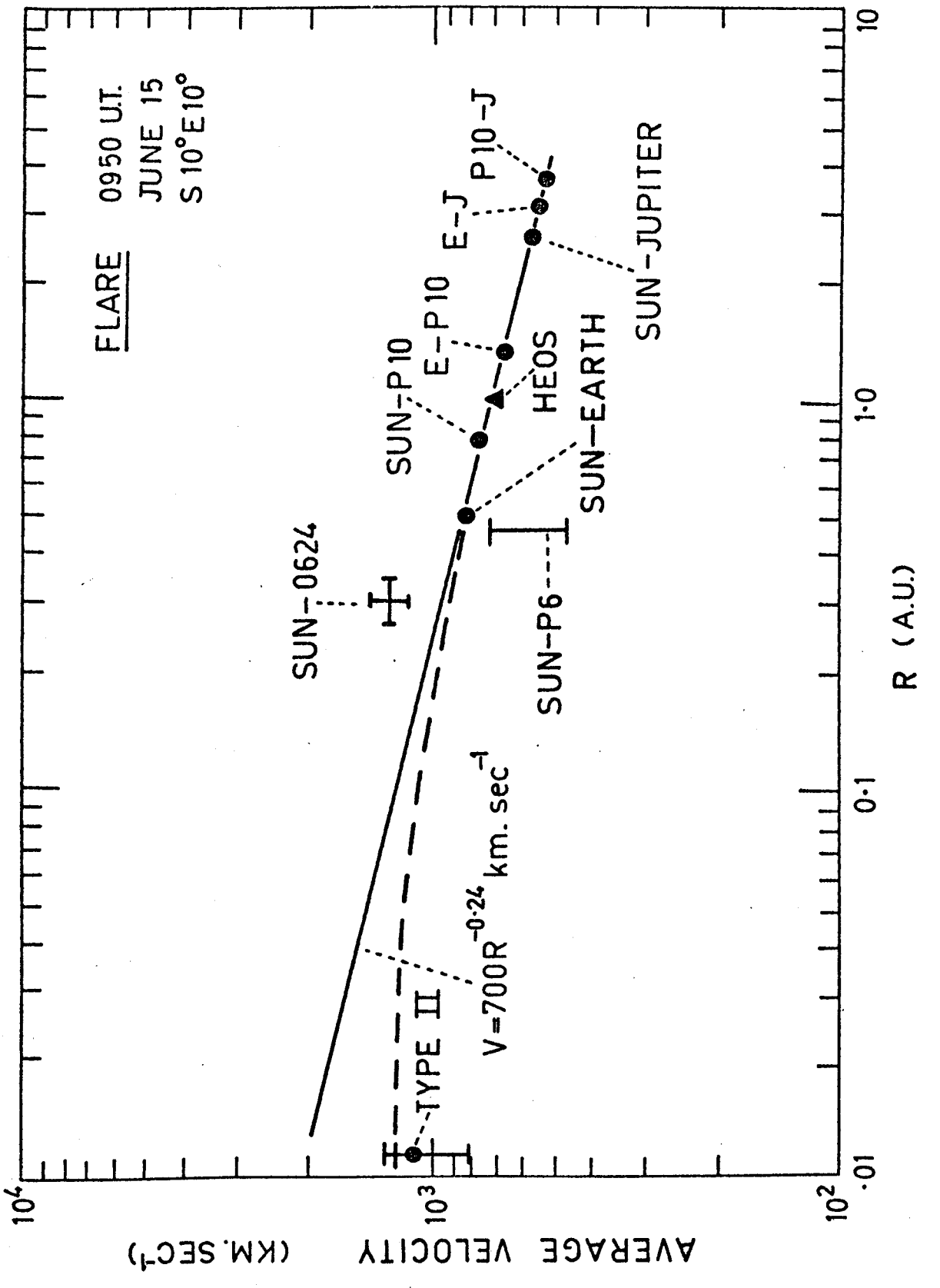

FIGURE 5.9 Velocity of the shock wave as a function of heliocentric distance.

for comparison with theory.

One technique used to compare observed shock velocities with theory is to fit a power-law variation of the form

$$V(R) = \alpha R^{\beta} \qquad \text{--- (5.4)}$$

where R is the heliocentric distance, since similarity theory predicts a variation of this form with blast waves being characterized by values $\beta \lesssim -0.5$ and piston-driven disturbances by $\beta > -0.5$ (Dryer, 1974). The power-law variation fitted to Figure 5.9 has $\beta = -0.24$ suggesting that the disturbance was piston-driven. This model clearly overestimates the shock velocity close to the sun, and a better fit can be obtained if it is assumed that the velocity is of the form

$$V(t) = a + bt \qquad \text{--- (5.5)}$$

where t is the time which has elapsed since the flash phase of the flare. This model is shown by the dashed line in Figure 5.9 and suggests that the disturbance propagated outwards to ~ 0.1 AU at constant velocity before undergoing any deceleration. This is in contrast to the numerical models of Hundhausen and Gentry (1971) in which the greatest deceleration occurs close to the sun where the shock velocity and ambient density are high. The evidence for a piston-driven shock, rather than a blast wave, is consistent with the earlier suggestion that the shock originated in the 0950 UT flare but that plasma injection continued for some time, especially as a result of the 1220 UT flare.

5.3 AUGUST 1972

The period August 1 - 10, 1972 was marked by a complex series of

solar events in McMath region 11976 which have been the subject of much discussion. During that period there was good coverage of IPS observations with groups of 5 sources being observed with the 111.5MHz Adelaide array (Buckland Park Station only) and the 78MHz Californian (Armstrong et al, 1973) and 69MHz Japanese (Watanabe et al, 1973) spaced-receiver arrays. The ecliptic plane projection of the line of sight to sources used in these observations is shown in Figure 5.10.

Scintillation index measurements recorded with the Adelaide array are shown in Figure 5.11 together with proton densities measured at Pioneer 9 (Mihalov et al, 1974) and the mean electron content along the path from Pioneer 9 to Earth (Croft, 1973). The scintillation observations clearly reveal the existence of two major disturbances during the period, with several days in between of abnormally low scintillation. The scintillation on August 5 and 6 at 111.5MHz was in fact not measurable with the existing signal to noise ratio and the index values given in Figure 5.11 are upper limits. The Pioneer 9 data show that the cause of the low scintillation during this period was the abnormally low densities in the medium at this time.

The solar wind velocities measured by the Japanese and American groups are combined in Figure 5.12, together with the Pioneer's 9 and 10 solar wind velocity measurements. The scintillation measurements clearly show the second of these two events but there is little data covering the first event. The Pioneer 9 spacecraft detected (Mihalov et al, 1974) five plasma shocks during this period and these are marked by arrows in Figure 5.12 .

The optical flare activity in McMath region 11976 has been studied by Zirin and Tanaka (1973) and will be combined here with solar radio observations, as reported in Solar Geophysical Data, to locate the solar origin of the interplanetary disturbances. Major activity in the region began on August 2 with a series of complex flares. There were two large, long-lived, slowly-rising flares at 0310 UT (importance 1B, location N14E27) and 1958 UT

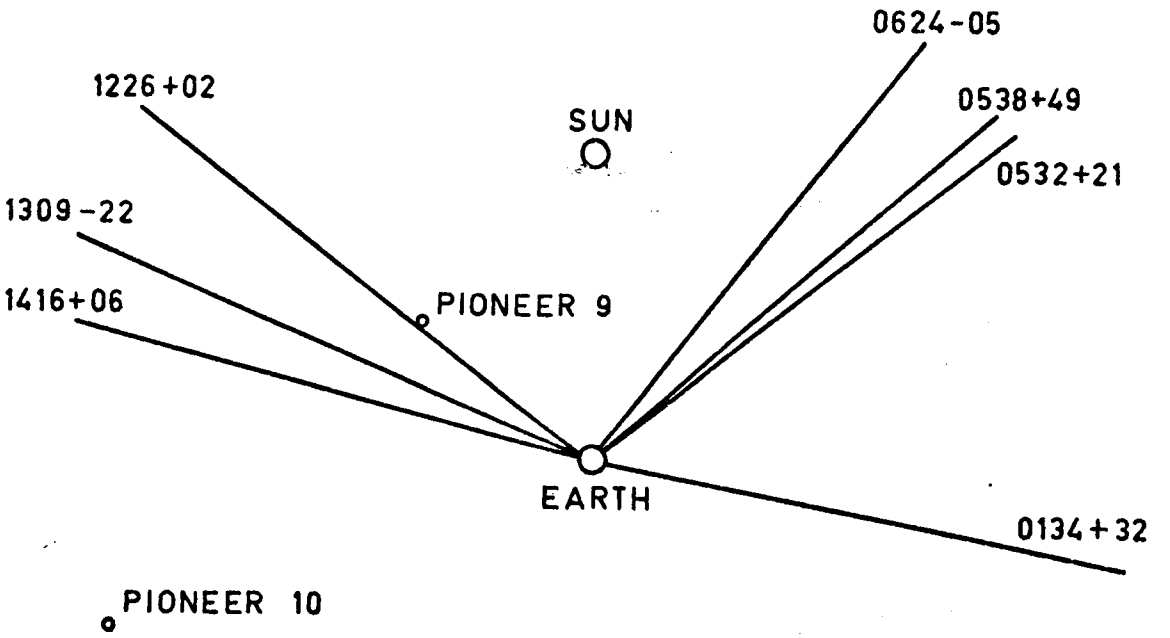

FIGURE 5.10 Ecliptic plane projection of the line of sight to each of the sources during August 1972.

Sources 0532+21, 0624-05, 1226+02, 1309-22, and 1416+06 were observed with the Buckland Park array.

Sources 0134+32, 0532+21, 0538+49, 0624-05, 1226+02, and 1416+06 were observed with the American and Japanese spaced receiver arrays.

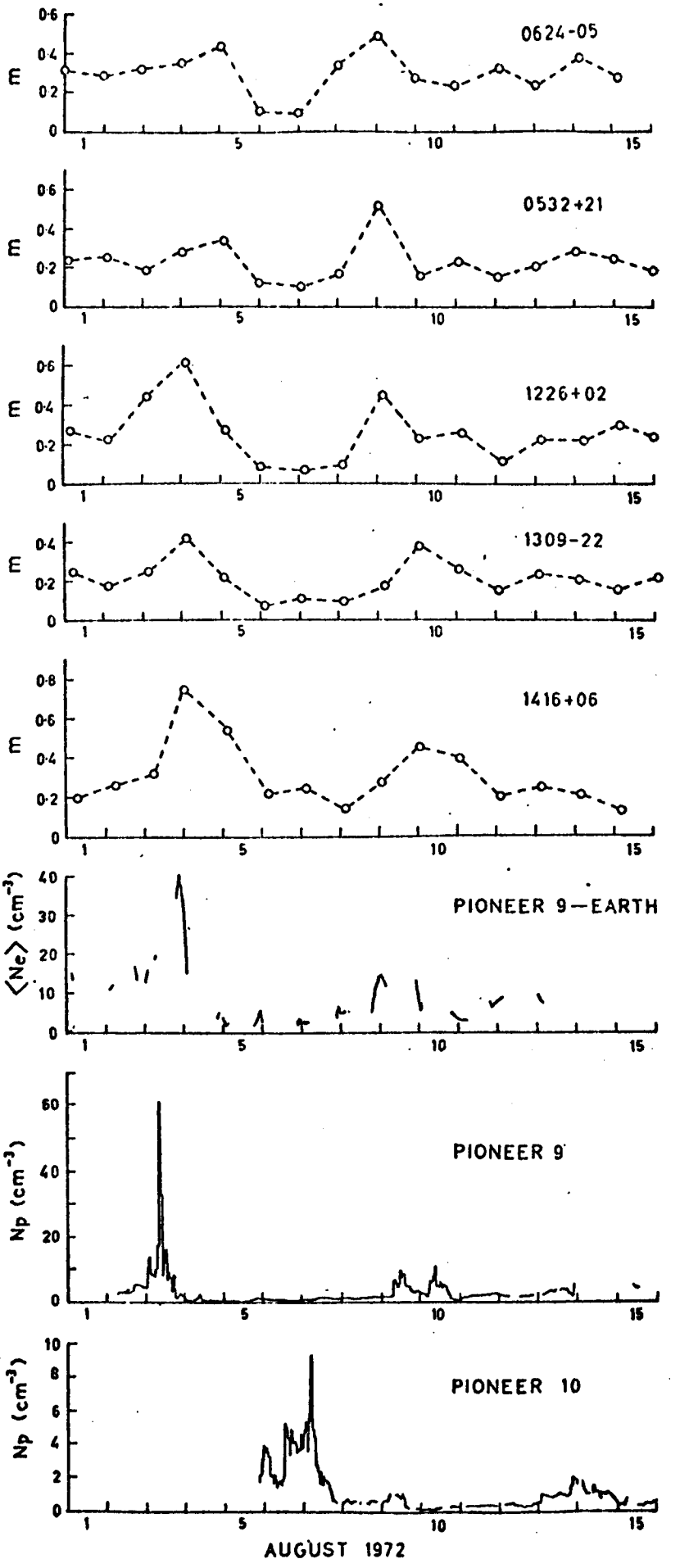

FIGURE 5.11 Scintillation index measurements from the 111.5 MHz Buckland Park array, average electron content between Pioneer 9 and Earth, and proton density measurements at Pioneer's 9 and 10 during August 1972.

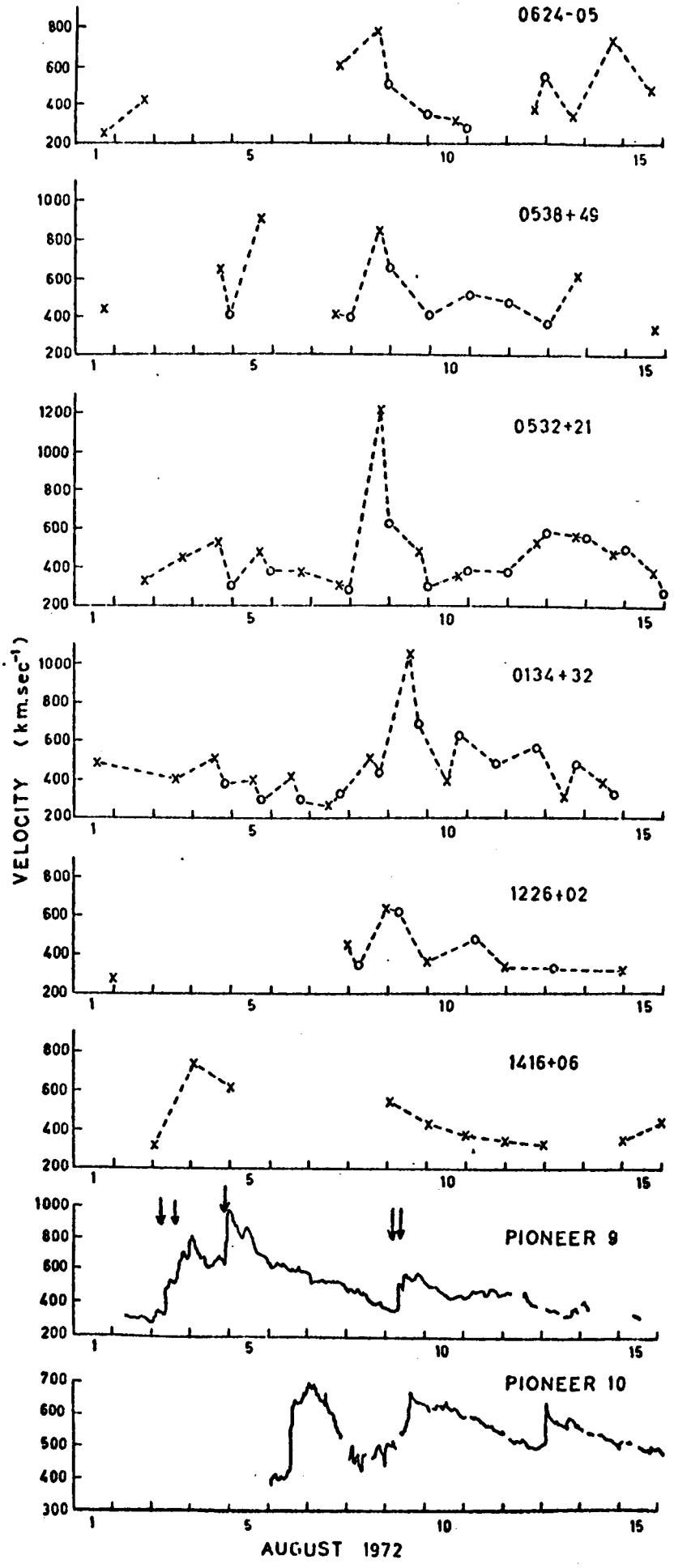

FIGURE 5.12 Solar wind velocity measurements from the Japanese (×) and American (o) spaced receiver arrays, and from the Pioneer's 9 and 10 spacecraft.

(2B, N14E28) and a small, violent but short-lived flare at 1838 UT (1B, N14E27). Each of these flares was associated with the ejection of energetic material from the chromosphere. The 0310 UT and 1838 UT flares were associated with metre-wave continuum radio emission, but the final flare was associated with an intense type IV burst which persisted for several days and a multiple-component type II burst (Maxwell, 1973).

The activity in the interplanetary medium on August 3-4 was almost certainly connected with the flares on August 2. Although all these flares were large and violent events only the 1958 UT flare showed all of the signs which can be taken to imply the generation of an MHD shock during the flash phase of the flare. On this basis we assume that this flare was the source of the disturbance. The type II burst was intermingled with the type IV radiation and the shock velocity in the corona could not be deduced from the record. Of the two shocks detected by Pioneer 9 on August 3, the first was the most significant and can be associated with the onset of the large disturbance. The shock front was marked by a rapid increase in velocity (370 to 580 km sec^{-1}) and density (5 to 14 cm^{-3}). The velocity and density behind the shock continued to increase, reaching maximum values of 800 km sec^{-1} and 60 cm^{-3}, respectively and are typical of conditions in flare-produced disturbances. The shock reached Pioneer 10 at 1206 UT on August 6. The arrival of the shock at the Earth on August 4 (0221 UT) was marked by a geomagnetic SSC and was detected by the Prognoz - 2 satellite (Tamnyi et al, 1973). At the Earth the velocity jumped from 420 to 600 km sec^{-1} and was followed by a region of enhanced density (N_p increased from 5 to 36 cm^{-3}).

The average propagation speed between the Sun and other detectors can be estimated as in the previous section. Figure 5.13 shows the average velocities between pairs of detectors and the instantanteous shock velocity at Pioneer 9 and Prognoz - 2. Mihalov et al (1973) were able to calculate a

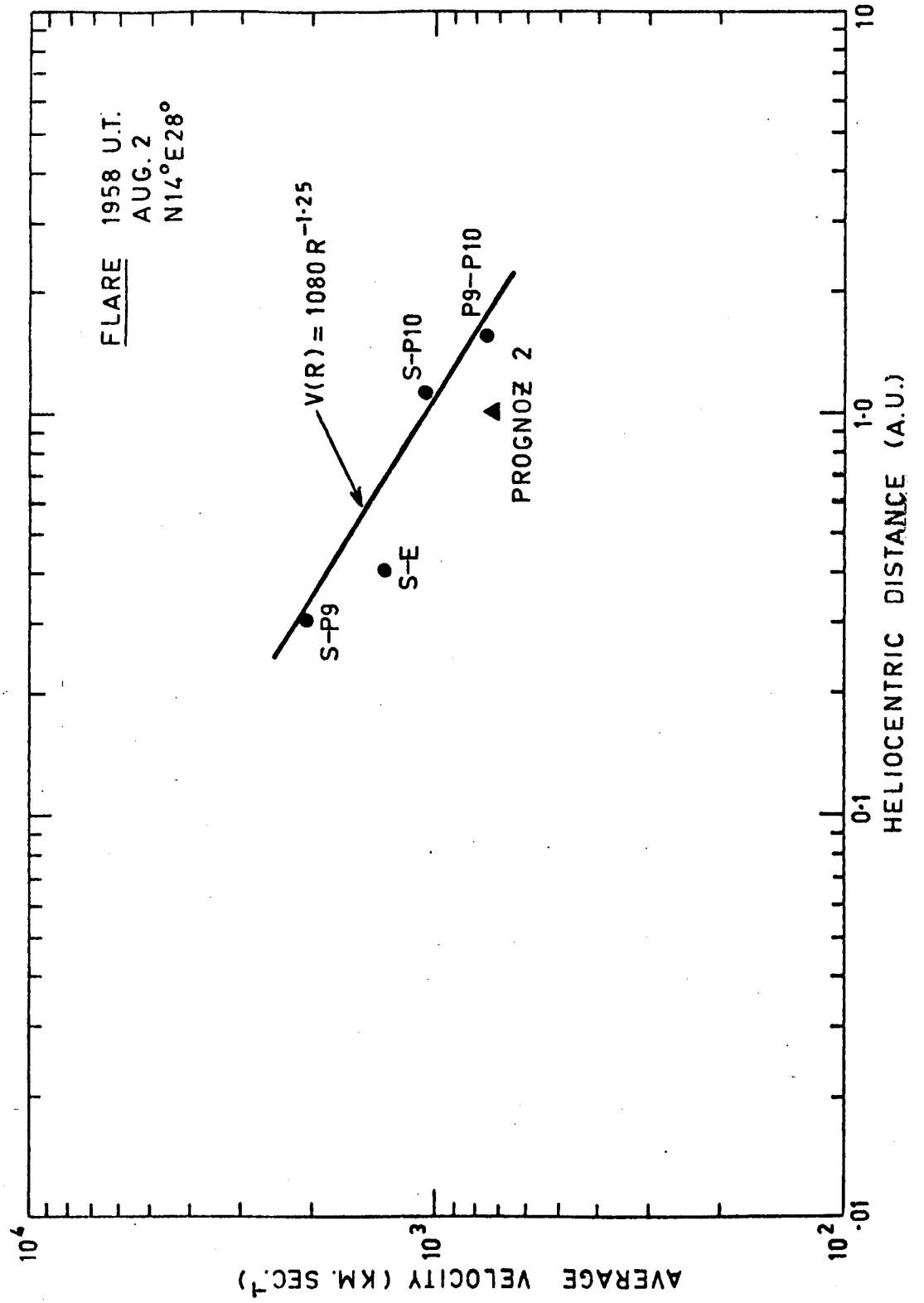

FIGURE 5.13 Velocity of the shock wave as a function of heliocentric distance.

shock normal from the original Pioneer 9 data and found that it was within 4^0 of the radial direction. The straight line fitted to the Pioneer 9 and Pioneer 10 data (in the normal direction from the flare site) has a value $\beta = -0.75$, which similarity theory would suggest was a decelerating blast wave. This is rather surprising in views of the large amount of material behind the shock front. It may be that the material seen in the large density enhancement was all plasma swept-up from the ambient medium and that there was very little plasma actually ejected from the flare region. As can be seen in Figure 5.13 the average speed between the Sun and Earth is considerably lower than between the Sun and Pioneer 9. This implies that the propagation speed of the shock is greater in the normal direction from the flare site than it is at angles away from the normal, suggesting a nonspherical shape for the shock front. Although the scintillation data are limited in their detail comparison with the models discussed in Section 5.6 shows that they are consistent with the theoretical models of De Young and Hundhausen (1971) for plasma ejection into a cone of 60^0 half-angle (see Figure 1.11). The scintillation observations also show that this event extended well out of the ecliptic on both sides, covering at least 60^0 in heliocentric latitude.

The period August 5-6 was marked by an almost total lack of scintillation due to the abnormally low plasma densities. The passage of a shock wave through the interplanetary medium "sweeps up" the ambient plasma and pushes it ahead of the shock leaving a rarefaction in the medium behind the disturbance. While this is a well-observed feature of such disturbances the degree of rarefaction in this event is larger than has ever been observed in previous events.

There is however evidence for a fresh shock injection into the interplanetary medium during this time. A major flare occurred at 0634 UT

(3B, N14^{0}E08^0) on August 4 and showed oscillation of a filament, which Zirin and Tanaka (1973) suggest implied an MHD shock wave with velocity ~1000 km sec^{-1} and types II and IV radio emission. A shock was detected at Pioneer 9 on August 4 (2323 UT), at Earth on August 4 (2054 UT) and at Pioneer 10 on August 9 (1526 UT). The shock front was associated with a large velocity increase but negligible density enhancement. The average transit times for this event show that it had a very high propagation speed through the medium, presumably because it met little resistance to its motion as a consequence of the low densities. Again it showed evidence of non-spherical symmetry, with the average velocity between the Sun and Earth being considerably larger than between the Sun and Pioneer 9. In view of the low level of scintillation and the high shock speed it is not surprising that none of the scintillation observations recorded details of this event.

The largest flare of the period occurred at 1449 UT on August 7 (3B, N14W37). This flare also showed signs of MHD wave propagation in the corona with V ~ 600 km sec^{-1} (Zirin and Tanaka, 1973) and was associated with both types II and IV radio bursts. The IPS and spacecraft observations reveal the existence of a second major disturbance in the interplanetary medium on August 8 or 9 associated with the August 7 flare. Again the scintillation and spacecraft observations are consistent with a disturbance which propagated over a wide portion of the medium with a higher velocity in the direction normal to the flare site than at angles away from it.

The velocity derived from the type II burst close to the Sun was ~1500 km sec^{-1} (Maxwell and Rinehart, 1974). The type II burst was also detected at low frequencies by a spacecraft receiver (Malitson et al, 1973). Radio emission from the shock was first detected at a frequency of 2.6MHz at 1554 UT on August 7 and its progress was followed down to a frequency of 0.03MHz at 2300 UT on August 8. It was deduced that the shock was travelling at an average velocity of 1270 km sec^{-1} and that the velocity remained

approximately constant from 0.005 to 1AU. The average velocities derived from spacecraft and SSC times are shown in Figure 5.14. Again it would appear that the disturbance propagated at different speeds in different directions. The observed variations in velocities shown in Figure 5.14 suggest that the shock propagated into the medium at approximately constant speed before decelerating. Possible shapes for the disturbances of August 2 and August 7 are shown in Figure 5.15. These have been based on a comparison of the scintillation and spacecraft data with the models discussed in Section 5.6.

5.4 JUNE 1969

A group of 14 scintillating sources were observed at Culgoora during June 1969 and an interpretation of the results has been presented by Wiseman and Dennison (1972) and Wiseman (1972). The original data has been re-analyzed to correct several errors in the original computer program and to improve the statistical errors in the measurement of the scintillation index as discussed in Chapter 4. This re-analysis resulted in only a minor correction to most indices, although a few were changed by a large amount, and the basic picture available from the scintillation data is not significantly altered from that discussed by Wiseman and Dennison (1972). However, a considerable amount of spacecraft data has become available since the original analysis and a detailed discussion of this event will be given.

The projection of the lines of sight to the sources on to the ecliptic plane is shown in Figure 5.6 and the daily values of the scintillation indices and power spectra second moments are shown in Figures 5.17 and 5.18. The most significant feature in these variations is the large increase in scintillation index shown by most sources on June 7 and 8. As with the events discussed previously the rapid rate at which the sources were affected implies a transient, rather than corotating, disturbance. Two other features of interest are the sequential changes in index during the periods June 10-14 and

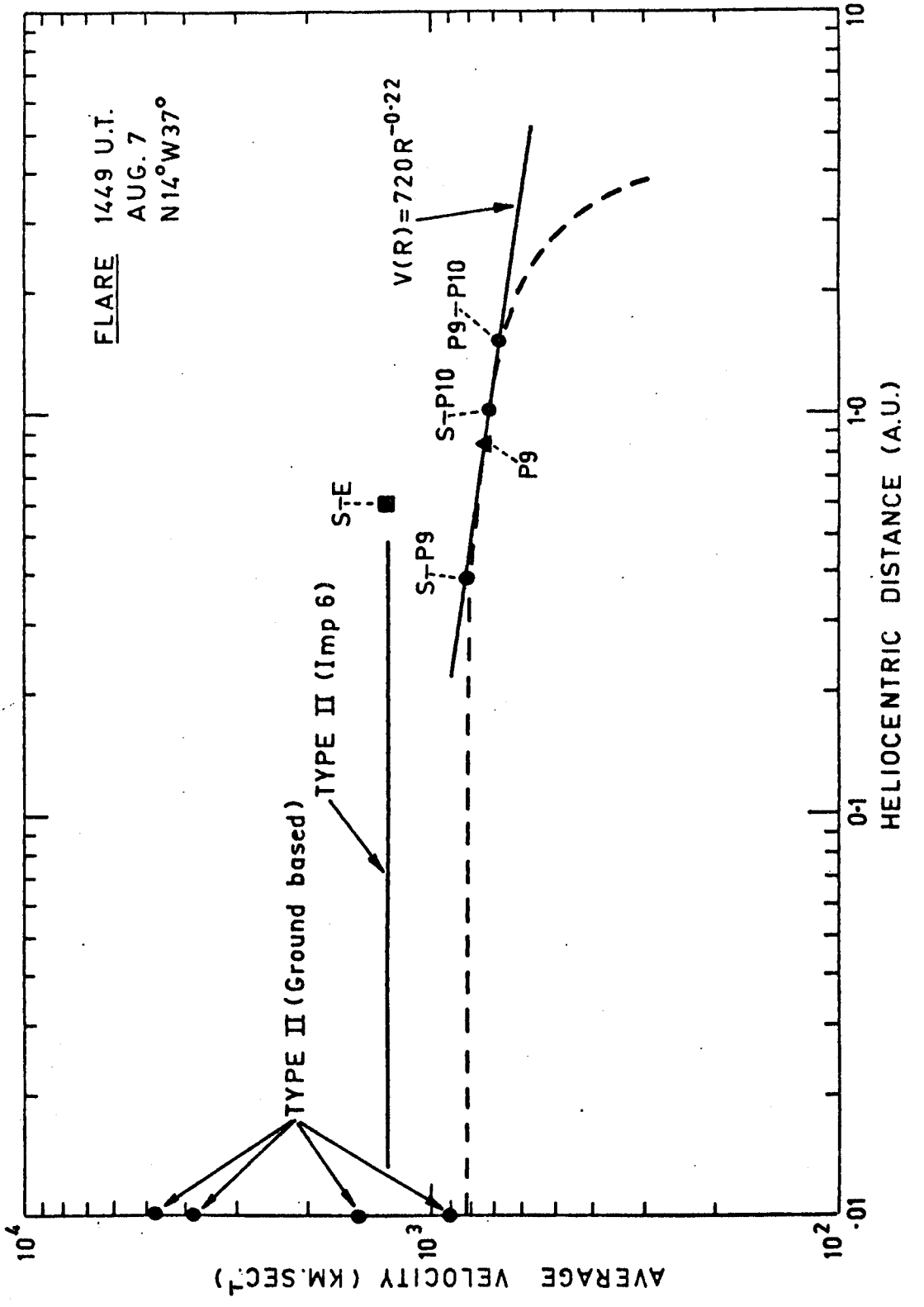

FIGURE 5.14 Velocity of the shock wave as a function of heliocentric distance.

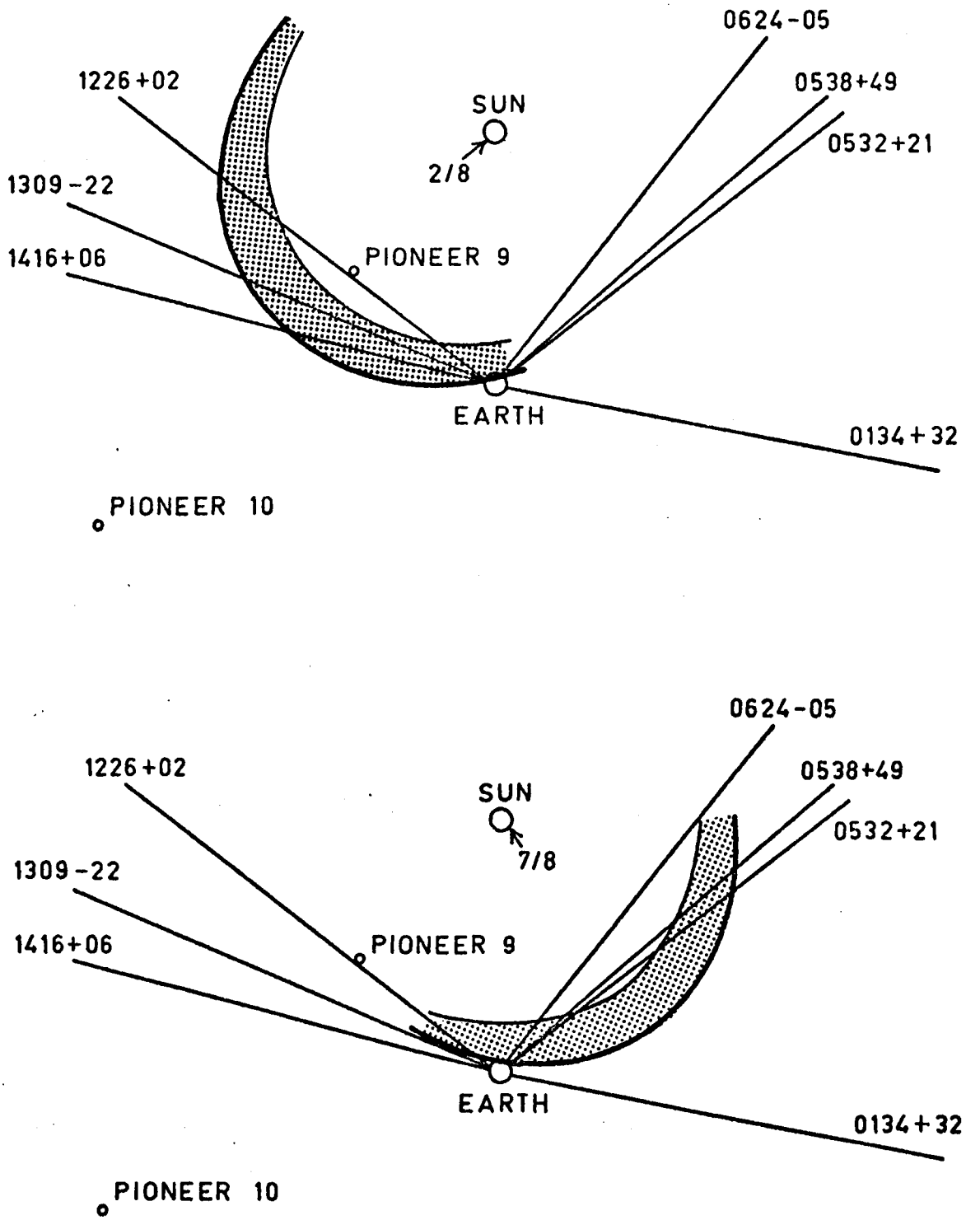

FIGURE 5.15 Estimated shapes of the disturbances during August 1972. The solar longitude of the flares responsible for the events are marked by arrows.

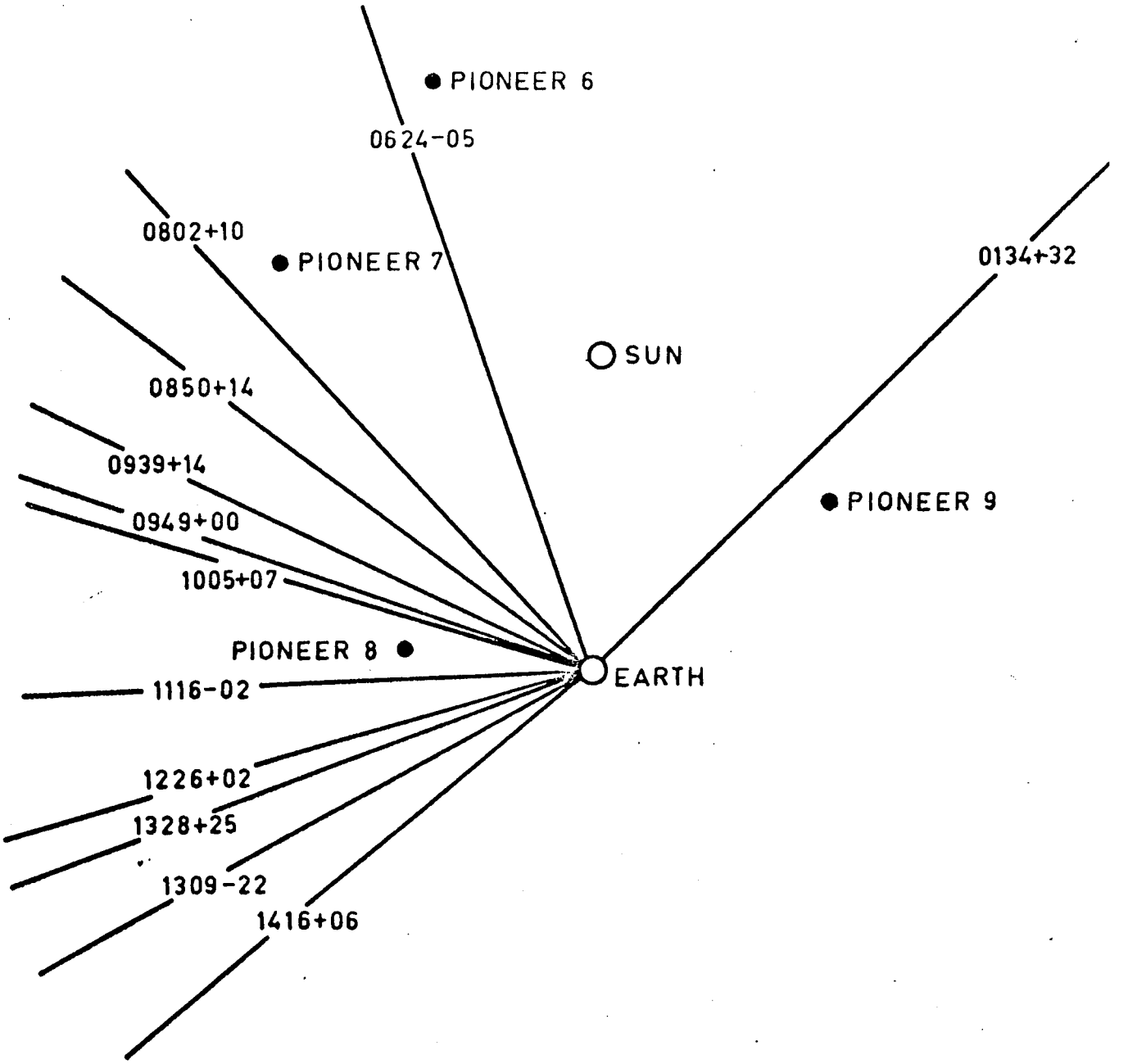

FIGURE 5.16 Ecliptic plane projection of the line of sight to each of the sources during June 1969.

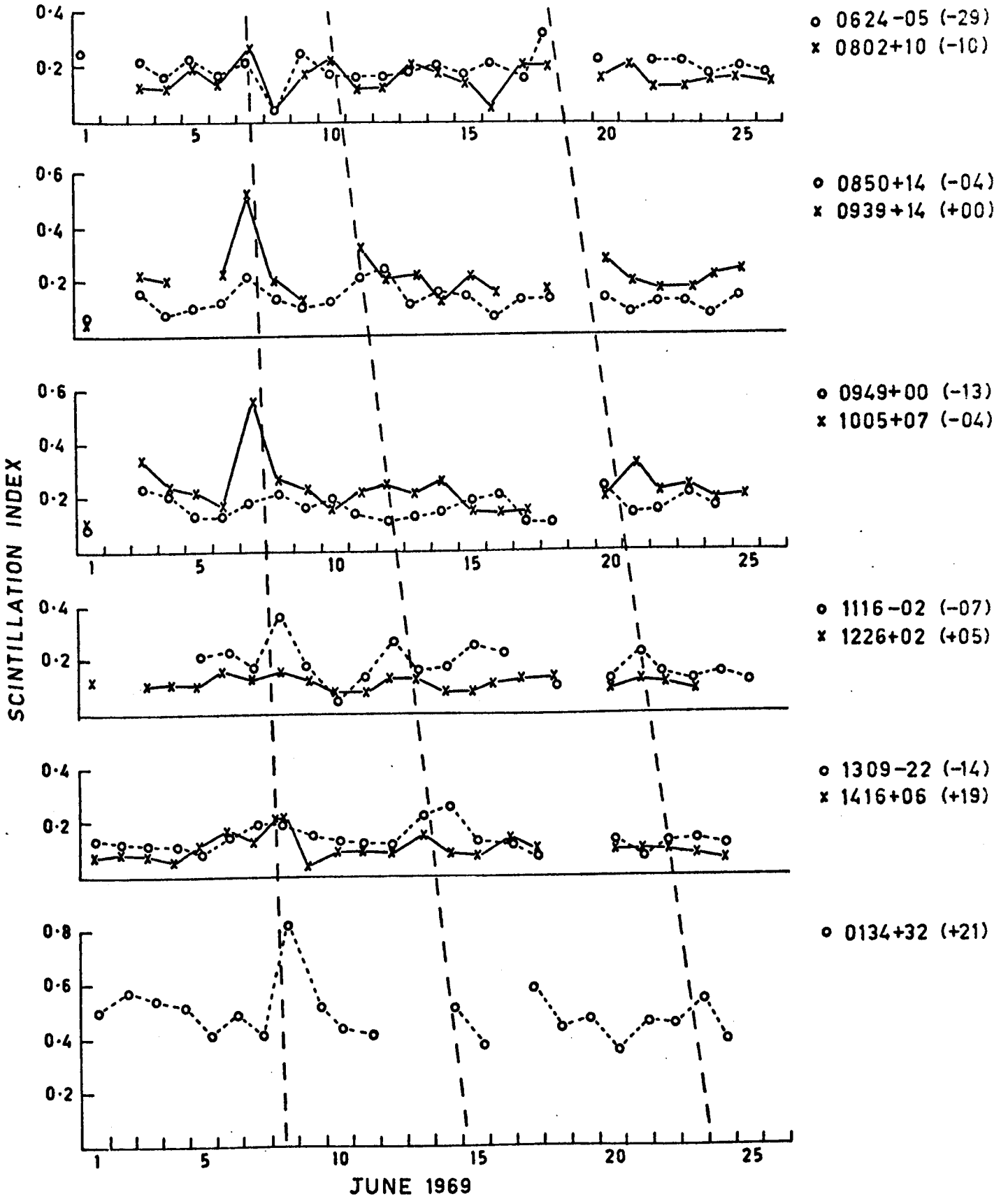

FIGURE 5.17 Scintillation indices during June 1969

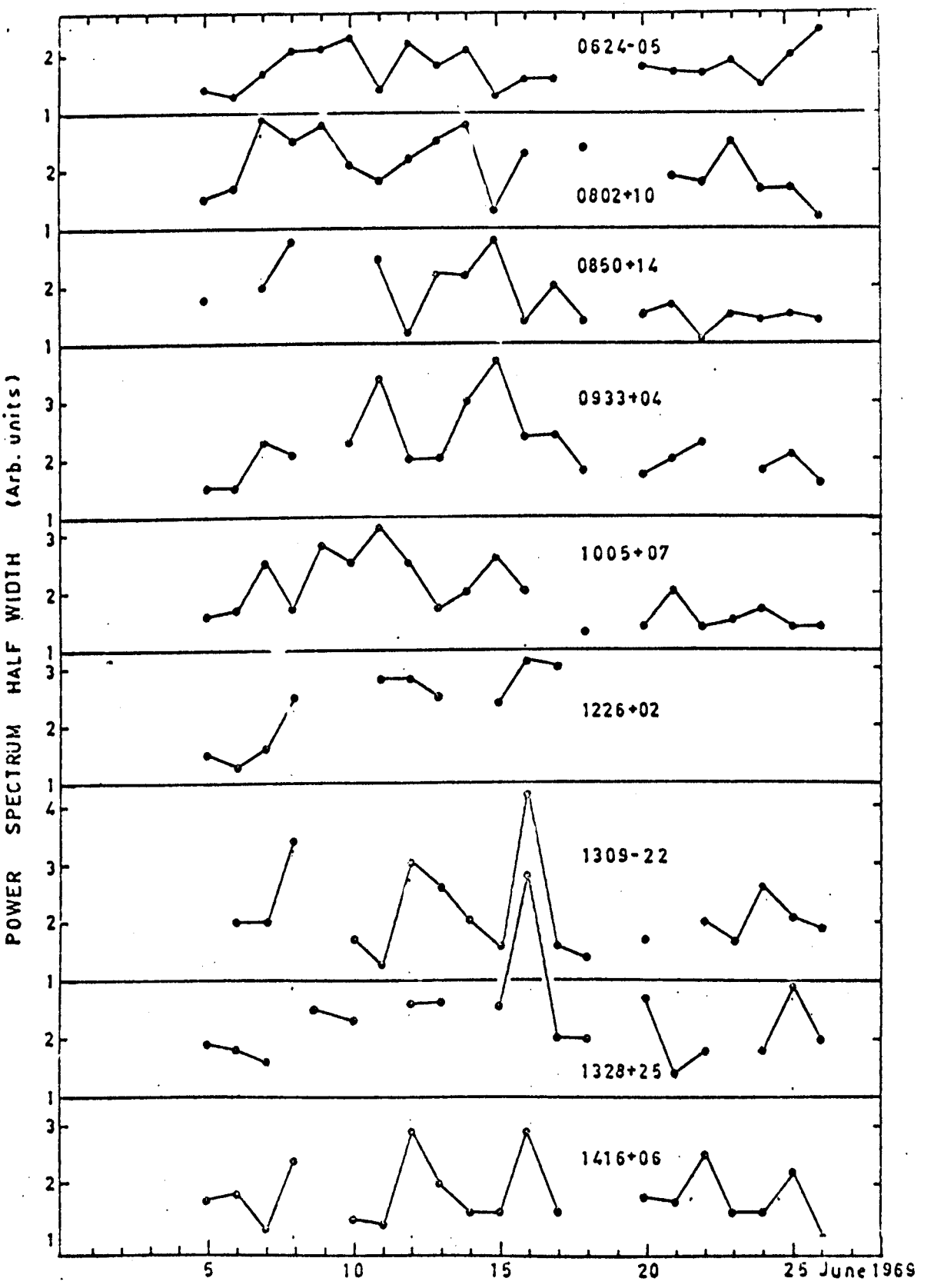

FIGURE 5.18 Width of Power Spectrum during June 1969

June 19-23. These two disturbances take a longer period to affect the range of sources and behave in a manner expected for a corotating disturbance.

The major active region on the visible disk during this period was McMath region 10134. This region was particularly active on June 5 producing several major flares between 0930 and 1700 UT. Of these a 3B flare which occurred at 0953 UT (location $N12^{0}E63^{0}$) is of particular interest since its flash phase features included a high velocity dark surge and sudden filament activation, a large group of type III bursts and microwave and x-ray bursts. A type II radio burst was observed between 0955 and 1014 UT and a type IV burst between 0954 and 1025 UT (Solar Geophysical Data # 300 - I) Thus this flare had the characteristics indicative of a sudden particle acceleration during the flash phase, with the subsequent generation and propagation of a shock wave through the chromosphere and corona. The type II burst was later observed further out in space at low frequencies (Stone and Fainberg, 1974) superimposed on a type III burst originating in the same active region at 1416 UT the same day. The shock velocity in the lower corona (deduced from a spectrum supplied by Dr H. Ubarz and assuming a 2x Newkirk active streamer density model) is ~1200 km sec^{-1} and that deduced from the low frequency burst drift rate (Figure 2 of Fainberg and Stone, 1972) was ~1150 km sec^{-1}.

Figure 5.19 combines the available spacecraft data for this period. The locations of the Pioneer spacecraft were shown in Figure 5.16; Vela 3 was in geocentric orbit and Explorer 35 in lunar orbit. The disturbance arrived at Pioneers 6 and 7 on or before 1500 UT June 7, as revealed by the high solar wind velocities on that date. Its arrival at Pioneer 8 was marked by a large increase in the magnetic field intensity and at Explorer 35 by a smaller increase in the field. The arrival at the Earth was marked by a geomagnetic sudden commencement and a solar wind velocity increase at Vela 3.

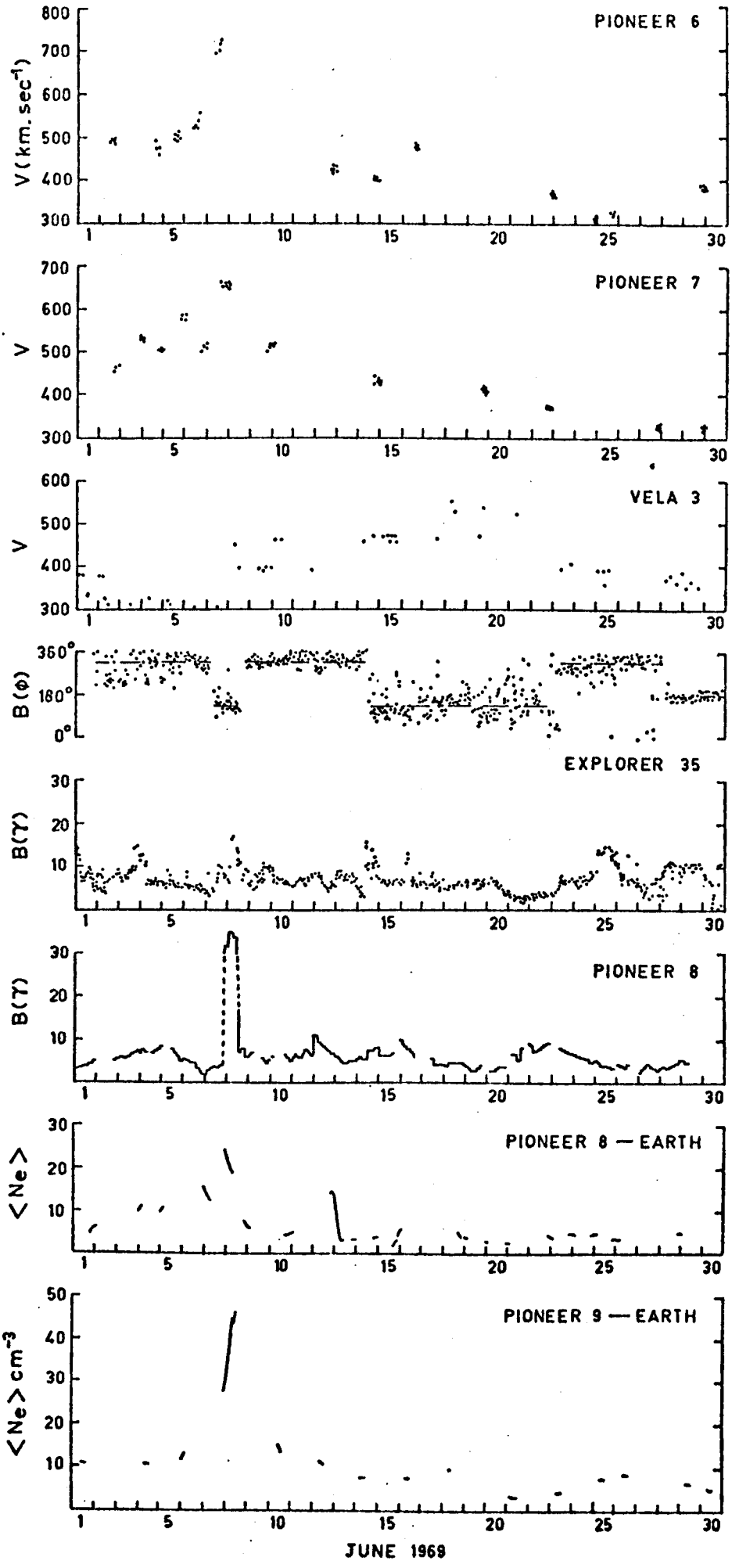

FIGURE 5.19 Spacecraft measurements of solar wind parameters during June 1969.

Also shown in Figure 5.19 is the average electron density along the path from Pioneer's 8 and 9 to the Earth, determined by the Stanford dual-frequency radio propagation experiment (Croft, 1971).

By the time it had reached 1AU the disturbance had extended over approximately 180^0 in the ecliptic plane, ranging from Pioneer 6 around to the paths to source 0134+32 and Pioneer 9. Although it covered a very large area it was clearly not spherically symmetric. The average propagation speed from the Sun to Pioneer 6 was $\gtrsim$ 780 km sec^{-1}, to Pioneer 7 ~820 km sec^{-1}, to Pioneer 8 ~700 km sec^{-1}, and to the Earth ~620 km sec^{-1}. This is also shown by the fact that sources from 0624-05 around to 1005+07 were affected during June 7, the Pioneer 8 - Earth electron content and sources 1116-02 to 1416+06 were affected early on June 8, and source 0134+32 and the Pioneer 9 - Earch electron content were affected late on June 8. This pattern suggests that shock propagation was fastest in the normal direction from the flare-site, and was faster to the east of this direction than to the west.

During 1969, the sector structure was very stable throughout the year and as a result it is possible to estimate the location of the sector boundaries on any given day with a fair degree of accuracy. Figure 5.20 shows the sector pattern on June 6 interpolated from the data of Wilcox and Colburn (1971). The spiral angle shown is based on the assumption that the solar wind velocity in the vicinity of the boundary was ~550 km sec^{-1}. This interpolated position of the boundary is consistent with the fact that Pioneer 7 recorded an enhanced velocity early on June 6, presumably indicating the high speed plasma stream associated with the boundary. The two boundaries rotated past the Earth on June 14 and June 22-23 as can be seen from the change in the Explorer 35 $B(\phi)$ data in Figure 5.20.

There is some evidence to suggest that solar wind velocities in the vicinity of the 'away' sector were somewhat higher than those near the centre of the large 'toward' sector. The Pioneer 6 and 7 measurements tend

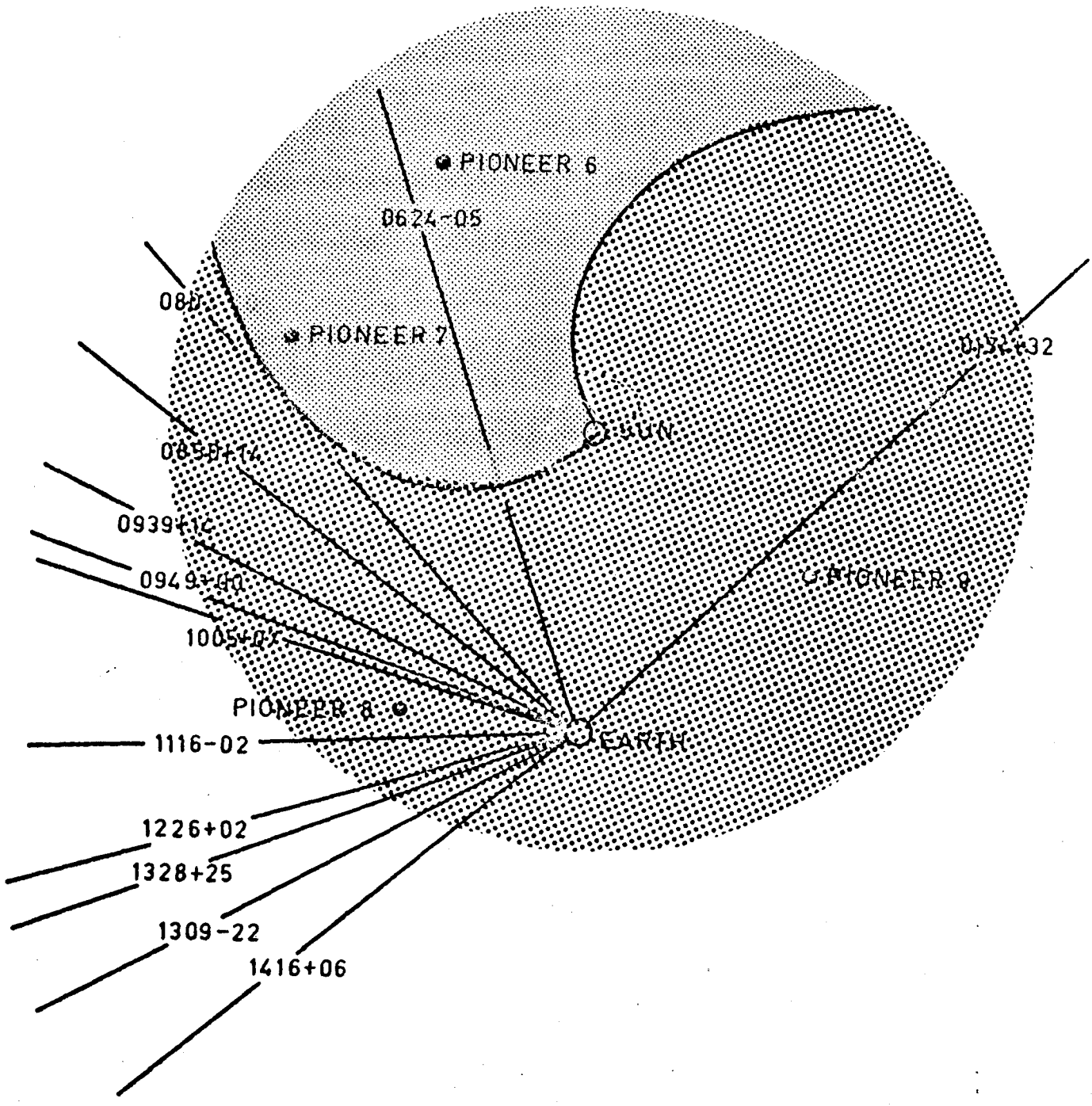

FIGURE 5.20 Sector structure of the interplanetary magnetic field on June 6, 1969.

Positions of the sector boundaries at 1 AU are interpolated from the data of Wilcox and Colburn (1971) and the spiral shapes shown assume $V \sim 550$ km sec^{-1} in the vicinity of the boundary.

to be ~500 km sec^{-1} during early June and appear to be generally $\lesssim$ 400 km sec^{-1} later in the month. This pattern also appeared to exist at Pioneer 6 on the previous and subsequent solar rotations. Also the Vela 3 data tends to be higher during the period June 10-22, when the Earth was embedded in the 'away' sector, than at other times during the month (except, of course, the period June 8-10 following the flare-produced disturbance). This non-homogeneous velocity distribution in the ambient medium probably accounts for the observed shape of the disturbance front since the theoretical studies of Hirshberg et al (1974) showed that the shock front propagates most rapidly in regions of high ambient solar wind velocity. In the previous cases we found that the disturbance propagated fastest in the normal direction from the flare site. In this case we could expect this pattern to be modified by a tendency for faster propagation to the east of the normal, into the 'away' sector, than to the west, as has in fact been observed Figure 5.21 shows an approximate shape for the disturbance which would be consistent with the scintillation and spacecraft data.

As was noted previously, the scintillation data suggests the existence of two corotating streams later in the month. These are clearly associated with the two sector boundaries. The first of these crossed Pioneer 7 on June 5, Pioneer 8 on June 12 and the Earth (Explorer 35) on Jun e 14. The effects of this boundary can be seen in the scintillation of sources to the east of the Sun, as well as the Pioneer 8 - Earth electron content, before June 14 and on source 0134+32 on June 15. The second boundary passed Pioneer 8 on June 20 and the Earth on June 22-23. This boundary was not as clearly definable as the earlier boundary in either the scintillation or spacecraft data. The general features of these corotating disturbances are in agreement with those found by Houminer and Hewish (1972) and provide evidence that their

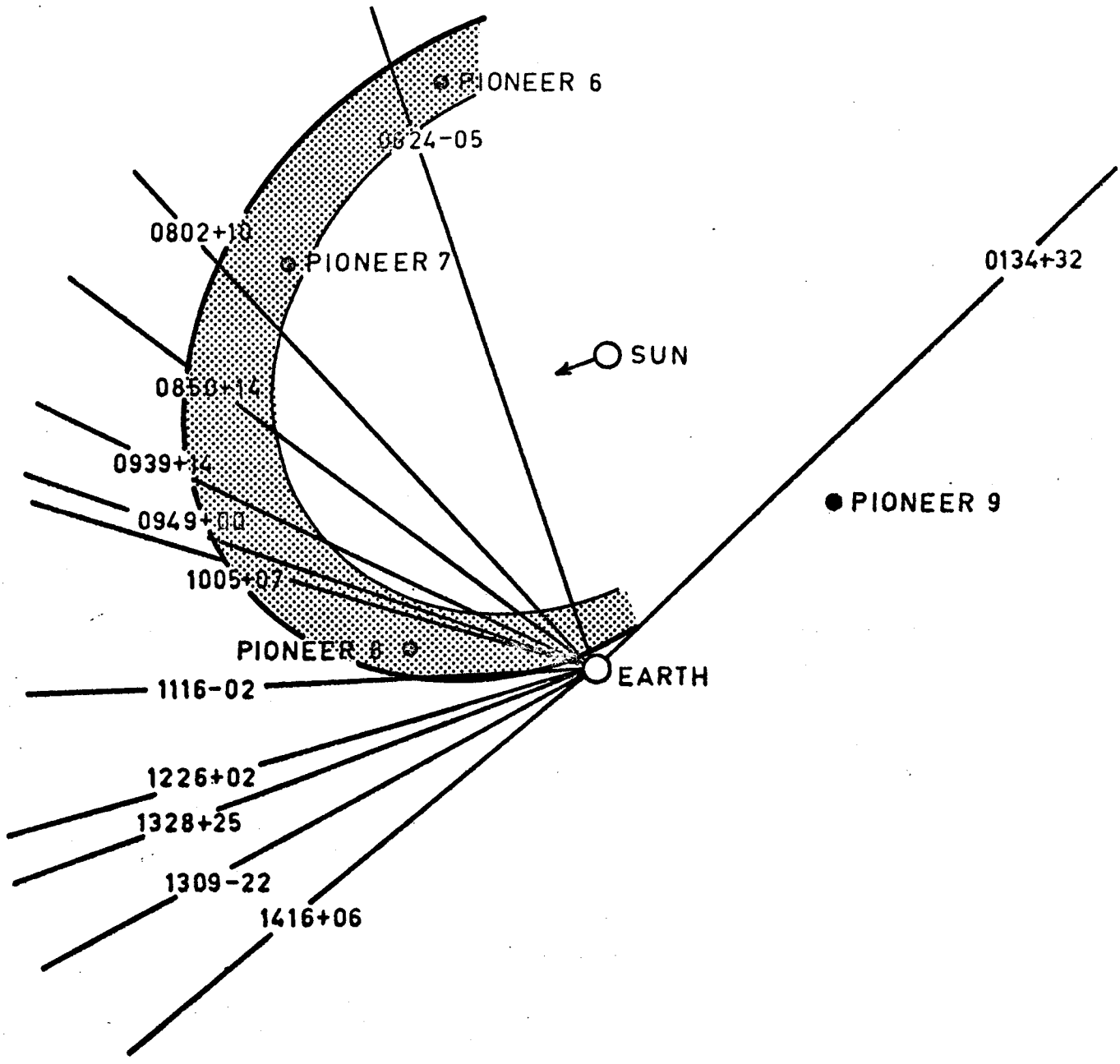

FIGURE 5.21 Approximate shape of the disturbance near 1 AU as inferred from the scintillation and spacecraft data. The solar longitude of the flare is indicated by the arrow.

suggestion that the corotating streams they observed are in fact associated, at least in some cases, with magnetic sector boundaries, is correct.

5.5 JUNE 1970

80MHz data from Culgoora is available for a similar group of 14 sources during June 1970. Figures 5.22 to 5.24 shows the source positions and daily variations in the scintillation indices and power spectral widths. Although less distinct than the previous examples there are three separate events within this data, one transient and two corotating.

The transient event can be seen in the effect on the scintillation indices for sources on June 16-17. As in the previous events it is possible to find a flare in a major active region (McMath region 10789) which shows signs of a sudden flash phase with subsequent propagation of a shock wave through the corona. This flare started at 1322 UT June 14 (importance , location N21E42) and its optical features included sudden activation or disruption of a filament and a high velocity dark surge. The flash phase was associated with emission of multiple type III bursts and large microwave and x-ray bursts. A type II burst occurred between 1324-1344 UT and a type IV burst between 1338-1425 UT. This flare was the only event during this period which possessed all of these features.

Spacecraft data for this event is limited to density and velocity measurements from Pioneer 6 and average electron content measurements between Pioneer 8 - Earth and Pioneer 9 - Earth (Croft, 1971) shown in Figure 5.25. The shock was detected at Earth (SSC) at 0750 UT on June 17 and with the magnetometer experiment on Explorer 41. Chao and Lepping (1974) have included this event in a list of spacecraft-derived shock normals determined from the Explorer 41 data. The shock normal ($\theta_s = -18^0$, $\phi_s = 167^0$) was within 13^0 of the radial and was tilted only slightly south of the ecliptic, as could be

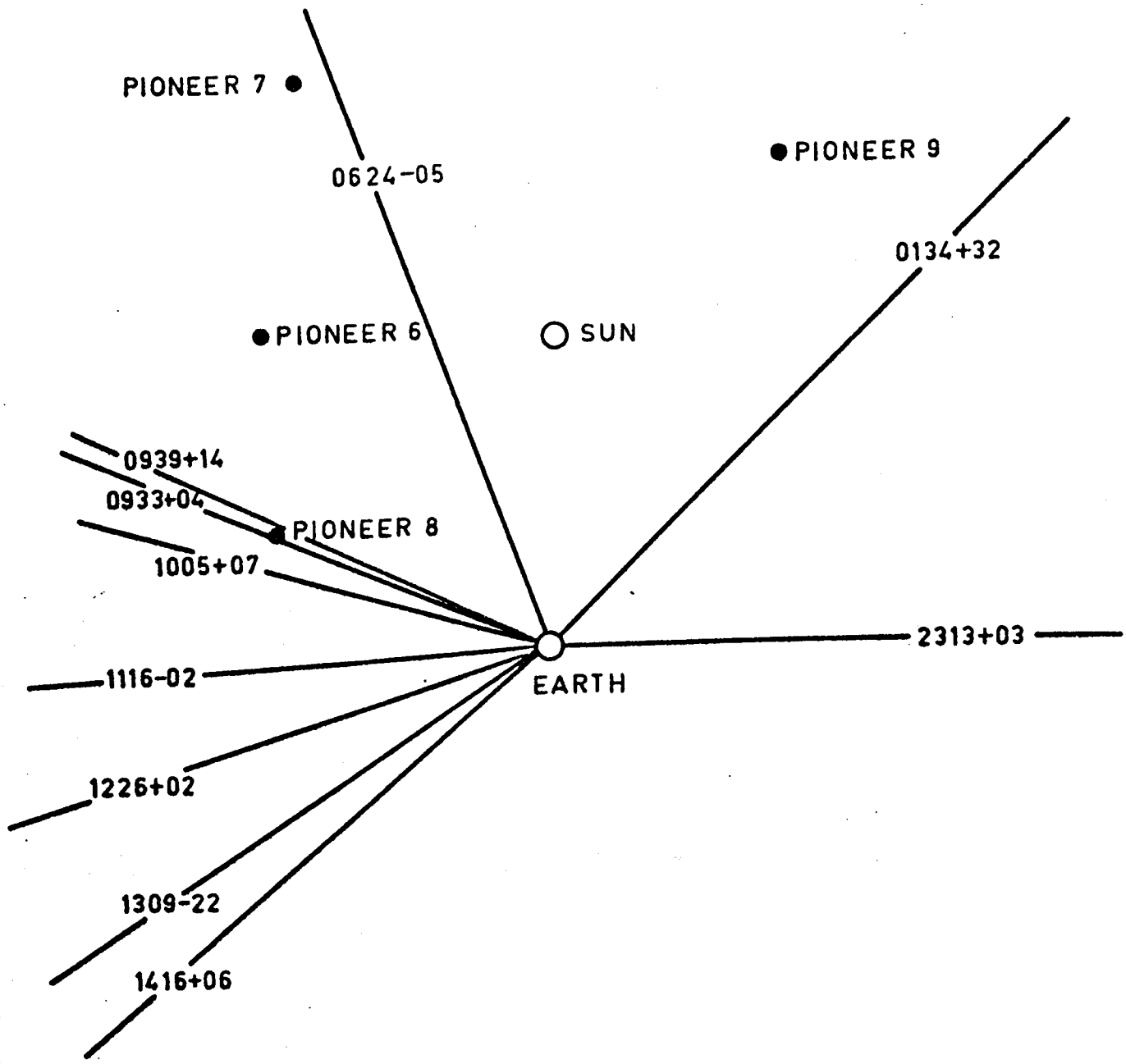

FIGURE 5.22 Ecliptic plane projection of the line of sight to each of the sources during June 1970.

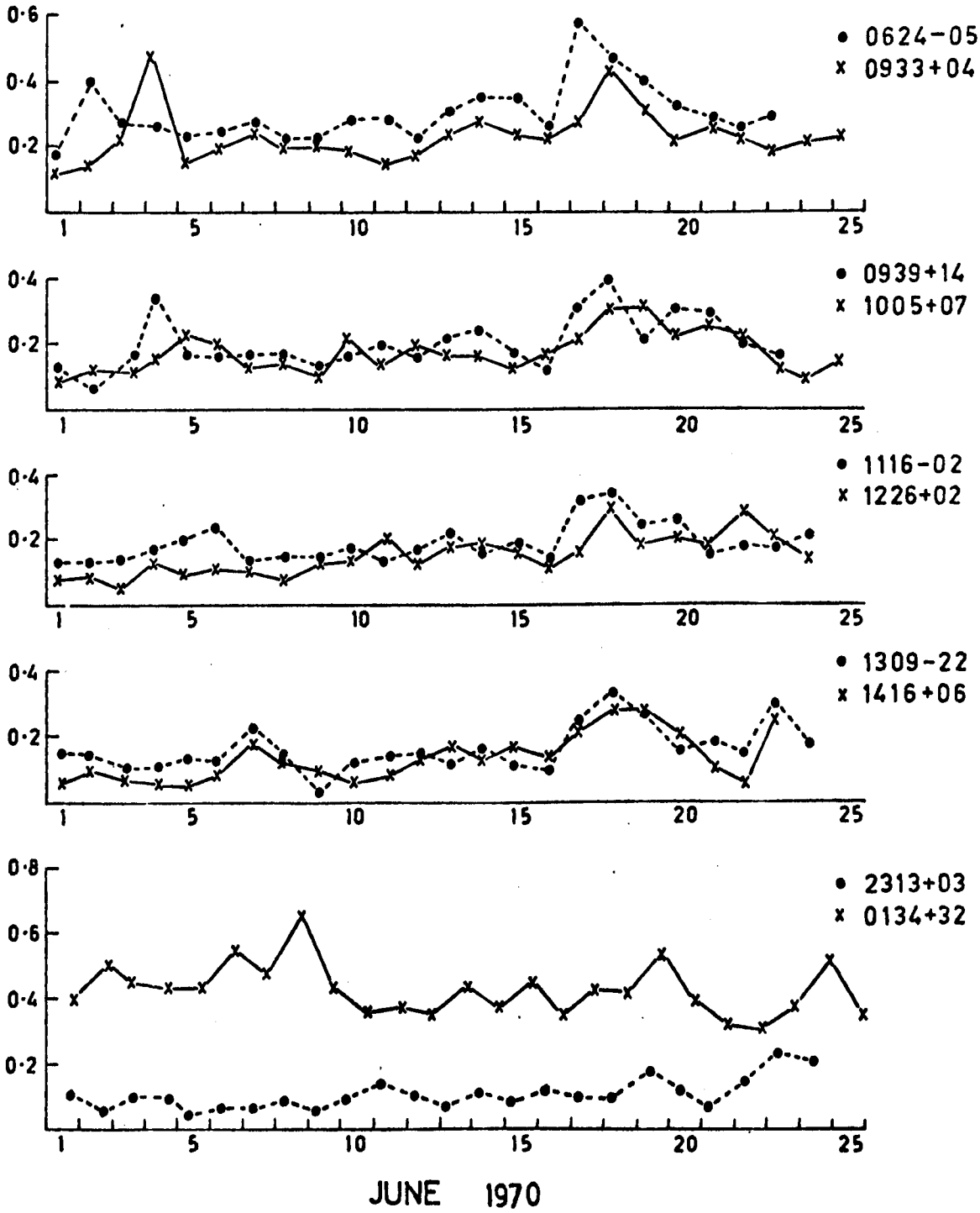

FIGURE 5.23 Scintillation indices during June 1970

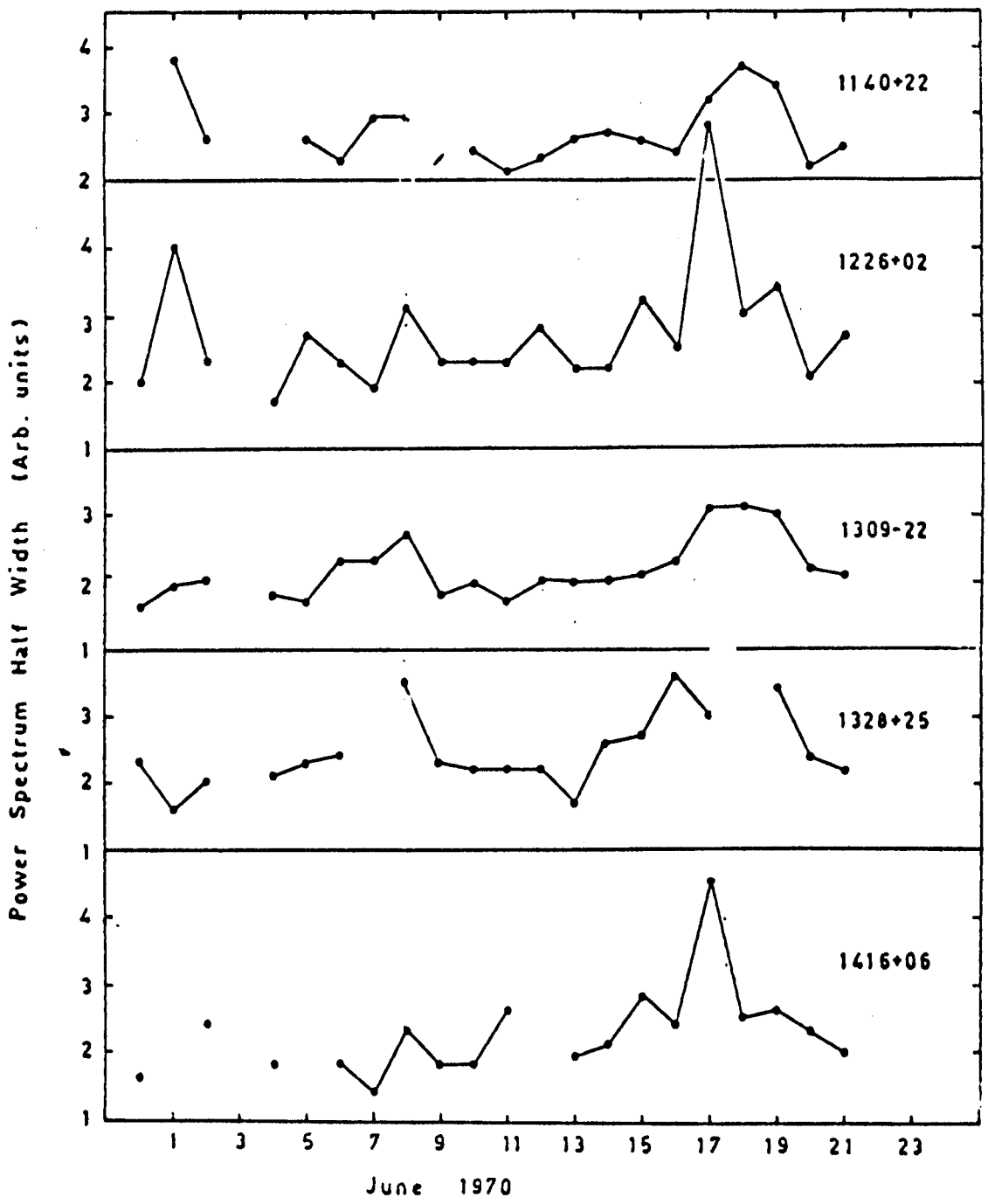

FIGURE 5.24 Width of Power Spectrum during June 1970

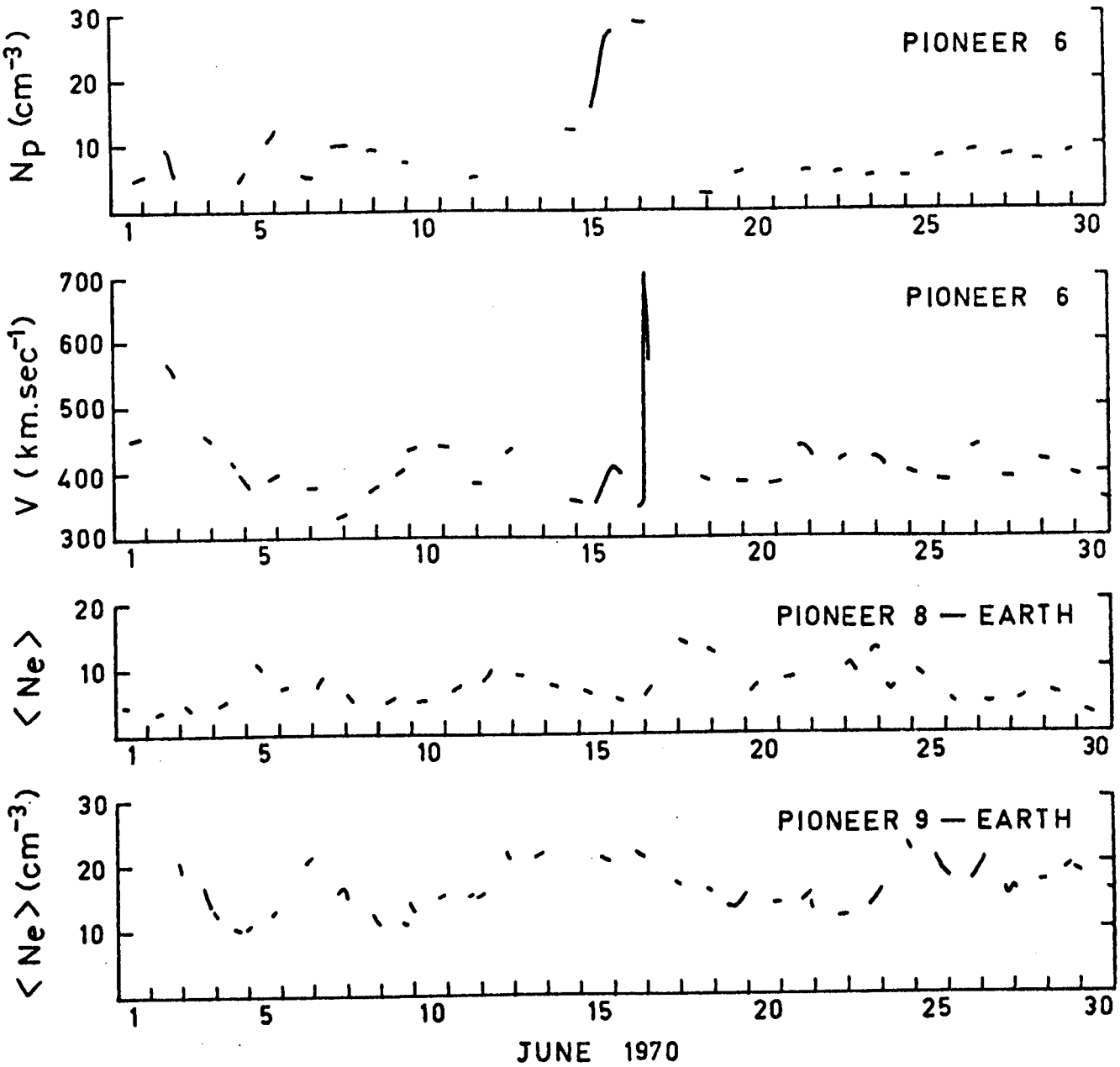

FIGURE 5.25 Spacecraft measurements of the solar wind plasma parameters during June 1970.

expected for a flare origin in the northern hemisphere. This event was typical of the 34 shock normals which they calculated.

The scintillation data and spacecraft-derived shock normal are consistent with a model which is basically similar to those discussed previously, with the disturbance extending over a broad front. The relative weakness of this event makes it difficult to detect the degree of asymmetry in the shape of the shock front but it would appear to be retarded at angles away from the flare normal.

The average propagation speed of the shock between the Sun and Pioneer 6 (0.87 AU) was ~610 km sec^{-1} and between the Sun and Earth ~630 km sec^{-1} These two detectors were both spaced approximately 45^0 away from the direction normal to the flare site. The type II drift rate suggested a velocity ~950 km sec^{-1} near the Sun (2 times Newkirk model) and the instantaneous shock velocity at Explorer 41 (Chao and Lepping, 1974) was ~480 km sec^{-1}. Once again the shock clearly decelerated on its way out from the sun. Since Pioneer 6 is closer to the Sun than the Earth is the average transit speeds noted above suggest that propagation was slightly slower toward Pioneer 6 than toward the Earth.

The interplanetary sector structure for this period can be interpolated from the sector diagrams of Fairfield and Ness (1974) using the method discussed previously. Figure 5.26 shows the interpolated pattern on June 17 with spiral curves calculated for a solar wind velocity of 450 km sec^{-1} and a probable accuracy in position ~$\pm 8^0$. The sector boundary rotated past Pioneer 6 on June 16 and was probably responsible for the enhanced density 24 hours prior to the arrival of the shock. In this instance there was very little velocity enhancement associated with the boundary. This could explain the apparent greater deceleration in the direction of Pioneer 6 since the

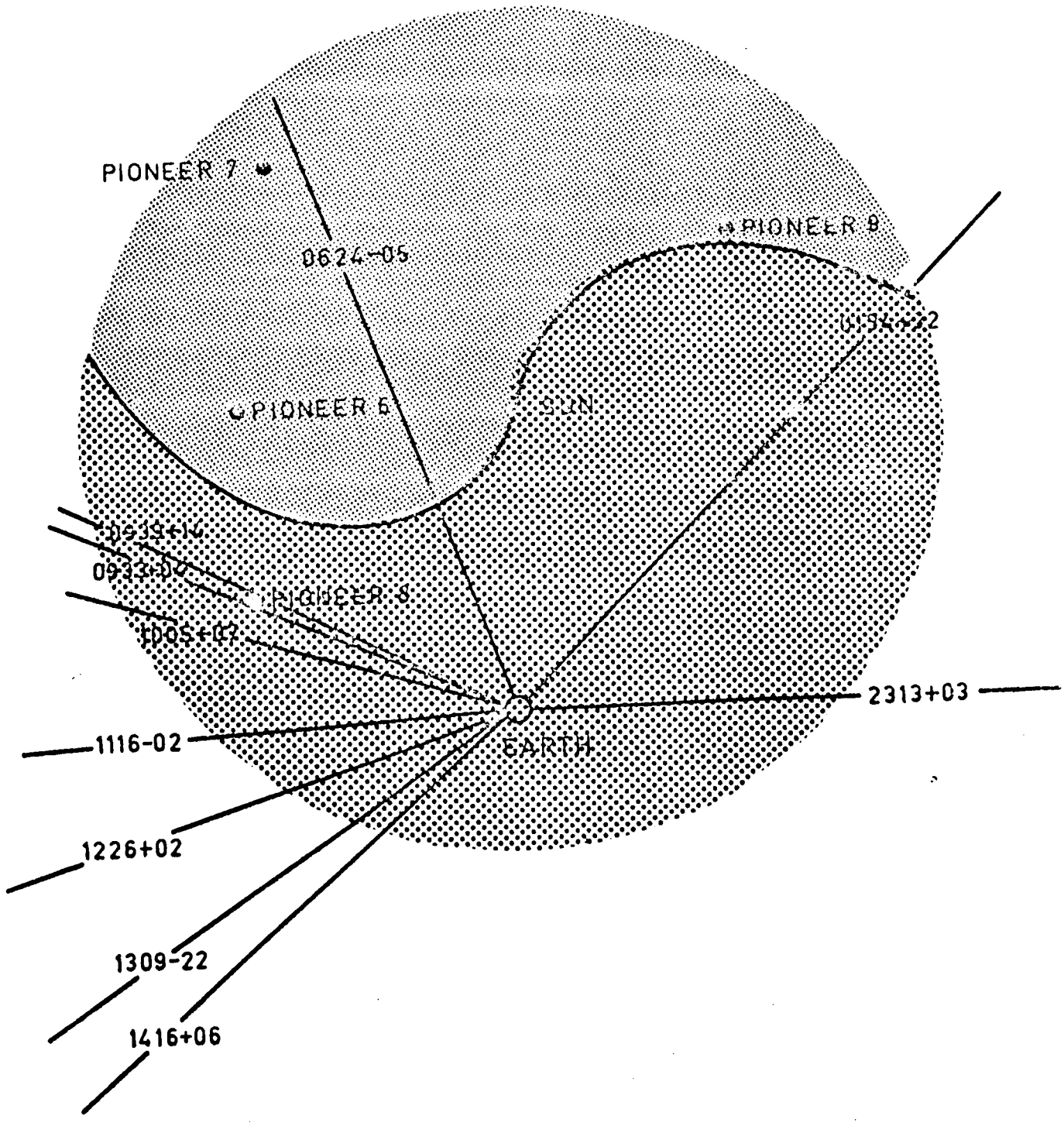

FIGURE 5.26 Sector structure of the interplanetary magnetic field on June 17,1970.

Positions of the sector boundaries at 1 AU are interpolated from the data of Fairfield and Ness (1974). The shapes of the boundaries assume a velocity $\sim$ 450 km sec^{-1} in the vicinity of the boundary.

theoretical models of Hirshberg et al (1974) suggest that the disturbance travels faster in regions of higher than average ambient solar wind speed but is impeded in regions of high ambient density. A possible shape for the disturbance is shown in Figure 5.27.

The sector boundary which in Figure 5.26 is in the vicinity of Pioneer 9 rotated past the Earth on June 7. Its effect on the sources can be seen to start with 0933+04 and 0939+14 on June 5 and 1005+07 on June 6. Sources 1226+02 to 1416+06 were affected early on June 8. These observations are consistent with the existence of a turbulent region behind the leading edge of the boundary. Comparison with the model discussed in Section 5.6 leads to an estimate of the shape of the spiral and consequently the solar wind speed near the boundary. The results are consistent with a velocity ~400-450 km sec^{-1} and a stream ~15^0 wide in the ecliptic plane. As the stream affected both 1309-22 (14^0 south of ecliptic) and 1328+25 (34^0N) in much the same way it was of considerable extent perpendicular to the ecliptic plane.

The second sector boundary rotated past the Earth on June 23 and its effects can be seen on the scintillating sources during the period June 19-24 and on the Pioneer 9 - Earth electron content on June 24-25. This stream was similar in characteristics to that associated with the other sector boundary.

5.6 DISCUSSION

The events discussed in the preceding sections have a number of features in common which will be summarized in this section. In all cases it has been possible to find (in the appropriate time interval) one, and only one, flare possessing most or all of the features which point to a sudden acceleration of plasma during the flash phase e.g. (multiple groups of type III bursts, and large microwave and x-ray bursts) and the subsequent

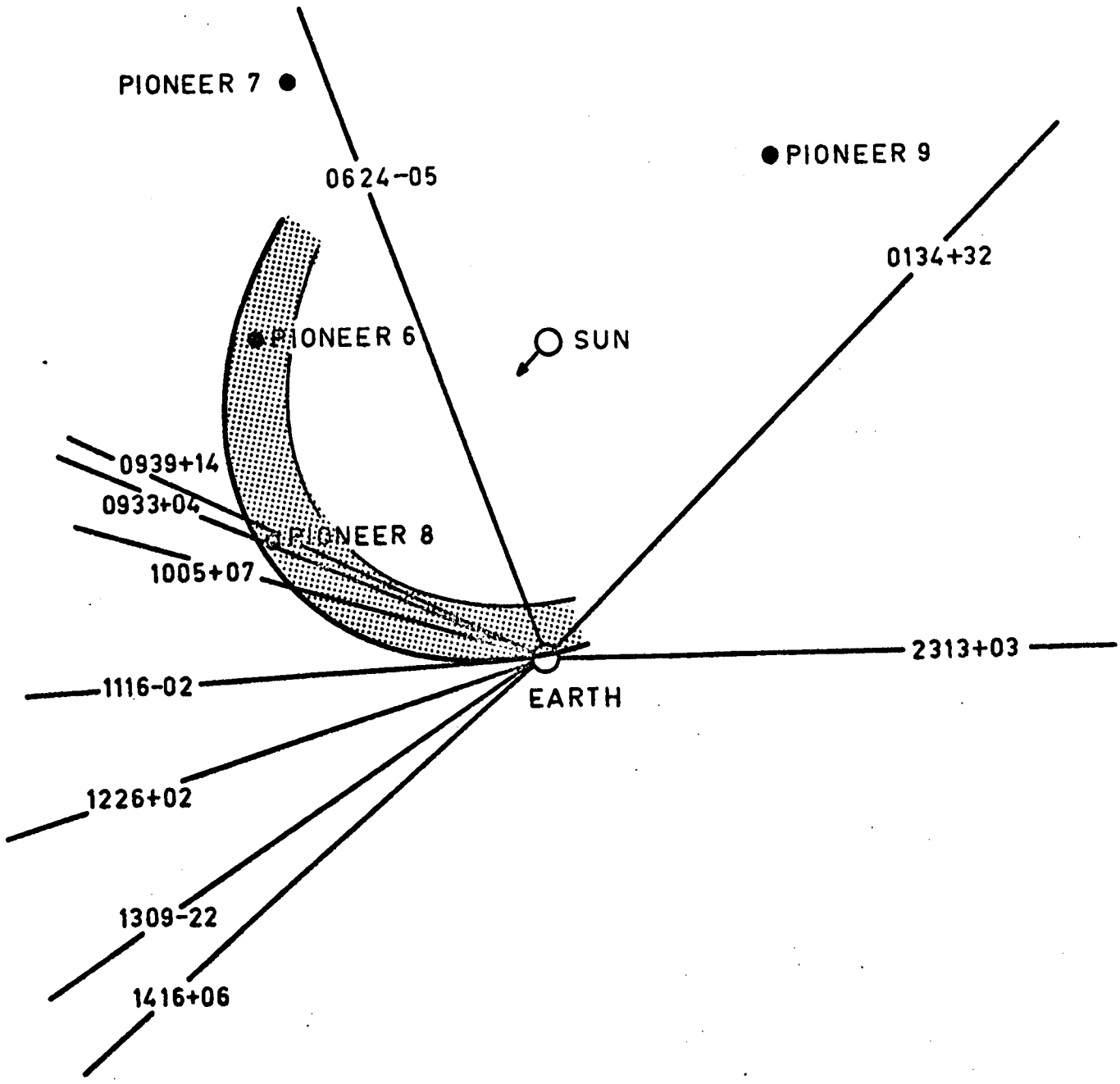

FIGURE 5.27 Estimated shape of the disturbance near 1 AU inferred from the scintillation and spacecraft data. The solar longitude of the parent flare is marked by an arrow.

generation and propagation of an MHD wave in the chromosphere and corona (e.g. oscillating and disrupted filaments, Moreton waves, and type II bursts). Each of these flares also showed signs of injection of energetic material into the corona for some time after the flare, as evidenced by continued activation of filaments and type IV radio bursts. Smerd (private communication) has suggested that late stage noise storms may be more reliable indicators of plasma injection than the type IV bursts. Although each of these events was associated with a type I noise continuum source the spectra available to the author only covered the period of the type II bursts and it is not possible to investigate this suggestion further. Although the individual features noted above are not uncommon, flares which involve all of them are much less frequent. In fact during the periods of observation, including a number of observing sessions in which transient events were not detected, those flares listed in the preceding sections were the only flares possessing all of these features.

The observed scintillation is the integrated effect of scattering occurring along the line of sight to the source. In the ambient medium most of the scattering occurs in a region near the point of closest approach to the sun, as shown in Figure 2.7. In the case of non-stationary perturbations in the ambient medium the exact effect will depend upon the location and properties of the disturbance. A numerical model was developed to investigate this effect. The ambient medium was assumed to be spherically symmetric and to have a velocity which varied with heliocentric distance in the form

$$V(R) = 400\, R^{0.2} \qquad R > 0.14 \text{ AU} \qquad \ldots(5.6)$$

and a mean electron density of the form

$$N(R) = 2.75 \times 10^6 \quad (R-0.95)^{-2.38} \qquad (R \text{ in AU}) \qquad ---(5.7)$$

The rms fluctuation in the ambient electron density was assumed to be 5% of the mean density. The density irregularities were also assumed to possess a Gaussian auto-correlation function with a characteristic scale of the form

$$a(R) = 250R^{1.0} \qquad (R \text{ in AU}) \qquad ---(5.8)$$

Relations (5.6) to (5.8) are based on observational results reviewed in Chapters 1 and 2. The scintillation index was calculated using relations (2.12) and (2.29) for sources with different solar elongations. The contribution of elements of the line of sight to the total scintillation in the model of the ambient medium was similar to the distributions derived from observational data by Redhead (Figure 2.7).

Non-stationary perturbations in the medium were introduced by changing the model parameters over the appropriate region of space. Usually the velocity V, density N and rms fluctuation $\frac{\Delta N}{N}$ were increased in a step-wise fashion within the region of disturbed plasma. A range of disturbance shapes were used, including spherically symmetric models and axially symmetric models based on the shapes derived in the numerical simulations of DeYoung and Hundhausen (1971). The extent of the disturbance in the radial direction was based on observations and at 1AU and numerical models of shade propagation. Figure 5.28 shows the geometry and index varies for a disturbance ejected into a cone of 60^0 half-angle from a solar longitude of 45^0E with $V = 1.5V_{amb}$, $N = 3N_{amb}$, $\frac{\Delta N}{N} = 0.2$ and a radial thickness of 0.1AU. The time scale shown is dependent on the initial energy of the disturbance and is slower than the events discussed in this chapter. The maximum scattering occurs when the disturbance affects a large part of the line of sight, that is, when the line of sight is approximately tangential to the leading edge of the disturbance.

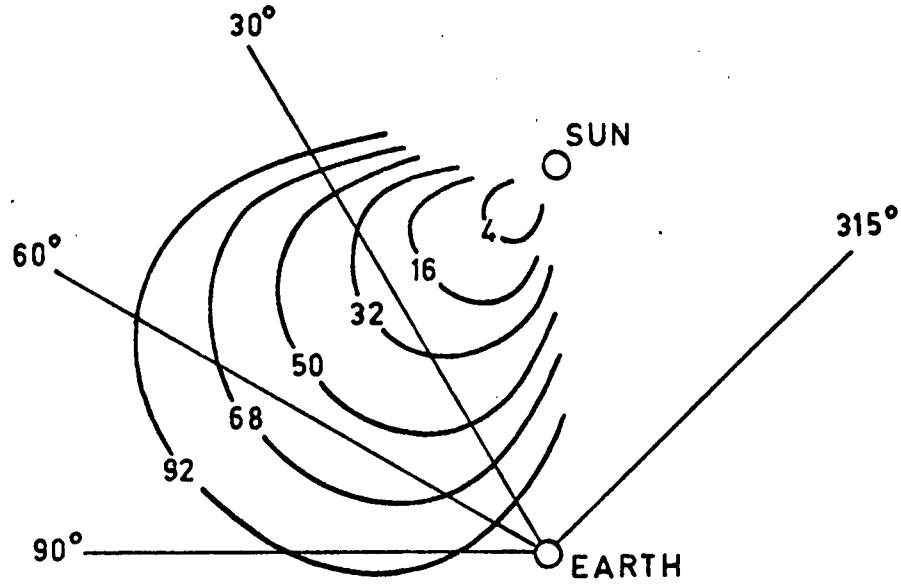

(a) Shape of the shock front as a function of time after initiation

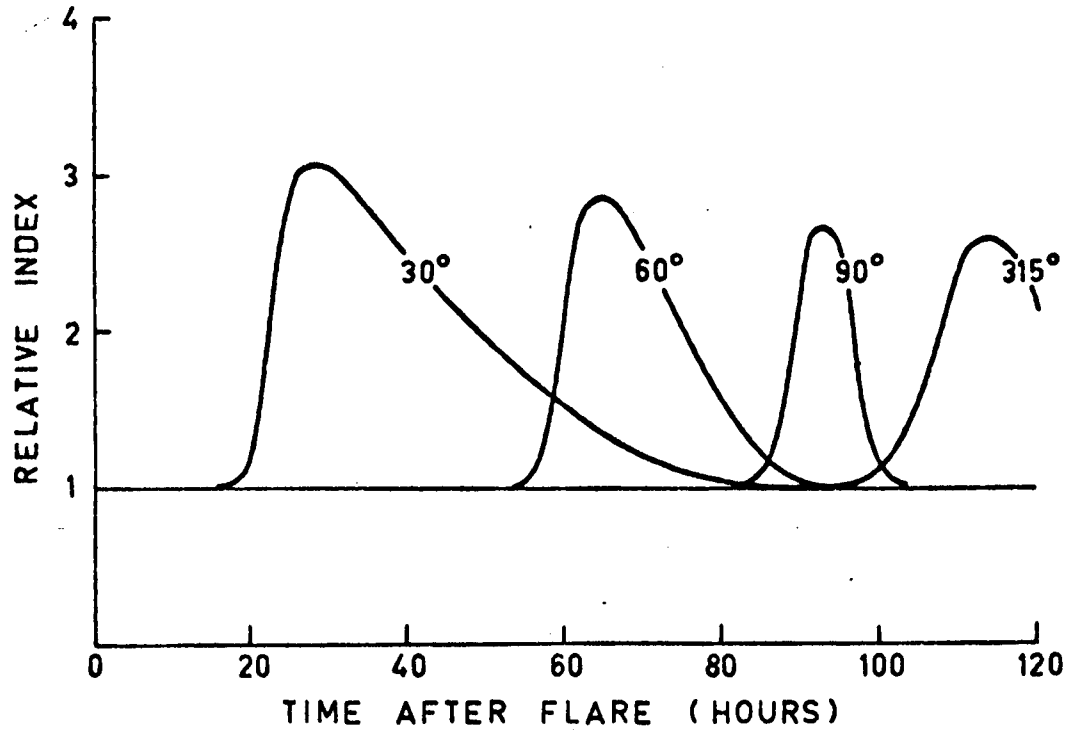

(b) Relative changes in scintillation index as a function of source elongation ε.

FIGURE 5.28 Details of the model used to investigate the effect of transient disturbances on scintillation indices.

In principle it should be possible to determine the shape of the shock front from the changes in scintillation index for sources at various solar elongations. In practice the poor temporal coverage means that at best it is only possible, in combination with spacecraft data, to show that the disturbance is not spherically symmetric and to estimate the degree of non-symmetry.

The disturbance transit time to 1AU can be used to estimate the initial energy injected into the disturbance. Since we have shown that the disturbance is not spherically symmetric we can use the numerical results of De Young and Hundhausen (1973) for asymmetric shock waves. Table 5.2 lists the disturbance energies derived for the two limiting cases, blast-waves and piston-driven shocks. Hundhausen et al (1970) have shown that disturbance energies typically lie in the range 5×10^{30} to 2×10^{32} ergs.

All of the disturbances showed deceleration on their way out from the sun as is usual for such events. The rate of deceleration suggests that some of the events were piston-driven, although at least one appears to have been a blast-wave. These two types of events can also be differentiated on the basis of the post-shock plasma parameters (Hundhausen et al, 1970), but there was insufficient spacecraft data to use this method to check these identifications. The shock velocities in the corona, derived from the type II bursts, were consistently lower than would be predicted by a continuation of the power-law variation at larger heliocentric distances. This would suggest that the disturbance moved away from the sun at approximately constant speed, presumably driven by material ejected as a consequence of continued activity in the flare region, before undergoing deceleration. This certainly appears to be the case in the one event for which a type II burst at low frequencies was observed over a large range of heliocentric distances. This is in conflict with numerical models which suggest that the greatest deceleration occurs

TABLE 5.2 DISTURBANCE ENERGY OF THE FIVE EVENTS

EVENT	TRANSIT TIME TO 1AU (Hours)	ENERGY (ERGS)	
		Blast-wave	Piston-driven
June 5-8 1969	43	1.5×10^{31}	10^{32}
June 14-18 1970	66	2×10^{30}	5×10^{30}
June 15-18 1972	51	6×10^{30}	4×10^{31}
Aug 2-5 1972	30	3×10^{31}	$> 10^{32}$
Aug 7-9 1972	30	3×10^{31}	$> 10^{32}$

close to the sun where the shock velocity and ambient density are higher.

In conclusion, the use of a grid of scintillating radio sources is a valuable addition to spacecraft observations of flare-produced disturbances. Spaced-receiver observations would be a valuable addition to this method since they provide an estimate of the velocity of the disturbed plasma. However, observations at a single location on the Earth are of limited value because the period of observation is only about 15 mins in every 24 hours. Much more comprehensive information could be obtained from a co-operative study using systems at several locations on the Earth to obtain greater resolution in the sequential changes in scintillation. Such a study has been proposed as part of the program for the 'Study of Travelling Interplanetary Phenomena' arranged by SCOSTEP.

CHAPTER 6

PROBABILITY DENSITY FUNCTIONS OF INTERPLANETARY SCINTILLATIONS

6.1 INTRODUCTION

The interpretation of interplanetary scintillation observations has in the past been largely based on the behaviour of the scintillation index and temporal power spectrum of the intensity fluctuations. Only recently have attempts been made to examine the probability density function (p.d.f.) of the intensity fluctuations in a systematic manner. In this chapter we investigate the form of the probability density functions of IPS observations recorded at 80, 111.5 and 160MHz and compare them with theoretical predictions.

6.2 THEORETICAL PROBABILITY DENSITY FUNCTIONS

For a continuous random variable I the probability density function p(I) may be defined (Bendat and Piersol, p56) by the differential relation

$$p(I) = \lim_{\Delta I \to 0} \left[\frac{\text{Prob } (I \leq I(k) \leq I + \Delta I)}{\Delta I} \right] \qquad \text{---- (6.1)}$$

where

$$\int_{-\infty}^{\infty} p(I)\, dI = 1 \qquad \text{---- (6.2)}$$

A probability density function can also be characterized by the central moments about the mean

$$M_p = \left\langle (I - \langle I \rangle)^p \right\rangle \qquad \text{---- (6.3)}$$

where $\langle I \rangle$ is the mean intensity.

As defined in Chapter Two, the scintillation index is

$$m = \frac{M_2^{\frac{1}{2}}}{I_o} \qquad \text{---- (6.4)}$$

where I_o is the mean intensity of the source in the absence of scintillation.

The higher central moments can be used to test for departures of the p.d.f. from the symmetrical Gaussian form predicted by the thin screen scattering theory in the limit of small phase deviations. In particular, two coefficients based on the moments of order 3 and 4 are (Abramowitz and Stegun, p928) the coefficient of skewness

$$\gamma_1 = \frac{M_3}{M_2^{\frac{3}{2}}} \qquad \text{---- (6.5)}$$

and the coefficient of kurtosis

$$\gamma_2 = \frac{M_4}{M_2^2} - 3 \qquad \text{---- (6.6)}$$

For a Gaussian p.d.f. $\gamma_1 = \gamma_2 = 0$. In his summary of the theory of interplanetary scintillation Salpeter (1967) used an alternative definition of the skewness coefficient (ξ) which is related to the normal statistical definition (6.5) by

$$\xi = \frac{\gamma_1^2}{4} \qquad \text{---- (6.7)}$$

One advantage of these coefficients is that, unlike the scintillation index, they are independent of the estimate of the mean source intensity I_o. Analysis of the experimental data presented in this chapter showed that the signal to noise ratio was insufficient to allow reliable estimation of central moment of order 4, so we will only consider the coefficient

of skewness in the following discussion.

Two models for the scattering medium may be considered, leading to two different forms of the probability density function. The first is the thin screen theory in which the scattering occurs in a thin screen at a large distance from the receiver. This theory predicts (Mercier, 1962) that the intensity fluctuations possess what has become known as a Rice-squared p.d.f. This function reduced to the limiting Gaussian and exponential forms when the rms phase deviation $\phi_0 \to 0$ and ∞ respectively. If, however, the scattering occurs over an extended region in which the receiver is immersed, the thin-screen theory must be replaced by a summation over many independent layers. In this case the 'method of smooth perturbations' (Tatarski, 1961) predicts that the intensity fluctuations possess a lognormal p.d.f.

The Rice-squared and lognormal functions are discussed in detail in Appendix I. The Rice-squared p.d.f. is defined by

$$p(I) = \frac{1}{2\sigma^2} \exp\left[\frac{-(I + 1 - 2\sigma^2)}{2\sigma^2}\right] I_0\left[\frac{[I\,(1-2\sigma^2)]^{\frac{1}{2}}}{\sigma^2}\right] \qquad \text{--- (6.8)}$$

where $I_0(x) = J_0(ix)$ is a zero-order modified Bessel function of the first kind, and σ is a parameter defining a family of such functions. The intensity has been normalised such that $\langle I \rangle = 1$. As devised in Appendix I, the scintillation index m and skewness coefficient γ_1 are

$$m = 2\sigma\,(1 - \sigma^2)^{\frac{1}{2}} \qquad \text{--- (6.9)}$$

and

$$\gamma_1 = \frac{3\sigma - 4\sigma^3}{(1 - \sigma^2)^{3/2}} \qquad \text{--- (6.10)}$$

Figure 6.1a shows the form of the Rice-squared p.d.f. as a function of the

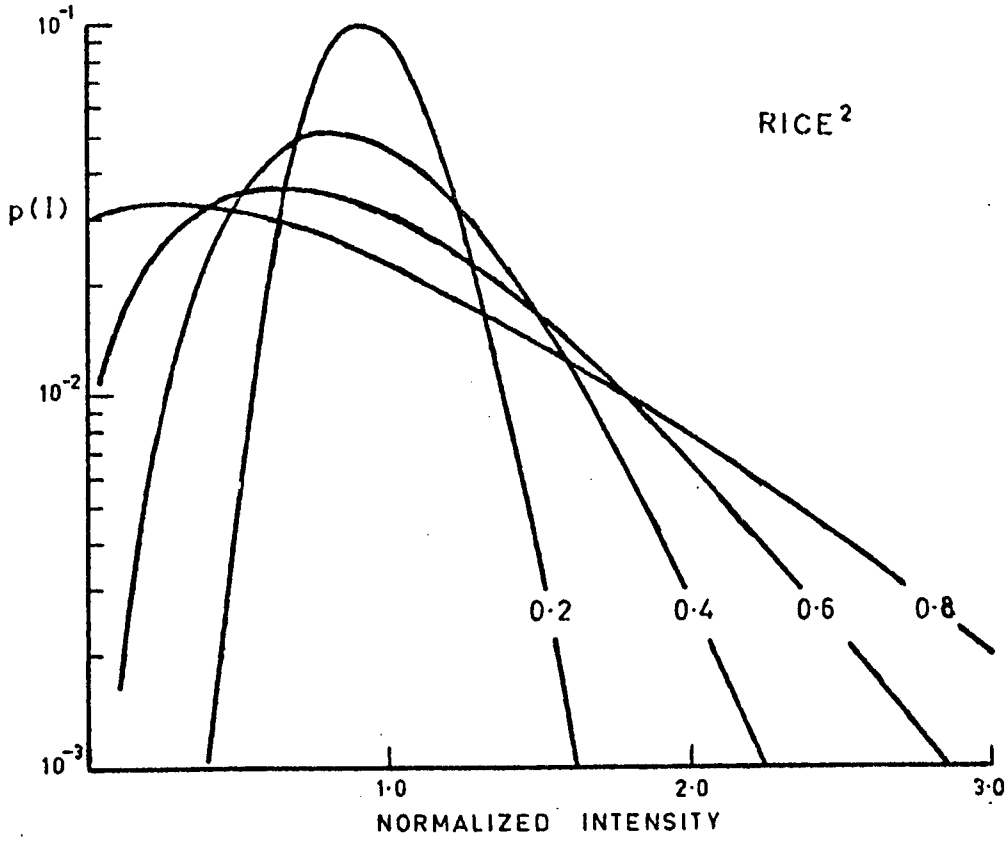

(a) Rice-squared p.d.f. as a function of the scintillation index

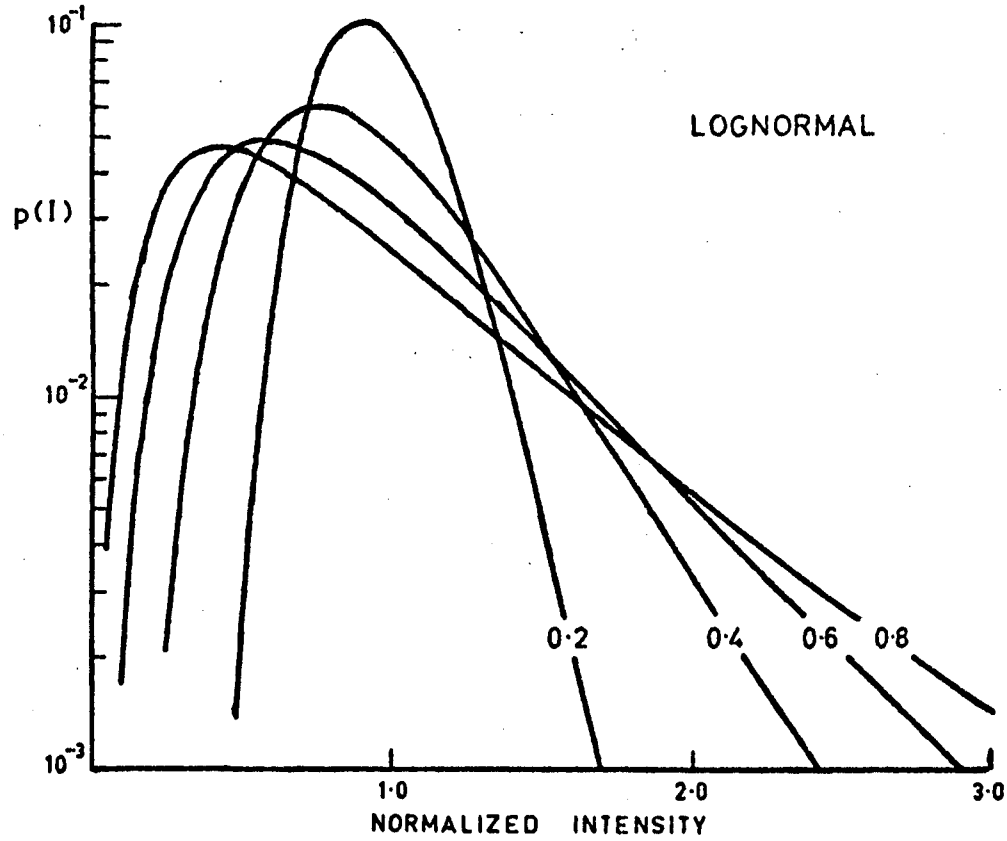

(b) Lognormal p.d.f. as a function of the scintillation index

FIGURE 6.1 Theoretical probability density functions

scintillation index.

The lognormal p.d.f. is defined by

$$p(I) = \frac{1}{\sigma I \sqrt{2\pi}} \exp\left[\frac{-1}{2\sigma^2}\left(\log I + \sigma^2/2\right)^2\right] \quad \text{--- (6.11)}$$

where σ is again a parameter defining a family of functions. The scintillation index m and skewness coefficient γ_1 are

$$m = (e^{\sigma^2} - 1)^{\frac{1}{2}} \quad \text{--- (6.12)}$$

and

$$\gamma_1 = 3m + m^3 \quad \text{--- (6.13)}$$

The form of the lognormal p.d.f. as a function of the scintillation index is shown in figure 6.1b.

In sections 6.3 and 6.4 of this chapter, we examine the form of the probability density functions for IPS observations at 80, 111.5 and 160MHz.

6.3 SCINTILLATION INDEX - SKEWNESS RELATIONS

The probability density functions were calculated from the experimental records as part of the analysis discussed in Chapter 4. The 111.5MHz results were obtained from single 4 min transit records for each source. The 80 and 160MHz results were recorded in 90 sec blocks, with between 3 and 30 blocks per observation. In these observations the p.d.f. was computed for each block and then averaged over all available blocks. The observed p.d.f's were corrected for the effect of noise by deconvolving with the p.d.f. of the associated noise record. The scintillation index and skewness coefficient were calculated for both the individual data blocks and the average p.d.f. In the analysis which follows care has been taken to eliminate any records which appeared to be affected by interference. This was particularly easy to do for the Culgoora records because of the multiple beam facility.

One method for comparing the experimental data with theory is to plot the skewness coefficient against the scintillation index, together with curves predicted by the Rice-squared and lognormal functions. Figures 6.2a,b show plots for two sources at 80 and 160MHz which are typical of records obtained for ten sources at these frequencies during June each year between 1969 and 1974. Both of these diagrams were constructed from data collected when the sources were in the weak scattering region.

As pointed out by Bourgois and Cheynet (1972) diagrams such as these are sensitive to the angular structure of radio sources. For example, if the source possesses a core-halo structure, consisting of a scintillating point source and non-scintillating extended halo, the total source intensity is the sum of the two components; $< I > = < I_{pt} > + < I_{halo} >$ and the apparent scintillation index

$$m = \frac{M_2^{\frac{1}{2}}}{< I >} < \frac{M_2^{\frac{1}{2}}}{< I_{pt} >}$$

Thus, the scintillation index will be less than that of a point source but the skewness coefficient γ_1 which is independent of $< I >$, will not necessarily be affected. The effect of diameter blurring on a scintillating source of finite angular diameter has been discussed in Chapter 2, and causes a similar reduction in the scintillation index close to the sun.

The source 0134+32 has an angular diameter $\sim 0''.3$ at 80MHz (Little and Hewish, 1968; Anderson and Donaldsen, 1967) so that at the elongations for which the observations were made the measured index would be within 6% of that for a point source (Redhead, 1971). Similarly 0624-05 has an angular diameter $\lesssim 1''$ (Allen, 1961). Thus neither source should be significantly affected by angular structure effects.

A similar skewness-index plot is shown in Figure 6.3a for the source 0532+21 at 111.5MHz. The compact, scintillating component of the

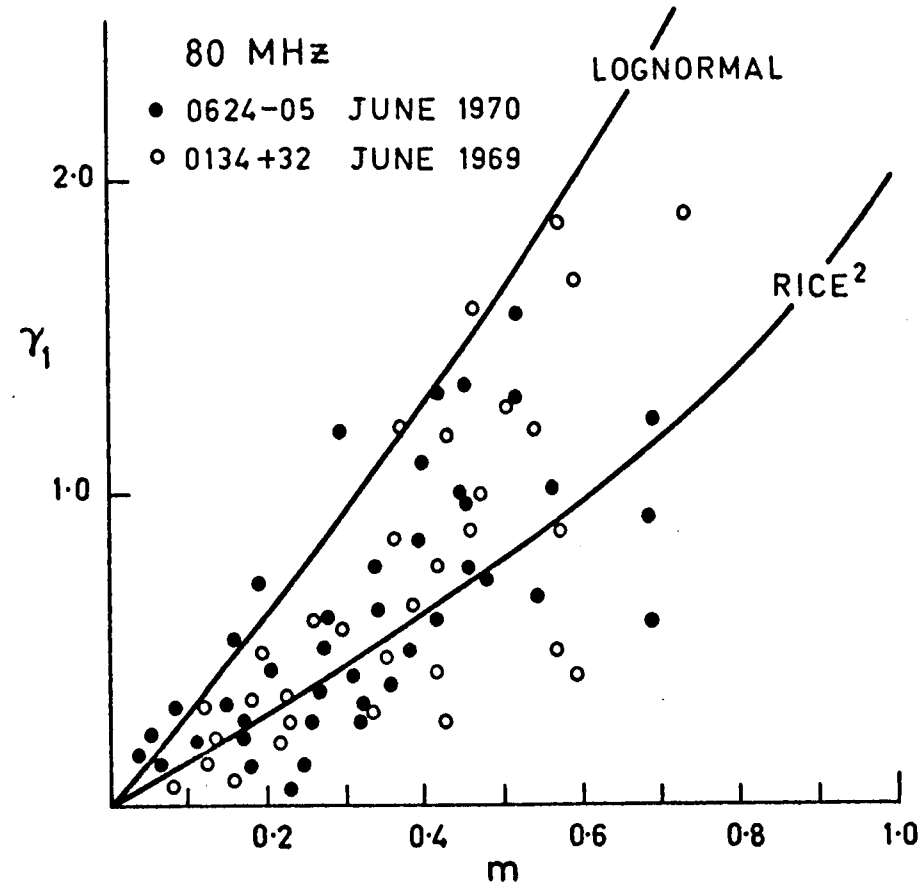

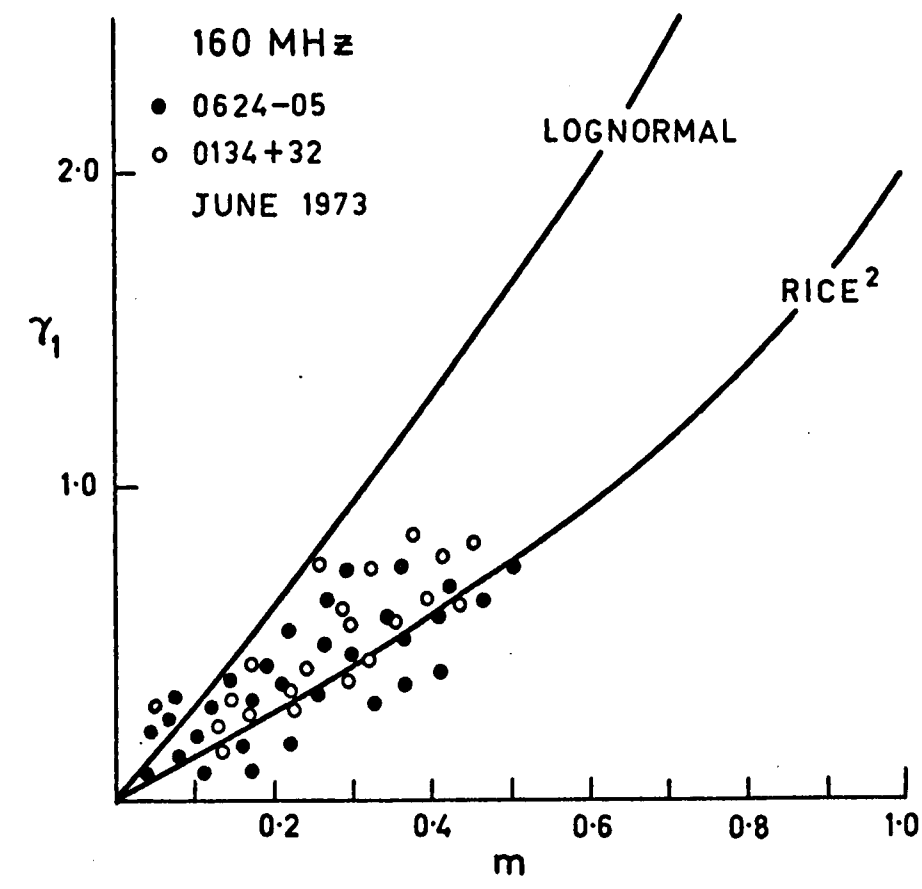

FIGURE 6.2a Scintillation index - skewness coefficient relations at 80 and 160 MHz.

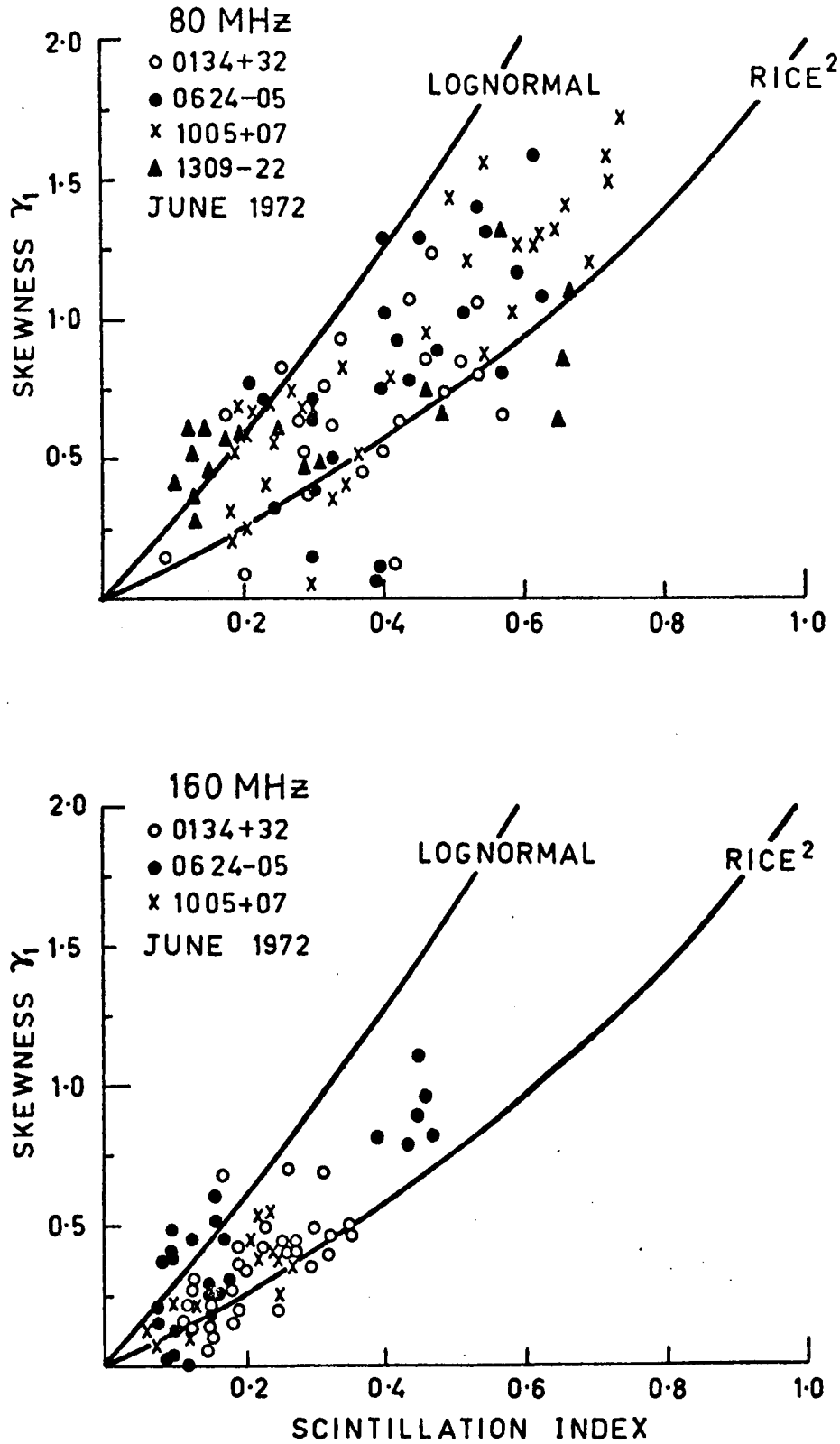

FIGURE 6.2b Scintillation index - skewness coefficient relations at 80 and 160 MHz.

Crab Nebula (0532+21) is the pulsar NP0532. At frequencies less than ~150MHz the effect of scattering in the interstellar medium is to broaden the pulses to such an extent that the source appears to be a compact continuum source with angular dimensions equal to the scattering angle θ_s (Cronyn, 1970a). At 74MHz the (half-power) diameter of the source is ~0".15 (Armstrong et al, 1973) and at 111.5MHz is ~0".07 (Vandenberg et al, 1973). Calculation of the scintillation index is therefore dependent on an estimate of the ratio of the pulsar intensity to the total intensity of the Nebula. This ratio is ~0.08 at these frequencies (Erickson et al, 1972). For elongations $\varepsilon > 30^0$ the correction for diameter blurring is again $\lesssim 5\%$.

Figure 6.3a differs from the previous diagrams in that the results were obtained over several months during which the source varied in position, between $\varepsilon = 90^0$ and $\varepsilon = 10^0$ and hence includes observations in both the strong and weak scattering region. The values of the index and skewness are shown in figures 6.3 b as a function of the heliocentric distance $p = \sin \varepsilon$ The scintillation index shows the expected decrease in the strong scattering region. The skewness values however do not appear to be affected to the same degree although they are quite widely scattered. A similar effect has been noted close to the sun at 1420MHz (Bourgois and Cheynet, 1972)

The spread of scintillation indices in Figures 6.2 and 6.3 are largely due to day-to-day variations in the interplanetary medium but the larger scatter in the skewness values are primarily statistical (see section 6.5). We can conclude from these diagrams that the intensity p.d.f. is closer to the Rice-squared than the lognormal form. These diagrams are typical of most of the sources examined. Sources with elongations $\gtrsim 120^0$ showed a tendency to be scattered more uniformly between the two forms. This suggests that the lognormal form may be more appropriate at these elongations where the scattering occurs over an extended region close to the Earth.

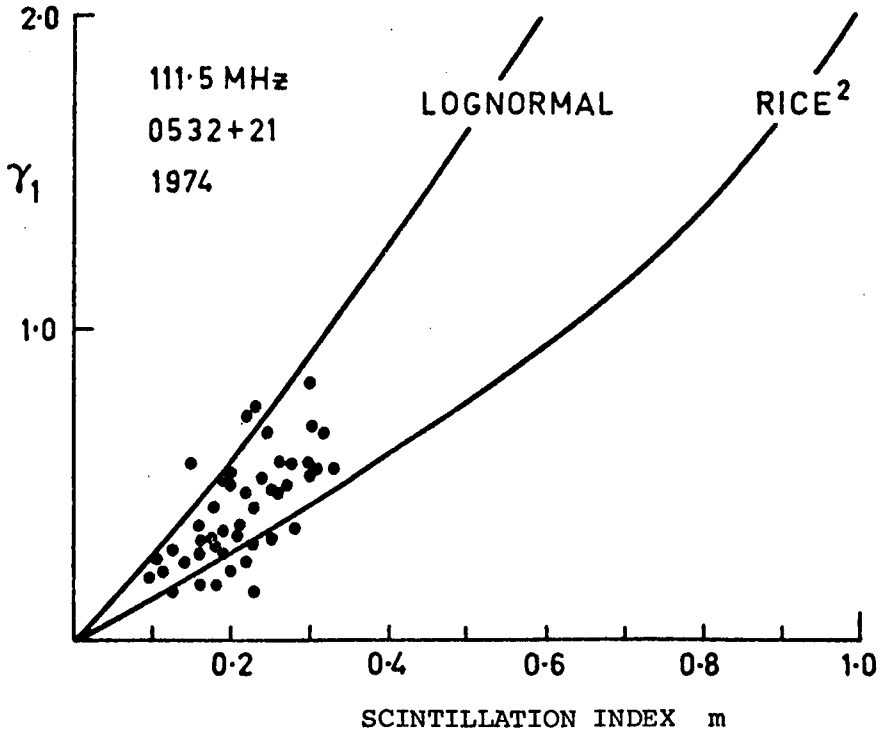

(a) Scintillation index - skewness coefficient relations

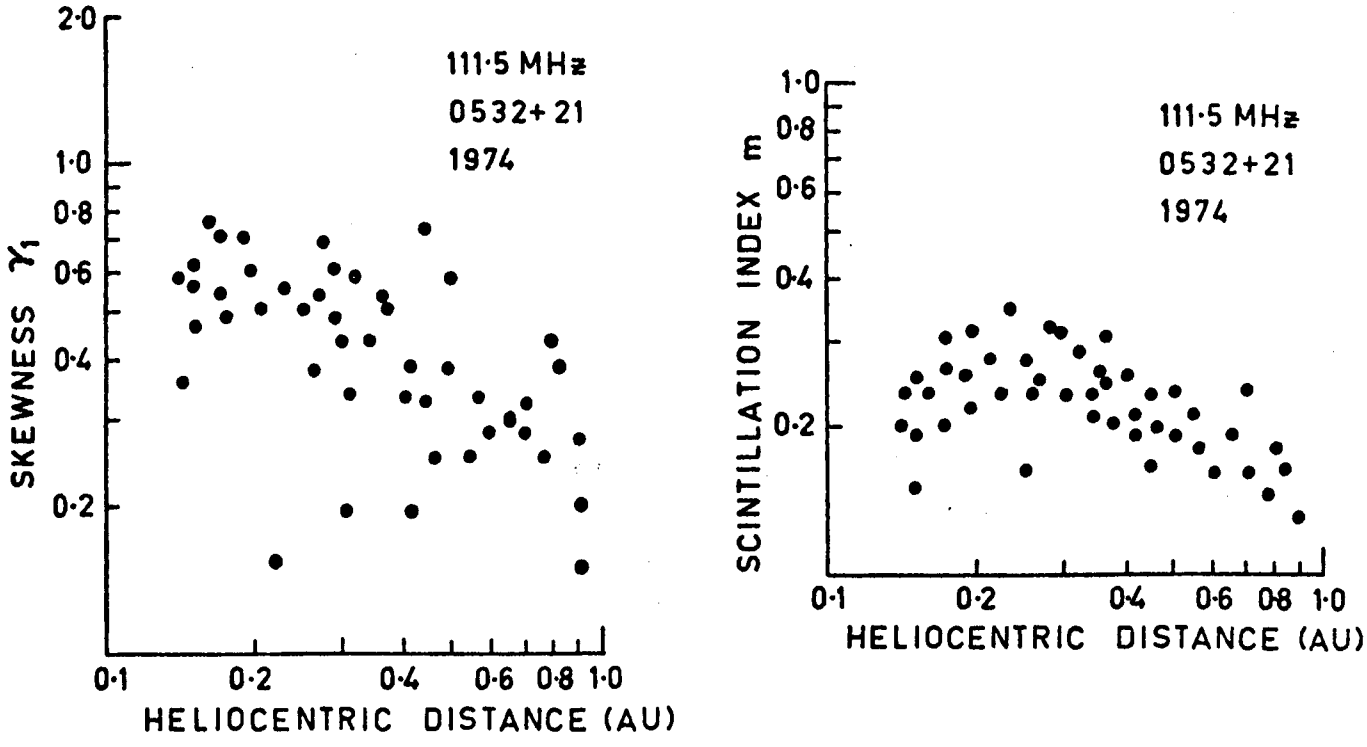

(b) Variation of scintillation index and skewness coefficient with heliocentric distance

FIGURE 6.3 Scintillation index and skewness at 111.5 MHz

The low signal to noise ratio for these sources prevented a conclusive decision about this change.

It should be noted that the use of such diagrams to estimate source angular structure, as suggested by Bourgois and Cheynet (1972), should be carried out with some care. Even though only a few per cent of the values of I occur in the high intensity 'tail' in the p.d.f. they are weighted as I^2 in their contribution to the index and as I^3 in their contribution to γ_1 and they must therefore be measured carefully. The effect is seen in figure 6.4a where the different curves show the result of using data to increasingly high intensity levels. For a true index of 0.8 for example, and a lognormal distribution, a measured index of 0.59 would be obtained if intensities up to $3 < I >$ were included in the calculation. The error represents the importance of peaks above $3 < I >$ and implies that long lengths of data are needed to obtain reasonable accuracy at high scintillation indices. At 80MHz ~40 independent samples per minute are obtained in typical scintillation records, and since only ~3-4% of these occur for $I > 3 < I >$ for $m \sim 0.8$, approximately 20 minutes of data are needed to obtain ~15% accuracy in the tail.

Apart from the length of data one should bear in mind the instrumental requirements in examining the wide range of intensities encountered in strong scintillation. The tendency of many square-law detectors to over-square at high signal levels, for example, could give rise to anomalously high skewness and index values. When the scintilling component amounts to only a small fraction of the total source flux, such as in the Crab Nebula, this effect can become increasingly important.

The effect on the skewness-index plot is shown in figure 6.4b where

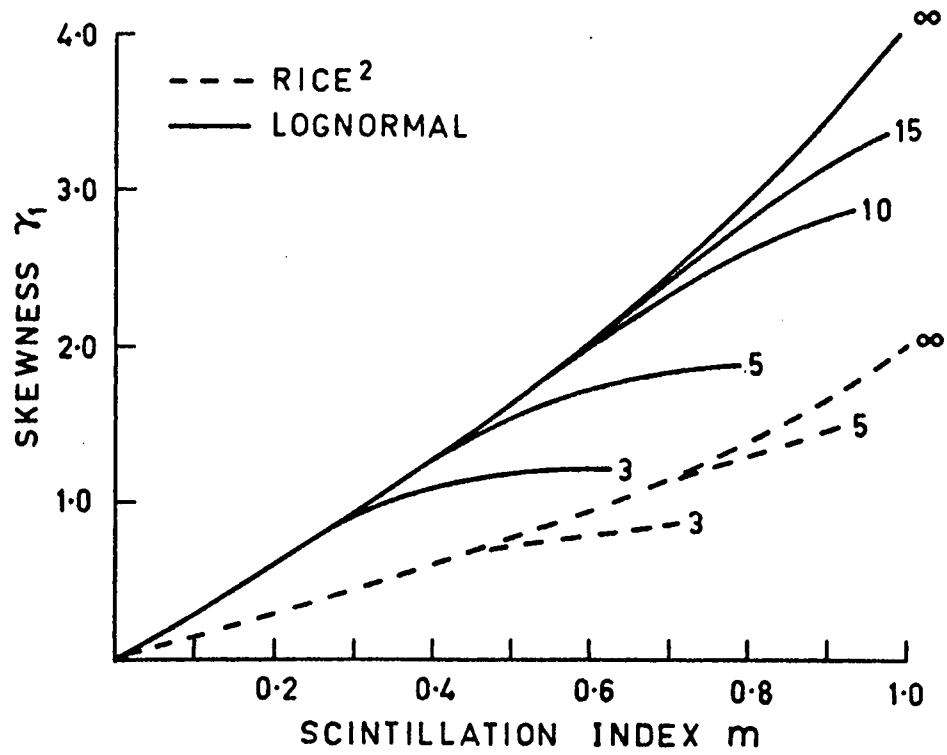

(a) Dependence of index - skewness relation on accuracy of p.d.f. The number beside each curve is the maximum intensity value used in the p.d.f. to derive m and γ_1.

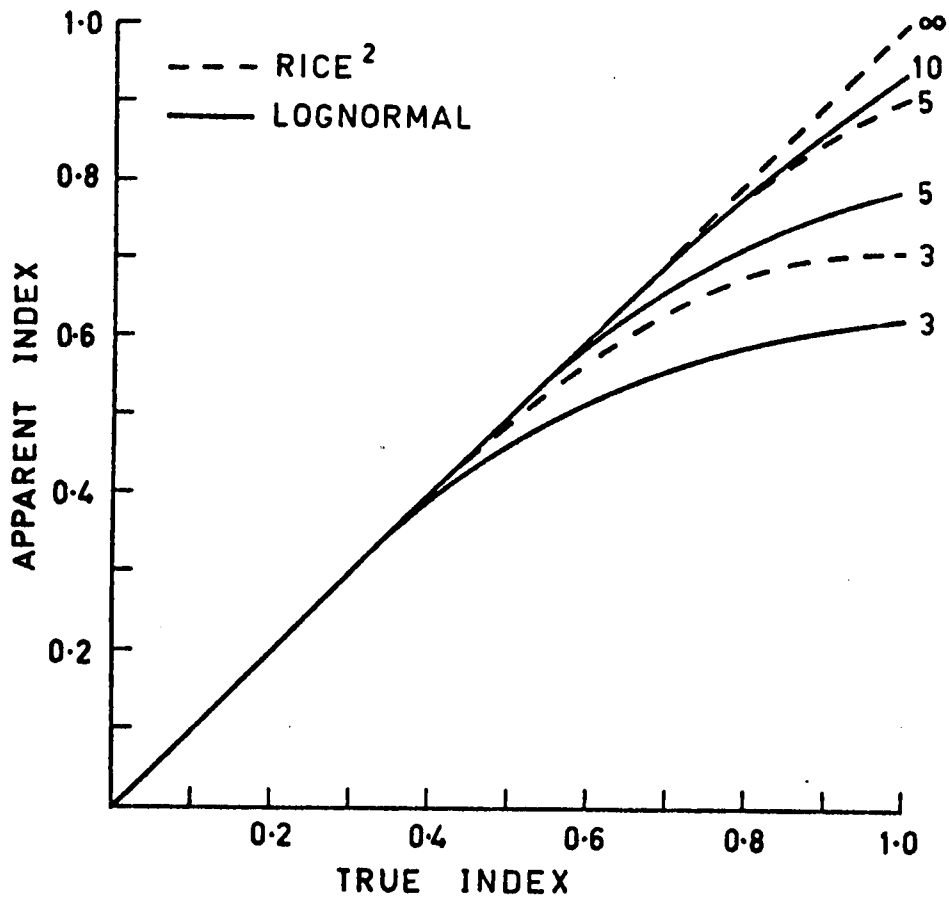

(b) Dependence of scintillation index on the accuracy of the p.d.f. The index has been evaluated from a p.d.f. calculated to different maximum intensity values.

FIGURE 6.4 Dependence of index and skewness on accuracy of p.d.f.

the index and skewness have again been calculated to different intensity levels. Clearly very good statistics would be needed to be able to apply this method quantitatively to studies of source angular structure. In fact even a distinction between the lognormal and Rice-squared functions based on such diagrams should be treated with some caution.

6.4 EXPERIMENTAL P.D.F's

In view of the limitations of the approach discussed in the previous section, it is desirable to examine directly the form of the observed p.d.f. in relation to the theoretical lognormal and Rice-squared forms. The 80 and 160MHz experimental p.d.f's used in this section were the result of averaging a number of consecutive blocks (~ 10 - 30 min data) to improve the statistics. The error bars were calculated from the block-to-block fluctuations and represent the standard deviation. The 111.5MHz p.d.f's were obtained by averaging several successive days observations where the scintillation index remained relatively constant, and the error bars were derived from the day-to-day variations. Examples of fits to both the Rice-squared and lognormal distributions have been found in the experimental p.d.f's while many of the records are intermediate between the two forms.

Examples of (80MHz) experimental pdf's which fit the Rice-squared form are shown in figure 6.5. Each of these was obtained from ~ 20 min data. The examples shown cover a range of indices and distances from the sun as shown on the diagrams. Examples of 80MHz p.d.f's which fit the lognormal function, again over a range of conditions, are plotted in figure 6.6. Similar results have been found at 160MHz, as shown in figure 6.6b The need to average observations over several days at 111.5MHz has introduced much greater uncertainty into the experimental p.d.f's and it is not possible to choose decisively between the models.

On occasions experimental p.d.f's occur which do not fit either

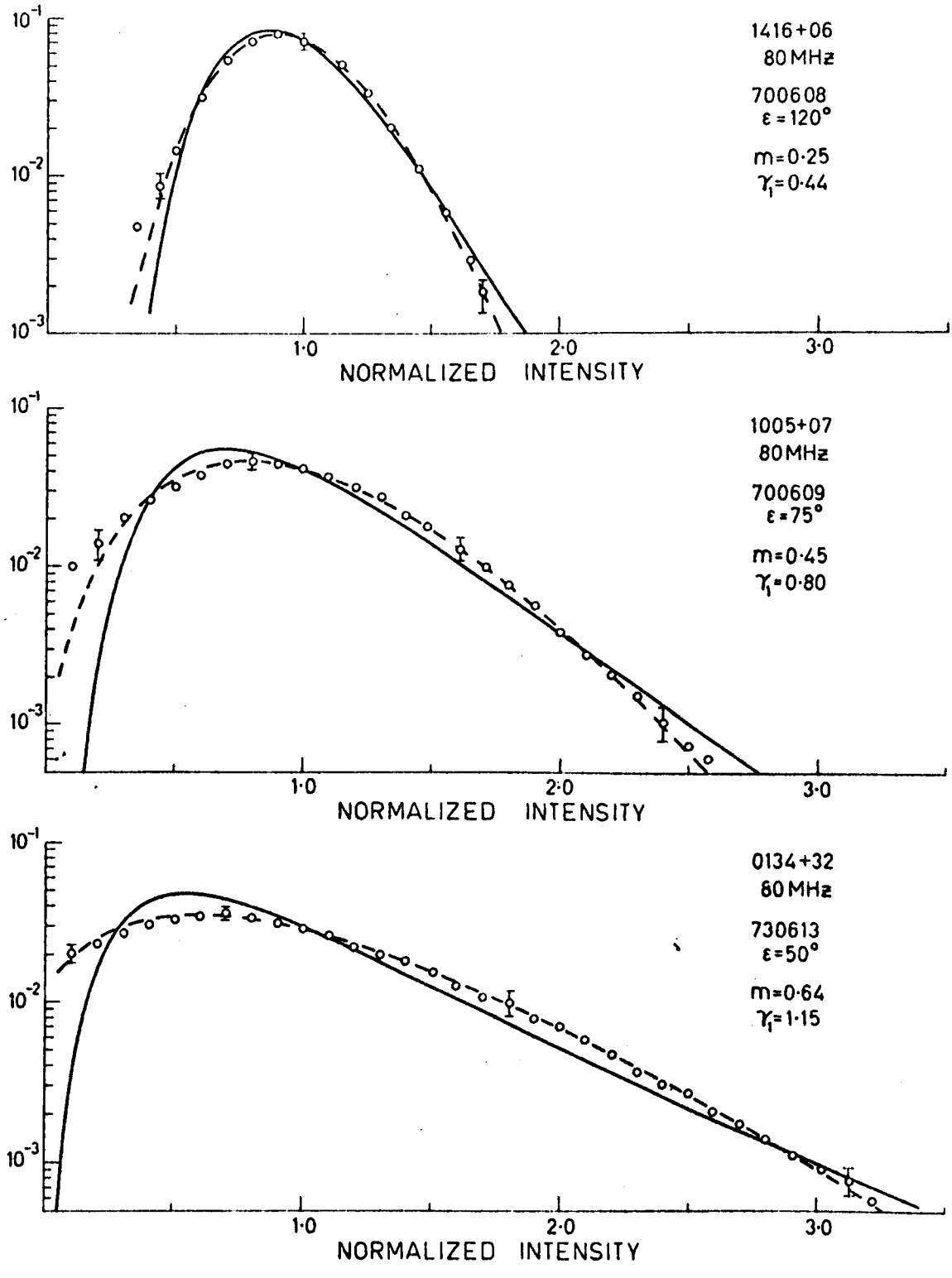

FIGURE 6.5 Examples of experimental p.d.f's which fit the Rice-squared function (- - -) .

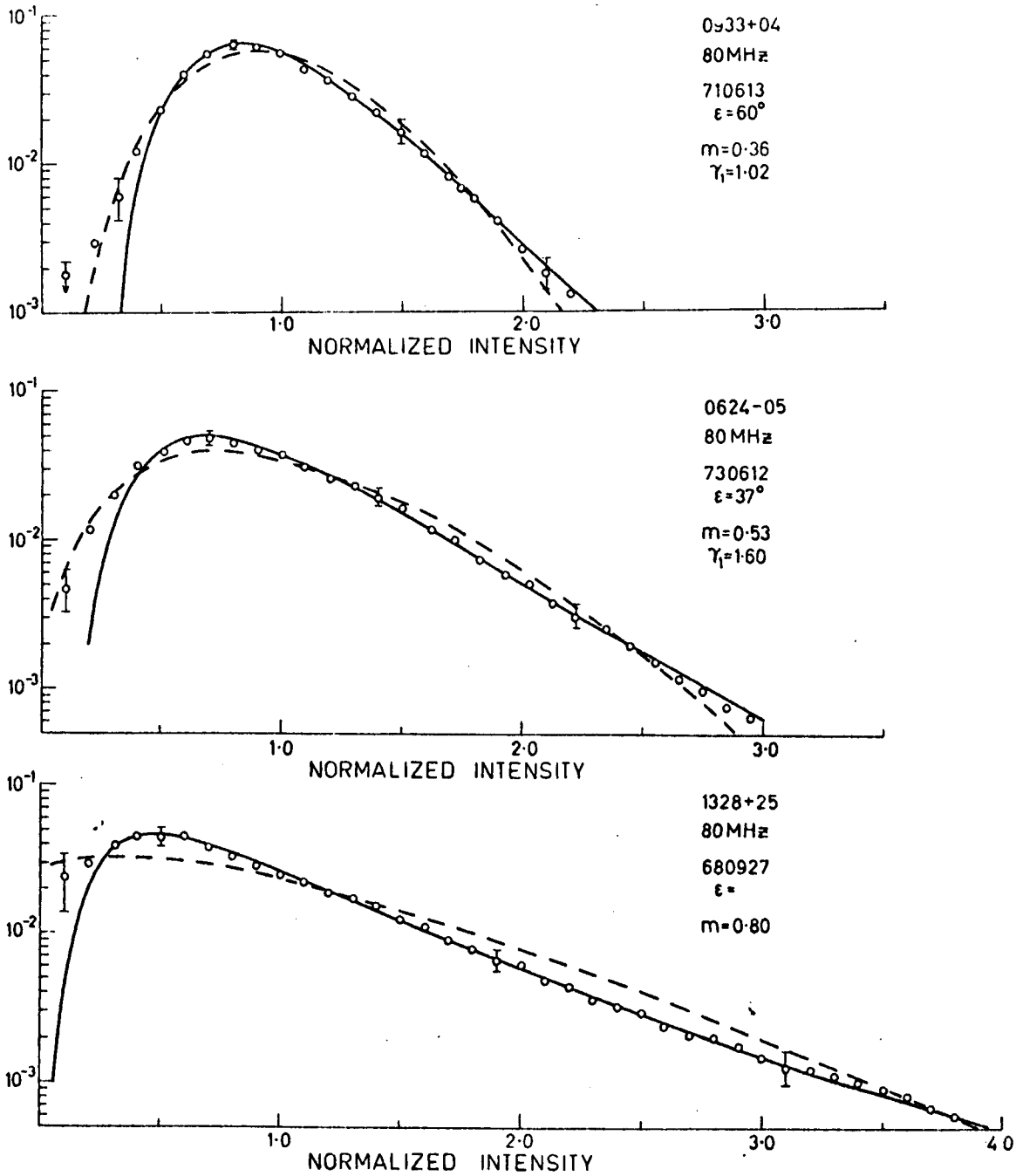

FIGURE 6.6a Examples of experimental pdf's which fit the lognormal function (———).

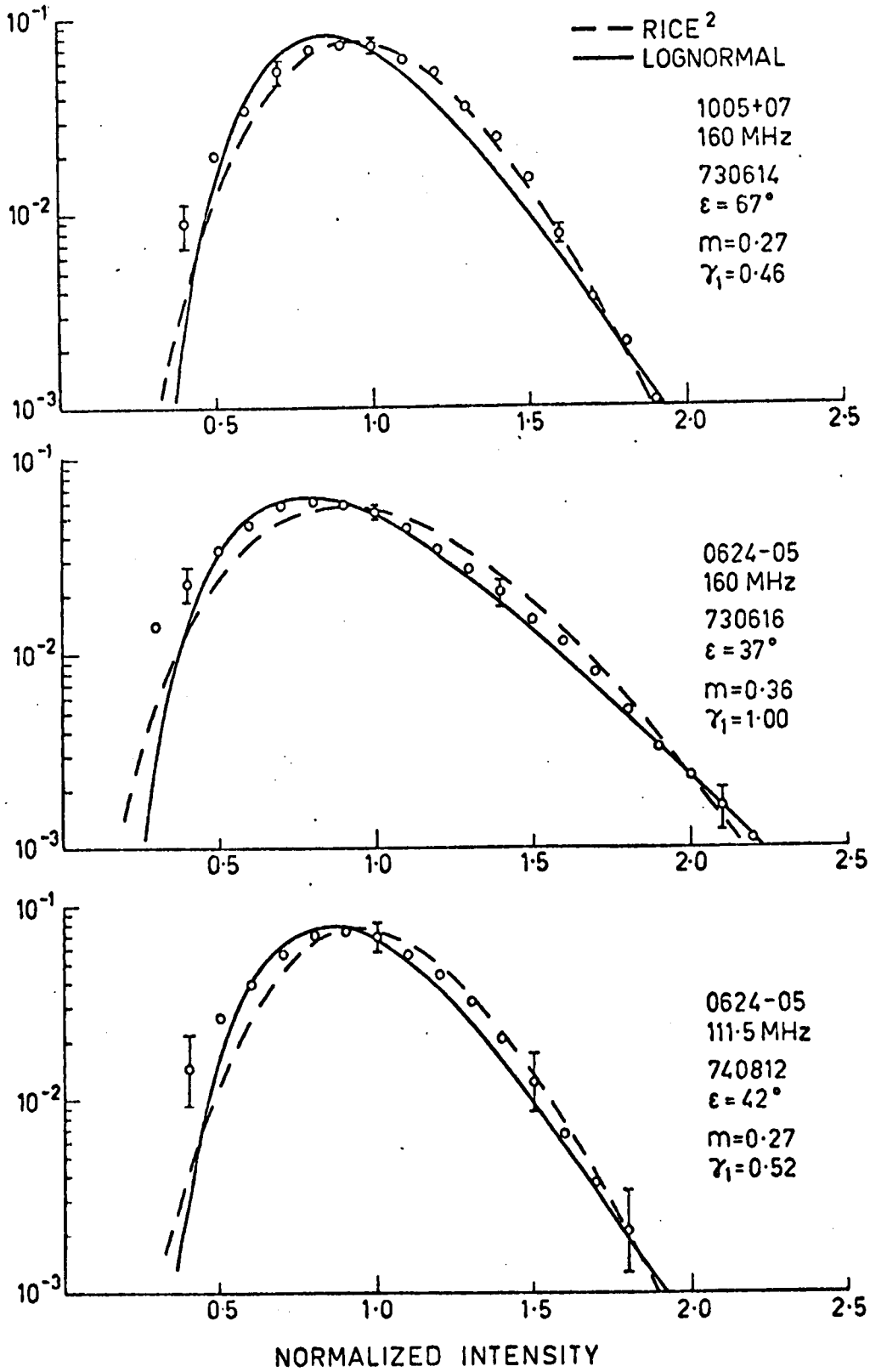

FIGURE 6.6b Examples of experimental p.d.f.'s for observations at 111.5 and 160 MHz.

distribution well and are not intermediate in form. Examples are shown in figure 6.7. The 80 MHz results were obtained when the sources were affected by the passage of flare-associated disturbances in the interplanetary medium across the line of sight. (see Chapter 5). Both of these show a feature which is peculiar to distributions obtained for relatively high indices ($\geq$0.7) which is a 'shoulder' or enhanced probability for $1.0 < I > 1.3$ and a fluctuation between the lognormal and Rice-squared forms. This effect has been noted on several sources during such disturbances.

The final p.d.f. in Figure 6.7 was obtained at 111.5MHz within the strong scattering region close to the sun. It appears to be marked by a high intensity tail but the need to average daily observations and the large day-to-day variations close to the sun precluded a detailed examination of the form of the p.d.f. This effect is responsible for the observed decrease in index without a significant a decrease in skewness close to the sun.

One other feature which consistently appeared in the experimental p.d.f's was a systematic departure from the Rice-squared and lognormal forms in the low intensity region $I < 0.75 < I >$. This effect was found to some degree in almost all of the experimental p.d.f's. Considerable care was taken in establishing the zero intensity level in these records to eliminate that source of error.

6.5 NUMERICAL SCATTERING MODEL

Analytical solutions for the statistics of the diffraction pattern resulting from wave propagation through a thin random phase-changing screen have been developed in several limiting cases. The theory is well-developed in the limit of small rms phase deviation $\phi_0 < 1$ rad (e.g. Ratcliffe, 1956; Bowhill, 1961; Salpeter, 1967) and some approximations are available for large values of ϕ . (Mercier, 1962; Bramley and Young, 1967; Buckley, 1971a, b). There are several conditions for which analytic solutions have not been derived

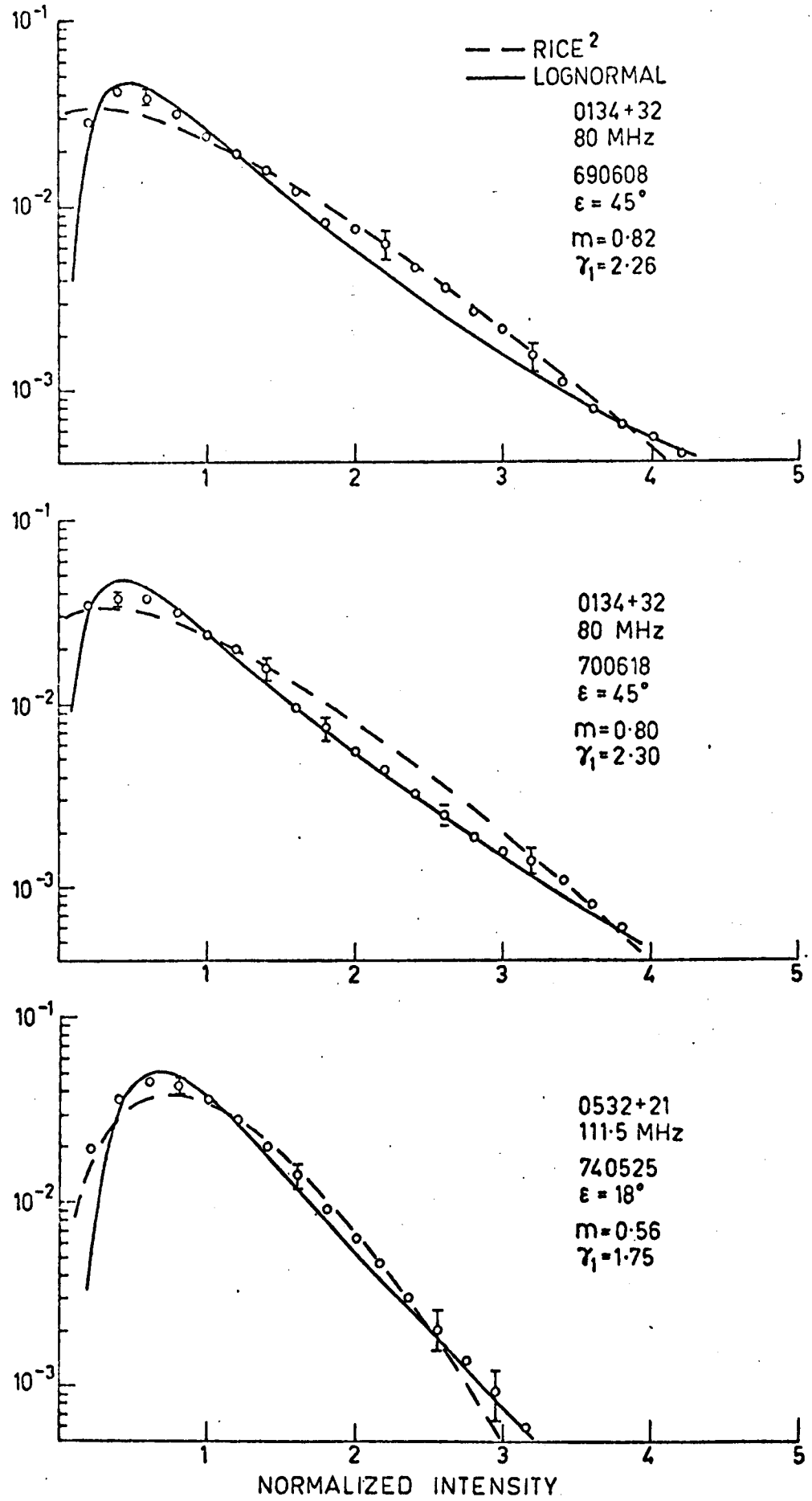

FIGURE 6.7 Examples of observed p.d.f.'s which do not adequately fit either theoretical model.

to date, and, in particular, the nature of the p.d.f. has not been predicted analytically in some regions. In the far-field the intensity fluctuations possess a Rice-squared distribution which approaches a Gaussian form as $\phi_0 \to 0$ and an exponential form as $\phi_0 \to \infty$. The form of the p.d.f. in the near-field is rather uncertain, especially for $\phi_0 > 1$ where there exists a 'focal distance' at which large fluctuations in intensity are caused by the tendency of individual irregularities to act as converging lenses.

Buckley (1975) has shown that if a random phase screen is represented by a long sequence of random numbers with prescribed statistical properties it is possible to calculate the diffraction pattern at any distance from the screen by a double application of the Fast Fourier Transform algorithm to the angular spectrum of phase waves emerging from the screen. The statistics of the diffraction pattern can then be derived from the numerically-generated pattern. These records are of course noise free and by computing a sufficient number of such patterns it is possible to reduce the error limits to any desired level.

A numerical model based on Buckley's algorithm has been developed to investigate the form of the p.d.f. as a function of both the distance from the screen and the rms phase deviation. The model is one-dimensional, for practical computing reasons, and employs a random phase screen with a Gaussian autocorrelation function. Distance is measured in terms of the dimensionless parameter $Z = z/ka^2$. In the far-field ($Z \gg 1$) the p.d.f. for weak scattering ($\phi_0 < 1$) possesses the Rice-squared form predicted by the analytical thin screen theory. Figure 6.8 shows a skewness-index plot similar to Figure (6.2) in which twenty different models, each of the same length as the experimental records used in Figure 6.2, were calculated for each value of ϕ_0 at $Z = 50$. It can be seen that, with the length of data available in the experimental records discussed in the previous sections the scintillation index will be a reliable estimate but the skewness coefficient can be expected to show quite large statistical variations. This suggests that the variations in scintillation index in Figure 6.2 are largely due to day-to-day variations in the interplanetary medium while the larger

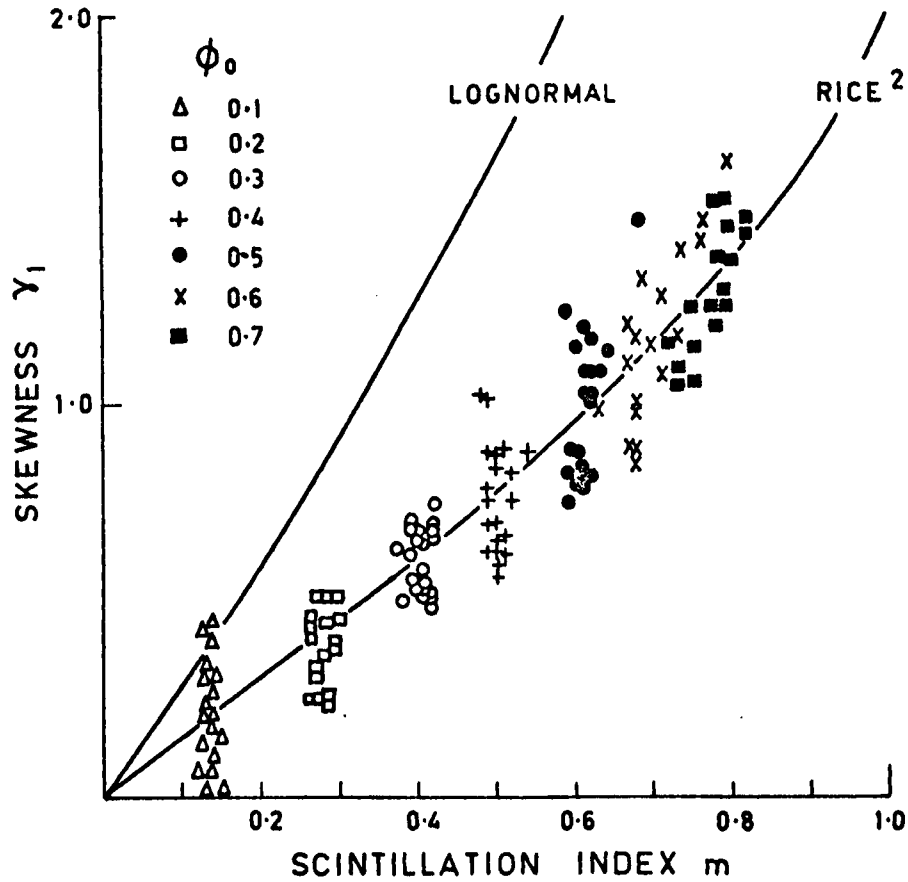

FIGURE 6.8 Scintillation index - skewness coefficient relations derived from a numerical model of diffraction from a thin random phase screen. Twenty records, each of the same length as the observational records discussed in this chapter, were generated for each value of ϕ_0.

scatter in the skewness values is at least partly a consequence of the length of data available. Fluctuations in the coefficient of kurtosis from record to record were even larger than those of the skewness coefficient. The results of the numerical model suggest that with the length of data available the coefficient of kurtosis has insufficient statistical significance to be of any practical use, even in a noise-free record.

We can also use this model to investigate the way in which the scintillation index and skewness coefficient vary as a function of distance from the screen. The scintillation index will increase as the intensity pattern develops, reaching the limit (Mercier, 1962)

$$m = (1 - \exp(-2\phi_0^2))^{\frac{1}{2}} \qquad \text{--- (6.14)}$$

in the far-field, while the skewness coefficient has the limit (Bourgois, 1972)

$$\gamma_1 = 2(1 + 2E)(1-E)^{\frac{1}{2}}(1+E)^{-3/2} \qquad \text{--- (6.15)}$$

where $E = \exp(-\phi_0^2)$. Figure 6.9 shows the variation in the scintillation index and skewness coefficient as a function of distance from the screen and the rms phase deviation. The variations in the scintillation index are in good agreement with analytical solutions (Bramley and Young, 1967; Buckley 1975), the increase in the index beyond unity for large ϕ_0 corresponding to the occurrence of focussing effects. The variation of the skewness with distance is in agreement with the analytic expression derived by Bourgois (1972) in the weak scattering limit but there are no analytic solutions available for $\phi_0 > 1$.

An interesting feature of the skewness variation is the tendency for the distribution to be more asymmetrical close to the screen than for a Rice-squared distribution of the same apparent index, especially in the case of large phase deviations. The change in the p.d.f. as a function of distance from the screen can be seen in Figure 6.10 where the p.d.f. of the fluctuations at several distances are plotted for a screen with $\phi_0 = 0.5$. As $Z \to \infty$ the p.d.f.

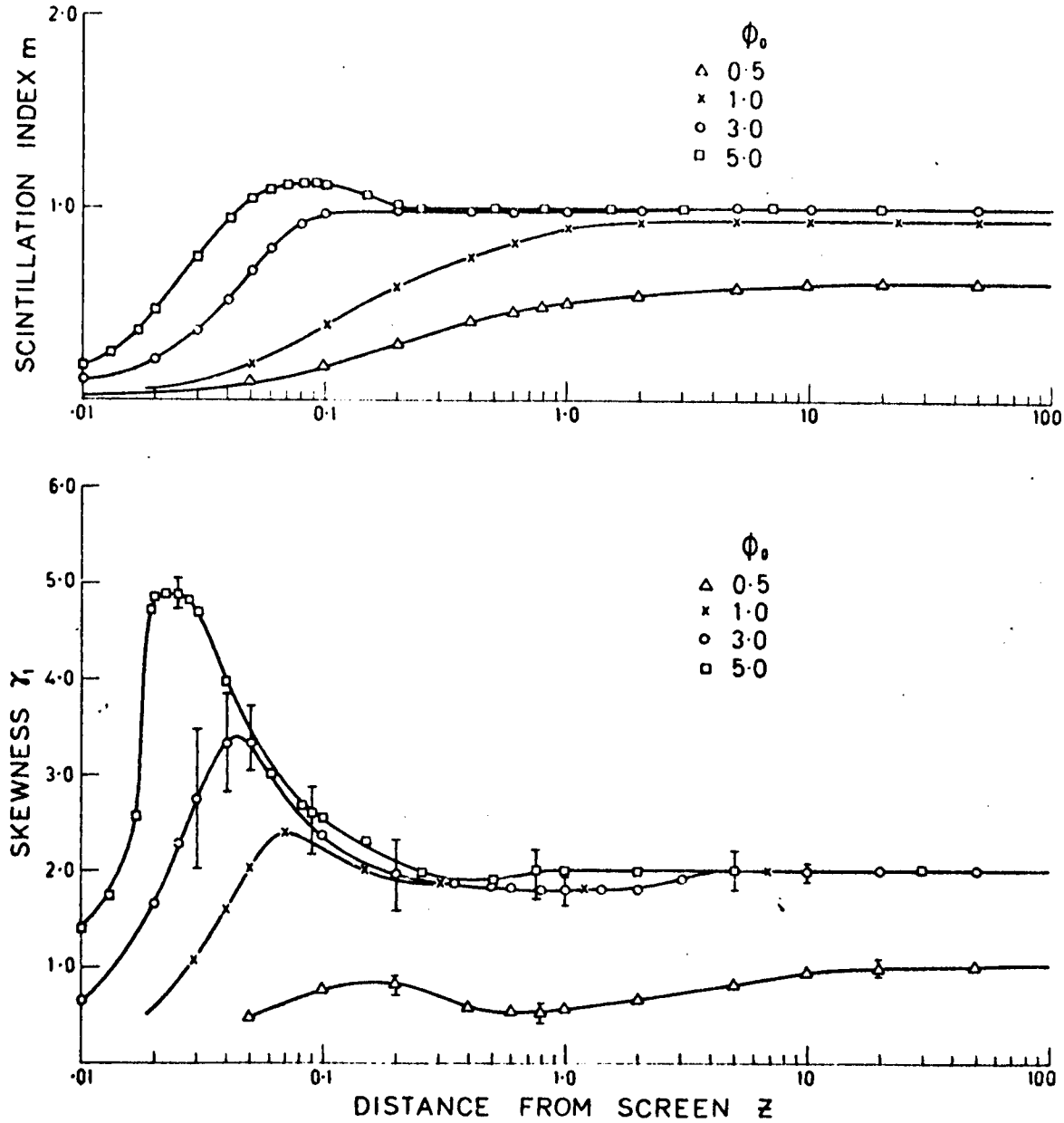

FIGURE 6.9 Variation of scintillation index and skewness coefficient as a function of distance from the scattering screen.

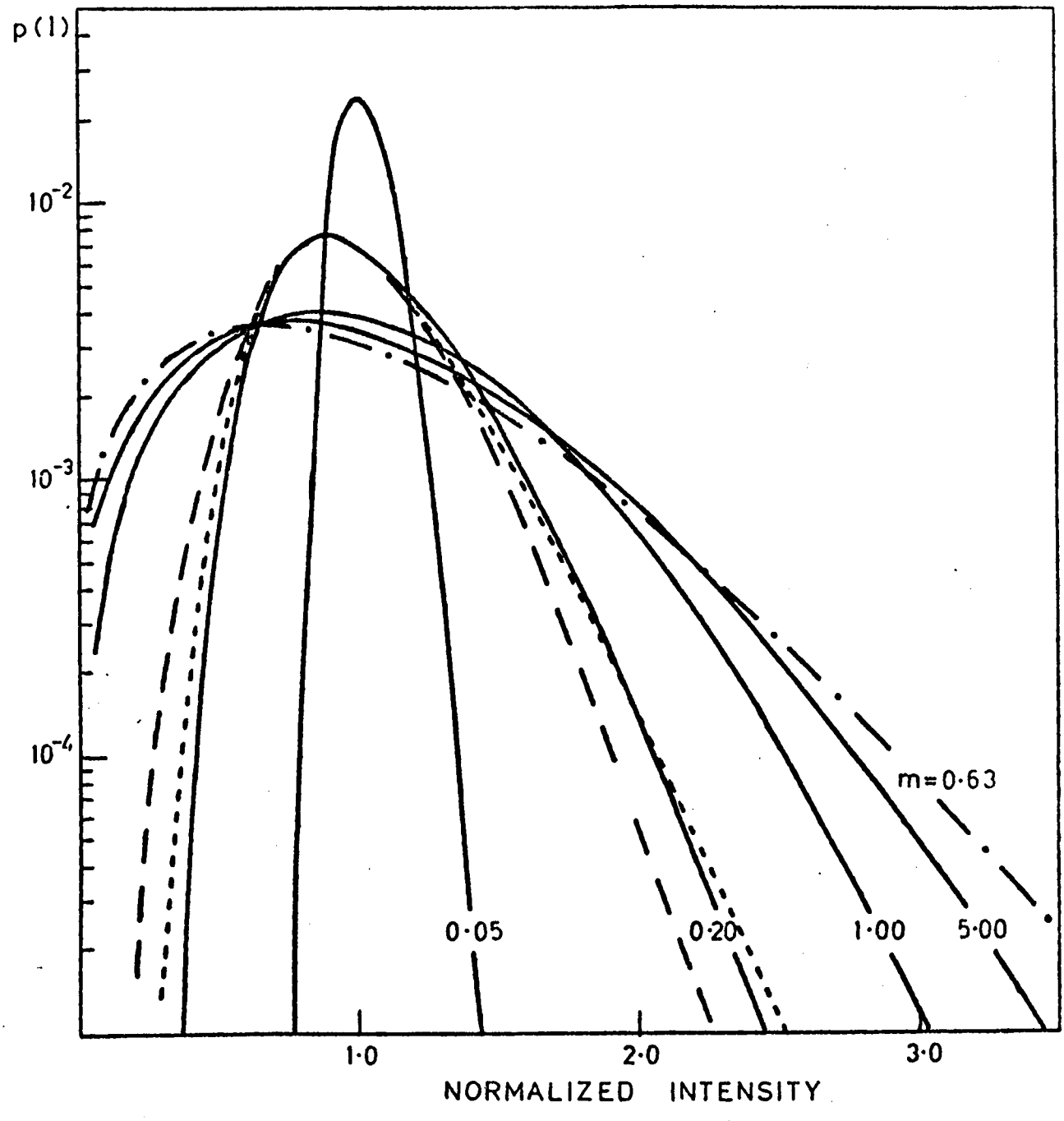

FIGURE 6.10 P.d.f.'s of the intensity fluctuations as a function of distance from a thin random phase screen with $\phi_o = 0.5$. As $Z \to \infty$ the p.d.f. approaches the Rice-squared p.d.f. with m = 0.63 (— · — · —·).

Curves plotted for comparison with p.d.f. at Z = 0.20:

— — — — Rice-squared m = 0.29 $\gamma_1 = 0.46$

---------- Lognormal m = 0.29 $\gamma_1 = 0.91$

approaches a Rice-squared distribution of index m = 0.63 as predicted by equation (6.14). The asymmetry close to the screen can be seen in the p.d.f. for Z = 0.2 where the apparent index is m = 0.29 and the skewness γ_1 = 0.82. Also plotted are the Rice-squared (m = 0.29, γ_1 = 0.46) and lognormal (m = 0.29, γ_1 = 0.91) functions for the same scintillation index. It can be seen that the p.d.f. is more nearly lognormal than Rice-squared at this distance.

The variation of the p.d.f. for ϕ_0 = 3 as a function of distance is shown in Figure 6.11. Again as $Z \to \infty$ the distribution approaches the predicted exponential form. The high skewness coefficient at Z = 0.05 is caused by the assymmetry of the distribution with the development of a 'tail' at high intensity values, due to focussing 'spikes'.

6.6 DISCUSSION

The results presented in sections 6.3 and 6.4 lead to the conclusion that the p.d.f. is generally intermediate in form between the Rice-squared and lognormal functions, with examples of each being found in experimental p.d.f's. There is however a tendency for the p.d.f's to be more nearly Rice-squared on average than lognormal. This is in marked contrast to the work of Armstrong et al (1972) who presented an analysis similar to Figure 6.2 using observations of 0532 + 21 at 74MHz. They found that their experimental points lay around or above the lognormal curve. However, they assumed the pulsar flux was ~12% of the total flux of the Crab Nebula which would appear to be an over-estimate. In addition they used an approximation for the Rice-squared skewness-index variation wh which is only valid for $m \leq 0.4$. When both of these corrections are applied to their figures 5 and 6, as shown in Figure 6.12, the results provide index-skewness variations which tend to lie beyond even the Rice-squared variation.

The deviation of the experimental p.d.f's from both theoretical curves at low intensity values is a consistent feature of most of the records. This effect was also evident in the examples of Armstrong et al (1972). At this stage

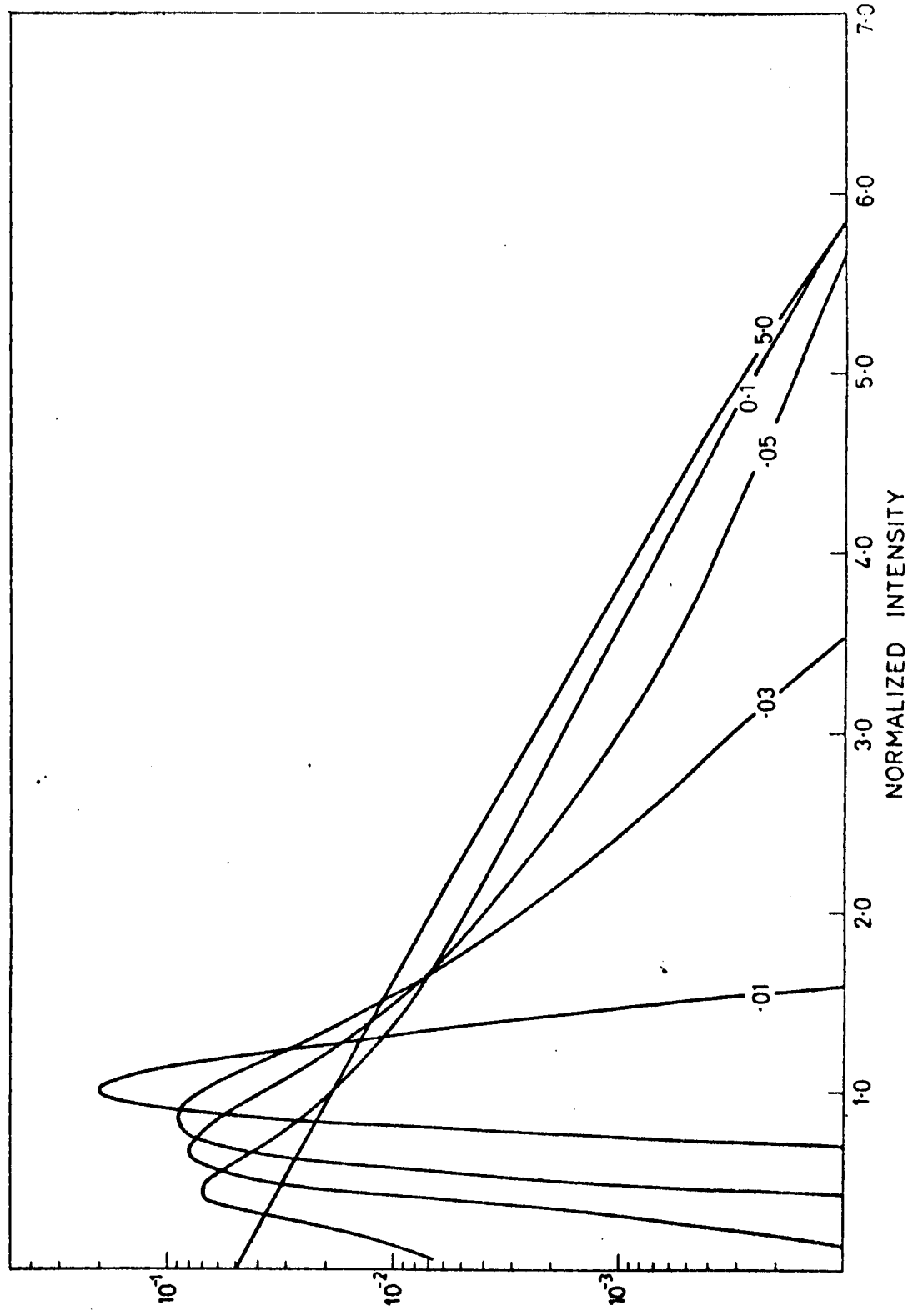

FIGURE 6.11 P.d.f.'s of the intensity fluctuations as a function of distance from a thin random phase screen with ϕ_o = 3 rad. As $Z \to \infty$ the p.d.f. approaches the exponential form.

there is no apparent instrumental explanation for this deviation and it would appear to be a real effect, possibly with an origin in the scattering mechanism. Armstrong et al suggested that a better fit to the lognormal distribution can be obtained in the low intensity region by using a lognormal function computed for a lower index than observed, with the resulting excess 'tail' on the distribution being the result of focussing in the interplanetary medium. We find that good fits can be obtained to experimental p.d.f's without postulating a focussing component. The p.d.f's of Armstrong et al will also be affected by the apparent over-estimation of the source intensity. In this respect we agree with Young (1971), in that what appears subjectively to be focussing on an analogue record is just the expected small percentage of scintillations at high intensity levels. This is particularly so for log-normal distributions but is also true for Rice-squared functions with indices $m \geq 0.5$. At $m \sim 0.8$, for example, 3% of the fluctuations have $I > 3\langle I \rangle$ for a Rice-squared distribution. It would appear however that the anomalous skewness behaviour close to the sun could be explained by invoking focussing effects, which affect the skewness more significantly than the index, as ϕ_0 becomes greater than unity. The 111.5MHz records were not sufficiently long to test this suggestion accurately.

Bourgois and Cheynet (1972) found close agreement with a Rice-squared p.d.f. at 1420MHz close to the sun. At our lower frequencies the scattering region becomes more extended but apparently is still sufficiently thin for the Rice-squared distribution to be a better approximation on average than the log-normal. At larger elongations, where the scattering occurs over a more extended region and in which the earth is embedded, would appear to approach the lognormal form. Systematic observations over a wide range of solar elongations, and at several frequencies, would be capable of determining the point at which the Rice-squared model begins to break down.

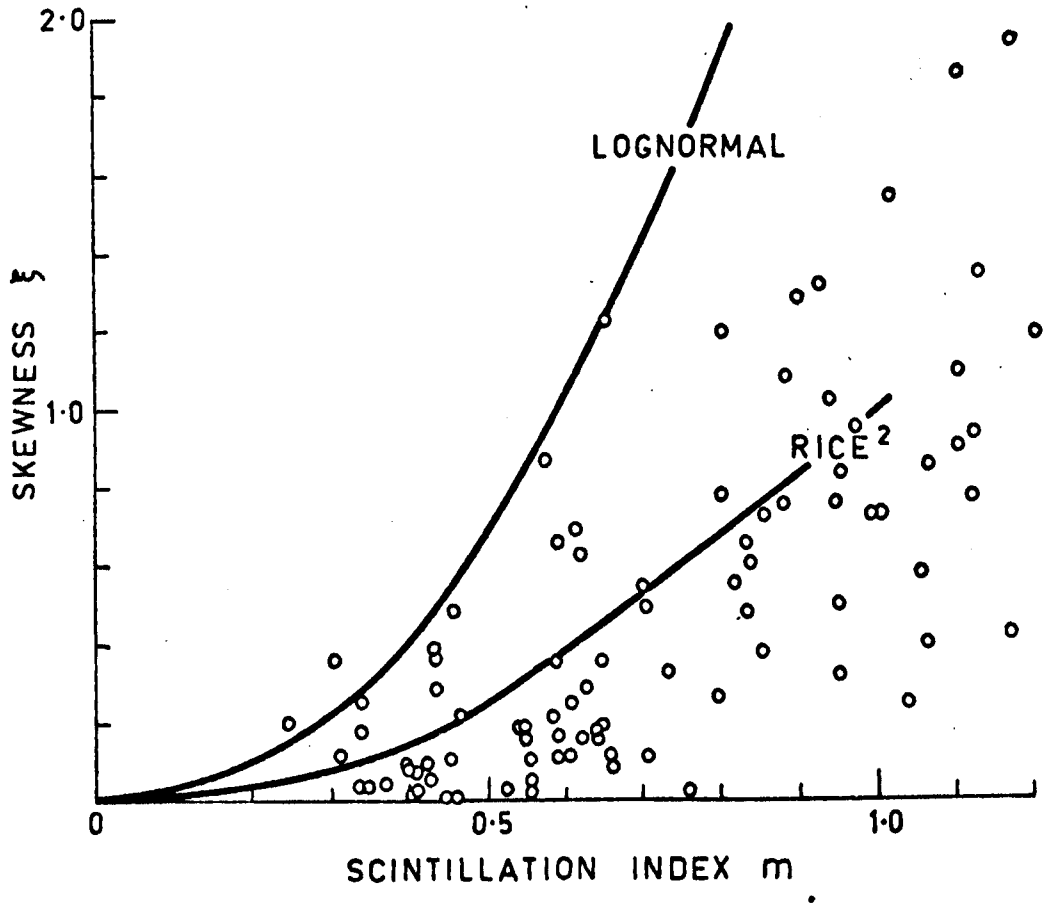

FIGURE 6.12 Scintillation index - skewness coefficient relations for source 0532+21 at 78 MHz. The data points are taken from figure 5 of Armstrong et al (1972) and the index values increased by a factor of 2, as discussed in the text.

One other feature that was investigated during the analysis of the probability density functions was the effect of transient disturbances. In general no overall pattern could be observed in the events discussed in Chapter 5 although some general trends could be discerned. Sources at large elongations tended to become more nearly Rice-squared when affected by a disturbance. This probably reflects the fact that the disturbance is confined to a relatively thin region whereas the ambient scattering at large elongations occurs over a more extended region of space. Sources closer to the Sun showed no systematic effects other than the tendency for the p.d.f. to deviate from either of the two theoretical models for large scintillation indices, as discussed previously.

CHAPTER 7

SPECTRAL ANALYSIS OF INTERPLANETARY SCINTILLATION

7.1 INTRODUCTION

One of the most active areas of solar wind research has been concerned with the distribution of energy within the interplanetary plasma since this is of fundamental importance to an understanding of the dynamics of the solar wind. Of the various mechanisms involved in the storage and distribution of energy in the solar wind the role of turbulence is the least well understood. However, as more detailed observations and theoretical models have become available it has become evident that a complete understanding of even the average properties of the interplanetary plasma depends on an understanding of the role of the turbulence and wave motions which occur within the plasma.

Interplanetary scintillation observations can provide one technique for investigating the nature of the turbulence within the interplanetary plasma provided that the relationship between the fluctuations in electron density in the plasma and the intensity fluctuations in the radio wave observed on Earth is understood. In this chapter the results of experimental observations at metre wavelengths are compared with theoretical models in an attempt to derive some information about the structure of the irregularities in the electron density in the medium.

7.2 THEORETICAL SPECTRAL ANALYSIS

The relationship between the density irregularities in the scattering screen and the intensity fluctuations in the radio wave at a distance from the screen has been discussed in some detail in Chapter 2. Since the observational data discussed in this chapter are limited to the

weak scattering regime (elongations $\varepsilon > 25^{o}$) the discussion of the theoretical models will also be limited to the weak scattering case.

We recall from the discussion in Chapter 2 that if the electron density irregularities are described in terms of a 3D spatial wavenumber spectrum, $P_{Ns}(k_1,k_2)$, and the intensity fluctuations in terms of a 2D spatial wavenumber spectrum, $P_{Is}(k_1,k_2)$, then

$$P_{Is}(k_1,k_2) = 8\pi(r_e\lambda)^2 L P_{Ns}(k_1,k_2,0)\ \sin^2(k^2/k_f^2) \qquad ...(7.1)$$

where $k^2 = k_1^2 + k_2^2$ and $k_f^2 = 4\pi/\lambda z$. The temporal power spectrum, $P_{It}(f)$, of the intensity fluctuations observed as the diffraction pattern is swept past an observer with velocity V in the x_1 direction is related to the spatial intensity spectrum, $P_{Is}(k_1,k_2)$, by

$$P_{It}(f) = \frac{2\pi}{V}\int_{-\infty}^{\infty} P_{Is}(k_1,k_2)\ .dk_2 \qquad ...(7.2)$$

Relations (7.1) and (7.2) have been derived on the assumption that radiation from a point radio source is being scattered in a 'thin' region of space such that the total rms phase deviation imposed on the wave is $\phi_o << 1$ rad. In the case of an extended source the observed diffraction pattern is the convolution of the pattern which would be observed from a point source with the brightness distribution of the source being observed. The effect is to modify equation (7.1), giving

$$P_{Is}(k_1,k_2) = 8\pi(r_e\lambda)^2 L\ P_{Ns}(k_1,k_2,0)\ \sin^2(k^2/k_f^2)\ \left|V(k_1,k_2)\right|^2 \qquad ...(7.3)$$

where $V(k_1,k_2)$ is the source visibility function as defined in Chapter 2.

If the scattering occurs along an extended length of the line of sight the contributions from a number of independent thin screens must be summed and the observed spectrum becomes

$$P_{It}(f) = \int_o^z P_{It}(f,z).dz \qquad ...(7.4)$$

Salpeter (1967) has shown that in the case of an extended medium relation (7.1), which is valid for a thin screen, must be replaced by

$$P_{Is}(k_1,k_2) = 8\pi(r_e\lambda)^2 L\, P_{Ns}(k_1,k_2,0)\quad G(k,z,L) \qquad ...(7.5)$$

where $G(k,z,L) = \left[1 - \frac{4\pi}{L\lambda k^2}\sin\{\frac{L\lambda}{4\pi}k^2\}\cos\{\frac{2z\lambda}{4\pi}k^2\}\right]$

and $k^2 = k_1^2 + k_2^2$.

The discussion to this point has been completely general with respect to the form of the spectrum of the electron density irregularities. In order to calculate theoretical spectral models for comparison with observed spectra it is now necessary to assume some particular form for $P_{Ns}(k_1,k_2,k_3)$. The traditional approach to this problem has been to assume that the density irregularities possess a characteristic scale a_i in the x_i direction, as defined by a Gaussian autocorrelation function. The 3D spatial wavenumber spectrum then becomes

$$P_{Ns}(k_1,k_2,k_3) = \frac{(r_e\lambda\Delta N_o)^2 a_1 a_2 a_3}{2\pi}\ \exp\left[\frac{-k_1^2a_1^2}{2} - \frac{k_2^2a_2^2}{2} - \frac{k_3^2a_3^2}{2}\right] \qquad ...(7.6)$$

Substitution of equation (7.6) into (7.1) and (7.2) gives (Bourgois,1972)

$$P_{It}(f) = \frac{2^{\frac{1}{2}}\phi_o^2}{\pi^{\frac{1}{2}}\alpha_1^2}\exp\left[\frac{-f^2}{2\alpha_1^2}\right]\left[1 - \cos^{\frac{1}{2}}\{\theta_2\}\cos\left\{\frac{2\pi\lambda z f^2}{V^2} + \frac{\theta_2}{2}\right\}\right] \qquad ...(7.7)$$

where

$$\phi_o^2 = (2\pi)^{\frac{1}{2}}(r_e\lambda\Delta N_o)^2 L a_3 \qquad ...(7.8)$$

$$\tan\theta_i = \frac{2Z}{Z_i} \qquad ...(7.9)$$

$$Z_i = \frac{2\pi a_i^2}{\lambda} \qquad ...(7.10)$$

$$\alpha_i = \frac{V}{2\pi a_i^2} \qquad ...(7.11)$$

As was noted in Chapter 2 (see equations 2.24 and 2.26) the use of the Bessel transform is logical in those cases where the irregularities are isotropic. Bourgois (1972) has calculated the Bessel transfom in the more general case

of anisotropic Gaussian irregularities, for which

$$B_{It}(f) = \frac{\phi_o^2}{\pi a_1^2} \exp\left(\frac{-f^2}{2a_1^2}\right)\left[1 - \frac{\cos^{\frac{1}{2}}\theta_2}{\cos^{\frac{1}{2}}\theta_1} \cos\left[\frac{2\pi\lambda z f^2}{V^2} + \frac{\theta_2 - \theta_1}{2}\right]\right] \quad ...(7.12)$$

The $\sin^2$ term in relation (7.1), commonly known as the Fresnel filtering function, represents the effect of propagation in the near-field or Fresnel diffraction zone. The effect is to act as a low-pass filter, rejecting spatial fluctuations with wavenumbers less than $(4\pi/\lambda z)^{\frac{1}{2}}$, and to produce periodic zeros at larger wavenumbers where the fluctuations exist purely in the form of phase fluctuations. The effect of the projection from two dimensions onto one dimension is represented by the terms in square brackets in relations (7.7) and (7.12). In general, for a two dimensional pattern the projection will fill in the periodic zeros, with a greater effect on the Fourier transform than the Bessel transform, as shown in figure 7.1. The effect of the degree of anisotropy, as defined by the axial ratio $R = a_1/a_2$, is shown in figure 7.2. The minima in the spectra occur at the zeros of the $\sin^2$ function and are given by

$$f_n^2 = \frac{nV^2}{z\lambda} \quad ...(7.13)$$

The effect of increasing distance from the screen is shown in figure 7.3 where the temporal power spectrum is shown at two different distances. The distance is measured in terms of a dimensionless parameter $Z_x = f_F/\alpha_1$ where the Fresnel frequency f_F is defined by

$$f_F^2 = \frac{V^2}{\pi\lambda z} \quad ...(7.14)$$

In the near field ($Z_x<1$) the spectrum is severely distorted by the removal of energy at the low frequencies. At large distances ($Z_x>1$) the low frequency depression is less severe and 'Fresnel oscillations' may appear at higher temporal frequencies.

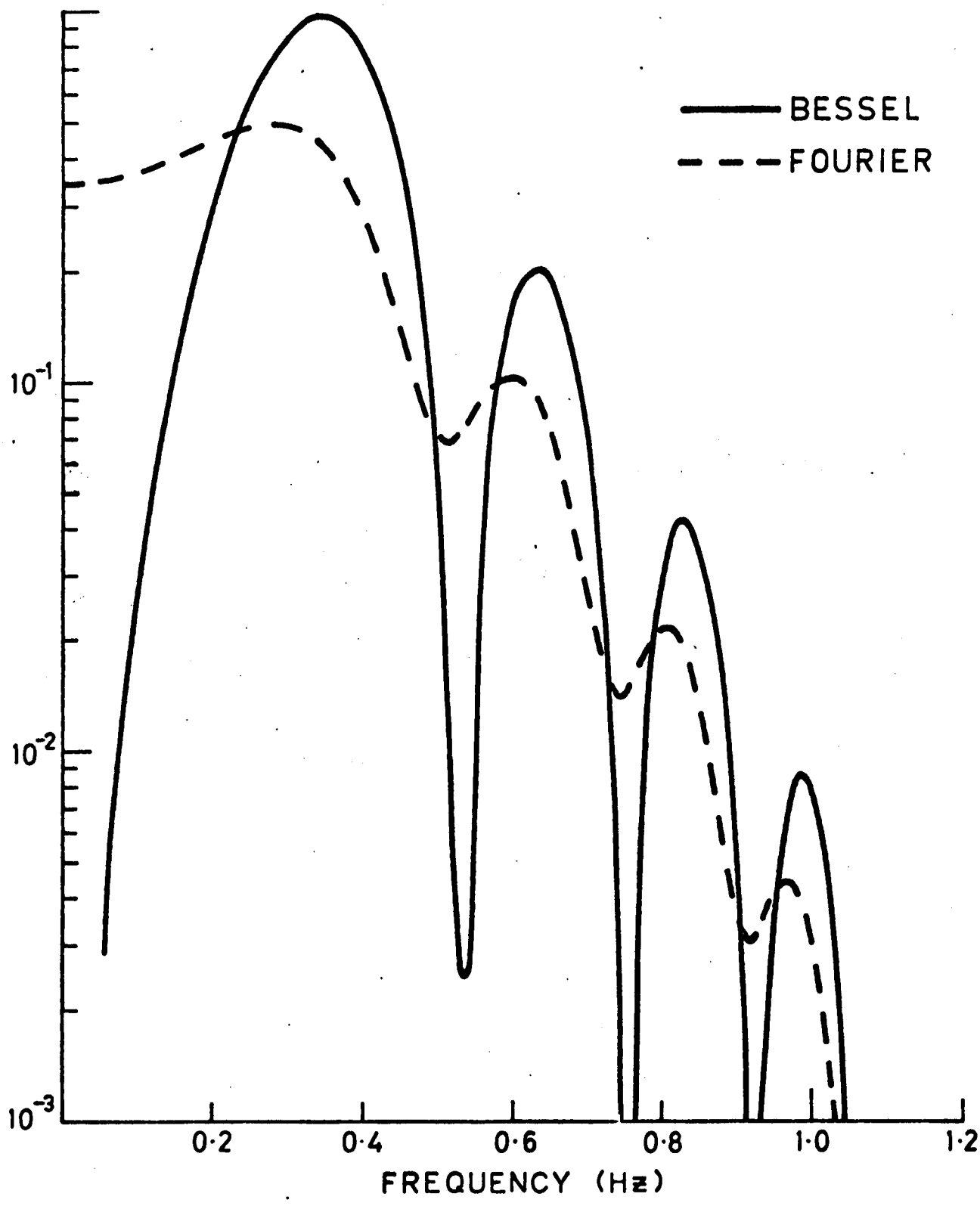

FIGURE 7.1 Comparison of Fourier and Bessel transforms for a Gaussian screen with R = 1 and Z_x = 1.

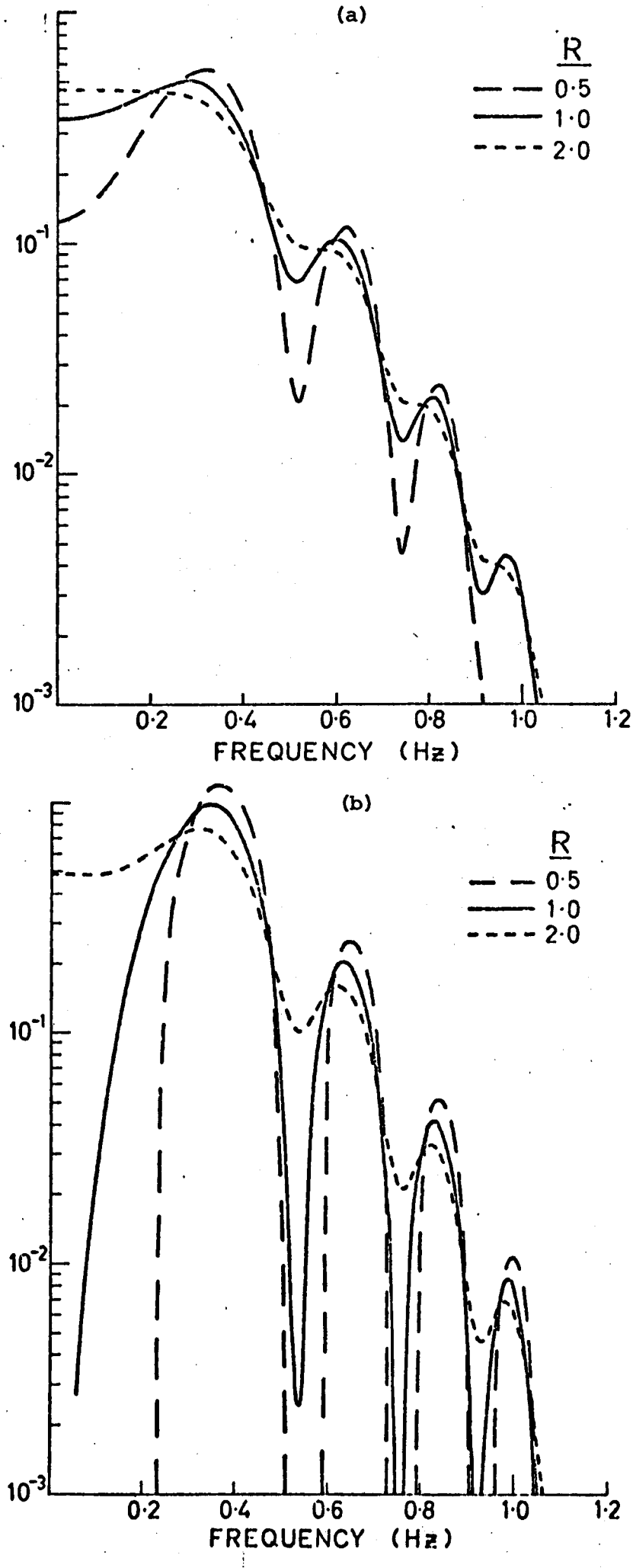

FIGURE 7.2 Effect of anisotropy of the density irregularities on (a) Fourier and (b) Bessel transforms.

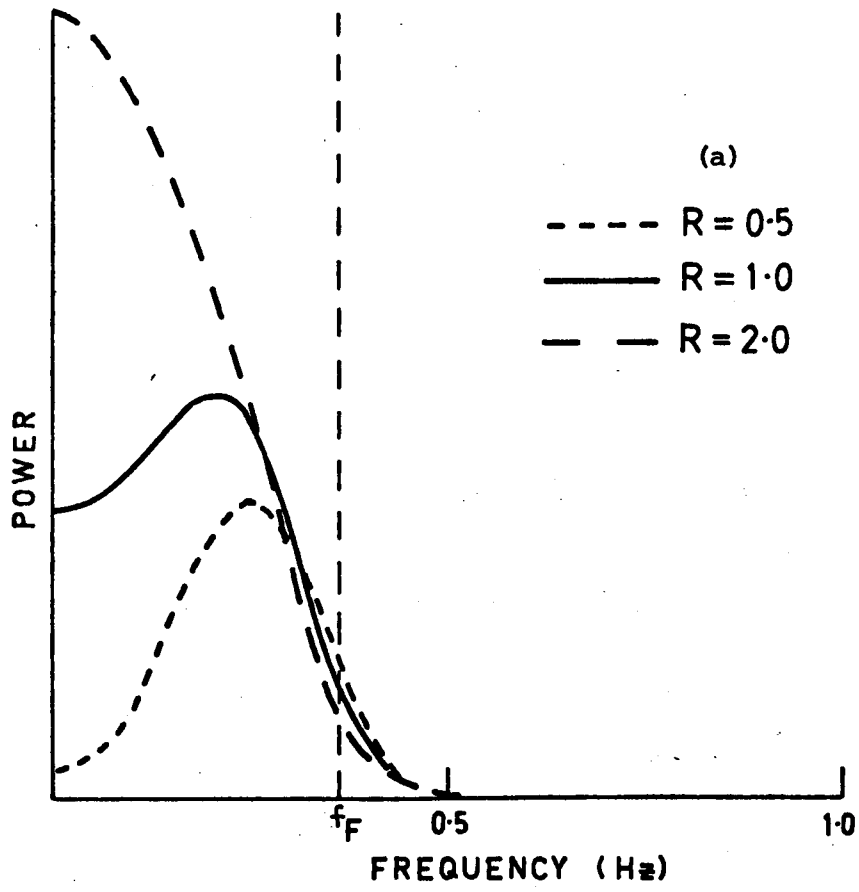

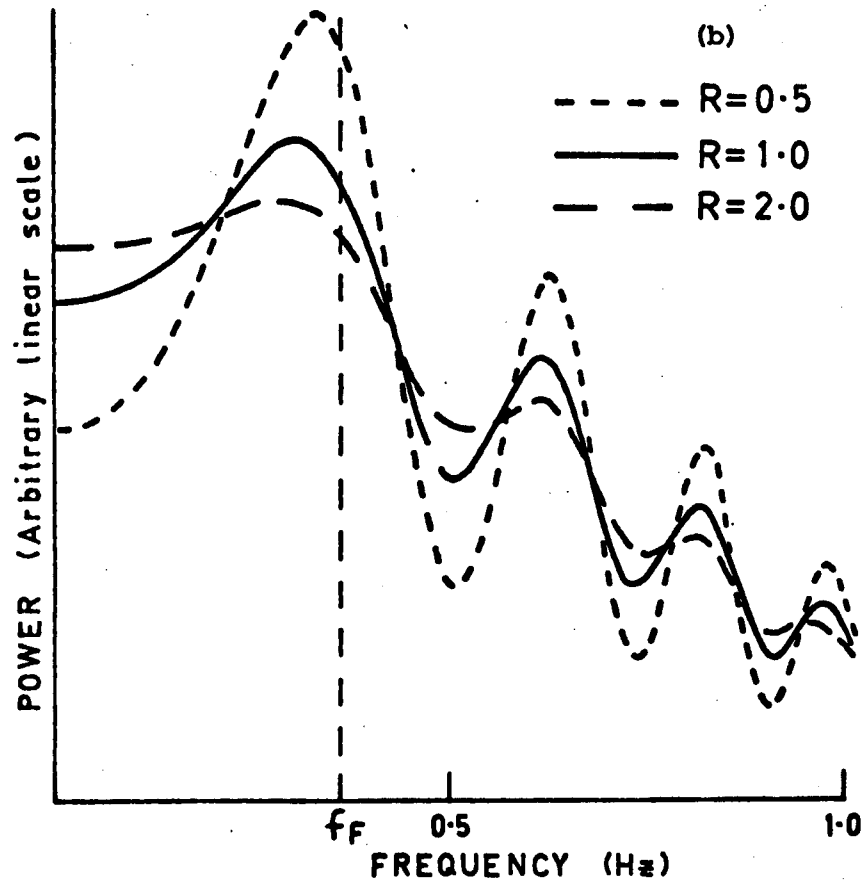

FIGURE 7.3 Temporal power spectra (a) in the near field Z_x = 0.5 and (b) in the far-field Z_x = 5.0.

There are two features in these spectra which may prove useful in the analysis of experimental observations. The first is the depression at low temporal frequencies and the second is the possible occurrence of Fresnel oscillations at higher frequencies. For a Gaussian screen the extent to which these features are evident will depend upon the scale, the axial ratio and the velocity of the irregularities and the distance of the observer from the scattering screen.

The low frequency depression can be defined in terms of a depression factor, D, defined by

$$D = \frac{P_{It}(f=0)}{P_{It}(f_{max})} \qquad \ldots(7.15)$$

where f_{max} is the frequency at which the maximum power occurs. Relation (7.7) has been evaluated for a range of values of the axial ratio, R, and the distance factor Z_x. Figure 7.4 shows contours of equal values of D as a function of R and Z_x represented by the solid lines and contours of equal values of the ratio f_{max}/f_2, where f_2 is the square-root second moment as defined previously, represented by the dotted lines. Given these two parameters, which can be derived from experimental records, it should be possible to determine the values of R and Z_x.

As was noted in Chapter 2, the diffraction pattern is not fully developed within the near-field. The effect on the scintillation index, m, and square-root second moment, f_2, can be determined by substituting (7.6) into (4.7) and (4.8). Evaluation of these integrals gives (see Appendix 3)

$$m^2 = 2\phi_o\left[1 - \cos\left(\frac{\theta_1+\theta_2}{2}\right)\cos^{\frac{1}{2}}\theta_1\cos^{\frac{1}{2}}\theta_2\right] \qquad \ldots(7.16)$$

$$f_2^2 = \alpha_1^2\left[\frac{1 - \cos\left(\frac{3\theta_1+\theta_2}{2}\right)\cos^{3/2}\theta_1\cos^{\frac{1}{2}}\theta_2}{1 - \cos\left(\frac{\theta_1+\theta_2}{2}\right)\cos^{\frac{1}{2}}\theta_1\cos^{\frac{1}{2}}\theta_2}\right] \qquad \ldots(7.17)$$

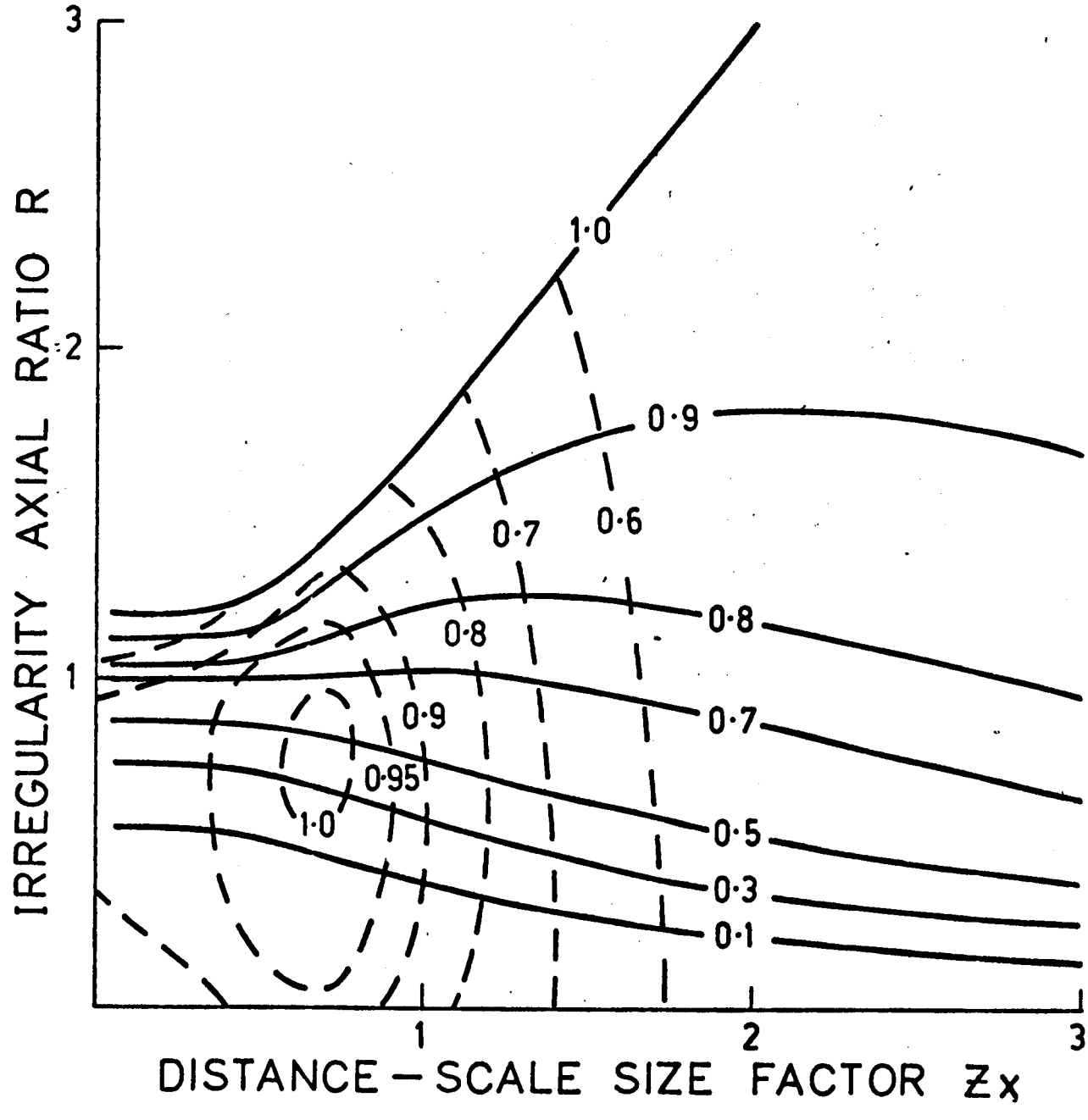

FIGURE 7.4 Contours of equal values of D (solid lines) and the ratio f_{max}/f_2 (dotted lines) as a function of the axial ratio and distance-scale factor.

Relations (7.16) and (7.17) have the limits $m^2 \to 2\phi_o$ and $f_2^2 \to \alpha_1^2$ as $z \to \infty$, which are the well-known limits for observations of weak scattering in the far-field. The terms in square brackets, which tend towards unity as $z \to \infty$, represent the effects on the scintillation index and second moment when observations are made within the near-field. These terms are plotted in figure 7.5 as a function of R and Z_x, where it can be seen that the effect of observation in the near-field is to reduce the index and to overestimate the second moment. These diagrams can be used to estimate the corrections which need to be applied to the observed values of m and f_2 to compensate for these effects once R and Z_x have been determined.

The second useful feature in the power spectra is the possible occurrence of periodic Fresnel oscillations. As noted previously, these scillations are deeper in the Bessel transform than in the Fourier transform. Provided that they can be observed it is possible to determine the ratio $V/z^{\frac{1}{2}}$ from the locations of the minima using relation (7.13).

An alternative form for the spectrum of the electron density irregularities is a power-law function of the form

$$P_{Ns}(k) = A\, k^{-\alpha} \qquad \ldots(7.18)$$

where A is a constant and $k^2 = k_1^2 + k_2^2 + k_3^2$. Any realistic power-law spectrum must erminate at some small wavenumber, k_o, in order to keep the rms fluctuation finite, and at a large wavenumber, k_c, in order to keep the second moment finite. The reciprocals k_o^{-1} and k_c^{-1} are commonly known as the inner and outer scale respectively. Analytical solutions of equation (7.2) incorporating a spectrum of the form of (7.18) have so far proved intractable. Numerical solutions are also quite difficult because of the oscillatory nature of (7.2). Young (1972) has found a semi-analytic, semi-numerical approximation to this problem. Figure 7.6 shows a temporal power spectrum from a thin Kolmogorov power-law (α=11/3) screen calculated using Young's approximation.

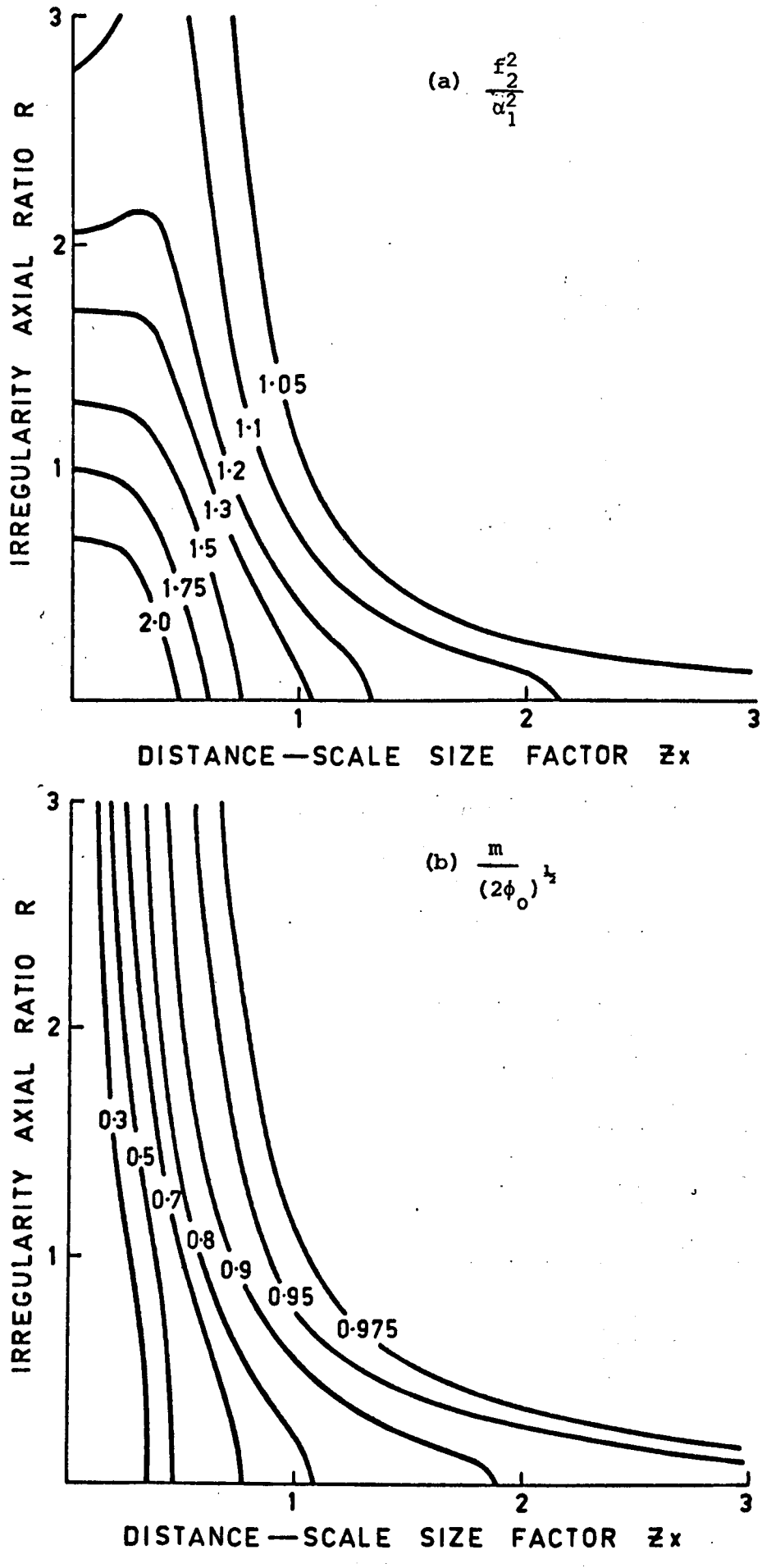

FIGURE 7.5 Near-field effects on the scintillation index and the second moment of the power spectrum.

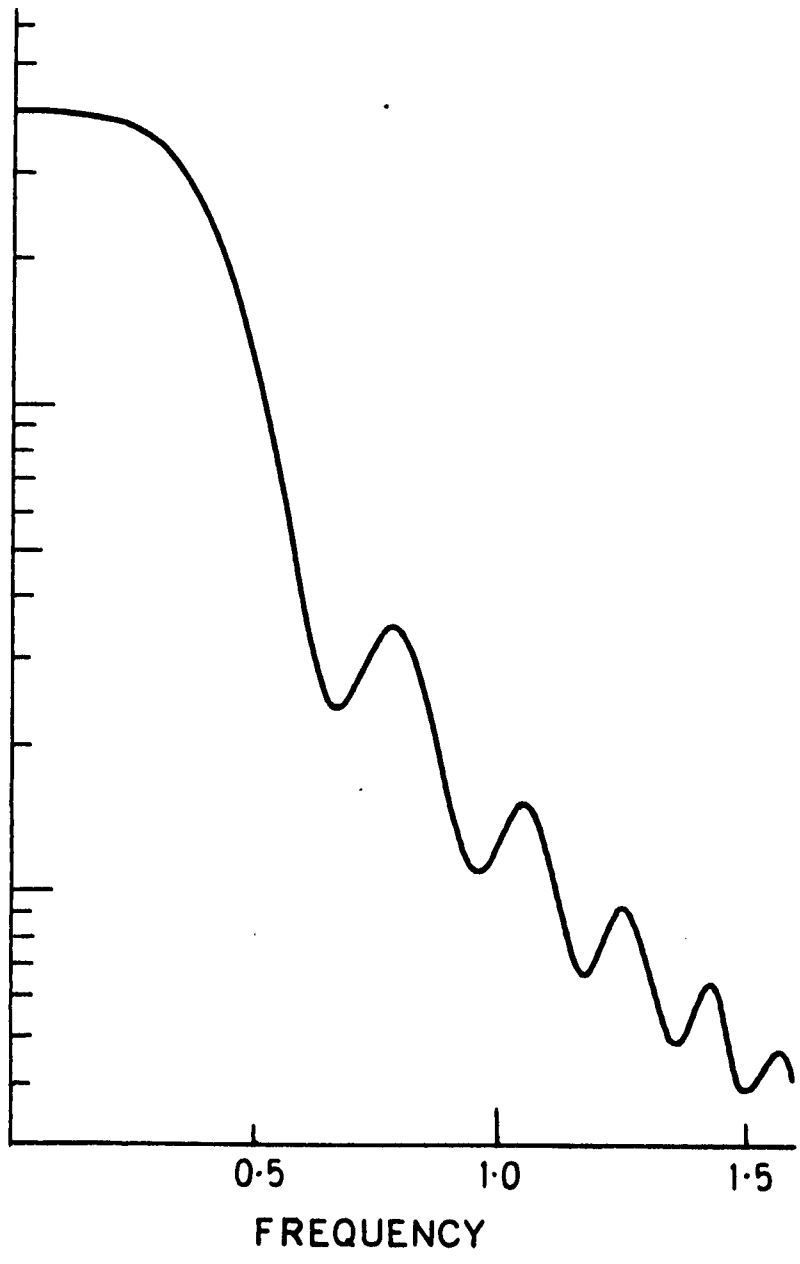

FIGURE 7.6 Power spectrum for a thin Kolmogorov screen with V = 400 km sec^{-1} and Z = 0.6 AU.

The two most significant differences between the temporal spectra for the Gaussian and Kolmogorv turbulence screens are the rate at which the spectrum falls as a function of frequency beyond the Fresnel frequency, and the relative lack of a depression at low frequencies in the case of the Kolmogorov turbulence model. The lack of a significant depression at low frequencies in the Kolmogorov model probably arises because Young's approximation does not include the inner and outer scales but considers a power-law spectrum ranging from 0 to ∞. Young argues that this approximation is valid because low frequencies are weighted as k^4 and high frequencies as $k^{-\alpha}$. A more realistic power-law model would be a function of the form

$$P_{Ns}(k) = \begin{cases} A & 0 < k < k_c \\ B\, k^{-2} \exp(-k^2/2k_o^2) & k > k_c \end{cases} \qquad \ldots(7.19)$$

where a,b are constants. This spectrum is constant at spatial wavenumbers smaller than k_c , follows a power-law variation between k_c and k_o, and decreases rapidly beyond k_o. Comparison with spacecraft observations would suggest that $k_o > 10^6$ km and scintillation observations suggest that $k_c < 10^2$ km. Numerical evaluation of (7.2) using relation (7.19) did not, however, produce a spectrum with a more significant depression at low frequencies than did Young's approximation.

The analysis of p.d.f. observations discussed in Chapter 6 suggested that at metre wavelengths the scattering region cannot be regarded as thin, especially at large distances from the sun. A spherically-symmetric 3D model was therefore developed to calculate the temporal spectrum at a given solar elongation by summing the contributions from a large number of independent layers within a realistic model of the solar wind. The electron density and solar wind velocity were based on the models

given by equations (5.6) and (5.7). The scale in the Gaussian model assumed a variation with heliocentric distance as given by (5.8) and the Kolmogorov model was based on the assumption that $\alpha = 11/3$ at all distances from the sun. Figure 7.7 shows the effect on the Gaussian model where it can be seen that both the low frequency depression and the Fresnel oscillations are badly smeared by integration over an extended medium. Similar results applied in the case of the Kolmogorov model.

The final feature which must be considered when considering theoretical spectra is the effect of extended source structure. Since source structures at metre wavelengths are rather uncertain, and there are several other factors which will blur the Fresnel oscillations, we will not consider this effect in any detail here. We simply note the result presented by Bourgois (1972) that in the case of a Gaussian source with half-diameter ψ_i in the x_i direction we can define a parameter

$$\mu_i^2 = \frac{1}{1 + 0.36\ (Z_i\psi_i/a_i)^2} \qquad \ldots(7.20)$$

then the observed temporal power spectrum will be given by relations (7.7) and (7.12), but with the parameters θ_i replaced by Ψ_i where

$$\tan \Psi_i = \mu_i^2 \tan \theta_i \qquad \ldots(7.21)$$

The effect of this modification is also to blurr out the Fresnel oscillations if they are present.

7.3 COMPARISON WITH OBSERVATIONS

The power spectra of the observational data were derived from the experimental records using the techniques discussed in Chapter 4 and Appendix 2. The final power spectral resolution was 0.084 Hz and the variances of the spectral estimates, $P_k(f)$, derived from a single block of data were

$$\mathrm{Var}(P_k) = P_k^2/8$$

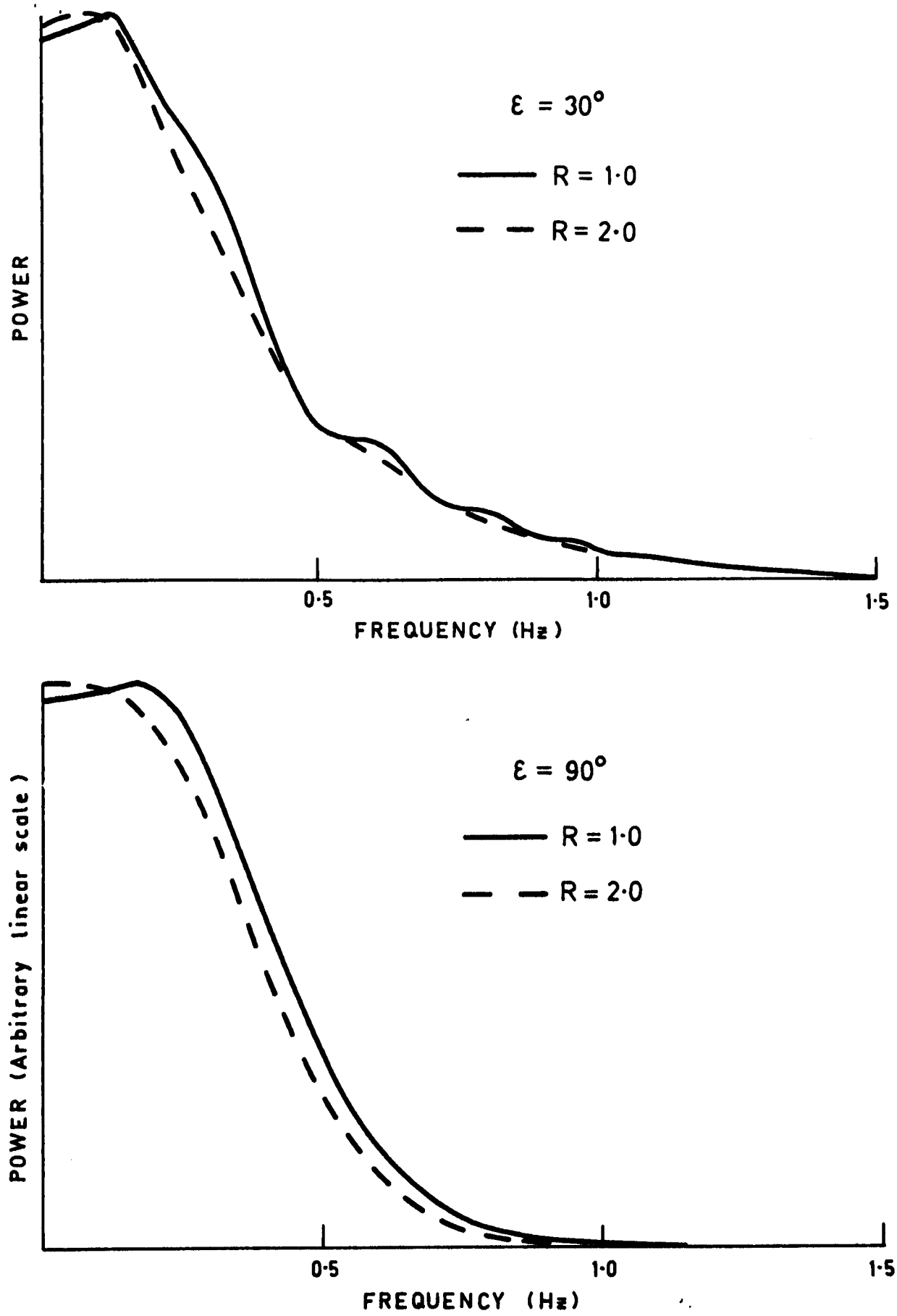

FIGURE 7.7 Power spectra for a 3D Gaussian model

That is, the rms deviation of the spectral estimates, σ_{P_k}, was

$$\sigma_{P_k} = P_k/8^{\frac{1}{2}} \simeq 35\% \; P_k \qquad \ldots(7.22)$$

The spectra for each source observation were averaged over N blocks of data giving a final power spectrum with variance

$$\mathrm{Var}(P_k) = \frac{P_k^2}{8N} \qquad \ldots(7.23)$$

where N ranged from 3 to 15. Altogether some 600 observations were processed in this manner. Selected records were also processed to provide the Bessel transfom, either from the pre-whitened transform (Lovelace et al, 1970)

$$B_{It}(f) = \frac{-1}{(2\pi)^2 f} \int_0^{\tau_m} \tau \, d\tau \, J_1(2\pi f\tau) \, \frac{d\rho(\tau)}{d\tau} \qquad \ldots(7.24)$$

where $\rho(\tau)$ is the temporal autocorrelation function of the record, or alternatively by the equivalent sec θ transform (Ward et al, 1972)

$$S(f \sec\theta) = \frac{-d}{df} \int_0^{\pi/2} P_{It}(f \sec\theta) \, d\theta \qquad \ldots(7.25)$$

The final variance in the Bessel transform was generally in the order of 25%, and the Bessel transforms were always much less stable than the power spectra. Approximately 100 records were processed to produce the Bessel transform in addition to the power spectrum.

Analysis of the final average power spectra involved fitting the spectra to several models, including Gaussian, exponential and power-law models. Care had to be taken during this process to eliminate those records which displayed any of several artifacts introduced by the system. The most serious of these was a severe leakage of power at a frequency of 1 Hz into the data. This component arises because the beam forming in the heliograph is carried out once each second and the beam is destroyed for a short period each second while the scanning counters are updated. Although this feature could in many cases be removed by careful filtering with a high-Q digital filter it provided a serious limitation to the interpretation of the

observed spectra.

The power spectra are likely to be affected by the Fresnel filter at frequencies less than about 0.4 Hz and rarely exceeded the noise spectra beyond about 1.5 Hz. Consequently there is only a relatively narrow frequency range over which the observed spectra can be compared with the theoretical models. It was found that all three of the models could be fitted to a significant proportion of the observed spectra and no particular model could be chosen in preference to any other model. A similar result was found when trying to compare the observed spectra directly with theoretical spectra derived from the relations discussed in the previous section of this Chapter. In general the effects of an extended medium, probably containing considerable variations in the form of localized plasma streams, and unknown source structure limit the interpretation of power spectra at these wavelengths.

Relation (2.26) shows that in the case of nearly isotropic irregularities it should be possible to reconstruct the two-dimensional form of the density irregularities from the Bessel transform. The temporal spectra must first be converted into spatial functions using an estimate of the solar wind velocity. The spatial spectrum is then obtained by applying the inverse-Abel (or sec θ) transform. The effects of the Fresnel filter can be removed by dividing the reconstructed spatial spectrum by the $\sin^2$ Fresnel factor. This process was attempted on a number of the records but the results were also rather inconclusive, partly because the solar wind velocity is not known and must be guessed for most of the records, and partly because of the limited statistical accuracy in the Bessel transforms obtained.

One feature which allows some conclusions to be derived from the observed spectra was the occurrence of dips in the power spectrum at low frequencies. In general the power spectrum was flat between o.1 and 0.4Hz, as has been found by most observers, but on several rare occasions the spectra exhibited depressions at low frequencies. These were also the only occasions on which the Bessel transform displayed Fresnel oscillations which could be determined with any confidence. These observations were all related to transient or corotating disturbances in which the majority of the scattering occurred in a relatively thin region in space. The Bessel transforms were used to determine V by assuming a value of Z. The analysis of the low frequency depression was made using the methods outlined in the previous section. Fig 7.7 shows one example of the power spectrum and sec 0 transform for such an event. Table 7.1 presents the values derived from all events. The scale of the irregularities is consistent with previous observations but the axial ratio is consistently less than unity, unlike the usual values of 1.2-2.0 found by spaced received observations. The velocities tended to be lower than expected on the basis of the available spacecraft data for these events.

7.4 DISCUSSION

A combination of practical difficulties in obtaining reliable spectra and the effects of integration through an extended medium have precluded any significant results being obtained from this analysis. Houminer (1972) presented an analysis of power spectra at metre wavelengths and concluded that the spectrum was a power-law of the form $P(f) \alpha f^{-1.4}$. Many of the observations analyzed in our data were consistent with power-law variations with exponents ranging between 1.5 and 2.2. However, just as

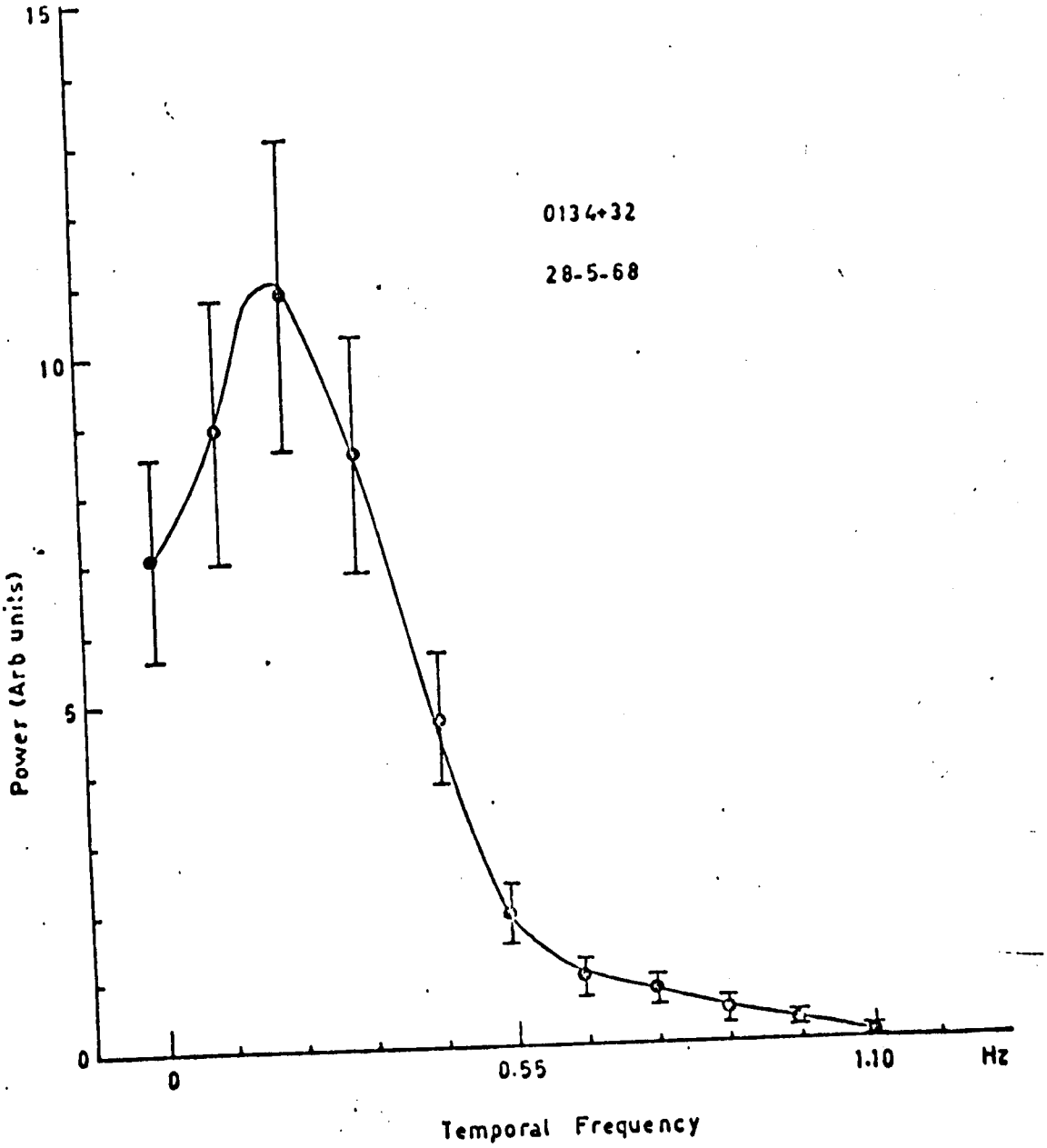

FIGURE 7.8a Power spectrum for a source affected by a thin region of turbulent plasma.

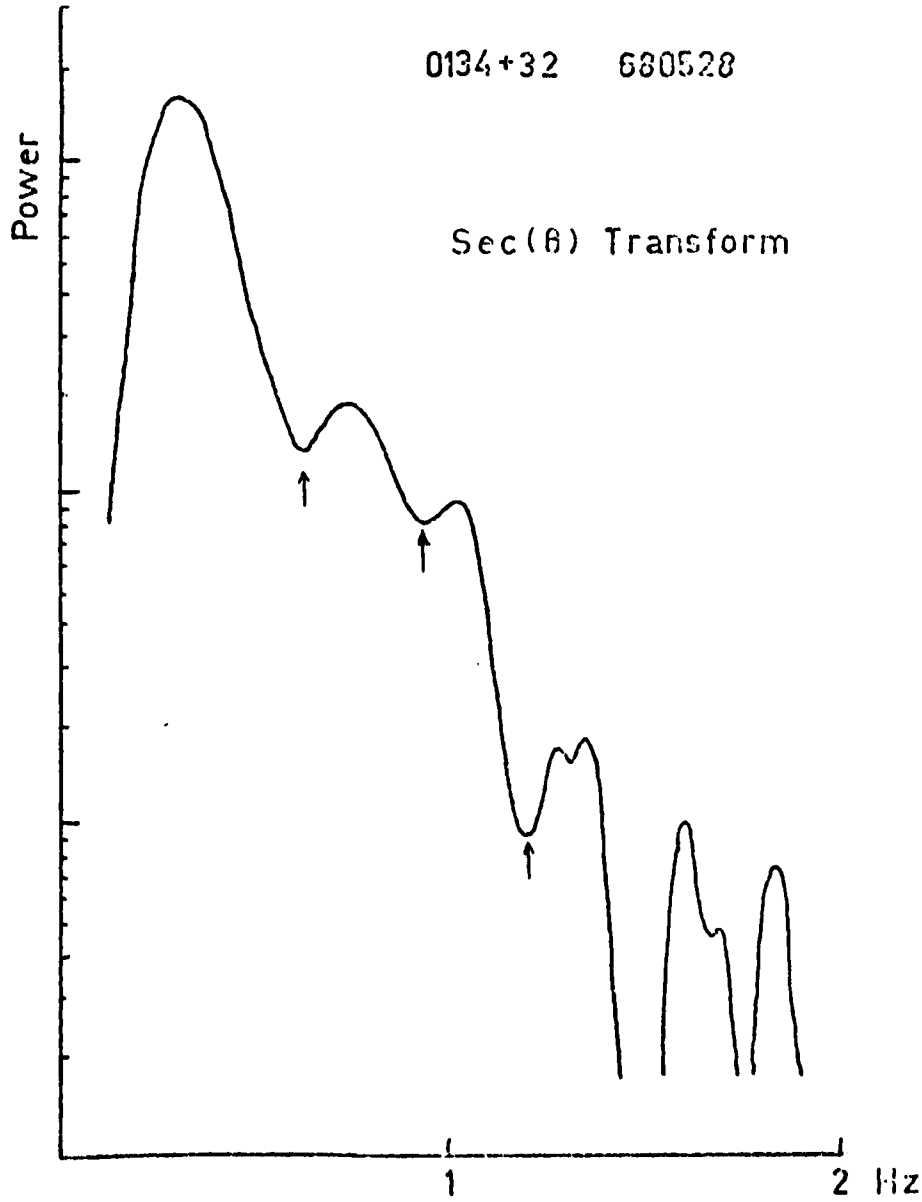

FIGURE 7.8b Bessel transform for a source affected by a thin region of turbulent plasma.

TABLE 7.1 PARAMETERS DERIVED FROM SPECTRAL OBSERVATIONS

Source	Date	a (Kms)	R	v (Km sec^{-1})	Z (AU)
0134+32	680528	80	0.85	315	0.4
0933+04	690611	78	0.70	350	0.4
1226+02	690611	95	0.72	340	0.5
1309-22	690612	88	0.80	380	0.6
1309-22	690616	75	0.80	350	0.6
1226+02	700608	85	0.90	370	0.4
1226+02	700617	83	0.74	360	0.4

many observations were consistent with Gaussian spectra and no preference could be discerned.

Cronyn (1972) has shown that an electron density spectrum with exponent α will be characterized by an IPS spectrum with exponent $\alpha - 1$ and a spacecraft spectrum $\alpha - 2$. The available observations provide estimates for the exponent of the density spectrum ranging from 1.4 to 4.5. Thus although most recent observations suggest a power-law model there is wide disagreement as to the details of that model. Recently detailed spacecraft observations have become available which suggest that the density spectrum is basically power-law, with an additional component with scales of the order of the proton gyroradius. Future scintillation observations should be made closer to the sun at higher frequencies, in order to avoid the problems of an extended medium, and should consider the possibility of a two component model consistent with the spacecraft observations.

CHAPTER 8

CORONAL BROADENING OF THE CRAB NEBULA

8.1 INTRODUCTION

The outer corona, at heliocentric distances between 5 and $20R_o$, is of particular interest to studies of the solar wind since it is the region in which the coronal plasma is accelerated to beyond the gravitational escape velocity. The exact nature of the acceleration mechanism is dependent on conditions existing in this region, and in turn the acceleration process determines the conditions existing within the solar wind plasma at larger heliocentric distances. Radio-wave scattering studies provide one convenient means of probing this region which, at least until the recent advent of spacecraft-borne coronagraphs, has been completely outside the range of white-light coronagraphs.

Interplanetary scintillation studies of the outer corona have been relatively limited, but coronal broadening observations have been carried out since 1955. These observations have yielded information on the variation in scattering as a function of distance from the sun, observing frequency and solar cycle. Since most observations have employed at most 2 or 3 interferometers the major limitation of these studies has been the need to assume a model for the brightness distribution of the broadened image. This limitation was removed with the use of the Culgoora Radioheliograph to measure the complete two-dimensional brightness distribution (Harries et al, 1970).

The results of observations recorded from 1969 to 1971 using the Radioheliograph at 80MHz have been discussed by Blesing and Dennison (1972)

These observations have been continued over the decreasing phase of the solar cycle, from 1972 to 1974, at frequencies of 80 and 160MHz and the results are presented in this chapter. Before proceeding with the discussion of the analysis and interpretation of the results however, it is necessary to briefly discuss the mode of operation of the radioheliograph in order to understand its use, and possible limitations, for coronal broadening observations.

8.2 OBSERVATIONAL TECHNIQUES

The radioheliograph has been fully described by Wild (1967) and his colleagues. The aerial system consists of 96 steerable parabolic reflectors spaced evenly around a circle of 3km diameter. Connecting the aerials in phase results in the formation of a beam with a power polar diagram represented by the squared Bessel function J_o^2. This beam has the undesirable feature that it possesses relatively large sidelobes, with the first sidelobe being ~15% of the main lobe. Introducing phase increments $\frac{2\pi k}{96}$ between adjacent aerials produces other beams represented by higher order Bessel functions J_k^2, where k is an integer. By adding and subtracting beams of different orders a polar diagram with sidelobes reduced to less than 2% of the main lobe can be formed.

By the use of a branching network the radioheliograph simultaneously produces 48 such independent beams aligned in a N-S direction. At the zenith these beams have a separation of 2'.1 arc and a half-power width of 3'.75 arc at 80MHz; the corresponding values at 160MHz are a factor of two smaller. In the normal mode of operation these 48 beams are simultaneously swept from East to West across a 2^0 square of sky, taking up

60 discrete positions within each scan. Thus each scan produces two arrays of 48 x 60 data points, one in each of two polarizations, with RH and LH circular polarizations being used for these observations. The data was displayed in real time as an array of intensity modulated points on a c.r.t. display and recorded in digital form on magnetic tape. With a full scan in the E-W direction the picture repetition rate is 1 sec^{-1} but by reducing the field to 30 points in the E-W direction, a repetition rate of 2 sec^{-1} can be obtained.

The method of beam steering employed by the radioheliograph has an effect on the shape of the sampled section of sky as well as on the shape and widths of the beams. To convert the picture into an RA-Dec co-ordinate system the array of points must be skewed and elongated. The 'distortion coefficients' associated with this transformation are approximately linear over the 2^0 field of view and are dependent on the Hour Angle and Declination settings.

Since the 96 aerials constitute a ring of discrete receiving points, rather than a continuous annulus, grating responses occur at specific angular distances from the central beam. The spacing of the aerials around the circle was chosen to place the first grating response just outside the field of view. The height of this first grating response is ~5% of the main lobe and although it presents no significant problem for solar observations, confusion can occur when a strong radio source is situated on the grating response. This proves to be a problem when using the radioheliograph for observations of the coronal broadening of the Crab Nebula since at certain Sun-Crab separations the sun will lie in the direction of the grating response, producing an arc-shaped image across the picture. This problem was found to be much more serious at 160MHz than at 80MHz.

Records were obtained during June 10-20 in each of the years 1972 to

1974 at frequencies of 80 and 160MHz. The position of the Sun relative to the Crab Nebula on each of these days is shown in Figure 8.1. Observations, lasting between five and thirty minutes depending on the signal to noise ratio, were made each day at the time of source transit and approximately two hours before and after transit. During those days when the source was not significantly broadened a picture repetition rate of 2 sec $^{-1}$ (half-scan) was used. Each of the 48 integrator outputs has a DC offset and a calibration was required to enable the pictures to be corrected for these offsets during the analysis. Each 80MHz observation was preceded by a calibration recording in which a resistive load replaced the aerials. A resistive load was not available at 160MHz and the calibration was performed by recording data with 49 dB attenuation inserted in the aerial inputs.

The data was recorded in real time on 7200 ft reels of magnetic tape and a log was kept of all interference occurring during each recording. The data on this tape was photographed, with an integration being achieved by advancing the film once every 16 scans. This film was used to select appropriate sections of the data for transferral to computer-compatible magnetic tape. The length of data selected for each observation depended on the signal to noise ratio, and ranged from 3 min for the unbroadened source to 20 mins on June 15.

8.3 DATA ANALYSIS

In order to improve the signal to noise ratio of the data the individual scans were integrated over a number of frames in the computer. During this process all scans containing faulty data (due to tape transmission errors or impulsive interference) were removed. The data was integrated over 30, 120 and the total number of frames recorded, and the analysis procedure was carried out on all three sets of integrated data. The best signal to noise ratio was obtained from the integrated record of all the data, but the shorter integrations were used to provide a check on ionospheric

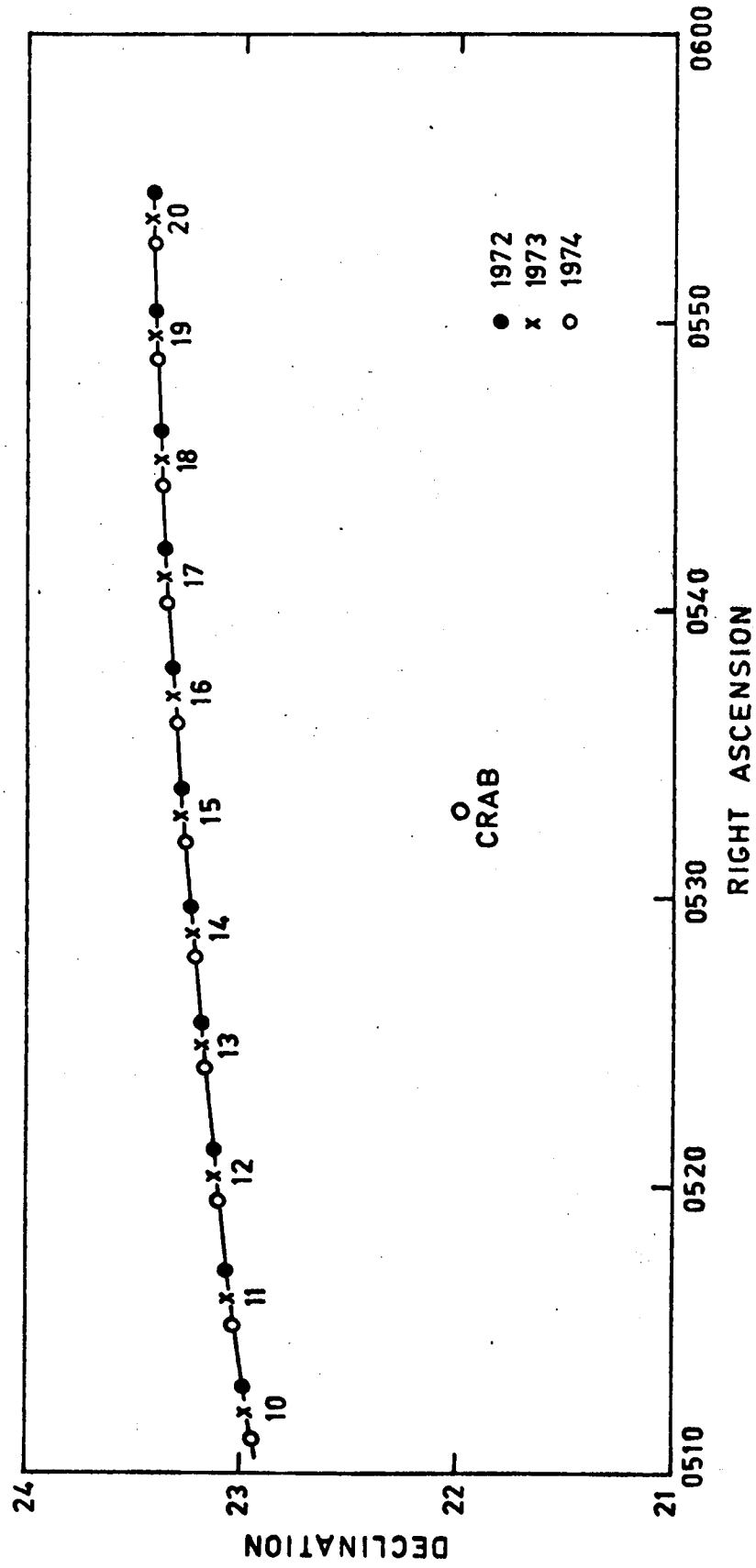

FIGURE 8.1 Positions of the Sun relative to the Crab Nebula during June 1972 to 1974.

refraction.

As noted above, each of the 48 integrator outputs has a DC offset and these offsets must be normalized during the computer reduction in order to level the picture background. A set of 48 normalizing coefficients were evaluated for each observation by finding the average value of the 60 points in each scan when the resistive load was attached. These absolute offset values were subtracted from the Crab Nebula data prior to the subsequent analysis.

During June 1972 there was considerable solar activity and although the sidelobes are small compared with the power gain of the beam, the sidelobe intensity from the active sun is much more intense than the response from the Crab Nebula in the main beam. Consequently the picture was frequently dominated by sidelobe interference and it was necessary to carefully select the data for analysis. Although there was no major flare activity during the 1973 and 1974 observations there was a persistent noise storm on at least one of the two frequencies during both sets of observations. Frequently one or more aerials was switched out of the system for maintenance purposes and this also served to degrade the sidelobe structure.

In those cases where the active region on the sun was emitting polarized radiation it was possible to suppress the effects of the sidelobes by taking advantage of the two polarizations which were recorded. The method is based on the assumption that the sidelobe structure in the two polarizations is identical but that one polarization is more intense than the other. The Crab Nebula is unpolarized and possesses the same intensity in both pictures and therefore by increasing the amplitude of the picture with the weaker sidelobe structure until it matched the stronger structure, in a least-squares sense, and then subtracting the two pictures it is possible to

reduce the sidelobe structures relative to the image of the Crab. The effectiveness of this reduction is dependent on the degree of polarization of the solar noise; application of the technique to a picture containing unpolarized sidelobe structures results in a picture with increased variance and a reduced image of the Crab.

Another procedure was necessary on those days when the sun lay in the direction of the grating response, producing an arc-shaped image across the picture. On these days the time of the observations was arranged so as to avoid the grating response as far as possible. The average cross-section of the observed response was estimated from the data, and an arc-shaped enhancement with this average cross-section centred on the sun was subtracted from each picture. This method relies on a knowledge of the exact distance between the centre of the sun and the line of sight to the source. Consequently, this method was not particularly successful on those occasions when there was a strong active solar noise source towards the solar limb. Some reduction was of course achieved in the process of sidelobe reduction in the case of polarized noise storms. Figure 8.2 shows a contour plot illustrating the sidelobe structures and grating response. The sun in this diagram is above the top LH corner at a distance of 8 R_o from the Crab. The sidelobe structures have been reduced in this contour plot but are still visible to some degree. The grating response has not been removed and is clearly visible on the RH side of the diagram. The beam shape and the contour levels are shown below the diagram.

A series of contour plots were produced for all the integrated data containing 120 frames and the total integration. These were used to check the quality of the data before carrying out model-fitting to be described below, and to look for any unusual image shapes. The results of the model-fitting were also compared with the contour plots as a check on their validity. Figure 8.3 shows a typical contour plot when the source was 6.4R_o

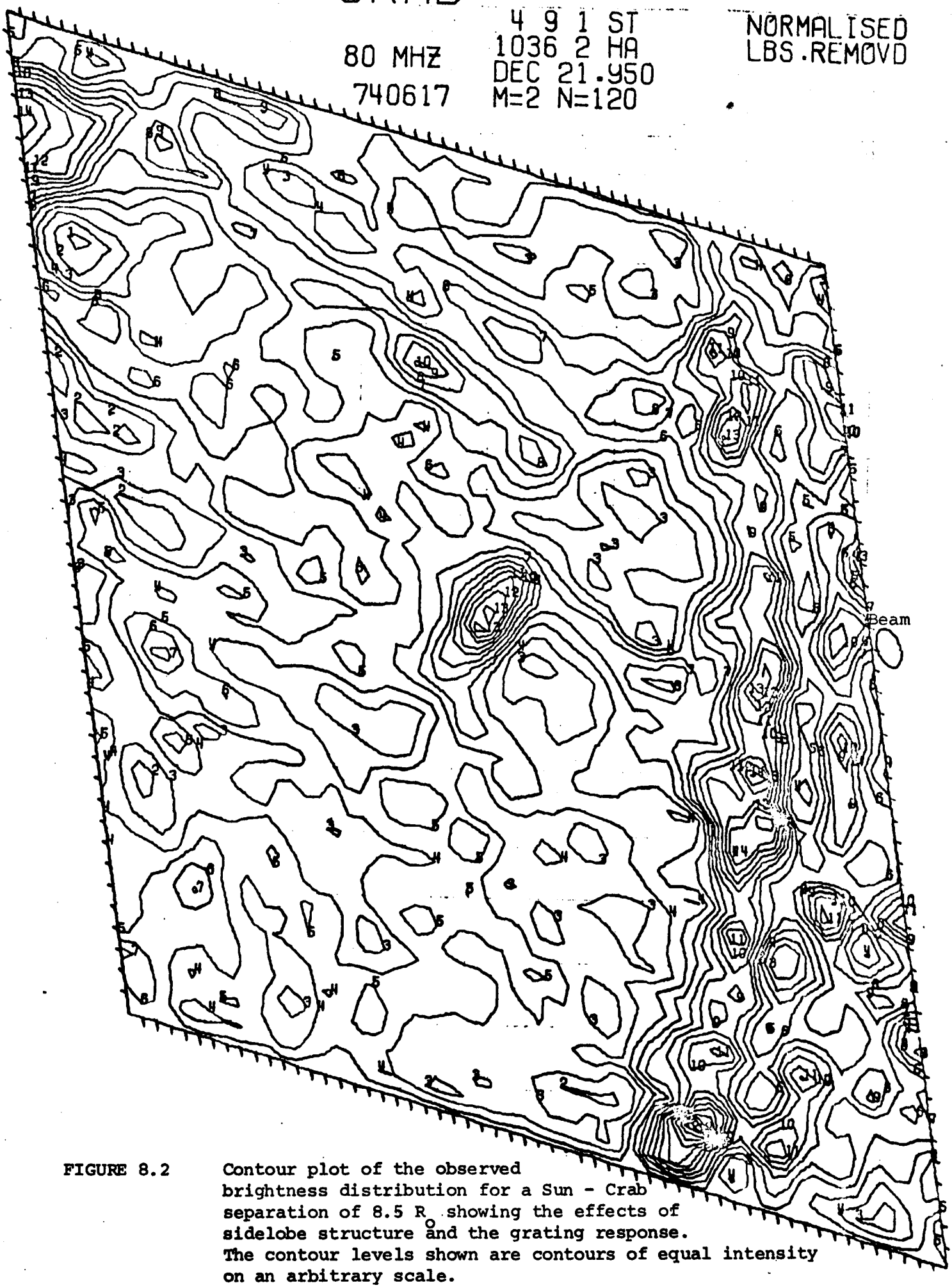

FIGURE 8.2 Contour plot of the observed brightness distribution for a Sun - Crab separation of 8.5 R_o showing the effects of sidelobe structure and the grating response. The contour levels shown are contours of equal intensity on an arbitrary scale.

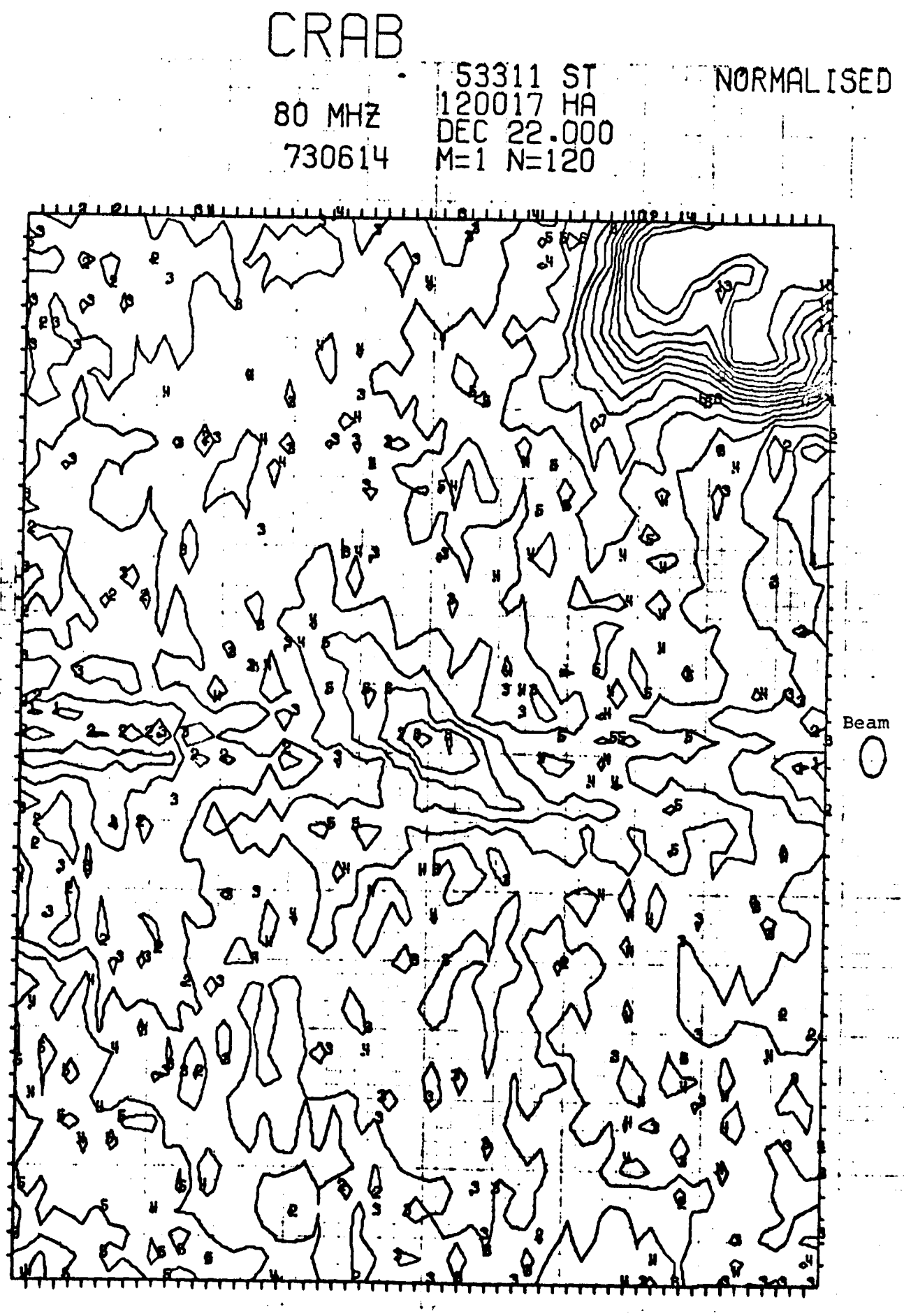

FIGURE 8.3 Contour plot of the brightness distribution for a Sun - Crab separation of 8.5 R_o showing the effects of imperfect normalization.

from the sun, which appears in the top RH corner. The general linear trend in the centre of the diagram is a fault in the initial normalization and illustrates the usefulness of these contour plots in correcting the reduction procedures and determining the quality of the data. The beam positions are marked by tick marks along each axis and the beam shape is illustrated by the ellipse on the RH edge of the plot.

A least-squares procedure was used to fit an elliptical Gaussian model of the form

$$B(x,y) = A \exp(-Bx^2 - Cy^2) \qquad \ldots (8.I)$$

to a section of the picture centred on the image of the Crab Nebula. Although this model does not take into account the slight curvature of the image close to the sun, tests have shown that the errors introduced are small. This least-squares fit provided estimates of the background intensity, the peak intensity of the source, the radial and tangential widths, and the orientation of the image. An example of the model fitted to some observed data is shown in Figure 8.4. The observed brightness distribution represents a convolution of the scattered distribution with both the radioheliograph beam and the intrinsic brightness distribution of the Crab Nebula. The scattering parameters were obtained by deconvolving the beam shape and the intrinsic source shape from the fitted ellipse parameters.

8.4 RESULTS

The numerical model fitting and deconvolution procedure provided estimates of the widths of the major and minor axes and the orientation of the scattering ellipse. On all occasions except June 12, 1973, the broadened image was aligned with the minor axis in the radial direction, the mean deviation from the radial being $3^0 \pm 5^0$. The variations in tangential and radial scattering at 80MHz are shown in Figure 8.5 as a function of distance from the sun. During 1973 and 1974 there was no discernible difference between approach and recession of the source. During 1972 there were some

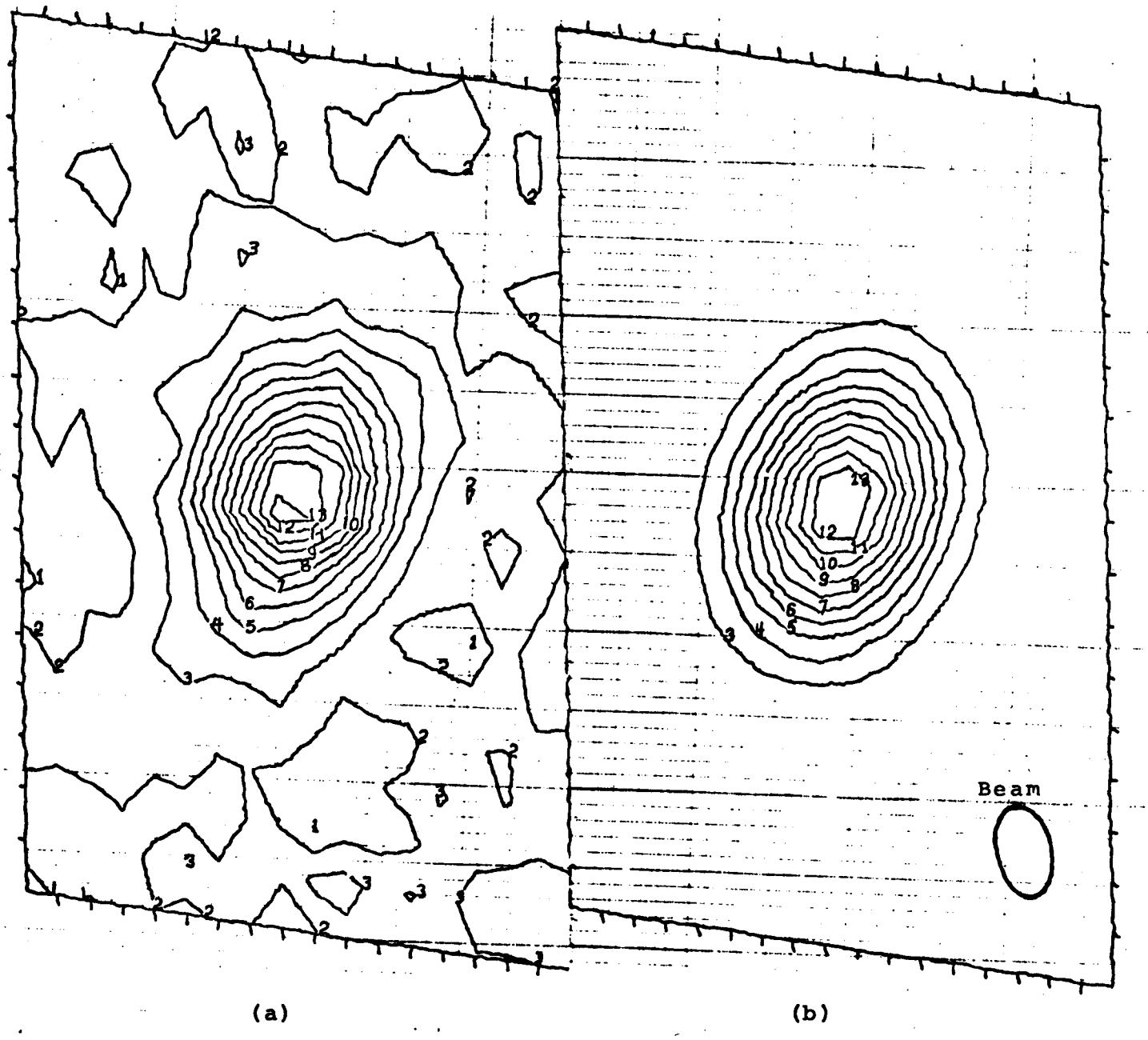

FIGURE 8.4 Comparison of the observed brightness distribution (a) with the fitted elliptical Gaussian distribution (b) on June 18, 1973 when the Crab was 12 $R_\odot$ from the Sun. This diagram is an enlargement of the central region covered by the previous contour plots. The beam separation is marked by the ticks on the axes and the shape and orientation of the beams are shown in the lower RH corner.

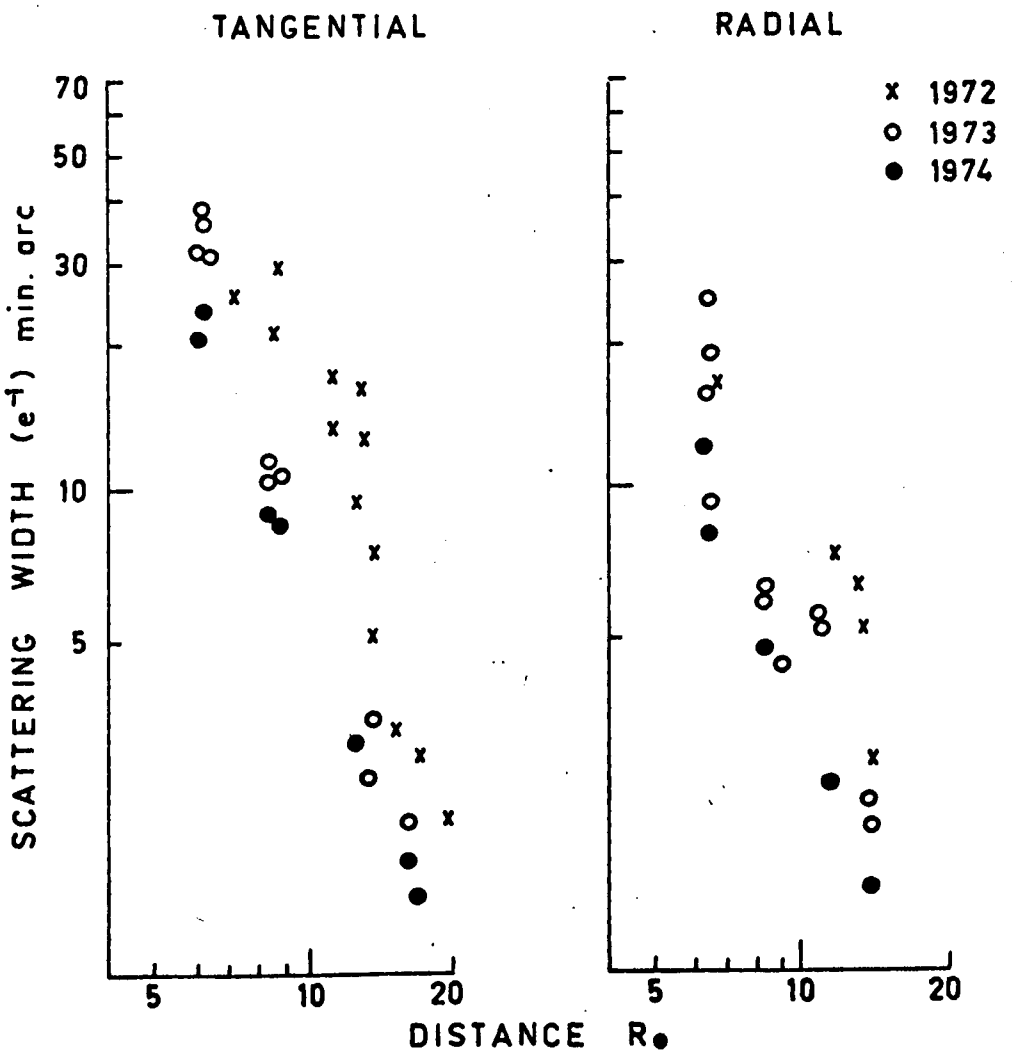

FIGURE 8.5 Variation of radial and tangential scattering at 80 MHz as a function of distance from the Sun.

differences evident, with scattering during the period June 14 to 19 being somewhat greater than the scattering at comparable distances during the period June 10 to 14.

Previous studies have shown that the variation of scattering with distance from the sun can, at least in the range 5 - 20R_o, be expressed as a simple power-law variation of the form $\theta(R) \propto R^{-\alpha}$. Power-law models of this form were fitted to the 80MHz data for each of the three years giving exponents

$$\left.\begin{aligned} \alpha_t &= 2.4 \pm 0.3 \\ \alpha_r &= 2.2 \pm 0.2 \end{aligned}\right\} \text{1972}$$

$$\left.\begin{aligned} \alpha_t &= 1.8 \pm 0.2 \\ \alpha_r &= 1.7 \pm 0.2 \end{aligned}\right\} \text{1973, 74} \qquad \ldots (8.2)$$

where the subscripts t, r represent the tangential and radial scattering, respectively. The major difference between the 1973 and 1974 observations was the overall decrease in scattering. The axial ratio rarely exceeded 2:1 between 1972 and 1974. These results can be compared with the previous Culgoora observations for which

$$\left.\begin{aligned} \alpha_t &= 2.5 \pm 0.3 \\ \alpha_r &= 2.1 \pm 0.4 \end{aligned}\right\} \text{1969- 70}$$

$$\left.\begin{aligned} \alpha_t &= 2.0 \pm 0.2 \\ \alpha_r &= 1.6 \pm 0.3 \end{aligned}\right\} \text{1971} \qquad \ldots (8.3)$$

The variation of axial ratio as a function of distance from the sun is shown in Figure 8.6. During 1969-71, the axial ratio was generally ~2:1 beyond about 10R_o but appeared to increase to ~4:1 between 5 and 10R_o

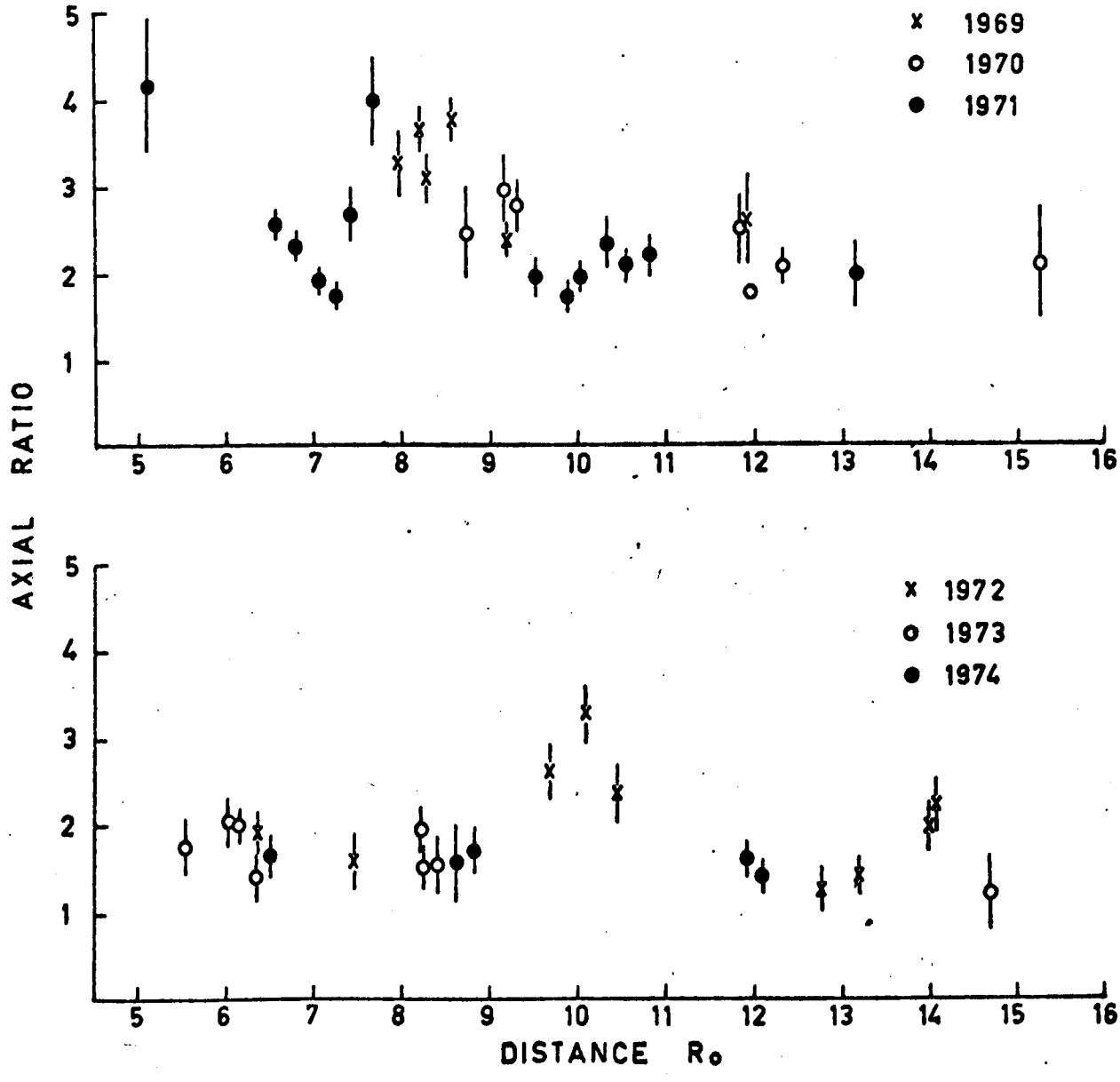

FIGURE 8.6 Variation of the axial ratio of the scattering distribution as a function of distance from the Sun. The 1969 to 1971 results of Dennison and Blesing (1972) are also shown for comparison.

(Dennison and Blesing, 1972). No such trend was obvious during 1972-74 when the axial ratio was between 1.5:1 and 2:1 at all distances.

Solar activity, as indicated by the smoothed sunspot number, temporarily increased during the period May - August 1972 and Koomen (private communication) has suggested that the whole corona was undergoing a major structural change during this period. This probably accounts for the enhanced scattering during 1972 relative to 1971 and 1973.

Analysis of the 160MHz data was considerably more difficult than the 80MHz data. This was partly because in all three years there were many days in which solar noise storms seriously contaminated the data and because removal of the grating response proved more difficult at the higher frequency. In addition, deconvolution of the scattering ellipse from the observed brightness distribution was quite difficult because the scattering is much weaker at 160MHz and the source itself is elongated at this frequency. Figure 8.7 shows the ratio of the tangential scattering at 80MHz and 160MHz as a function of distance from the sun. In general, when reliable estimates of the scattering could be determined, the results were consistent with the λ^2 dependence, predicted by strong scattering theory.

8.5 DISCUSSION

The variation in the tangential scattering as a function of distance from the sun is compared with previous observations. (Okoye and Hewish, 1967; Blesing and Dennison, 1972) in Figure 8.8, where the 80MHz data have been scaled to 38MHz assuming a λ^2 dependence. The results are in good agreement with previous observations, both with respect to the degree of scattering and the general radial gradient. It is interesting to compare the change in scattering during the decreasing phase of the present solar

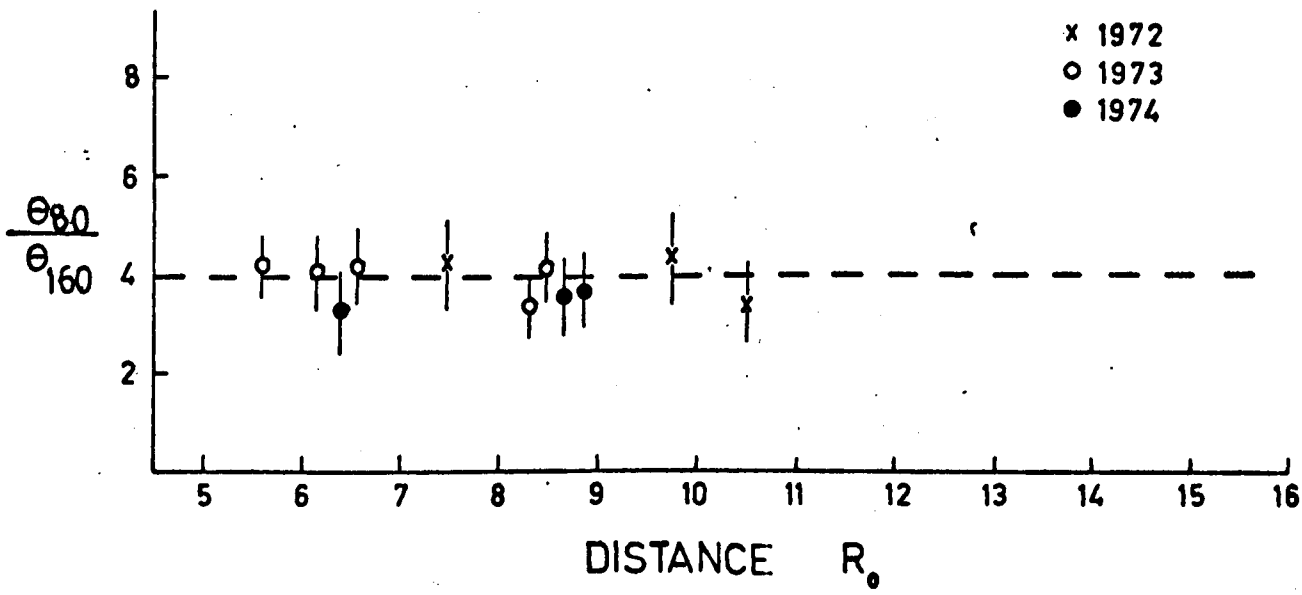

FIGURE 8.7a Comparison of the tangential scattering widths at 80 and 160 MHz as a function of distance from the Sun.

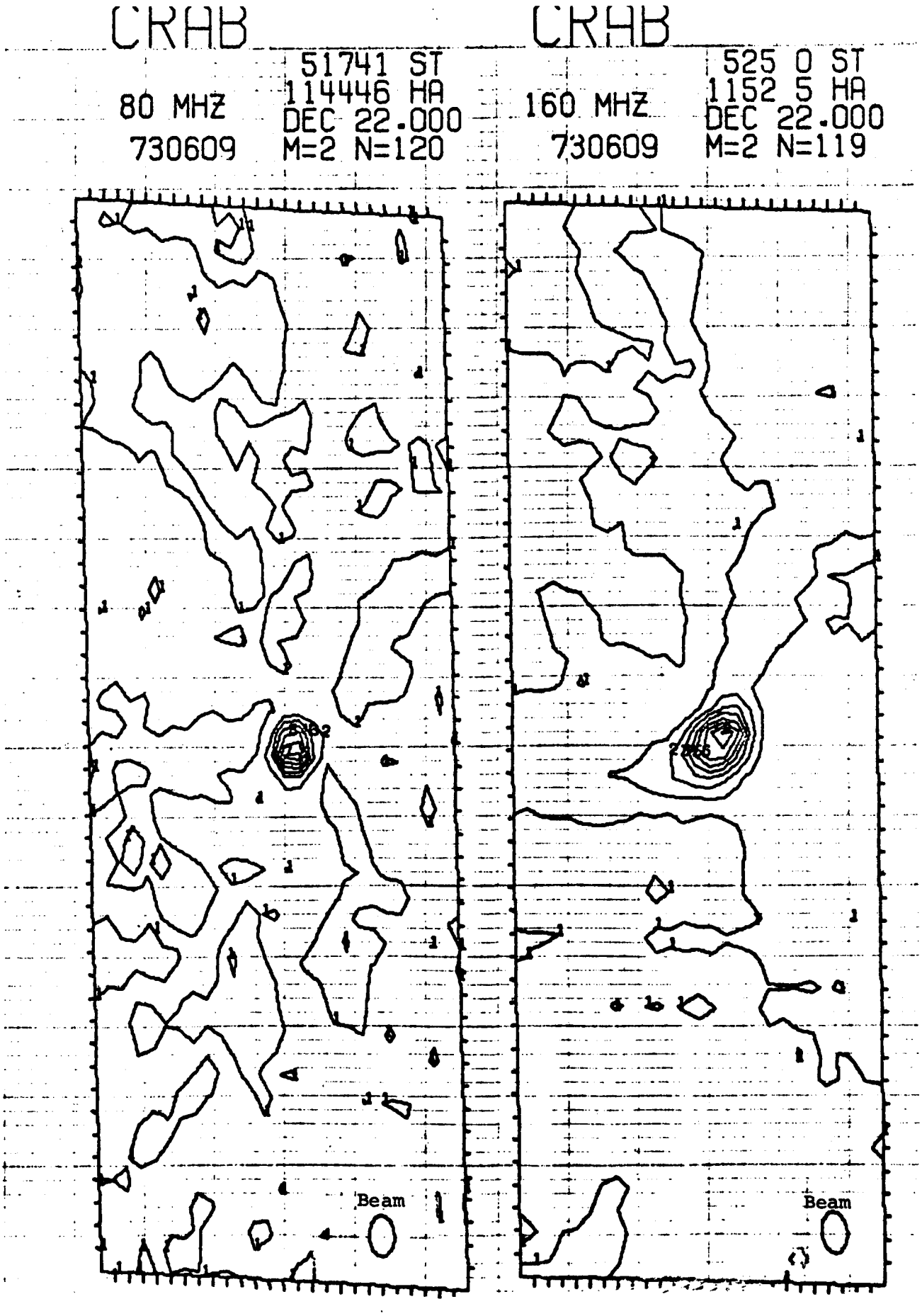

FIGURE 8.7b Unbroadened images at 80 and 160 MHz for a Sun - Crab separation of 21.5 $R_\odot$. Note that the scale of the 160 MHz diagram is twice that of the 80 MHz diagram in order to show the contours clearly.

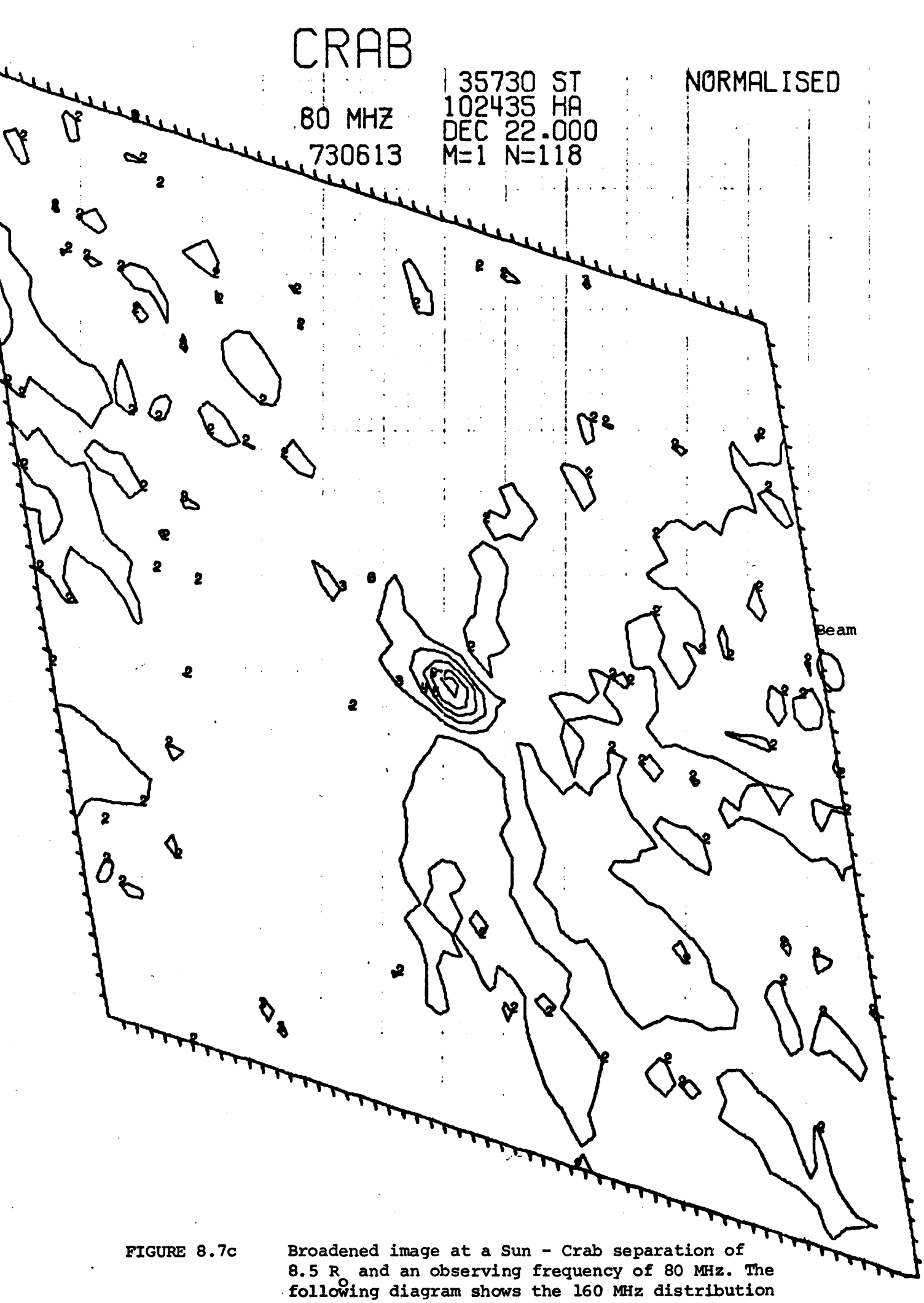

FIGURE 8.7c Broadened image at a Sun - Crab separation of 8.5 R_o and an observing frequency of 80 MHz. The following diagram shows the 160 MHz distribution observed seven minutes prior to this diagram.

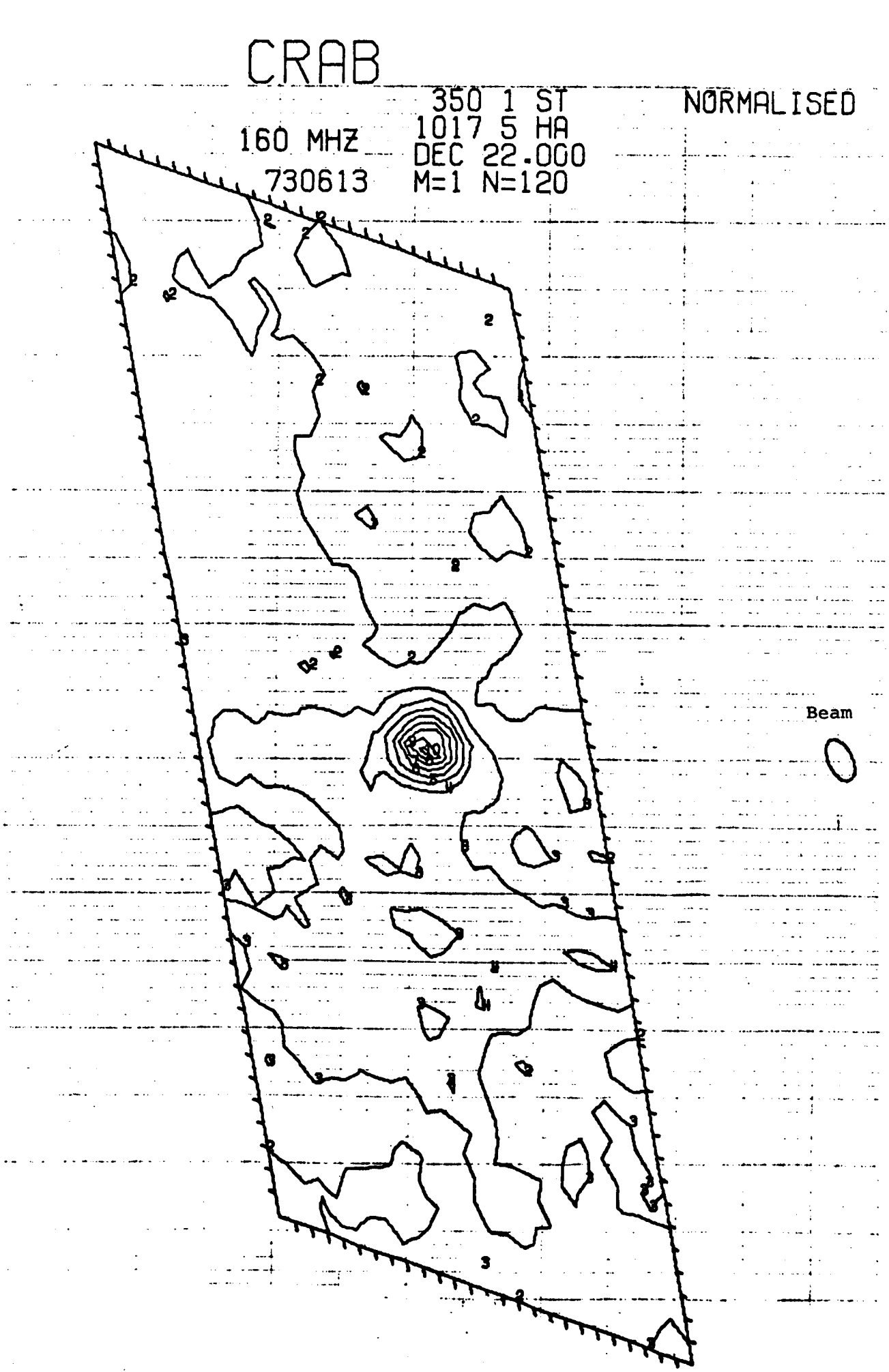

FIGURE 8.7c Broadened image at a Sun - Crab separation of 8.5 R_o and an observing frequency of 160 MHz.

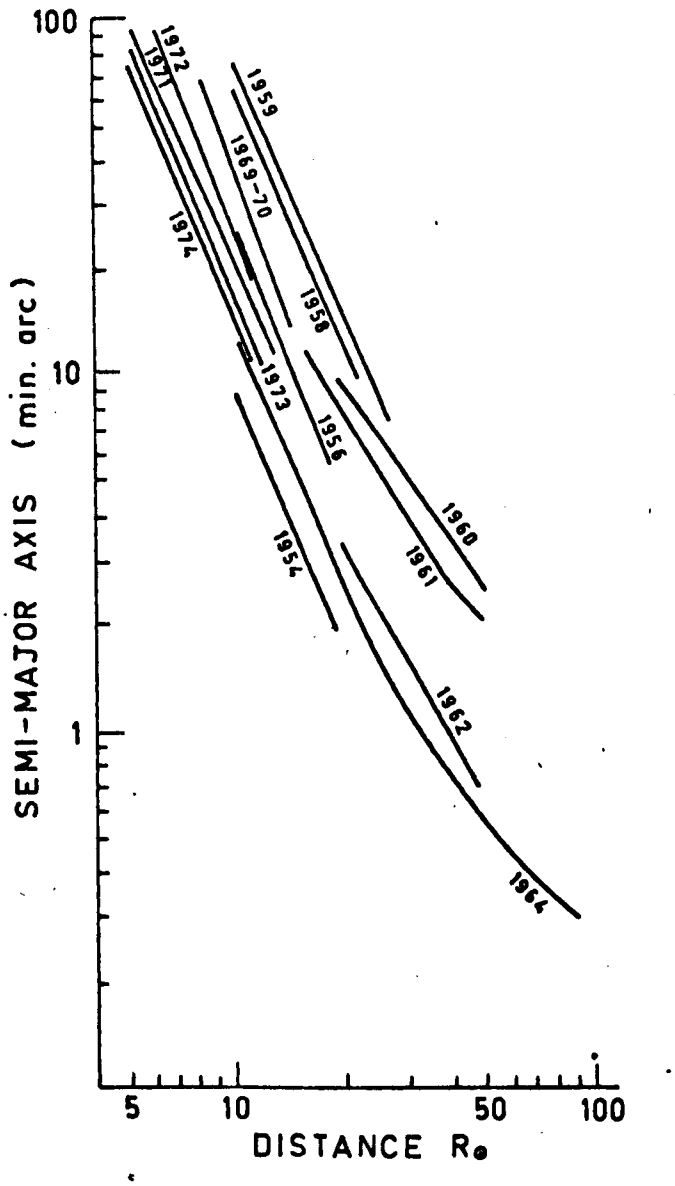

FIGURE 8.8 Variation of the tangential scattering as a function of distance from the Sun and phase of the solar cycle. All values are scaled to 38 MHz assuming a λ^2 dependence. Data prior to 1968 are taken from Okoye and Hewish (1964) and the 1969 - 71 data are from Blesing and Dennison (1972)

cycle, with that observed during the same portion of the previous cycle. During the 1959 maximum the radial gradient was ≈ -2.2 (Hewish and Wyndham, 1963) and during the decline in activity (1960-62) was ~ -1.4 (Slee, 1966). The axial ratio was $\sim 2:1$ during the period of maximum activity but had decreased to $\sim 1.4:1$ by 1962. Similar changes have occurred during the current cycle with the radial gradient (of the tangential scattering) changing rapidly from -2.2 in 1969-70 to -1.9 in 1971 and, with the exception of June 1972, remaining constant thereafter. The axial ratio of the scattering irregularities also decreased during this period, although not as significantly as found by Slee (1966) during the previous cycle. This decrease in axial ratio has also been evident in spaced receiver IPS observations at larger distances from the sun (e.g. Coles and Maagoe, 1972) While there are some differences between the radial gradients and axial ratios in the two cycles it is not possible to say whether these are real variations or limitations imposed by the use of interferometers to estimate the scattering parameters during the previous cycle.

It is well known that the corona is nearly spherical at solar maximum and becomes highly elongated in equatorial regions towards solar minimum. Indeed recent observations show that the corona is in fact generally quite non-uniform (see frontispiece). The use of a simple power-law model for scattering as a function of distance from the sun may therefore be an over-simplification, especially near solar minimum. It had been hoped that it would be possible to compare the scattering observations with coronagraph data from OSO-7 and Skylab . Unfortunately technical problems have meant that detailed coronagraph data for the periods covered by the coronal broadening observations are not available at this time from either source. The frontispiece, the last Skylab coronagraph picture available before a camera failure, clearly shows that during the 1973 occultation the corona was much denser in the equatorial regions than near the poles. An attempt

was made therefore to fit the 1973 scattering data to a modified power-law model which included a dependence on the solar latitude of the point of closest approach to the sun of the line of sight to the Crab. However, with a single occultation it is not possible to distinguish between a latitude dependence of scattering and a radial distance dependence, and the results were highly ambiguous.

The solar occultation of the Crab Nebula pulsar has been observed from Arecibo during 1969- 71 and 1973 (Counselman and Rankin, 1972, 1973; Weisberg, 1975). Measurement of the pulse arrival times enables an estimation of the effects of dispersion and multi-path scattering. During 1969 and 1970 the corona appeared to be spherically symmetric with the mean density varying as $r^{-2.9}$. In 1971 and 1973 the corona was clearly non-spherical and the results are dependent on the model chosen to represent the coronal density and its variation with solar latitude. The results suggest that in both years the power-law exponent had decreased but was $\gtrsim 2.0$. It is interesting to note that the radial gradients of the density and the scattering angle both decreased with decreasing solar activity, but that the radial gradient of density always appears to be higher than that of the scattering. Unfortunately, the scattering angle is dependent on several factors other than the density and it is necessary to assume some form of a coronal mode. Høgbohm, (1963) has shown from a consideration of equation (2.36) that if the corona is spherically symmetric with the scattering angle varying as $R^{-\alpha}$ then the scattering function

$$\Delta N(R) \left[\frac{k(R)}{a(R)} \right]^{\frac{1}{2}} \propto R^{-(\alpha + \frac{1}{2})}$$

where a(R) and k(R) are the scale and space-filling factor as defined previously. Thus the broadening observations suggest that the scattering

function was $\alpha R^{-3.0}$ in 1969-70 and $\alpha R^{-2.3}$ in 1971-74. As discussed in Chapter 2 spaced-receiver IPS observations suggest that $a(R) \alpha R^{-1.0}$. Combination of the broadening and dispersion results therefore suggest that $k(R) \alpha R^{-1.0}$.

The pulsar experiment was also capable of determining the effects of multipath scattering. During 1969-70 the scattering delay was αR^{-3} (Counselman and Rankin, 1972) which would be consistent with an angular - broadening dependence $\alpha R^{-1.5}$, a figure somewhat lower than the broadening observations yielded. During 1971 and 1973 the scattering was, except on several isolated occasions, below the detectable limit of the experiment. This leads us us to the question of local variations in the scattering. During 1973 and 1974 the only 'abnormal' scattering occurred on June 12 1973 when the broadened source was elongated in the radial rather than tangential direction. Apart from this radial orientation there was nothing unusual in the degree of scattering or the shape of the observed image. This could arise if the scattering irregularities were aligned along the field lines forming part of a closed loop. Although magnetic loops are a common feature of the corona (e.g. Eastern equatorial regions in frontispiece) they rarely extend to great heights above the surface, while this explanation would imply the existence of a loop out to $11.5R_o$, Weisberg (1975) noted a marked decrease in the integrated density on June 12 1973 and suggested the existence of a coronal hole. The magnetic field lines within a coronal hole are radial and one would expect a tangential orientation for the broadened source with a decrease in the overall scattering due to the decreased density in the hole. Further explanation of this event awaits detailed observations of the corona (out to $10R_o$) from either the OSO-7 or Skylab coronagraphs.

Figure 8.9 shows the correlation that exists between the degree of scattering and solar activity, as defined by the smoothed sunspot number

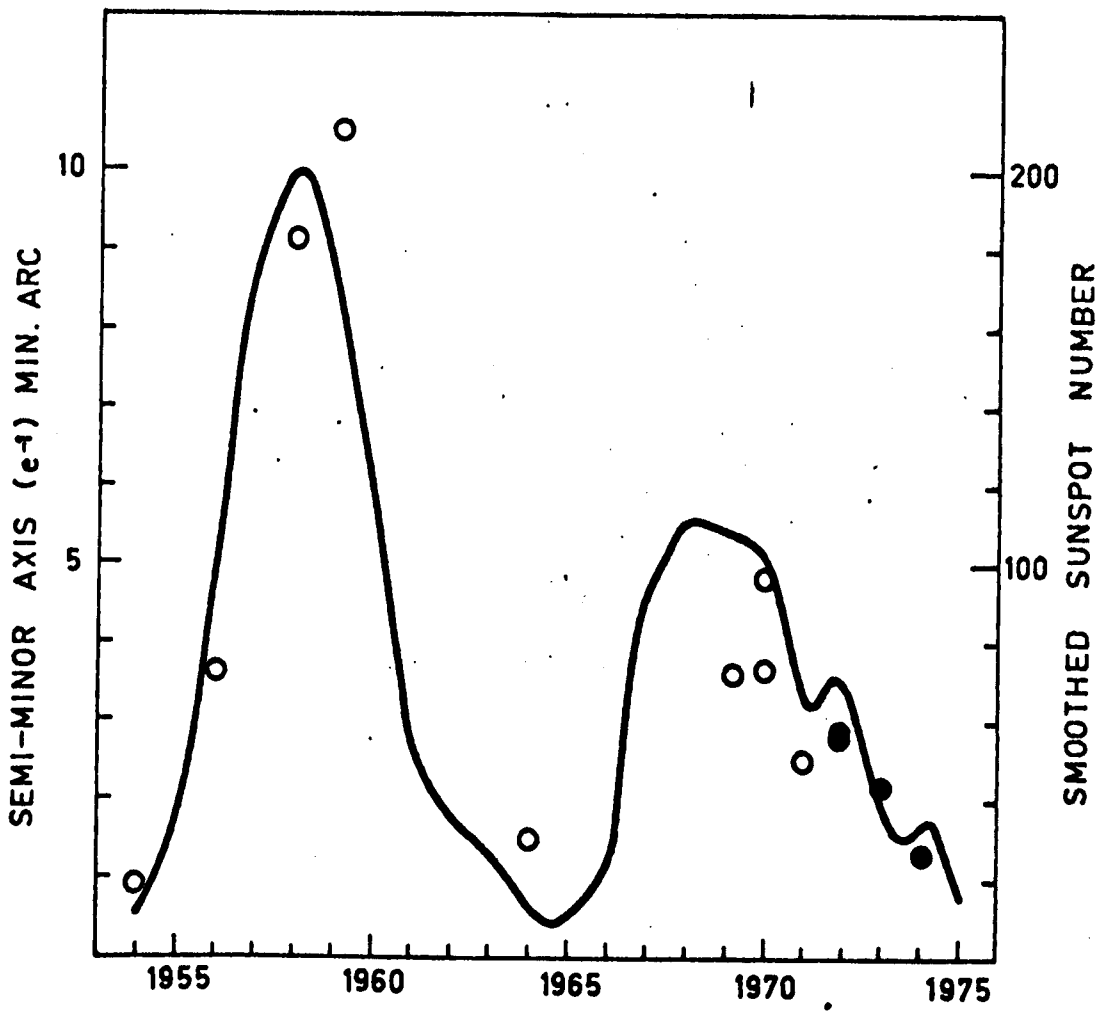

FIGURE 8.9 Degree of scattering (radial) for a Sun - Crab separation of 12 $R_\odot$ at an observing frequency of 80 MHz as a function of the phase of the solar cycle.

over two solar cycles. Although the degree of scattering close to the sun is highly correlated with the smoothed sunspot number recent interplanetary scintillation observations (Bourgois,private communication) at high radio frequencies and covering the same range of distances from the sun show no significant change with the changing phase of the solar cycle. Since the scattering angle $\theta \alpha \Delta N \ell^{-\frac{1}{2}}$ while the scintillation index $m \alpha \Delta N \ell^{\frac{1}{2}}$ the fact that

$$\frac{\theta}{m}_{1970} > \frac{\theta}{m}_{1973}$$

might suggest that the scale has decreased with the decreasing activity. It should be kept in mind however that as different sources were used for these two sets of observations they cover different parts of the corona and this may simply reflect the changing structure of the corona with the changing phase of the solar cycle. For example, the scintillating sources observed by Bourgois covered equatorial regions for which N showed very little change between 1969 and 1973, whereas the broadening observations included region near the south solar pole which showed a large decrease in N from 1969 to 1973 (Weisberg,1975).

Figure 8.10a-f shows the observed image on June 18 for each year from 1969 to 1974. The Crab Nebula is approximately 12 R_o from the Sun on this day. The overall decrease in scattering and the reduction in axial ratio is evident in these plots. Dennison and Blesing (1972) developed an expression for the two-dimensional brightness distribution resulting from scattering by irregularities possessing Gaussian or Power-law spectra. They concluded that the observed brightness distributions were in better agreement with the Gaussian model than the Power-law model. Comparison of the brightness distributions between 1972 and 1974 showed that this conclusion remained true during the decline in activity.

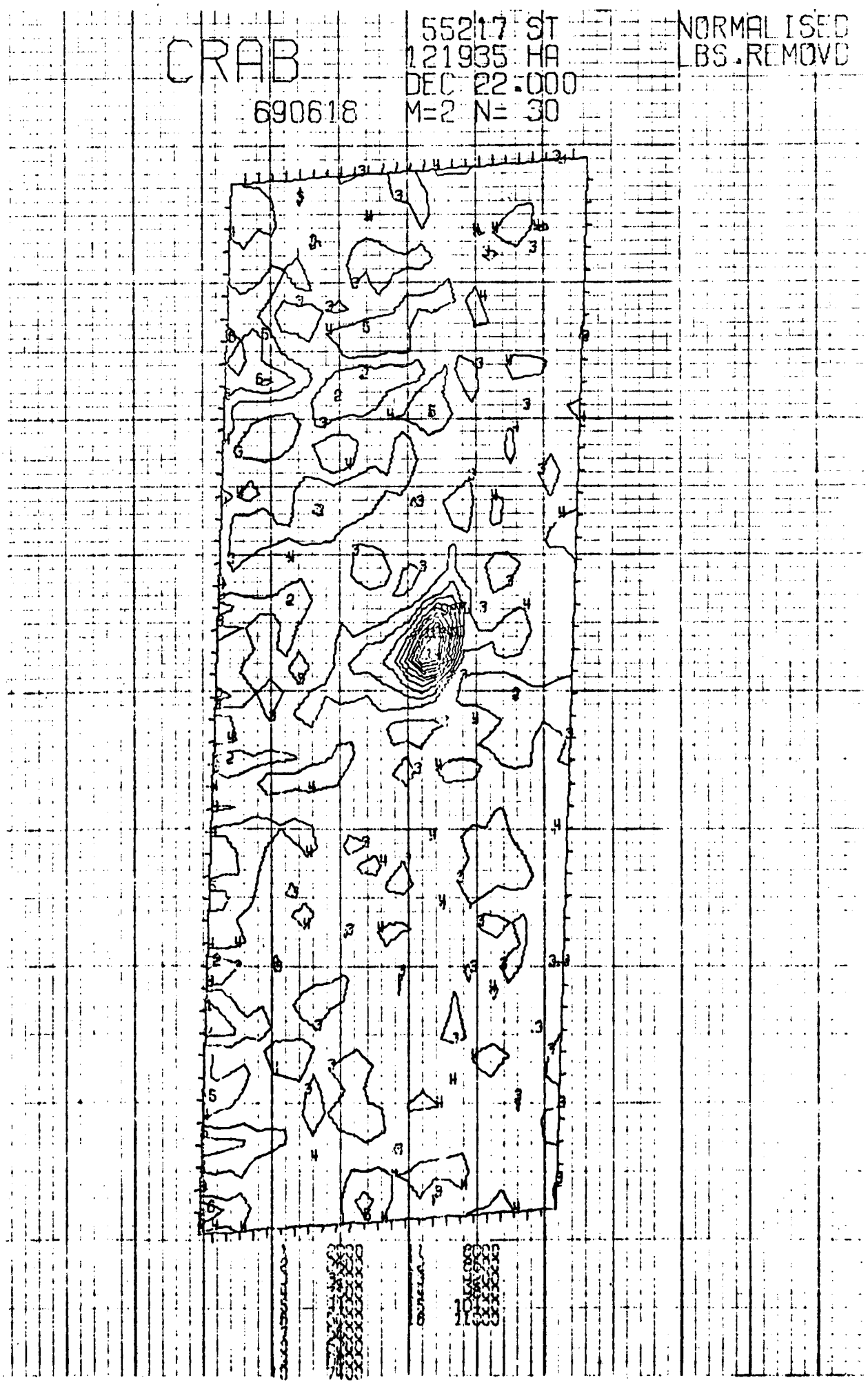

FIGURE 8.10a June 18 1969

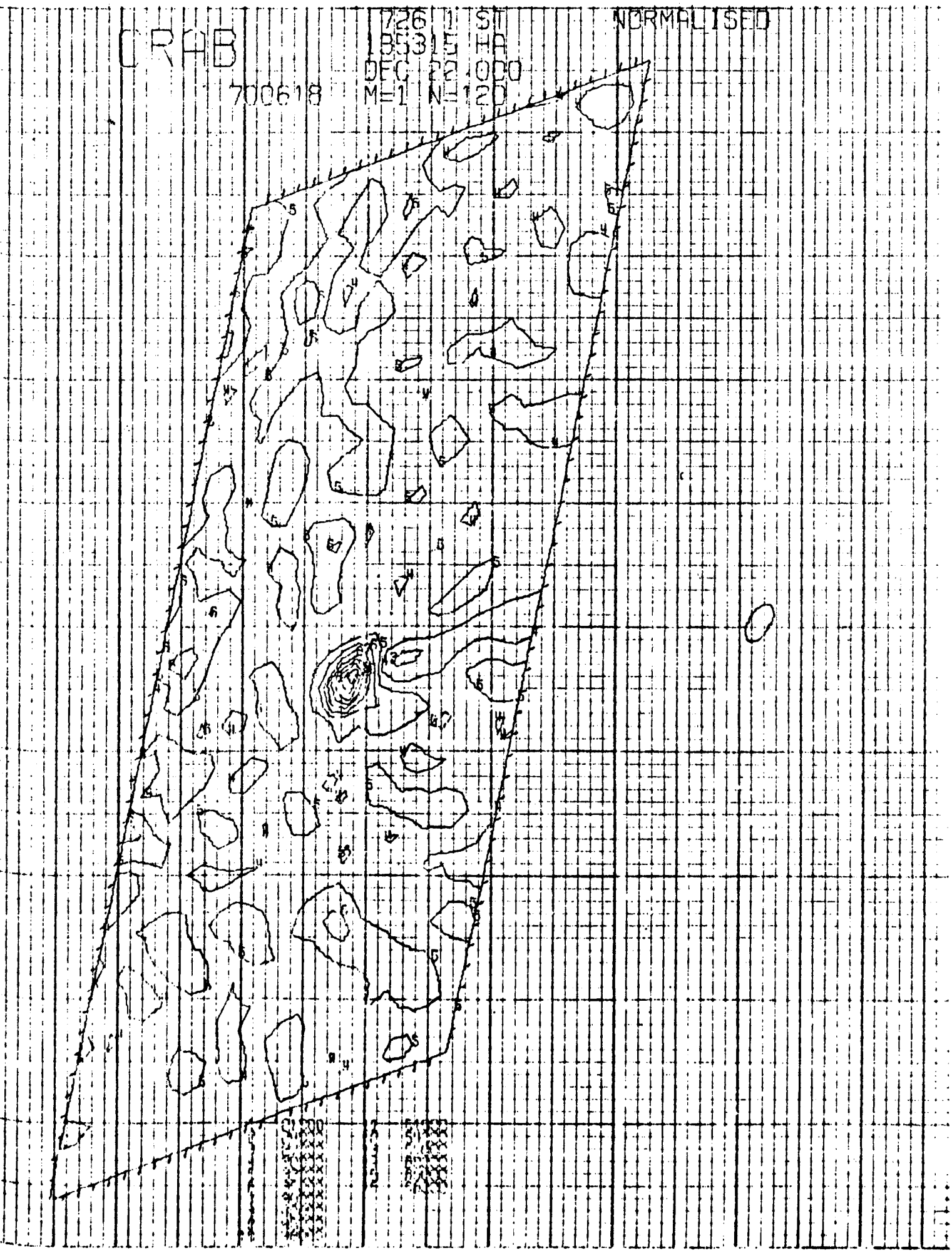

FIGURE 8.10b June 18 1970

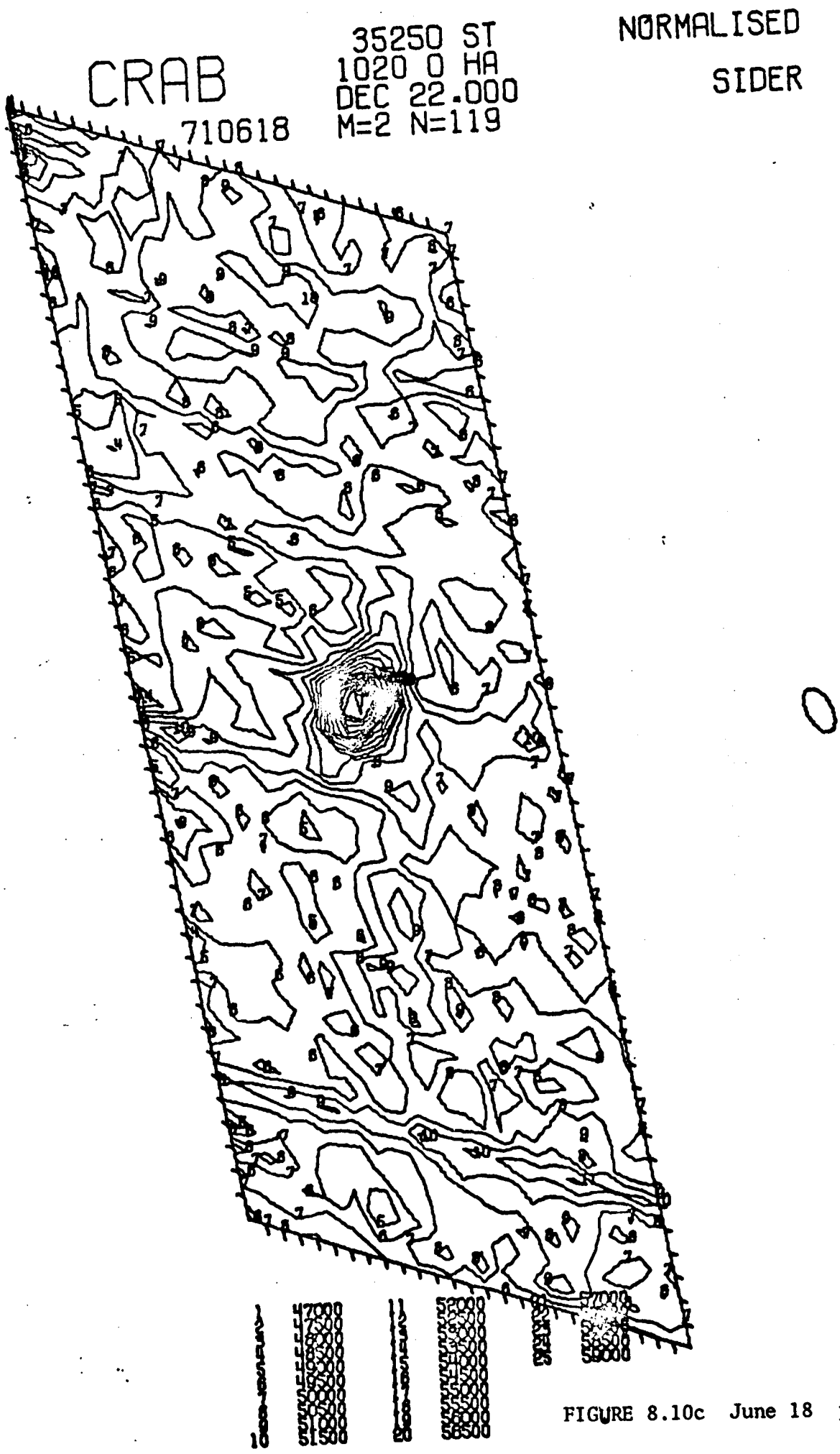

FIGURE 8.10c June 18 1971

FIGURE 8.10d June 18 1972

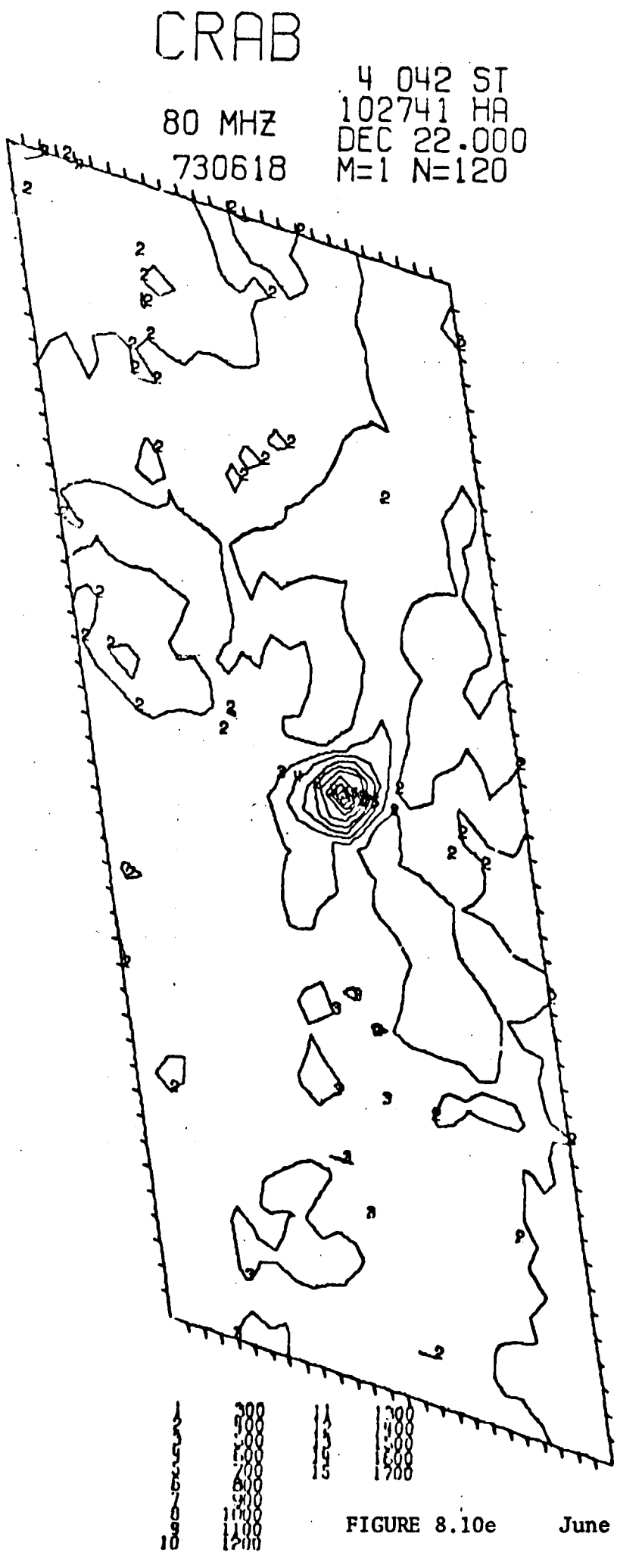

FIGURE 8.10e June 18 1973

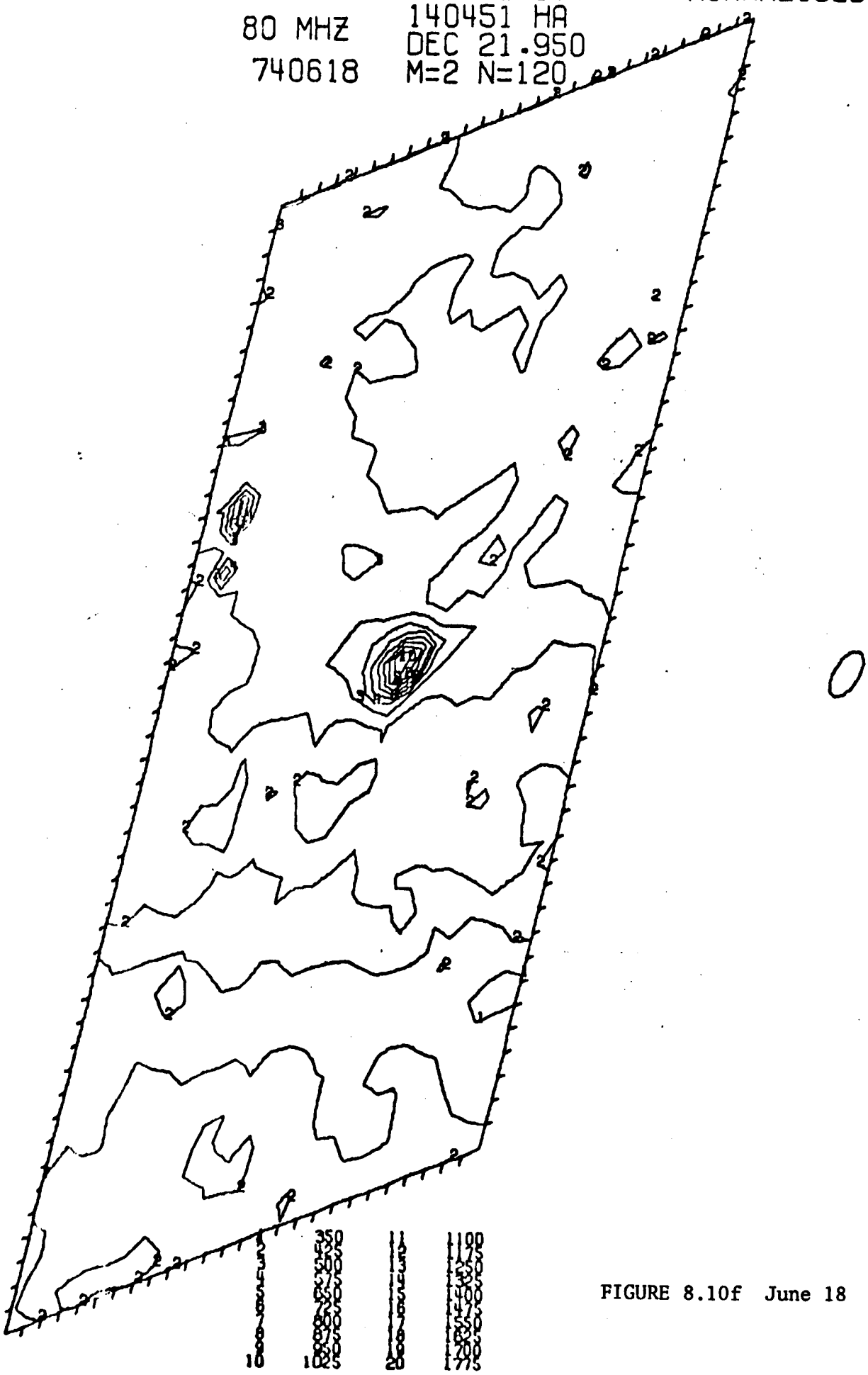

FIGURE 8.10f June 18 1974

Since previous observations have shown that the variation of scintillation index and scattering angle with distance from the sun can be expressed as a simple power-law it should be possible to examine the way in which ΔN and ℓ vary with distance from the sun by combining observations of coronal broadening at low frequencies with high frequency interplanetary scintillation observations of the same source. This is a difficult experiment since scintillating sources are relatively weak sources, making the coronal broadening observations difficult although it may be possible to carry out such an experiment during the current minimum while the sun is exceptionally quiet. One possible source is 1416+06 which passes through the equatorial regions of the corona during October each year.

Riddle (1974) has developed a numerical model for the scattering or radiation from solar radio bursts and has shown that the effects of scattering are important for the interpretation of such bursts. For example, when scattering is taken into account the coronal densities derived from type II and III source positions are in close agreement with the optically determined densities. Development of a similar model for the coronal broadening observations would enable an estimation of the relative importance of changes in the model parameters necessary to explain the observed variations with the changing phase of the solar cycle.

CHAPTER 9

CONCLUSIONS

The principal aim of the study of the scattering of radio waves by irregularities in the electron density within the interplanetary medium is to measure the properties of the plasma in the solar corona and interplanetary medium. Interpretation of the scattering observations is dependent upon an understanding of the relationship between the structure of the medium and its effects on the radio wave. The theory describing the propagation of radio waves through a random medium is well-developed in the case of weak scattering (rms phase deviation $\phi_0 << 1$) but is not complete for the case of strong scattering ($\phi_0 >> 1$). It is generally agreed that interplanetary scintillations observations at a given frequency are in the weak scattering region provided that the line of sight to the source passes sufficiently distant from the sun but they may enter the strong scattering region as the sun is approached. Coronal broadening observations are always in the strong scattering region.

9.1 MICROSTRUCTURE OF THE INTERPLANETARY MEDIUM

An insight into the scattering mechanism can be gained from a study of the probability density function of the intensity fluctuations. Results of an analysis of p.d.f.'s in the weak scattering region shows that at metre wavelengths the p.d.f. is generally intermediate in form between the predictions from two theoretical models, one for scattering from a thin screen, and the other for scattering in an extended medium which contains both the transmitter and the receiver. This would suggest that the scattering at the distances relevant to these observations occurs along an extended region of the line of sight, consistent with the interpretation of

the variation of scintillation index as a function of distance from the sun (e.g. Figure 2.7).

Observations closer to the sun at a higher frequency are in better agreement with the thin screen theory. Smultaneous observations at several frequencies over a range of heliocentric distances would enable the change from a thin screen to an extended medium to be determined more precisely. Of particular interest is the change from weak to strong scattering, at a given frequency, as the line of sight approaches the sun. The results from a numerical model analysis suggest that the p.d.f. is probably the most sensitive indicator of this change which could be determined by a series of metre or decimetre wavelength observations at varying heliocentric distances.

The interpretation of experimental observations of interplanetary scintillation is dependent upon the relationship between the structure of the irregularities in electron density in the solar wind plasma and the intensity fluctuations which develop as the wave propagates away from the scattering region. At the present time, the major problem in this area ia the nature of the density irregularities. One school of thought suggests that the electron density irregularities possess a single dominant scale defined by a Gaussian auto- correlation function and are independent of the larger scale structures measured by spacecraft experiments. The other suggestion is that there is no single scale but that instead the irregularities possess a power-law spectrum which is a continuation of the power-law spectrum measured at large wavenumbers by direct sampling from spacecraft.

The numerical model discussed in Chapter 6 shows that the p.d.f. is relatively insensitive to the form of the density irregularities, with the

exception of the strong scattering region in which the focussing phenomenon occurs over a more extended region for a Kolmogorov turbulence spectrum than for a Gaussian spectrum.

In principle the spectrum of the density irregularities can be derived from the scintillation power spectrum and the behaviour of the scintillation index as a function of the observing frequency and distance from the sun. The simplest case is that of a thin, weak-scattering screen in which there is a one-to-one relationship between the spectrum of the density irregularities and that of the intensity fluctuations. However, two factors limit the derivation of the density spectrum from scintillation observations at metre wavelengths. One is the uncertainty in the structures of the radio sources. Although VLBI observations have shown that some sources possess very small angular diameters these observations have generally been made at cm wavelengths in order to achieve the maximum resolution possible. However, recent observations suggest that radio source structures may be highly frequency dependent so that sources (e.g. CTA2I) which are effectively point sources at cm wavelengths may contain extended structures at metre wavelengths. The interplanetary scintillation of pulsars may provide a suitable point source calibration for future observations. The other major limiting factor in metre wavelength observations is the effect of scattering along an extended region of the line of sight.

A detailed investigation of this problem in Chapter 7 has shown that in general it is not possible to derive any significant information about the nature of the density irregularities from these observations. On some rare occasions distinct 'Fresnel' structures were evident in the spectra and for these special cases it was possible to derive some information about the structure of the irregularities. It was also shown in Chapter 7 that observations at much higher frequencies close to the sun

would not suffer from these two limitations. The general consensus at the present time is in favour of the power- law model. Recent spacecraft observations with high temporal resolution have however suggested that the real situation may in fact be a power-law spectrum with an additional component superimposed. Future scintillation observations should be carried out simultaneously at several higher frequencies closer to the sun and their interpretation may need to consider a more detailed model than those assumed to date.

9.2 LARGE SCALE STRUCTURE OF THE SOLAR WIND

Spaced receiver observations of interplanetary scintillation have made significant contributions to our understanding of the solar wind. One such contribution has been the identification of high speed solar wind streams with origins in coronal holes as discussed in Chapter 2. The Adelaide spaced-receiver system is now operational and the preliminary results discussed in Chapter 4 show that it is capable of providing observations on five sources. Improvements in the noise temperature of the receiver front-ends will increase the number of sources that can be included in the observations. Significant contributions to this field will depend upon a long sequence of systematic observations. The most significant results from the Adelaide project will be obtained when the high frequency system is completed, enabling simultaneous observations to be made at two frequencies. Further, the addition of phase coherent links to the system will enable pairs of aerials to be operated as long baseline interferometers. The rms phase deviation of the scattering will then be estimated from the ratio of the scintillation indices and the degree of correlation between the intensity fluctuations at the two frequencies. The phase deviation can also be estimated from the random fluctuations in the LBI fringes. Combining the spectral analysis of

the fluctuations with the size and shape of the diffraction pattern at the two frequencies will provide further insight into the structure of the electron density irregularities.

The relationship between solar flares and geomagnetic disturbances on the Earth has been of interest for many years. During the past decade a great deal has been learnt about the generation and motion of large scale disturbances in the interplanetary medium. Optical and radio solar observations have provided an insight into the generation mechanisms and spacecraft observations have provided information about the structure of the disturbed plasma near 1 AU. Interplanetary scintillation observations provide an alternative method of investigating the motion of large-scale disturbances in the solar wind which are complementary to the other techniques. In Chapter 5, it was shown that on several occasions it has been possible to combine the three methods to obtain a more comprehensive picture of the large scale structure of the disturbance.

Each of the disturbances originated in a flare which showed signs of a sudden acceleration of plasma during the flash phase, and the subsequent generation and propagation of a shock wave through the corona. By the time the disturbances had reached 1 AU they extended over a wide area of the interplanetary medium but were not spherically symmetric, as has been suggested in some studies of shock normals derived from spacecraft observations. Distortion of the shock front by propagation into an inhomogeneous medium containing a magnetic sector boundary was evident on several occasions. The disturbances appear to travel out to ~0.1 AU at approximately constant speed before undergoing significant deceleration.

Measurements of the velocity of the disturbed plasma can be obtained from spaced receiver observations and this will form one aspect of

the observations to be continued with the Adelaide system. However, observations using only a single system are of limited value because the period of observation is at most only 15-30 mins in every 24 hours. Much more comprehensive information could be obtained from a co-operative study using systems at several locations on the Earth to obtain greater resolution of the changes in the nature of the scintillation. Such a study has been proposed as a part of the program for the 'Study of Travelling Interplanetary Phenomena' organized by SCOSTEP.

9.3 CORONAL BROADENING

Coronal broadening observations of the Crab Nebula have been carried out more or less continuously since 1955 and a detailed picture is now available. The interpretations of results obtained with limited apparatus during the previous solar cycle have been confirmed by the complete two-dimensional observations recorded during the present cycle, as discussed in Chapter 8. The overall degree of scattering is closely correlated with the degree of solar activity. The radial gradient of the scattering appears to alter with the change from sunspot maximum to the decreasing phase of the solar cycle, but remains approximately constant during the decline. This is probably related to the change of the corona from spherical to non-spherical symmetry during this time. The axial ratio of the irregularities also decreases with the decreasing activity. This has also been observed by interplanetary scintillation observations at larger distances from the Sun.

Although coronal broadening and interplanetary scintillation have a common origin in the scattering of radio waves within the outer corona or solar wind, most workers have treated them as essentially independent phenomena. Future work in this area should consider the possibility of combining coronal

broadening observations at low frequencies with simultaneous scintillation observations at high frequencies on the same source as a method of probing the outer corona. One problem which needs investigation is the changes in the parameters of the coronal plasma which are required to explain the observed changes in the two phenomena as a function of the phase of the solar cycle. The use of a numerical scattering model would also be a useful method to investigate the changes in those parameters of the coronal plasma which are required to explain the variations in the two-dimensional coronal broadening observations between solar maximum (1969-70) and near minimum (1974).

REFERENCES

Abramowitz. M., Stegun. I.A.	1965	"Handbook of Mathematical Functions" Dover (NY).
Aitchison. J., Brown. J.A.C.	1957	"The Lognormal Distribution" Camb. Univ. Dept. Appl. Econ. Monograph S.
Allen. L.R., Anderson. B., Conway. R.G., Palmer. H.P., Reddish. V.C., Rwoson. B.	1962	Mon. Nat. Roy. Ast. Soc. 124, 477.
Allum. F.R.	1974	Air Force Camb. Res. Lab. Report Dec. 1974. (Ed by Smart D.F., Shea. M.A.)
Altschuler. M.D., Perry. I.F.	1972	Solar Phys. 23, 410.
Altschuler. M.D., Trotter. D.E., Orrall. F.Q.	1972	Solar Phys. 26, 354.
Alvarez. H., Haddock. F.T.	1973	Solar Phys. 29, 197.
Anderson. B., Donaldson. W.	1966	Mon. Nat. Roy. Ast. Soc. 137, 81.
Armstrong. J.B., Coles. W.C., Ricket. B.J.	1972	J. Geophys. Res. 77, 2739.
Armstrong. J.B., Coles. W.C.	1972	J. Geophys. Res. 77, 4602.
Armstrong. J.B., Coles. W.C., Kaufman. J.J., Rickett. B.J.	1973	Astrophys. J. 186, L141.
Bakhareva. M.F.	1959	Radiotekh. Elektron. 4, 88.
Bame. S.J. *et al*	1968	J. Geophys. Res. 73, 5761.
Barnes. A.	1968	Astrophys. J. 154, 751.
Barnes. A.	1969	Astrophys. J. 155, 311.
Barnes. A., Hartle. R.E., Bredekamp. J.H.	1971	Astrophys. J. 166, L53,

Bavassano. B., Mariani. F., Ness . N.F.	1973	J. Geophys. Res. 78, 4235.
Bendat. J.S., Piersol. A.G.	1971	"Random Data: Analysis and Measurement Procedures." Wiley (NY)
Billings. D.E., Roberts. W.O.	1964	Astrophys. Norv. 9, 147.
Blackwell. D.E., Petford. A.D.	1966	Mon. Nat. Roy. Ast. Soc. 131, 399.
Blesing. R.G.	1972	Ph.D Thesis - University of Adelaide.
Blesing. R.G., Dennison. P.A.	1972	Proc. Astron. Soc. Aust. 2
Bourgois. G.	1969	Astron. Astrophys. 2, 209.
Bourgois. G.	1972a	Astron. Astrophys. 19, 200.
Bourgois. G.	1972b	Astron. Astrophys. 21, 33.
Bourgois. G., Cheynet. C.	1972	Astron. Astrophys. 21, 25.
Bowhill. S.A.	1961	J. Res. Nat. Bur. Std. 65D, 275.
Bramley. E.N.	1954	Proc. Roy. Soc. A225, 515.
Bramley. E.N., Young. M.	1955	Proc. I.E.E.E., 102, 533.
Bramley. E.N., Young. M.	1967	Proc. Inst. Elec. Eng. 114, 553.
Briggs. B.H., Holmes. N.H.	1973	Nature. 243 111
Briggs. B.H., Phillips. G.J. Shinn. D.H.	1950	Proc. Phys. Soc. B53, 106.
Bruzek. A.	1974	Air Force Camb. Res. Lab. Report Dec. 1974 (Ed. Smart. D.F., Shea. M.A.)
Carovillano. R.L., Siscoe. G.L.	1969	Solar Phys. 8, 401.
Chao. J.K., Lepping. R.P.	1974	J. Geophys. Res. 79, 1799.
Chandrasekhar. S.	1952	Mon. Nat. Roy.Ast, Soc. 112, 475.

Cohen. M.H. Gundermann. E.J. Hardebeck. H.E., Harris. D.E., Sharp. L.F.	1966	Science 153, 745.
Cohen. M.H., Gundermann. E.J. Hardebeck. H.E., Harris. D.E. Sharp. L.F.	1967	Astrophys. J. 147, 449.
Cohen. M.H., Gundermann. E.J. Harris. D.F.	1967	Astrophys. J. 150, 767.
Cohen. M.H., Gundermann. E.J.	1969	Astrophys. J. 155, 645.
Coles. W.G., Maagoe S.	1972	J. Geophys. Res. 77, 5622.
Cottony. H.V., Wilson. A.C.	1958	I.R.E. Trans. Ant. Prog. 6, 366.
Counselman. C.C., Rankin. J.M.	1972	Astrophys. J. 175, 843.
Counselman. C.C., Rankin. J.M.	1973	Astrophys. J. 185, 357.
Couturier. P., Leblanc. Y.	1970	Astron. Astrophys. 7, 254.
Croft. T.A.	1971	Radio Sci. 6, 55.
Croft. T.A.	1973	J. Geophys. Res. 78, 3159
Cronyn. W.M.	1970	Astrophys. J. 161, 755.
Cronyn. W.M.	1972a	Astrophys. J. 171, L101.
Cronyn. W.M.	1972b	in "Solar Wind" NASA-SP-308 Washington (DC).
De Jager C.	1975	Solar Phys. 40, 133.
Dennison. P.A.	1969	Planet. Space. Sci. 17, 189.
Dennison. P.A., Hewish. A.	1967	Nature. 213, 343.
Dennison. P.A., Wiseman. M.	1968	Proc. Astron. Soc. Aust. 1, 142.
Dennison. P.A., Blesing. R.G.	1972	Proc. Astron. Soc. Aust. 2, 86.
De Young. D.S., Hundhausen. A.J.	1971	J. Geophys. Res. 76, 2245.
De Young. D.S., Hundhausen. A.J.	1973	J. Geophys. Res. 78, 3633.
Diodata. L., Moreno. G. Signorini. C.	1974	J. Geophys. Res. 79, 5095.
Dodge. J.C.	1973	NOAA-EDS Report UAG-28 p242, Boulder, Colorado.
Dodson. H.W., Hederman. E.R.	1968	Solar Phys. 4, 229.

Dryer. M.	1972	J. Geophys. Res. 77, 4851
Dryer. M.	1974	Space. Sci. Rev. 15, 403.
Dryer. M., Weber. E.J. Eviator. A., Frohlich. A., Jacobs. M., Joseph. J.H.	1974	Preprint - submitted to J.G.R.
Dulk. G.A., Altschuler. M.D. Smerd. S.F.	1971	Astrophys. Lett. 8, 235.
Ekers. R.D., Little. L.T.	1971	Astron. Astrophys. 10, 310.
Erickson. W.C.	1964	Astrophys. J. 139, 1290.
Erickson. W.C., Kuiper. T.B., Clark. T.A. Knowles. S.H. Broderick. J.J.	1972	Astrophys. J. 177, 101.
Fainberg. J., Stone. R.G.	1971	Solar Phys. 17, 392
Fairfield. D.H., Ness. N.F.	1974	J. Geophys. Res. 79, 5089.
Fejer. J.A.	1953	Proc. Roy. Soc. A220, 455.
Fooks. G.F.	1965	J. Atmos. Terr. Phys. 27, 979.
Forslund. D.W.	1970	J. Geophys. Res. 75, 17.
Frater. R.H.	1965	Rev. Sci. Instr. 36, 634.
Gentry. R.A., Hundhausen. A.J.	1969	Trans. A.G.U. 50, 302.
Gold. T.	1958	J. Geophys. Res. 64, 1665.
Goldstein. B.	1971	J. Geophys. Res. 77, 5455
Golley. M.G., Dennison. P.A.	1970	Planet. Space. Sci. 18, 95.

Gosling. J.T., Hansen. R.T. Bame. S.J.	1971	J. Geophys. Res. 76, 1811.
Gosling. J.T., Pizzo. V., Bame. S.J.	1973	J. Geophys. Res. 78, 2001.
Greenstadt. E.W., Dryer. H.D. Smith. Z.K.	1974	in "Flare Produced shock waves in interplanetary space" NOAA Conf. Boulder. p245.
Greenstadt. E.W., Green. I.M., Inouye. G.T., Sonett. C.P.	1970	Planet. Space. Sci. 18, 333.
Harries. J.R., Blesing. R.G. Dennison. P.A.	1970	Proc. Astron. Soc. Aust. 1, 319.
Harris. D.E., Hardebeck. E.G.	1969	Astrophys. J. (Supp) 19, 115.
Hartle. R.E., Barnes. A.	1970	J. Geophys. Res. 75, 6915
Hartle. R.E., Sturrock. P.A.	1968	Astrophys. J. 151, 1155.
Heinemann. M.A., Siscoe. G.L.	1974	J. Geophys. Res. 79, 1349
Hewish. A.	1951	Proc. Roy. Soc. A209, 81.
Hewish. A.	1952	Proc. Roy. Soc. A214, 494
Hewish. A.	1955	Proc. Roy. Soc. A228, 238.
Hewish. A.	1958	Mon. Nat. Roy. Ast. Soc. 118, 534.
Hewish. A.	1971	Astrophys. J. 163, 645.
Hewish. A.	1972	in "Solar Wind" NASA-SP-308 Washington (DC)
Hewish. A., Burnell. S.J.	1970	Mon. Nat. Roy. Ast. Soc. 150, 141.
Hewish. A., Dennison. P.A., Pilkington. J.D.H.	1966	Nature. 209, 1188.

Hewish. A., Scott. P.F., Wills. D	1964	Nature. 203, 1214
Hewish. A., Symonds. M.D.	1969	Planet. Space. Sci. 17, 313.
Hewish. A., Wyndham. J.D.	1963	Mon. Nat. Roy. Ast. Soc. 126, 469.
Hedgecock. P.C.	1974	Air Force Cambridge Res. Lab Report (Ed. Smart. D.F., Shea. M.A.) AFCRL-TR-0271 p49.
Hirshberg. J.	1968	Planet. Space. Sci. 16, 309.
Hirshberg. J., Alksne. A., Colburn. D.S., Bame. S.J., Hundhausen. A.J.	1970	J. Geophys. Res. 75, 1.
Hirshberg. J., Bame. S.J. Robbins. D.E.	1972	Solar Phys. 23, 467.
Hirshberg. J., Nakagawa. Y., Wellck. R.E.	1974	J. Geophys. Res. 79, 3726.
Hogbom. J.A.	1960	Man. Nat. Roy. Ast. Soc. 120, 350
Hollweg. J.V.	1968	Astron. J. 73, 972.
Hollweg. J.V.	1970	J. Geophys. Res. 75, 3715.
Hollweg. J.V.	1972	Cosm. Electrodyn. 2, 423.
Hollweg. J.V., Harrington. J.V.	1968	J. Geophys. Res. 73, 7221.
Hollweg. J.V., Jokipii. J.R.	1971a	in "The Solar Wind" NASA-SP-308 Washington (DC)
Hollweg. J.V., Jokipii. J.R.	1972b	J. Geophys. Res. 77, 3311.
Houminer. Z.	1971	Nature. 231, 165
Houminer. Z.	1973a	Planet. Space. Sci. 21, 1367.
Houminer. Z.	1973b	Planet. Space. Sci. 21, 1617.

Houminer. Z., Hewish. A.	1972	Planet. Space. Sci. 20, 1703.
Hundhausen. A.J.	1970	Rev. Geophys. Space. Sci. 8, 729
Hundhausen. A.J.	1972a	in "The Solar Wind" NASA-SP-308 Washington (DC).
Hundhausen. A.J.	1972b	"Coronal Expansion and Solar Wind" Springer-Verlag. (NY).
Hundhausen. A.J.	1973	J. Geophys. Res. 78, 3633
Hundhausen. A.J., Asbridge. J.R., Bamo. S.J., Gilbert. H.E., Strong. I.B.	1967a	J. Geophys. Res. 72, 87
Hundhausen. A.J., Asbridge. J.R., Bame. S.J. Strong. I.B.	1967b	J. Geophys. Res. 72, 1979
Hundhausen. A.J., Bame. S.J. Ness. N.F.	1967c	J. Geophys. Res. 72, 5265
Hundhausen. A.J., Bame. S.J., Asbridge. J.R., Sydoricek. S.J.	1970	J. Geophys. Res. 75, 4643.
Hundhausen. A.J., Gentry. R.A.	1969a	J. Geophys. Res. 74, 2908.
Hundhausen. A.J., Bame. S.J., Ness. N.F.	1969b	J. Geophys. Res. 74, 6229
Jokipii. J.R.	1970	Astrophys. J. 161, 1147
Jokipii. J.R.	1973	Ann. Rev. Astron. Astrophys. 11, 1
Jokipii. J.R., Coleman. P.J.	1968	J. Geophys. Res. 73, 5495
Jokipii. J.R., Hollweg. J.V.	1970	Astrophys. J. 160, 745

Jokipii. J.R., Lee. L.C.	1972	Astrophys. J. 172, 729
Jokipii. J.R., Lee. L.C.	1973	Astrophys. J. 182, 317.
Kakinuma. T., Washimi. H., Kajima. M.	1973	Pub. Astron. Soc. Jap. 25, 271
Kraus. J.K.	1966	"Radioastronomy' Mc Graw-Hill (NY)
Landecker. T.L., Wielebinsky. R.	1970	Proc. IRE (Aust) 31, 73
Leblanc. Y., Leroy. J.L. Pecantet. P.	1973	Solar Phys. 31, 343
Lee. R.P. , Chen. T.	1968	Planet. Space Sci. 16, 1483
Link. F	1951	Bull. Cent. Ast. Inst. Czech. 3, 6
Little. L.T.	1968	Planet. Space. Sci. 16, 749
Little. L.T.	1971	Astron. Astrophys. 10, 301
Little. L.T., Ekers. M.D.	1971	Astron. Astrophys. 10, 306
Little. L.T., Hewish. A., Dennison. P.A.	1966	Planet. Space. Sci. 14, 1221.
Little. L.T., Hewish. A.	1966	Man. Nat. Roy. Ast. Soc. 134, 221
Little. L.T., Hewish. A.	1968	Man. Nat. Roy. Ast. Soc. 138, 393
Lovelace. R.V.E.	1970	Ph.D Thesis - Cornell Univ.
Lovelace. R.V.E., Salpeter. E.E., Sharp. L.E., Harris. D.E.	1970	Astrophys. J. 159, 1047
Machin. K.E., Smith. F.G.	1951	Nature. 168, 599
	1952	Nature. 170, 319
Malitson. H.H., Fainberg. J., Stone. R.G.	1973a	Astrophys. J. 183, L35

Malitson. H.H., Fainberg. J., Stone. R.G.	1973b	Astrophys. Lett. 14, 111
Matheson. D.N., Little. L.T.	1971	Nature 234, 29.
Matheson. D.N., Little. L.T.	1972	Planet. Space. Sci. 19, 1615
Maxwell. A.	1973	NOAA - EDS Report UAG-28, Boulder, Colarado.
Maxwell. A., Rinehart. R.	1974	Solar Phys. 37, 437
Mercier. R.P.	1962	Proc. Camb. Phil. Soc. 58, 382.
Mihalov. J.D., Colburn. D.S., Collard. H.R., Smith. B.F., Sonnett. C.P., Wolfe. J.H.	1974	in "Correlated Interplanetary and magnetic observations" p545 (Ed. Page. D.E.)
Moreton. G.E.	1964	Astron. J. 66, 145
Nakagawa. Y., Wellck. R.E.	1973	Solar Phys. 32, 257
Ness. N.F.	1966	J. Geophys. Res. 71, 3319
Ness. N.F., Scearce. C.S., Seek. J.B.	1964	J. Geophys. Res. 69, 3531
Ness. N.F., Scearce. C.S. Cantara. S.	1966	J. Geophys, Res. 71, 3305
Ness. N.F., Hundhausen. A.J. Bame. S.J.	1971	J. Geophys. Res. 76, 6643
Ness. N.F., Wilcox. J.M.	1967	Solar Phys. 2, 351
Neugebauer. M.	1974	Preprint.
Neugebauer. M., Snyder. C.W.	1966	J. Geophys. Res. 71, 4469

Newkirk. G.	1959	Astrophys. J. 133, 983
Newkirk. G.	1961	Astrophys. J.
Newkirk. G., Altschuler. M.D.	1970	Solar Phys. 13, 131
Noble. L.M., Scarf. F.L.	1963	Astrophys. J. 138, 1169
Ogilvie Burlaga. L.F.	1969	J. Geophys. Res. 74, 2815
Okoye. S.E., Hewish. A.	1967	Man. Nat. Roy. Ast. Soc. 137, 287
Orhaug. T.A.	1965	Chalmers Tek. Hogsk. Handl. Nr 299
Parker. E.N.	1958	Astrophys. J. 128, 664.
Parker. E.N.	1963	in "Interplanetary Dynamical Processes" Interscience (NY)
Parker. E.N.	1964	Astrophys. J. 139, 72
Perkins. F.	1973	Astrophys. J. 179, 637
Petschek. H.E.	1964	in "AAS-NASA Symposium of the Physics of Solar Flares" NASA-SP50 (Ed. Ness. W.H.)
Petschek. H.E.	1966	in "The Solar Wind" (Ed. Madein. R.J., Neughebauer. M.) Pergamon (NY)
Phillips. G.J., Spencer. M.	1955	Proc. Phys. Soc. B58, 481.
Pinter. S.	1973	Nature 243 , 96
Ratcliffe. J.A.	1956	Rep. Prog. Phys. 19, 188

Redhead. A.C.S.	1971	Mon. Nat. Roy. Ast. Soc. 155, 185
Rice. S.O.	1954	in "Selected papers on noise and stochastic processes" p238 (Ed. Wax. N.) Dover (NY).
Ricket. B.J.	1973	J. Geophys. Res. 78, 1543
Riddle. A.C.	1970	Solar Phys. 13, 448
Riddle. A.C.	1970	Solar Phys. 35, 153
Robbins. D.E., Hundhausen. A.J., Bame. S.J.	1970	J. Geophys. Res. 75, 1178
Ryle. M.	1952	Proc. Roy. Soc. A211, 351.
Sakurai. K.	1973a	J. Geophys. Res. 78,
Sakurai. K.	1973b	Nature 246, 70.
Sakurai. K., Chao. J.K.	1973	Nature. 246, 72
Sakurai. K., Chao. J.K.	1974a	J. Geophys. Res. 79, 661
Sakurai. K., Chao. J.K.	1974b	J. Geophys. Res. 79, 661
Salpeter. E.E.	1967	Astrophys. J. 147, 433
Scarf. F.L.	1970	Space. Sci. Rev. 11, 234
Shea. D.F., Smart. M.A.	1974	USAF Cambridge Res. Lab Report Dec. 1974 (Ed Smart. D.F., Shea. M.A.)
Simon. M., Axford. W.I.	1966	Planet. Space. Sci. 14, 901
Singleton. D.G.	1974	J. Atmos. Terr. Phys. 36, 113

Singleton. R.C.	1969	IEEE Trans. Audio & Electro-acoustics. 17, 93.
Siscoe. G.L., Goldstein. B.J., Lazarus. A.J.	1969	J. Geophys. Res. 74, 1759
Siscoe. G.L., Finky. L.T.	1972	J. Geophys. Res. 77, 35.
Slee. O.B.	1959	Aust. J. Phys. 12, 134
Slee. O.B.	1961	Man. Nat. Roy. Ast. Soc. 123, 223
Slee. O.B.	1966	Planet. Space. Sci. 14, 255
Smith. F.G.	1961	Inst. Elect. Eng. 1088, 201
Smith. S.F., Harvey. K.L.	1971	in "Physics of the Solar Corona" (Ed. Macris. P.) p156
Snyder. C.W., Neugebauer. M.	1963	J. Geophys. Res. 68, 6361
Steinolfson. R.S., Dryer. M., Nakagawa. Y.	1974	J. Geophys. Res. (in press)
Stewart. R.J., McCabe. M., Koomen. M.J., Hansen. R.T., Dulk. G.A.	1973a	Solar Phys. 36, 203
Stewart. R.T., Howard. R.A., Hansen. F., Gergely. T., Kundu. M.	1973b	Solar Phys. 36, 219
Stone. R.G., Fainberg. J.	1973	in "High Energy Phenomena on the Sun" (Ed Ramaty. R., Stone. R.G.) NASA-SP342. p519
Strong. I.B. et al	1966	Phys. Res. Lett. 16, 631.
Sturrock. P.A., Hartle. R.E.	1966	Phys. Rev. Lett. 16, 628

Tatarski. V.I.	1961	"Wave propagation in a turbulent medium" trans. Silverman. R.A. McGraw-Hill (NY)
Taylor. H.E.	1969	Solar Phys. 6, 320.
Temnyi. V.V., Zertsalov. A.A., Vaisberg. O.L., Berezin. Y.E.	1974	Kosm. Issk. 12, 74
Tidman. D.A., Krall. N.A.	1971	"Shock waves in collisionless Plasmas" Wiley (NY)
Toichi. T.	1971	Solar Phys. 18, 150
Uchida. Y.	1968	Solar Phys. 4, 30.
Uchida. Y.	1970	Publ. Astron. Soc. Jap. 22, 341
Uchida. Y.	1973a	in "High Energy Phenomena on the Sun" (Ed Ramaty. R., Stone. R.G.) NASA-SP342
Uchida. Y	1933b	Preprint - IAU Synp 57 Surfers Paradise Sept 73
Uchida. Y., Altschuler. M.D. Newkirk. G.	1973	Solar Phys. 28, 495
Unti. M., Neugebauer. M.	1973	J. Gepphys. Res. 78, 7237
Unti. M., Neugebauer. M., Goldstein. B.E.	1973	Astrophys. J. 180, 591
Van de Hulst. H.C.	1970	B.A.N. 11, 150
Vandenburg. N.R. et al	1973	Astrophys. J. 180, L27
Vitkevitch. V.V., Vlasov. V.I.	1970	Sov. Astron - AJ 13, 669
Vitkevitch. V.V., Vlasov. V.J.	1972	Sov. Astron - AJ 16, 480

Ward. B.D.	1974	Air Force Cambridge Res. Lab Report Dec. 1974. (Ed. Smart. D.F., Shea. M.A.)
Ward. B.D.	1975	Proc. Astron. Soc. Aust. 3, (in press).
Ward. B.D., Blesing. R.G., Dennison. P.A.	1972	Proc. Astron. Soc. Aust. 2, 82
Watanabe. T.	1975	Publ. Astron. Soc. Jap. 27, in press.
Watanabe. T., Kakinuma. T.	1972	Publ. Astron. Soc. Jap. 24, 459
Watanabe. T., Kakinuma. T., Kojima. M., Shibasaki. K.	1973	Rep. Ionos. Space. Res. 27, 158
Watanabe. T., Shibasaki. K., Kakinuma. T.	1974	J. Geophys. Res. 79, 3841
Weisberg. J.	1975	Preprint - Univ. of Iowa.
Whang. Y.C., Chang. C.C.	1965	J. Geophys. Res. 70, 4175
Liu. C.K., Chang. C.C.	1965	Astrophys. J. 145, 255
Wilcox. J.M.	1968	Space. Sci. Rev. 8, 258
Wilcox. J.M., Colburn. D.S.	1969	J. Geophys. Res. 75, 6366
Wilcox. J.M., Ness. N.F.	1965	J. Geophys. Res. 74, 2388
Wild. J.P.	1967	Proc. IREE (Aust) 28
Wild. J.P.	1969	Solar Phys. 9, 260

Wild. J.P., Smerd. S.F.	1972	Ann. Rev. Astron. Astrophys. 10, 159
Wilson. A.C., Cottony. H.V.	1960	IRE Trans. Antennas Propag. 8, 144
Wiseman. M.	1972	Ph.D Thesis - Univ. of Adelaide
Wiseman. A., Dennison. P.A.	1972	Proc. Astron. Soc. Aust. 2, 79
Wolfe. J.H., Silva. R.W., Myers. M.A.	1966	J. Geophys. Res. 71, 1319
Wolff. C.L., Brandt. J.C., Southwick. R.G.	1971	Astrophys. J. 165, 181
Young. A.T.	1971	Astrophys. J. 168, 543
Zeissig. G.A., Lovelace. R.V.E.	1972	Astron. Astrophys. 16, 190
Zirin. H., Tanaka. K.	1973	Solar Phys. 32, 173

APPENDIX I

THEORETICAL PROBABILITY DENSITY FUNCTIONS

The Rice distribution was originally derived to describe the probability distribution of the amplitude of a randomly-scattered wave (Rice, 1954). It describes the probability distribution of the length of a vector which is the sum of a constant vector and two perpendicular vectors, one in phase and the other in quadrature with the constant vector, the lengths of which have identical but independent Gaussian distributions with zero means. The Rice distribution of amplitude can be converted to the so-called $(\text{Rice})^2$ distribution of intensity by making the transformation $I = A^2$ (Cohen et al, 1967) giving

$$p(I) = \frac{1}{2\sigma^2} \exp\left[\frac{-(I+c^2)}{2\sigma^2}\right] I_o\left[\frac{c\sqrt{I}}{\sigma^2}\right] \qquad \text{---- (1.1)}$$

where $I_o(x) = J_o(ix)$ is a modified Bessel function of the first kind of order zero, c is the length of the constant vector, and σ^2 is the variance of the Gaussian components. The first three central moments of this distribution are

$$\langle I \rangle = c^2 + 2\sigma^2 \qquad \text{---- (1.2)}$$

$$M_2 = 4\sigma^2 (c^2 + \sigma^2) \qquad \text{---- (1.3)}$$

$$M_3 = 8\sigma^4 (2\sigma^2 + 3c^2) \qquad \text{---- (1.4)}$$

As defined in equation (1.1) this distribution has two free parameters, but this can be reduced to a dependence on one parameter by normalizing in terms of the mean source intensity $\langle I \rangle$. Since energy must be conserved we can normalize the intensity values such that $\langle I \rangle = 1$, giving

$$c = (1 - 2\sigma^2)^{\frac{1}{2}} \qquad \text{---- (1.5)}$$

The scintillation index m and skewness coefficient γ_1 become

$$m = 2\sigma \left(1 - \sigma^2 \right)^{1/2} \qquad \text{---- (1.6)}$$

and

$$\gamma_1 = \frac{3\sigma - 4\sigma^3}{(1 - \sigma^2)^{3/2}} = \frac{4 (1 - m^2)^{3/2} + 6m^2 - 4}{m^3} \qquad \text{---- (1.7)}$$

Expressions for m and γ_1 in terms of the rms phase deviation ϕ_0 can be derived (Bourgois, 1972) from Mercier's (1962) exact expression for the moments of the intensity in the far-field

$$m = \left(1 - E^2 \right)^{1/2} \qquad \text{---- (1.8)}$$

$$\gamma_1 = 2(1 + 2E) (1 - E)^{1/2} (1 + E)^{-3/2} \qquad \text{---- (1.9)}$$

where $E = \exp (-\phi_0^2)$. These relations reduce to

$$m \approx \sqrt{2}\, \phi_0 \qquad \text{---- (1.10)}$$

$$\gamma_1 \approx \frac{2\phi_0}{\sqrt{3}} \qquad \text{---- (1.11)}$$

in the limit $\phi_0 \to 0$. Equating relations (1.6) and (1.8) gives

$$\sigma^2 = \tfrac{1}{2} \left(1 - \exp (-\phi_0^2) \right) \qquad \text{---- (1.12)}$$

As $\phi_0 \to \infty$, $\sigma^2 \to \tfrac{1}{2}$ and $c \to 0$; the p.d.f. approaches the exponential form

$$p(I) = \frac{1}{2\sigma^2} \exp \left(-I/_{2\sigma^2} \right) \qquad \text{---- (1.13)}$$

The lognormal distribution for the received intensity I is a distribution in which (log I) is normally distributed with mean μ and variance σ^2. Its properties have been described by Aitchison and Brown (1957). It is defined by

$$p(I) = \frac{1}{\sigma I \sqrt{2\pi}} \exp \left[\frac{-1}{2\sigma^2} \log (I - \mu)^2 \right] \qquad \text{---- (1.14)}$$

The intensity is lognormally distributed with mean $< I >$ and

variance M_3, with the inter-relations

$$< I > = e^{\mu^2 + \sigma^2/2} \qquad \text{---- (1.15)}$$

and $$M_2 = < I >^2 \eta^2 \qquad \text{---- (1.16)}$$

where $$\eta^2 = e^{\sigma^2} - 1 \qquad \text{---- (1.17)}$$

The third and fourth moments about the mean are

$$M_3 = < I >^3 (\eta^6 + 3\eta^4) \qquad \text{---- (1.18)}$$

$$M_4 = < I >^4 (\eta^{12} + 16\eta^{10} + 15\eta^8 + 16\eta^6 + 3\eta^4) \qquad \text{---- (1.19)}$$

Again, normalizing by the mean intensity, $< I > = 1$,

gives $$\mu = -\sigma^2/2 \qquad \text{---- (1.20)}$$

and the scintillation index and coefficients of skewness and kurtosis become

$$m = M_2^{1/2} = (e^{\sigma^2} - 1)^{1/2} \qquad \text{---- (1.21)}$$

$$\gamma_1 = 3m + m^3 \qquad \text{---- (1.22)}$$

$$\gamma_2 = 16m^2 + 15m^4 + 6m^6 + m^8 \qquad \text{---- (1.23)}$$

Relations (1.21) to (1.23) have also been derived by Bourgois and Cheynet (1972), although they replace μ by $\log < I >$ in equation (1.14) which is only a valid approximation in the limit $\sigma^2 \to 0$.

APPENDIX 2

PRACTICAL METHODS OF SPECTRAL ANALYSIS

The traditional approach to the practical spectral analysis of a time series has been via the cosine transform of the auto-correlation function (Blackman and Tukey, 1958). With the advent of the Fast Fourier Transform (FFT) it has become computationally faster to calculate the Fourier coefficients (and hence the spectral estimates) by a direct Fourier transform of the data rather than by the transform of the auto-correlation function. The mixed radix algorithm described by Singleton (1969) was used in the analysis described in this thesis because, unlike the original algorithm described by Cooley and Tukey (1965), it operates efficiently on a number of data points N which may have prime factors less than 11 and is not restricted to values of the form $N = 2^k$.

We consider a finite length, T seconds, of data sampled at time intervals Δt giving N data points

$$X_j = X(k.\Delta t) \qquad k = 0,1,\ldots,N-1 \qquad \text{---(2.1)}$$

where the mean has been removed such that

$$\sum_{j=o}^{N-1} X_j = 0 \qquad \text{---(2.2)}$$

The squared modulus of the finite Fourier transform, properly normalized, gives N equally spaced samples of the periodogram

$$P_k(f) = \frac{1}{T} \left| \Delta t \sum_{j=o}^{N-1} X_j \exp\left|(2\pi ikj/N)\right| \right|^2 \qquad \text{--- (2.3)}$$

at the discrete frequencies

$$f_k = \frac{k}{N.\ \Delta t} \qquad k = 0,1,\ldots N-1 \qquad \text{---(2.4)}$$

in units of power (X_0^2) per hertz.

Since $P_k(f)$ is an even function only $(\frac{N}{2} + 1)$ values are distinct, out to the Nyquist frequency

$$f_N = \frac{1}{2\ \Delta t} \qquad \text{----(2.5)}$$

If power exists at frequencies greater than f_N it becomes folded across this frequency and appears in the spectrum at frequencies

$$f = 2nf_N + f_o \qquad \text{----(2.6)}$$

where $f_o > f_N$ and n is an integer. In other words the measured spectrum

$$P^1(f) = P(f) + \sum_{n=1}^{\infty} P(2nf_N \pm f) \qquad o<f<f_N \qquad \text{----(2.7)}$$

where P(f) is the actual spectrum of the process being sampled. It is necessary therefore to ensure that the sampling rate is adequate to record all frequencies present otherwise the results may be rendered useless by a large amount of power being aliased into the spectrum.

With a finite length of record it is not possible to obtain an unbiased spectral estimate at a single frequency. Since the data can be considered as an infinite time series multiplied by a rectangular weighting function, $W_f(t)$, of length T seconds and unit amplitude, the calculated periodogram P_k is related to the "true" power spectrum S_k by the convolution theorem (Bracewell, 1964)

$$P_k = S_k * H_k \qquad \text{----(2.8)}$$

where H_k is the squared modulus of the Fourier transform of W_k;

$$H_k = \frac{\sin^2 (T\pi f)}{2\pi T \sin^2 (\pi f)} \qquad ---(2.9)$$

This spectral window has unit area, with a main peak of width 2/T centred at f = 0. The first sidelobes occur at $f \approx 3/2T$ and are ~4% of the main response. Consequently an estimate $P_k(f)$ contains a 4% contribution from frequencies $f \pm 3/2T$. This spectral leakage is not a problem for flat spectra but may become difficult to correct for in spectra with steep slopes or containing sharp lines. The leakage can be reduced by varying the shape of the original window $W_k(t)$ so that the sidelobes of H_k are much smaller. Blackman and Tukey (1958) have discussed three important windows (Bartlett, Hanning and Hamming) in detail. Buckley (1971) has investigated the effects of these windows on spectral leakage and has shown that, for a spectrum which is a decreasing function of frequency, at some stage leakage becomes predominant. This effect is shown in Figure (2.1) where a Gaussian spectrum has been evaluated with different data windows. The non-Gaussian tails which settle down to power-law variations of frequency are produced by the sidelobe leakage.

In the practical spectral analysis of a time series it is necessary to achieve a compromise between maximum spectral resolution, minimum variance and minimum bias for each spectral estimate. The raw periodogram P_k calculated from equation (2.3) with frequency resolution $\Delta f = \frac{1}{N\Delta t}$, is not a good estimate of the power spectrum since the standard deviation of the estimate is close to 100% of the mean value (Cooley et al, 1970). The resolution of the periodogram must therefore be reduced in order to obtain a reduction in the variance of the spectral estimates. There are two methods of achieving this. The first involves computing the high resolution periodogram from the whole data record and then averaging P_k over M successive values of k. The average value

$$\overline{P}_j = \frac{1}{M} \sum_{k=1}^{M} P_{Mj + k} \qquad j=1,\ldots,\frac{N}{2M} \qquad ---(2.10)$$

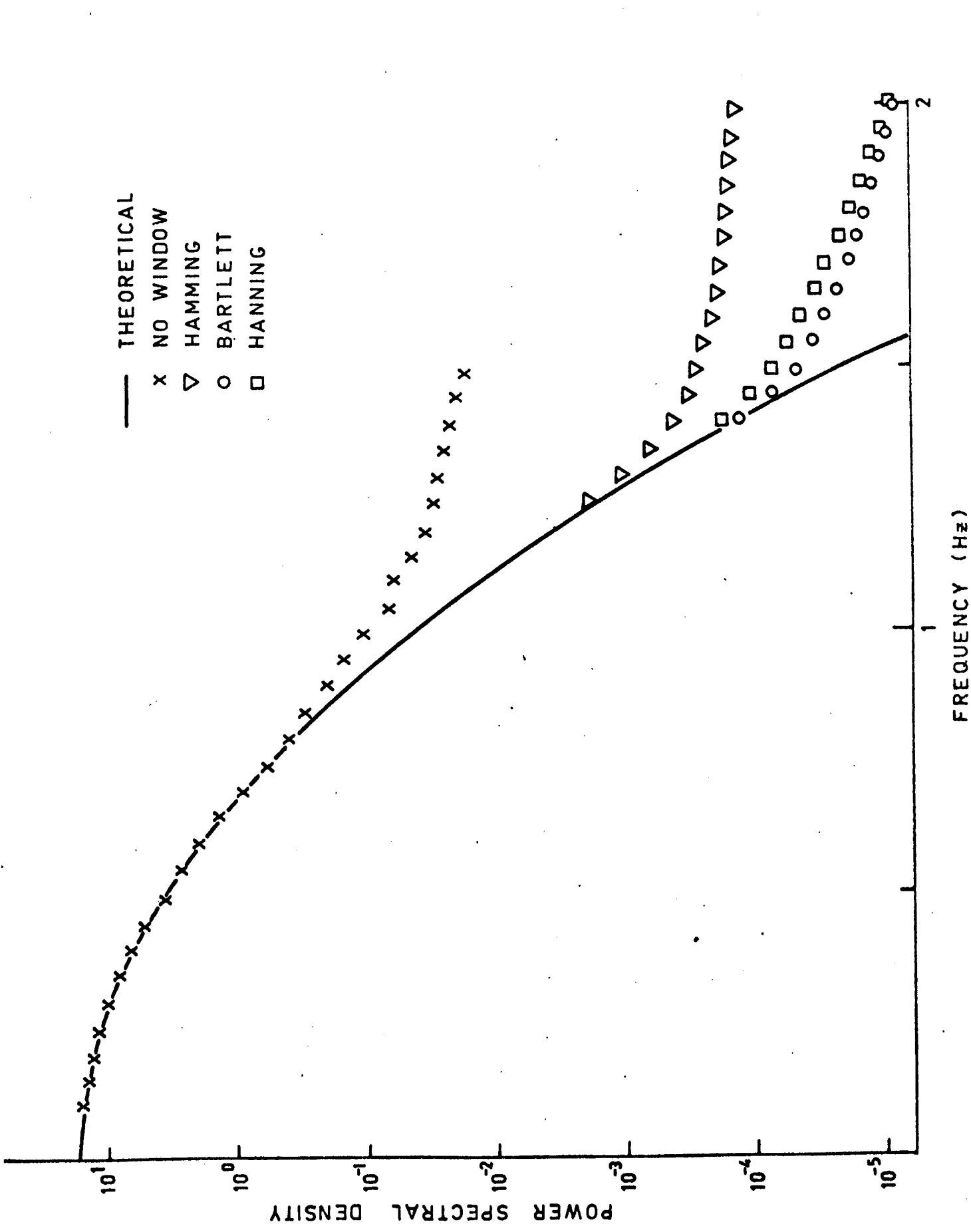

FIGURE II.1 Effect of data windows on spectral leakage for a time-series with a Gaussian power spectrum.

is assigned to the centre of the averaged frequency band. The frequency resolution is now $\Delta f' = M \Delta f$ but the variance of each estimate is reduced by a factor M. Alternatively the original time series may be separated into M non-overlapping segments, each of length $L = N/M$. The periodograms of each of these segments is computed separately and the spectral estimate for each frequency is then formed as the average of the L estimates

$$P_k = \frac{1}{M} \sum_{\ell=1}^{M} P'_{k\ell} \qquad \text{---(2.11)}$$

where $P_{k\ell}$ is the kM estimate from the ℓM block

The final frequency resolution is

$$\Delta f' = \frac{1}{L\Delta t} \qquad \text{---(2.12)}$$

and again, the variance of the estimates is reduced by a factor of M.

Filtering of data can be achieved via the FFT by setting the appropriate real and imaginary Fourier coefficients in the unwanted frequency bands to zero and applying an inverse Fourier transform (Buckley, private communication). This is equivalent to a circular convolution of the data with a $\frac{\sin x}{x}$ function and the end sections become contaminated with each other. This is overcome by adding zeros to each end of the data until the number of data points has been doubled, prior to applying the inverse transform.

The autocovariance function p(j) is the Fourier transform of the power spectrum

$$\rho(j) = \frac{1}{N\Delta t} \sum_{k=o}^{N-1} P_k \exp(2\pi i j k/N) \quad j = 0,1,..,N-1 \qquad \text{--- (2.13)}$$

where $\rho(j)$ is the value at a lag of $(j.\Delta t)$.

Normalization by the sample variance $\bar{X}^2 = \rho(o)$ yields the autocorrelation function. Since the power spectral estimates are also required in the data

analysis it is faster to apply the FFT to these estimates than to calculate the auto-correlation function directly as the sum of the lagged products

$$\rho\ (j.\Delta t) \;=\; \frac{1}{N} \sum_{n=1}^{N-j} x_n \; x_{n+j} \qquad j=0,1,\ldots,\ m \qquad \text{---(2.18)}$$

where M is the maximum lag required. There is one difference between these methods in that the FFT formulation performs a "circular" summation whereas the direct method performs a "linear" summation. (Bendat and Piersol, 1971). This reduces the maximum lag to T/2 for the auto-correlation function derived via the FFT but since we are normally only interested in cases where the data length is much greater than the correlation length it is not a serious problem. If necessary it can be overcome by adding zeros to the original data before applying the FFT.

APPENDIX 3

DERIVATION OF SCINTILLATION INDEX AND SECOND MOMENT IN NEAR-FIELD

The temporal power spectrum, $P_{It}(f)$, resulting from a thin Gaussian scattering screen can be expressed in the form (see equation 7.7)

$$P(f) = A \exp(-Bf^2) \left[1-\cos(Df^2+E) \right] \qquad \ldots(3.1)$$

where

$$A = \frac{2^{\frac{1}{2}}\phi_0^2}{\pi^{\frac{1}{2}}\alpha_1}$$

$$B = (2\alpha_1)^{-1}$$

$$C = \cos^{\frac{1}{2}} \theta_2$$

$$D = \frac{2\pi\lambda z}{v^2}$$

$$E = \theta_2/2$$

The scintillation index, m, and second moment, f_2, are defined by

$$m^2 = \int_{-\infty}^{\infty} P_{It}(f)\, df \qquad \ldots(3.2)$$

$$f_2^2 = \int_{-\infty}^{\infty} f^2\, P_{It}(f)\, df/m^2 \qquad \ldots(3.3)$$

Evaluation of (3.2) and (3.3) using $P_{It}(f)$ from (3.1) reduces to a solution of the two integrals

$$I_\alpha = \int_{-\infty}^{\infty} f^\alpha \exp(-Bf^2) \cos(Df^2+E)\, df \qquad \ldots(3.4)$$

where $\alpha = 0,2$. We can substitute

$$\cos\theta = \tfrac{1}{2}(e^{i\theta} + e^{-i\theta})$$

and split the integral into two parts

$$I_\alpha = J_\alpha + J'_\alpha$$

where

$$J_\alpha = \tfrac{1}{2} \int f^\alpha \exp(iE - Bf^2 + iDf^2)\, df$$

$$J'_\alpha = \tfrac{1}{2} \int f^\alpha \exp(-iE - Bf^2 - iDf^2)\, df$$

Complete the square of the exponent of the two integrals;

$$iE - Bf^2 + iDf^2 = -(af^2) + c$$

$$-iE - Bf^2 - iDf^2 = -(a'f^2) + c'$$

where $a^2 = B - iD$

$a'^2 = B + iD$

$c = iE$

$c' = -iE$

Now let $x = af$, so that

$$J_\alpha = \frac{\exp(c)}{a^{1+\alpha}} \int_{-\infty}^{\infty} x^\alpha \exp(-x^2)\, dx$$

Since $$\int_0^\infty \exp(-x^2)\, dx = \pi^{\frac{1}{2}}$$

we have $$J_0 = \frac{\exp(c)\pi^{\frac{1}{2}}}{a} \qquad \ldots(3.5)$$

We also have

$$\int x^2 \exp(-x^2)\, dx = -\tfrac{1}{2}\left[x \exp(-x^2)\right] + \tfrac{1}{2}\int \exp(-x^2)\, dx$$

which leads to the result

$$J_2 = \frac{\exp(c)\pi^{\frac{1}{2}}}{2a^3} \qquad \ldots(3.6)$$

Similar results are obtained for the integrals J'_0 and J'_2. Substitution of these results into the above expressions (3.2 to 3.5) leads, after some tedious algebraic manipulation, to the relations for m^2 and f_2^2 given in Chapter 7 (relations 7.16 and 7.17).